Controlling Cell Behaviour: the Connection Between Topography and Mechanical Properties of Biomaterials

Sören Hecht

Submitted in fulfilment of the requirements for the degree of Doctor of Philosophy in Biomedical Engineering. October 2025

James Watt School of Engineering
College of Science and Engineering
University of Glasgow, UK

Abstract

Cells respond to their mechanical environment *in vivo*, which can be separated into the stiffness and topography of the environment. It drives the cell phenotype. The topography within a range of 100 nm is of special interest because it falls within the size range of protein adhesions. Thus, it is replicated *in vitro* in fabricated biomaterials to study the effect of the mechanical environment. This thesis aims to investigate the response of the preosteoblast cell line MC3T3 as a well-studied standard cell line to its mechanical environment, with a focus on morphological profiling and traction force microscopy. We analyse the phenotype based on the morphology of the cells using the Cell Painting method. The cell response is dependent on the mechanotransduction pathway. Using activators and inhibitors of the mechanotransduction pathway in combination with 100 nm diameter nanopits showed a mechanotransduction response over time, from an initial Ca^{2+} signalling to a decrease in intracellular tension and adhesion after four days, and ultimately to senescence and commitment to osteogenic differentiation, as indicated by decreased filopodia and lamellipodia formation. The nanopits have a diameter of 100 nm, a depth of 100 nm, and a centre-to-centre spacing of 300 nm in both square and hexagonal arrays, with and without controlled disorder. We analyse 78 different types of nanopits with varying diameters, disorder, and pitch, as well as six gratings with depths of 200 nm and widths ranging from 200 nm to 10 µm, to have an in-depth analysis of the correlation between phenotype and topography parameters. The gratings cause a substantially different cell morphology compared to the nanopits. They need to be smaller than 5 µm to influence cell morphology. The disorder has the strongest correlation with changes in morphology from the studied topography parameters. We aim to combine the nanotopography with the material stiffness of the biomaterial in the analysis and study the effect of varying nanotopographies on cellular traction forces. However, we are unable to study it due to the challenging fabrication of the required hierarchical micropillars with nanopits on top. We successfully created polydimethylsiloxane (PDMS) micropillars with a diameter of 5.93 ± 0.15 µm and a height of 18.61 ± 0.28 µm using a SU-8 master. We measured a traction force of 10 nN, which aligns with the traction forces reported in the literature for smaller diameter pillars with lower spring constants.

Acknowledgement

First of all and foremost, I would like to thank Nikolaj Gadegaard for the opportunity to pursue my PhD in his lab and for his kind and helpful supervision. It was a joy working under you. Thank you for always encouraging me to try my ideas and pushing me into new directions and fields. I am also grateful for his vast network of contacts, which allows us to ask for advice when we run into a dead end with our knowledge.

I want to thank my second supervisor, Professor Laura Machesky, for her idea regarding the chemical perturbation library. I would also like to thank Professor Thomas Otto for advising me to try the Seurat method and for providing me with helpful guidance on data handling. I also must thank Professor Bjørn Sand Jensen for the great discussion on how we could analyse the large nanotopography library and possibly predict new topographies from it.

The last years would not have been the same without the people in the lab. Duarte and Iliyana, who have been there from the start, helped me feel at home when I arrived in Glasgow as part of the BIG group. Badri and Ramesh, with whom I spent only a short time in the lab, but had the joy of sharing an office, all the other people who joined later, like Maia, Rui, Euan, Nghia, Nicholas, Rakshit, and Viltenis, joined our lunches at the GUU and shared a portion of chips. Also, many thanks to the technicians who always kept the lab running, even when it sometimes felt like the building around it was falling apart. A special thanks there to Alysha, Karen, Kasia and Haitham. Not only in the Rankine lab, but I was also blessed with great colleagues; all the staff of the James Watt nanofabrication centre have been nothing but welcoming and helpful. A special thanks goes to Stephen Thoms, who helped me with his incredible knowledge of e-beam lithography, and Paul, who was always happy to answer any questions I had about e-beam lithography and helped me optimise my jobs to minimise the time they took up on the e-beam tool. To Linda, Sarai, and Archie, who took on the challenge of creating a negative copy of a photomask and delivered it in a short time.

I would also like to thank my family and friends for their constant support over the last four years. I would not be here without the BaNaNOS from my studies that made studying science a joy and always made it feel like coming back home when visiting Hamburg. A special thanks also to the Glasgow University handball club, with whom we had both less successful and more successful times, such as when becoming Scottish university champions. It was always a joy with you, and I know that I will miss going to Bank Street on Friday evenings when I come from the lab and you come from training. It was always a blast sharing some pints, free pizza, and a lot of laughs with you, and getting my head free from any PhD-related stress. It was always fun with you, both on and off the court, on adventures to away games, such as travels to Dundee, or at BUCS. I am glad that we continue to visit Liverpool with current and past players as a yearly reunion, and I hope this new tradition will continue for a long time.

Author's Declaration

I hereby declare that the contents of this thesis are original and my own. The fluorescence staining and imaging of a few inhibitor samples in Chapter 4 were performed by Viltenis Zilys under my supervision as part of his summer studentship. All work performed by colleagues and samples received by others are mentioned in the thesis. All the references made to the work of others are cited and included in the bibliography.

Sören Hecht, 2025

Poster Presentations

Hecht et al, MC3T3 Cells Morphology Correlates with Mechanotransduction Pathways, Osteogenesis, and Nanotopography Response. Poster presentation at: BioMedEng 2024 Conference, London, United Kingdom, September **2024.**

Contributions to Publications

Menezes et al, A membrane's blueprint: In silico investigation of fluid flow and molecular transport as a function of membrane design parameters in organ-on-a-chip. *Chemical Engineering Journal*, **2024**, 481.

Menezes et al, Scalable, Transparent, and Micro: 3D-Printed Rapid Tooling for Injection Moulded Microfluidics. *Advanced Engineering Materials*, **2024**, 26.

Table of Contents

Table of Figures

List of Tables

Glossary of Abbreviations

BAR protein	Bin/amphiphysin/rvs domain protein
BSA	Bovine Serum Albumin
BSSA	BioSurface Structure Array
CCA	Canonical Correlation Analysis
DESI	Desorption Electrospray Ionization
DMSO	Dimethyl Sulfoxide
DRIE	Deep Reactive Ion Etching
E-beam	Electron Beam
EC	Ethylene Carbonate
ECM	Extracellular Matrix
ER	Endoplasmic Reticulum
FAK	Focal Adhesion Kinase
FBS	Fetal Bovine Serum
FFT	Fast Fourier Transform
FITC	Fluorescein Isothiocyanate
FOTS	Trichloro(1H,1H,2H,2H Perfluorooctyl)silane
GJ	Gap Junctions
HBSS	Hanks' Balanced Salt Solution
HEX	Nanopits in hexagonal array with standard dimensions of 100 nm diameter, 100 nm depth, and 300 nm centre-to-centre spacing
HMDS	Hexamethyldisilazane
HMS-301	(25-35% Methylhydrosiloxane)-Dimethylsiloxane Copolymer, Trimethylsiloxane terminated
h-PDMS	Hard PDMS
HSQ	Hydrogen Silsesquioxane

IMP	Integrated Mechanobiology Platform
IPA	Isopropanol
LSM	Laser Scanning Microscope
MAD	Median Absolute Deviation
MAPK	Mitogen-Activated Kinase
MARC	MultiARChitecture
MCC 80/20	MicroChem Primer 80/20
MIBK	Methyl Isobutyl Ketone
MSC	Mesenchymal Stromal Cell
NHEX	Nanopits in hexagonal array with a disorder of 50 nm to the ideal HEX array
NIL	Nanoimprint Lithography
NSQ	Nanopits in square array with a disorder of 50 nm to the ideal SQ array
NSQP	Nanopits in square array with a disorder of 50 nm to the ideal SQ array with varying pitch
OCN	Osteocalcin
PBS	Phosphate-Buffered Saline
PCA	Principal Component Analysis
PDMS	Polydimethylsiloxane
PET	Polyethylene Terephthalate
PM acetate	Propylene Glycol Monomethyl Ether Acetate
PMMA	Poly(Methyl Methacrylate)
poLCA	Polytomous Variable Class Analysis
PS	Polystyrene
RO water	Reverse Osmosis Water
ROCK	Rho-Associated Protein Kinase

RPCA	Reciprocal PCA
RWC	Rank Weighted Colocalization
scRNA-seq	Single-Cell RNA Sequencing
SEM	Scanning Electron Microscopy
SIP 6831.2	Platinum-divinyltetramethyldisiloxane complex in xylene
SIT 7900	2,4,6,8-Tetramethyl-2,4,6,8-Tetravinylcyclotetra-Siloxane
SQ	Nanopits in square array with standard dimensions of 100 nm diameter, 100 nm depth, and 300 nm centre-to-centre spacing
SQP	Nanopits in square array with standard dimensions of 100 nm diameter, 100 nm depth, and varying pitch
TMAH	Tetramethylammonium Hydroxide
t-SNE	t-Distributed Stochastic Neighbour Embedding
UMAP	Uniform Manifold Approximation and Projection
VDT-731	(7.0-8-0 % Vinylmethylsiloxane)-Dimethylsiloxane Copolymer (Trimethysiloxyl Terminated)
WGA	Wheat-Germ Agglutinin
YAP	Yes-Associated Protein
ZCA	Zero-Phase Component Analysis

1.Introduction

1.1. Motivation

In tissue regeneration and stem cell differentiation, the biomechanical environment of cells has gained high interest, as it has been shown to influence cell behaviour[1-3]. The topography, as well as the mechanical properties, of a surface affect the cell response[4, 5]. A special focus has been placed on the differentiation of stem cells on nanotopographies, as different topographies can direct differentiation in different directions. The biomechanical environment is also of high interest in wound healing[6] and cancer migration[7, 8]. Thus, we are interested in gaining a better understanding of how the biomechanical environment affects the cellular behaviour, with the ultimate goal of contributing to the development of more effective tissue regeneration.

The cellular response to the biomechanical environment is driven by mechanosensing and subsequent mechanotransduction, which converts mechanical signals into biochemical signals within the cell[9-11]. The study of mechanotransduction through nanotopographies has many challenges. Conventionally, the response to topography is analysed by omics techniques that are expensive and time-consuming[12-14]. In our research, we will introduce a novel approach by utilizing the morphological profiling technique, Cell Painting, as a high-throughput method that stains the organelles of cells to obtain a comprehensive picture of the cell's morphological phenotype[15, 16]. We aim to map the morphological response of cells on nanopits, together with activators and inhibitors of mechanotransduction pathways, to gain insights into activated pathways on these topographies. The Cell Painting method has been widely used; however, this is the first study to attempt its application with nanotopographies.

Another challenge in working with nanotopographies is identifying the ideal topography. Different topographies elicit distinct responses from cells and few studies of large nanotopography libraries have been conducted so far [17]. Since many of the traditional analysis methods are expensive and time-consuming, only a limited number of topographies can be tested with them. Thus, most of the

time, only large differences in topographies, such as gratings, pits, or pillars, are tested, rather than the fine dimensions of the topographies. Only basic morphological features or general responses as the expression of differentiation markers are studied for the screening of extensive libraries. In our study, we have designed a comprehensive research plan that overcomes these limitations. We want to test the effects of small differences in nanotopography on cell response using a library of nanotopographies with pitch differences in steps of 10 nm and disorder in steps of 5 nm, with diameters ranging from 120 nm to 10 µm. We believe that small differences in the topographic arrangement have a significant influence on cell response. Our main goal is to see if we can use this systematic library of nanotopographies with a range of modified parameters to predict new topographies that replicate the morphome of a desired cell phenotype. If we have a cell with a morphology caused by a perturbation or differentiation, can we predict a new topography that will cause the same cell morphology? So far, nanotopography libraries have only been used to identify the optimal topography for a given application, such as differentiation into a desired cell line. We want to take it one step further to create a new topography from the cell's morphome in a given state and the nanotopography library used. We will use the high-throughput Cell Painting method to obtain an in-depth analysis of the cell state, combined with custom-made injection-moulded 24-well plates featuring a variety of nanopit arrangements and gratings, to ensure a thorough exploration of the cellular response to different topographies.

The cell responds to the topography of its environment and the mechanical properties, such as the material stiffness. Both influences have been widely studied, but they are most often examined individually rather than in combination[18, 19]. We aim to combine both parameters to obtain a complete picture of the biomechanical response. It is known that cellular traction forces are adhesion-dependent and that nanotopographies decrease the cellular adhesion[19]. Thus, we aim to study how different topographies affect the cellular traction force on material of varying stiffness. We want to know how the two factors of topography and material stiffness interact with each other and if one of the factors is dominant in the cell response.

1.2. Thesis structure

Following this introduction, the thesis embarks on a comprehensive literature review of the latest advancements in mechanotransduction analysis and morphological profiling, with a specific focus on Cell Painting and traction force microscopy in Chapter 2. This review, which underscores the importance of effective data integration and batch correction, is a crucial foundation for the subsequent research. The general methods employed across the various chapters are then presented in Chapter 3. Throughout the thesis, we utilize the well-studied pre-osteoblast cell line MC3T3, known for its robust response to the studied nanopits, as it differentiates into mature osteoblasts on said nanopits[20].

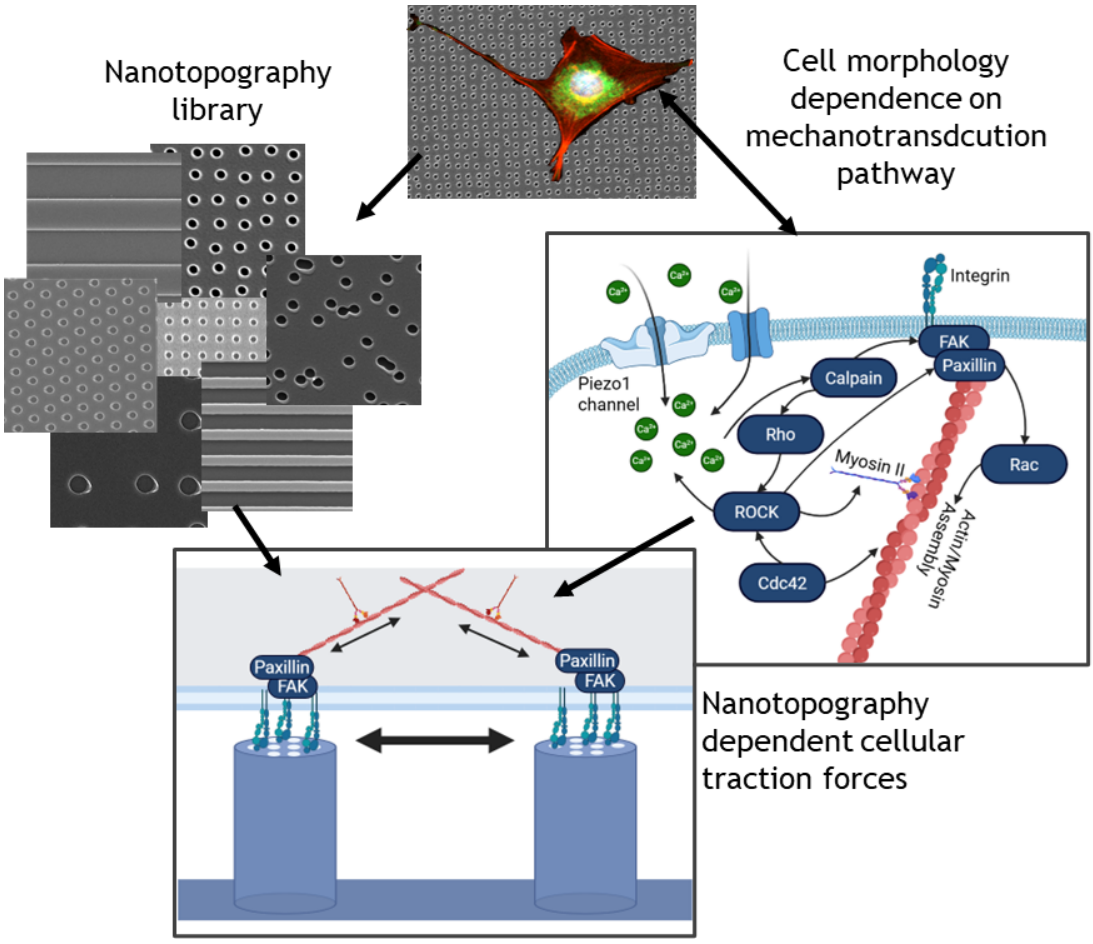

***Figure 1.1**: Schematic overview of the work performed in the thesis. The influence of nanotopography on the mechanotransduction pathway is studied using morphological profiling as well as cellular traction forces. Schematic created in BioRender.*

In Chapter 4, we aim to predict a mechanotransduction pathway during differentiation using the innovative Cell Painting method. We believe that the morphological changes observed in MC3T3 cells when perturbed with inhibitors and activators of key points in the mechanotransduction pathway will be similar to those of MC3T3 cells on nanopits. We aim to utilise these similarities to gain a deeper understanding of the differentiation of MC3T3 cells on nanopits over time.

We successfully mapped the nanotopography responses in relation to a variety of activators and inhibitors and found that cell differentiation through nanopits undergoes a journey. The first response is dominated by the calcium signalling, which is known to increase the expression of the early osteogenic marker Runx2. Then, intracellular tension and adhesion decrease, while oxidative glycolysis increases during differentiation, until the cell reaches senescence, characterised by reduced lamellipodia and filopodia formation. Additionally, we have demonstrated, as a proof-of-concept, that Cell Painting can be used to study the response to nanopits, even detecting differences in pit arrangement in a square lattice, with disorder, and in a hexagonal lattice. Furthermore, we pick up the concentration dependencies of activators and inhibitors, as well as their similarities and differences in their mechanisms of action.

In Chapter 5, we expand the morphological profiling to a library of 84 different nanotopographies. We have demonstrated that the morphome is dependent on the geometry of the nanotopography. Thus, we believe that we can utilise an extensive nanotopography library to identify an ideal topography and develop new topography designs from it.

We use nanopits with varying sizes, pitches, and disorder, as well as gratings of different sizes. We have noticed that the subtle changes we observe in the morphome through changes in topography are much more challenging to identify than those resulting from activators and inhibitors. Thus, careful feature selection is even more important, as is a good batch correction. We can correct for the batch effect using a Seurat method. The prediction of different nanotopographies from morphological features is possible using linear regression, as long as only one parameter is changed in the dataset. Predicting a new topography using the complete set of geometrical parameters remains a challenge.

In Chapter 6, we aim to combine the nanopits with the material's mechanical properties. We believe that by creating micropillars with nanopits of varying arrangements on top, we can study the topography-dependent cellular traction force. By varying the micropillar dimensions, we can alter the stiffness and investigate the impact of material stiffness on adhesion, thereby examining the traction forces associated with different topographies.

The fabrication of micro-/nanopillars proved to be highly challenging. We employed both electron beam lithography and photolithography, utilizing various resists and techniques. However, no fabrication method has yet produced reliable micropillars with nanopits on top. Operating at the limits of each fabrication method in a multi-step process, the fabrication remains extremely challenging. Despite these hurdles, we managed to create micropillar arrays of the desired dimensions, with a diameter of 6 µm and a height of 18 µm, suitable for traction force microscopy with MC3T3 cells; however, the addition of nanopits remains a challenge.

2. Literature review

2.1. Mechanotransduction

The environment surrounding cells, known as the cellular microenvironment, strongly affects their behaviour[2, 4, 11, 21-24]. This microenvironment can be broadly categorised into the chemical and biophysical environments. The chemical environment is described by the chemical composition and the charge of the biomaterial, as well as the composition of the media. The biophysical environment, on the other hand, describes the mechanical properties and topography of the substrate on which the cells grow. This work primarily focuses on the effect of the biophysical environment, with a special emphasis on the influence on cell differentiation. It has been shown in many studies that the mechanical properties of the extracellular matrix (ECM) strongly affect the cell fate *in vivo* and *in vitro*[1, 2, 22, 25-29]. The mechanical properties of the cell environment can be separated into the stiffness of the environment and its structure. Especially, the nanotopography, which refers to the surface topography at the nanoscale level, has been shown to have a significant impact on the cell response[8, 25, 26, 30-32].

Additionally, the importance of tissue or biomaterial stiffness on cell behaviour has been shown in many studies[4, 21, 33]. One example is the work of Engler et al., where they showed that matrix elasticity can direct mesenchymal stem cells (MSCs) differentiation towards different cell lineages[5]. For instance, collagen-coated polyacrylamide gels with varying elasticity are used to mimic the elasticity of brain tissue (E_{Brain} ~ 0.1-1 kPa), muscle tissue (E_{Muscle} ~ 8-17 kPa), and osteoid tissue ($E_{Osteoid}$ ~ 25-40 kPa)[34]. The majority of MSCs commit to the phenotype that the matrix elasticity corresponds to. That clearly shows that substrate stiffness plays a significant role in stem cell differentiation and must be considered when designing biomaterials. Tissue stiffness also plays an important role in cell migration as cells tend to move towards stiffer surface. This effect is called durotaxis[7, 35, 36].

The cellular mechanotransduction can be separated into three main parts. First, biomechanical sensing of the environment occurs, followed by the transduction of extracellular conditions into cells, and finally, cellular translation into biological responses, including increased and decreased protein expression and adaptation of transcription (see Figure 2.1C)[10, 11, 23, 30]. Cells sense their biomechanical environment through membrane proteins, where integrins and ion channels are of high importance. Integrins are heterodimers that change into an active formation when binding to the extracellular matrix[37]. Focal adhesion kinase (FAK) binds to the activated integrins to build focal adhesions and transfer the mechanical properties of the ECM to the cytoskeleton through the proteins talin, vinculin, and paxillin. More proteins are involved in this transfer, but talin, vinculin, and paxilin have been identified as essential proteins in transferring the mechanical signals[11]. The distribution and number of adhesion proteins, as well as the pull, affect further signalling cascades inside the cell. The focal adhesion proteins translate the pull to the actin-myosin cytoskeleton, where the forces are further transduced into signalling pathways[8, 38-43]. The focal adhesion is a loop, as the induced contraction of Actin is again enhancing the FAK activation. The formation of focal adhesions and adaptation of cytoskeletal arrangement and tension through the ECM activate signalling pathways and nuclear mechanotransduction. Yes-associated protein (YAP) is the essential protein in nuclear mechanotransduction to translate the cytoskeletal tension to the nucleus to activate transcription factors[28, 40, 44-47].

The transport of YAP into the nucleus is not yet fully understood. Nuclear compression can promote nuclear translocation of YAP. The cytoskeleton can mediate nuclear compression, translating external factors such as microstructures and substrate stiffness. Direct compression of the nucleus by external forces increases YAP transport within the nucleus as well[48]. During nuclear compression, nuclear pores are stretched to allow YAP transport; however, nuclear swelling does not allow the pores to open for YAP transport. Thus, the mechanism of YAP nuclear translocation is more complex than a simple membrane stretching to open the nuclear pores. The detailed mechanism is still under investigation[49]. Another part of the nuclear mechanotransduction is the direct deformation of the nucleus due to the cytoskeletal contractions, which results in

a rearrangement of chromatin in the nucleus[50]. In this work, we will not focus on nuclear mechanotransduction but on signalling pathways around the cytoskeletal arrangement and stability.

The Rho family proteins play a crucial role in the mechanotransduction pathways and cytoskeletal arrangement and stability[51-56]. We will focus on the most well-known proteins Cdc42, Rac, and RhoA. RhoA activates Rho-associated protein kinase (ROCK). ROCK is known to activate myosin II, a motor protein essential for actin contraction and the formation of stress fibres together with f-actin. Stress fibres are bundles of F-actin and myosin II that propagate the forces of the focal adhesions through the cell[57]. Thus, it has been shown in many studies that the ROCK signalling pathway plays a key role in mechanotransduction[58]. Rac is known to promote the formation of lamellipodia and is therefore essential for cell migration. Cdc42 promotes the formation of filopodia, which sense the extracellular environment. Cdc42 also activates Rac[54]. The effect of Cdc42, Rac and Rho on the actin organization is shown in Figure 2.1B.

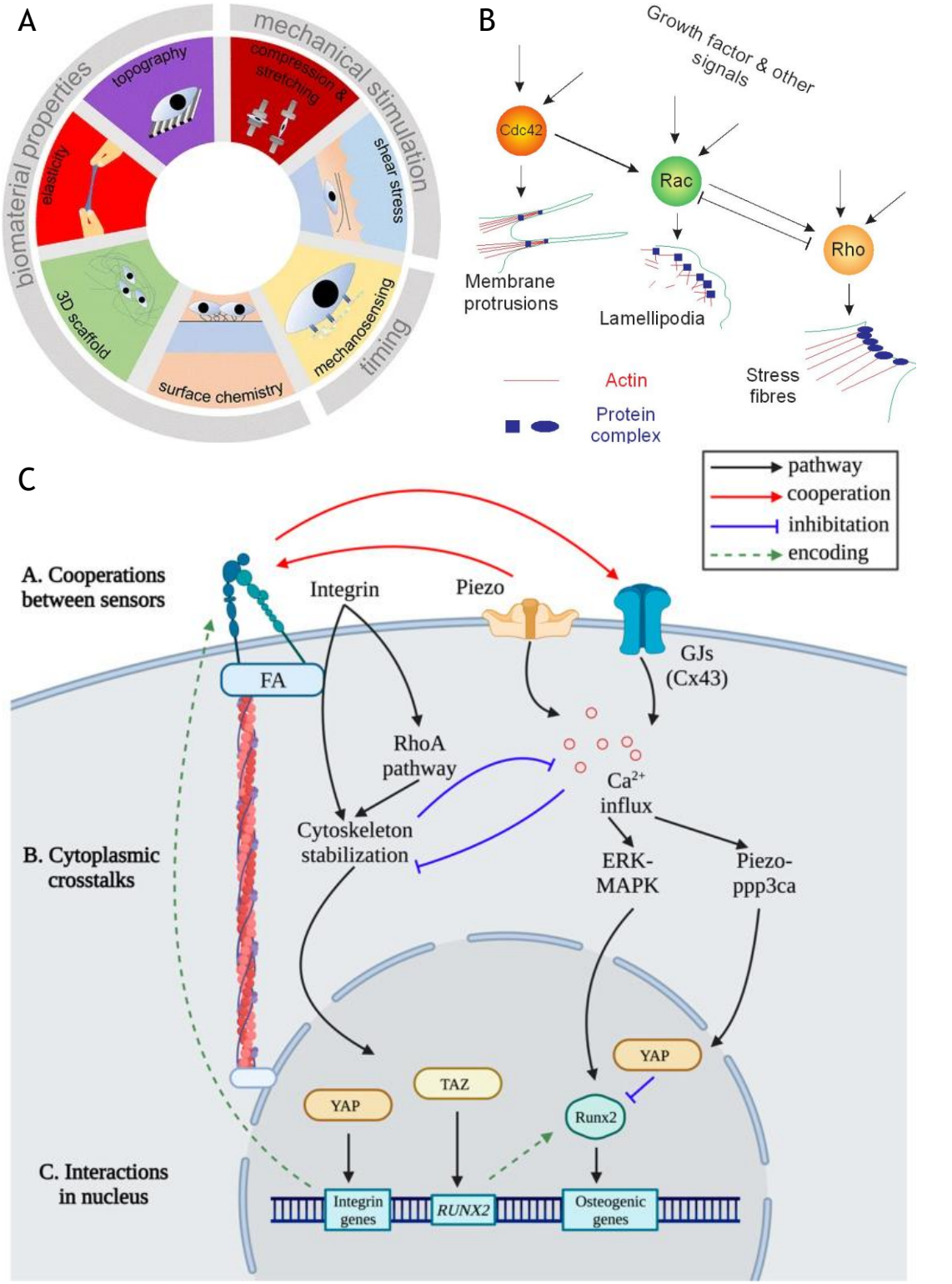

***Figure 2.1**: Overview of the cell response to its mechanical environment. Cellular functions depend on environmental influences of the biomaterials, and external forces (A). (B) shows a schematic representation how the Rho-GTPases RhoA, Rac1 and Cdc42 affect the actin structure organization. RhoA is responsible for stress fibre formation, Rac1 for lamellipodia formation, and Cdc42 for filopodia formation. [54] (C) shows a diagram of the interaction between the different mechanosensing and mechanotransduction pathways in osteogenesis. FA are the focal adhesions, GJs are gap junctions, piezo-ppp3ca and ERK-MAPK are Ca^{2+} dependent signalling pathways, and YAP and TAZ are transcriptional regulators. [59] The images are reprinted with permission of Goetzke et al.(A),[22] Samuel et al.(B),[54] and Liu et al.(C)[59]*

The cells respond to nanotopographies through focal adhesion arrangements and localised changes in membrane curvature. On soft materials, the focal adhesions are scarce, and the topography is sensed by curved adhesions[60]. In particular, nanostructures protruding from the surface induce strong membrane deformations[61]. The BAR domain (bin/amphiphysin/rvs) proteins are essential for membrane curvature sensing and generation[62, 63]. The BAR proteins have a curvature that is either concave at the membrane-binding site for BAR and F-BAR proteins and convex for I-BAR proteins. The F-BAR protein family is known to play a crucial role in sensing nanotopographies and translating membrane curvature into the mechanotransduction pathway via the Rho GTPases. FBP17, a curvature-sensing protein of the F-BAR family, is active when it is bound to the membrane and induces cytoskeleton remodelling through the Rho GTPase regulation[64]. Lou et al.[61] showed that high aspect ratio nanopillars with a diameter below 400 nm promote the formation of branched F-actin and reduce the formation of stress fibres and mature focal adhesions. The promotion of the branched F-actin is regulated by N-WASP, Arp2/3 and Toca-1, which in turn interact with Cdc42 that is essential for the actin cytoskeleton organisation as described above[65]. Zhang et al.[60] showed that the F-BAR domain of FCHo2 forms curved adhesions in combination with the integrin ITGB5 on soft nanostructures, where few focal adhesions are found. Curved adhesion transduces mechanical stimuli to the cytoskeleton via talin-1.

Ion channels are another key factor in mechanosensing[66, 67]. In particular, the force-activated PIEZO channels sense differences in the ECM, such as its stiffness, structure, and chemical composition. The PIEZO family includes the PIEZO1 and PIEZO2 channels. They are mechanosensitive Ca-ion channels that are activated by tension on the cell membrane. In a closed state, the channel is in a curved formation. Tension on the membrane flattens the channel and opens it[68, 69]. Thus, the PIEZO ion channels sense surface stiffness through the difference in membrane tension. The activation also depends on the focal adhesion organisation, as shown by Ellefsen et al.[70], who identified the most PIEZO1-dependent Ca^{2+} flickers in areas of high traction force. Cells were seeded with local constraints by plating them on square fibronectin islands. They noted the most flicker events at the corner of the squares, where the most focal adhesions

are also localised and the traction force is the highest. The intracellular Ca-ion concentration plays a crucial role in mechanotransduction, as it affects signalling pathways similar to those influenced by focal adhesions. It has been shown that an increase in intracellular Ca^{2+} concentration activates the ROCK pathway, stabilises the actin cytoskeleton and promotes focal adhesions. It is also essential for the mitogen-activated kinase (MAPK) pathway, an important pathway in osteogenic differentiation[59].

Depending on cell type and application, different nanotopographies are used to achieve the desired effect[71-73]. The desired effect can, for example, be differentiation into a specific cell lineage. It is well known that the ECM's properties are crucial for the state and behaviour of cells in vivo. Therefore, nanomaterial designs often mimic the ECM's in vivo properties to create a biomimetic substrate. Topographies can be created in a controlled manner, for example, by electron beam lithography[74, 75], ion beam lithography[76], UV lithography[77], or molecular self assembly[78, 79]. The nanotopographies can also be fabricated in a random manner, for example, using electrospinning[80], carbon nanotubes[81] or surface roughness[82] (Figure 2.2 A-H). The fabrication techniques can be divided into bottom-up and top-down techniques[83-85]. Bottom-up techniques work on guided self-assembly. The nanostructures are built from smaller building blocks, as in electrospinning[80], carbon nanotubes[81], colloidal self-assembly[78] or DNA origami[86]. Top-down methods are lithography techniques that write a pattern into a material. The methods are often based around a beam writing the desired structure into a resist. Some examples include the above-mentioned electron beam lithography[74, 75], focused ion beam lithography[76], photolithography[87], and x-ray lithography[88]. Dry[89] and wet etch techniques[90], which can be used to create controlled surface roughness, are another option for top-down lithography techniques.

The nanotopography features shown in Figure 2.2 span a wide size range, from 50-60 nm for the carbon nanotube bundles, to surface roughness in the 100 nm to micrometre range, to electrospun fibres with a diameter of around 500 nm. Depending on the fabrication technique, feature sizes can be tuned from as small as 50 nm to microfeatures. One example of nanotopographies are nanogratings that are often used to support the elongated shape of neuron cells[91, 92].

Gratings are also used to align cells along the gratings. Nanopillars and nanopits are used in many varying applications in slightly different formations. The nanotopographies guide the formation of integrin clusters[57]. Depending on the size and distance of features, the cells can build integrin clusters. To build the integrin clusters, they require sufficient space to attach. That can be a continuous surface or a surface with a small enough gap. The number, size and distribution of integrin clusters dictate the cell response (Figure 2.2 I).

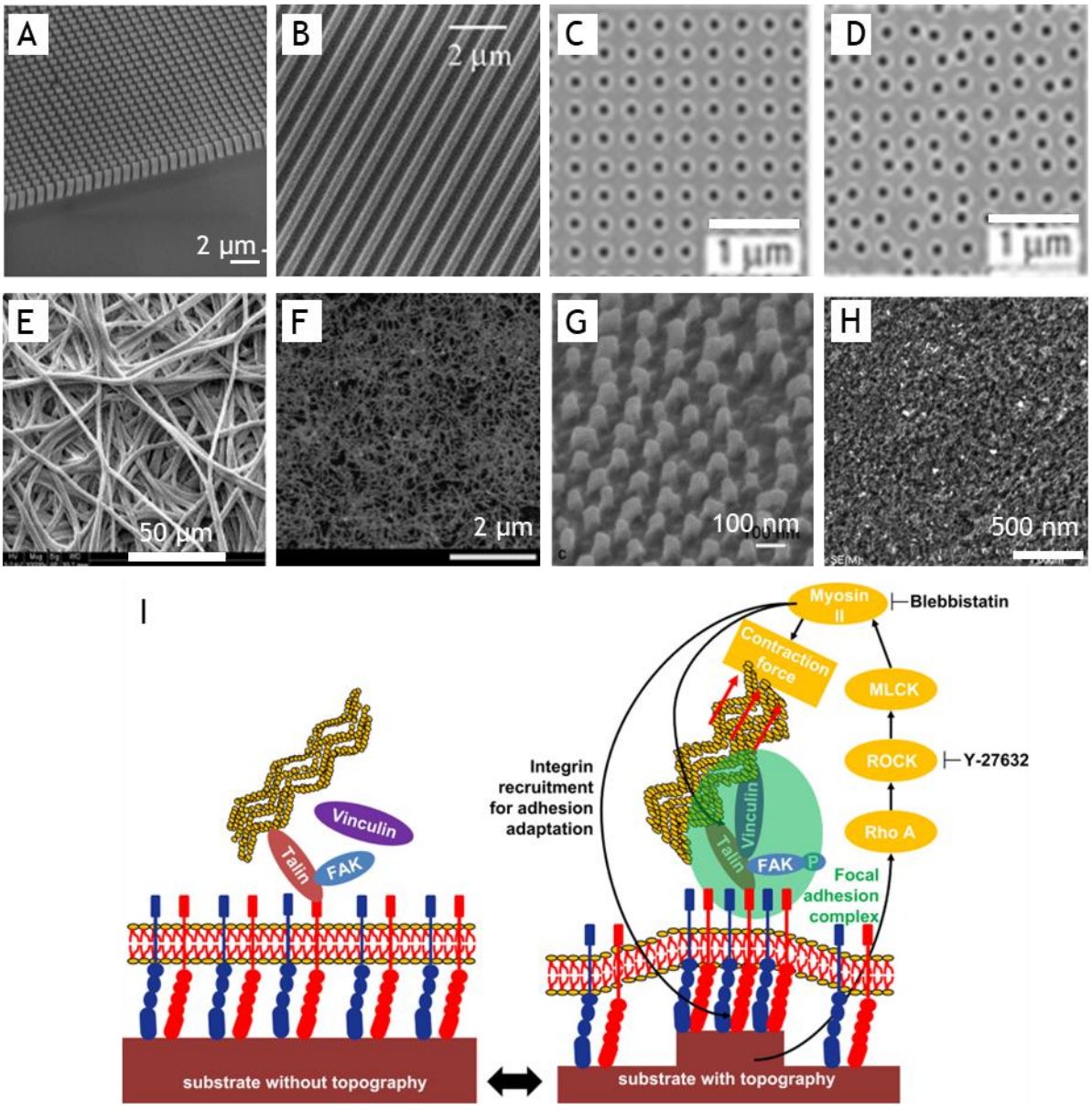

(caption for figure on previous page) ***Figure 2.2****: Overview of varying nanotopographies used in cell biology studies. SEM images of ordered nanopillars (A), nanogratings (B), nanopits in square (C) and near-square (D) formation, electro-spun nanofibers (E), carbon nanotubes (F), random nanopillars (G), and surface roughness (H). (I) shows a schematic representation how integrin clusters form due to topography to form focal adhesions that translate the forces into the cell through the actin cytoskeleton and ROCK signalling pathway. The images are reprinted with permission from Viela et al.(A)[93], Yim et al.(B)[94], Dalby et al.(C,D)[95], Chua et al.(E)[80], Tay et al.(F)[81], Sjöström et al.(G)[96], Ogino et al.(H)[82], and Seo et al.(I)[57].*

This work focuses on the nanotopography-induced osteogenic differentiation, as it has been widely studied with a range of nanotopographies, but the search for the optimal topography remains a challenge[27, 59, 97]. Mesenchymal stem cells and osteoprogenitor cells differentiate into mature osteoblasts on nanopillars and nanopits. Nanopillars of varying heights of 15, 55, and 100 nm[96, 98, 99], as well as nanopits of 120 nm diameter, 300 nm centre-to-centre spacing, and 100 nm depth, with varying geometrical arrangements, showed an increase in osteogenic differentiation[20, 25, 31, 100]. For the nanopillars, a height of 15 nm showed the highest increase of the early osteogenic marker Runx2 after 2 days and of osteocalcin (OCN) after 21 days. The focal adhesions increased in size with an increased height of nanopillars. The geometrical arrangement of nanopits affects the osteogenic differentiation by directing the focal adhesion arrangements. The nanopits are arranged in a square (SQ), hexagonal (HEX) and near-square lattice (NSQ50), where the pits are randomly displaced by 50 nm from an ideal square lattice. The NSQ50 topography shows the strongest expression of Runx2, osterix and OCN in the cells. The disorder produces areas that are large enough to form focal adhesions, while other areas are not big enough for the formation. It has been shown that focal adhesions need at least 70 nm to form[101, 102].

2.2. Morphological profiling – cell painting

Mechanotransduction pathways are analysed using many different methods. Often, omics techniques[12-14, 103-105] are used, which are time-consuming and expensive, limiting the number of experimental conditions that can be tested. The influence of different parts of the mechanotransduction pathway is not only analysed by omics techniques, but also by activation or inhibition of parts of the mechanotransduction pathway and study of the effect on cell functions, such as migration[106, 107], cellular traction forces[70, 108, 109], or protein

localisation[48, 60]. The expression of differentiation markers is not only analysed by omics techniques but also by fluorescence labelling of the markers[110]. Morphological profiling can be used as an alternative to omics techniques, offering a fast and cost-efficient approach that does not require specialised equipment beyond a basic fluorescence microscope[15, 16, 111-116]. In contrast to staining for differentiation markers or focal adhesions, morphological profiling provides general information about the state of the cell, similar to, for example, genomics or proteomics. Additionally, one of the key advantages of morphological profiling is its relatively unbiased approach, which provides a vast collection of features that are not selected based on known interactions. This open approach holds the potential for novel discoveries and relationships. In addition to image-based profiling, other profiling methods such as metabolomic[117-120], proteomic[119, 121-123], and gene expression[124, 125] profiling exist, with only gene expression profiling being truly high-throughput. While these techniques lack single-cell resolution, they are all aggregation methods, thus failing to report the heterogeneity in cell populations. However, current advances in classic omic techniques enable single-cell resolution, as demonstrated by two key examples: desorption electrospray ionisation (DESI) mass spectrometry[126-128] and single-cell RNA sequencing (scRNA-seq)[129-131]. Image-based profiling can be used in addition to omics techniques, as it can predict properties and provide new information, making it a valuable complementary tool. Image-based profiling has been used in conjunction with gene expression data, protein profiling, and proteome analyses[16, 113].

A special case of morphological profiling is Cell Painting, developed by the Carpenter lab[15], a renowned research group in the field of cell biology. Figure 2.3 visualizes the Cell Painting process. The Cell Painting method stains the F-actin cytoskeleton (phalloidin/Alexa Fluor 568 conjugate), endoplasmic reticulum (ER) (concanavalin A/Alexa Fluor 488 conjugate), Golgi and plasma membrane (wheat-germ agglutinin/Alexa Fluor 555 conjugate), mitochondria (MitoTracker Deep Red), nucleus (HOECHST 33342), and RNA (SYTO 14 green fluorescent stain) to visualise a wide range of organelles and, thus, cell functions. Depending on the experiment, adjustments are made to the used dyes to stain different relevant cell features. A major benefit of the chosen staining methods is the easy one-step

staining protocol, without the need for additional specific antibodies. This significantly speeds up the experimental process, reducing it from a full day to less than 2 hours. The stains are also chosen to paint a general picture of the cell state rather than an experiment-specific stain, as, for example, focal adhesions in the study of nanotopographies. The Carpenter lab's pioneering work in developing Cell Painting has significantly advanced the field of morphological profiling, providing researchers with a powerful and versatile tool for studying cell biology and disease mechanisms.

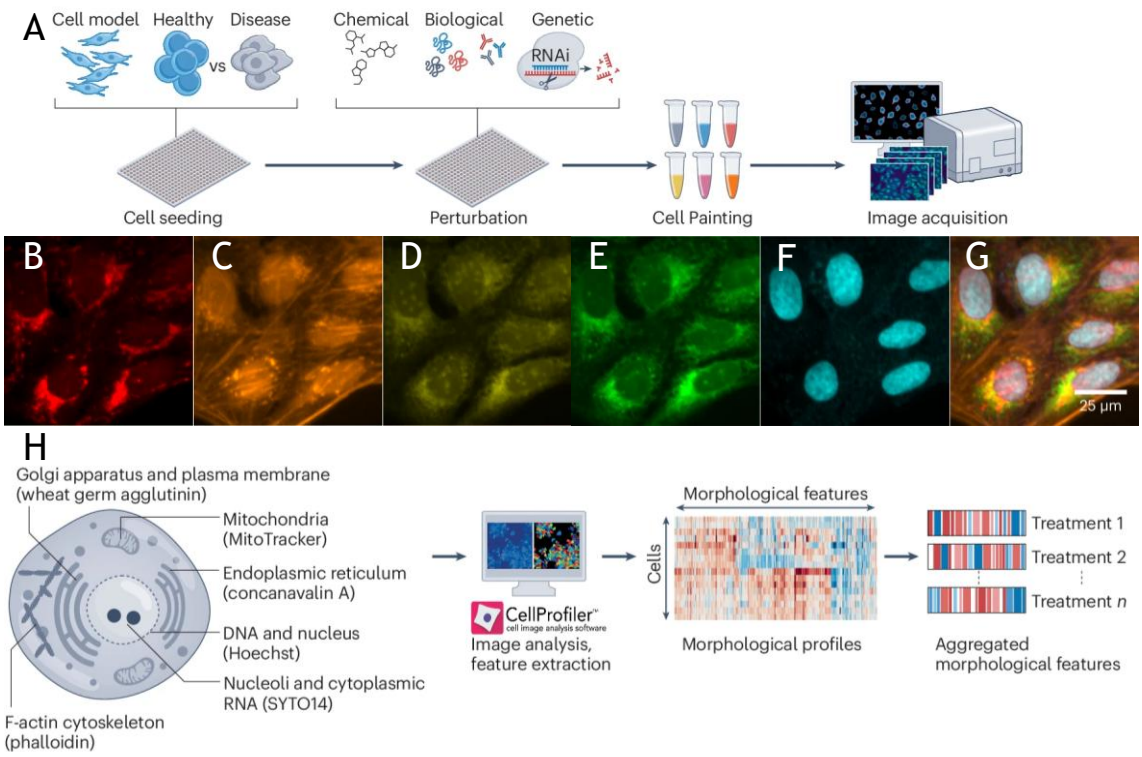

***Figure 2.3**: Diagram of the Cell Painting process. First, the cells are seeded, and perturbations are performed. Next, the Cells are stained and imaged by fluorescence microscopy (A). The obtained images are the mitochondria (B), actin cytoskeleton, Golgi and plasma membrane (C), nucleolar and cytoplasmic RNA (D), endoplasmic reticulum (E), DNA (F). A merged image is shown in (G). The information from the different organelle staining is analysed in CellProfiler, where per cell features are obtained. Those are then aggregated (H). Reprinted with permission of Seal et al.(A,H),[16] and Cimini et al.(C-G)[132]*

The state of a cell is reflected in its morphology, and many different types of perturbations to cells were used, as well as many different mechanisms of action analysed. The recent review by Seal et al.[16] about a decade of Cell Painting gives a detailed overview of the advancement and potential of morphological profiling and, especially, Cell Painting as the most used high-throughput image-

based profiling technique. It is used for a wide variety of perturbations and applications[133-136]. It is most commonly used with small-molecule compounds, as well as with CRISPR perturbations and gene or protein overexpression through open reading frames. An outstanding case of Cell Painting is the JUMP dataset[137], which consists of 116,750 different small-molecule compounds, over-expression of 12,602 genes and knockout of 7,975 genes in U2OS cells, which are human osteosarcoma cells. This dataset provides the barcode for all perturbations, enabling comparisons with drug treatments for purposes such as toxicity or phenotype identification. The JUMP dataset is a significant resource in the field of Cell Painting, providing a comprehensive library of perturbations for researchers to compare and analyse.

The applications of Cell Painting vary a lot. It is used for phenotypic profiling, compound toxicity, mechanism-of-action prediction, and to deepen the understanding of diseases. Its most common use is the prediction of the mechanisms of action of drugs or diseases[138]. It is used to analyse disruptions in the cytoskeleton, ion channels, metabolism, protein synthesis, oxidative stress, and more. The wide variety of mechanisms highlights the versatility of Cell Painting to identify not only a direct change in organelles, but also changes in protein expression, metabolism and the cell cycle[16]. It is also used to identify the morphological profiles of cancer cells to study the drug response and identify cancerous cells. Furthermore, it is used for the prediction of virus-infected cells and fibroblasts from patients with sporadic Parkinson's disease lines. A new connection between signalling pathways of tumour initiation and progression of U2OS cells was discovered by Rohban et al.[135] using Cell Painting. It has also shown its potential in predictive toxicology by correctly predicting the toxicity of compounds in vivo with an accuracy of 68%.

The pipeline for the Cell Painting assay consists of several steps. After cell fixation, staining and imaging, the image analysis starts with the cell segmentation and feature extraction. The image analysis is conventionally done in the powerful image analysis software CellProfiler. The extracted single-cell features are then aggregated, and feature selection and integration are performed. The feature selection is an important step, as not all features are informative depending on perturbation and cell type. Furthermore, one will find many redundant features,

which need to be deleted to avoid skewing the data in the wrong direction. Finally, a dimensionality reduction using t-SNE (t-distributed stochastic neighbour embedding) or UMAP (uniform manifold approximation and projection) is performed to visualise the findings. Hierarchical clustering is also often used to identify similarities between phenotypes/perturbations[16].

2.3. Data integration

One of the most daunting tasks in morphological profiling is the integration of data and the selection of features. This process, while crucial for extracting meaningful insights from a dataset, presents a significant challenge. Various approaches to data normalisation and feature selection are documented in the literature. A brief overview of these methods is provided below. When conducting experiments in different batches, it is essential to correct for batch effects without sacrificing the biological information. Arevalo et al. have extensively explored batch correction methods with Cell Painting, applying different methods to the JUMP dataset[139]. The results of their work will be discussed in more detail later.

After the image analysis of a Cell Painting image set, one is left with over 2000 features per cell. The high number of features makes the analysis computationally expensive, and many features lack significant information due to high noise, redundancy, or lack of correlation between different cell types/perturbations. The standard feature selection process involves removing redundant features that correlate with other features by more than a set threshold. The commonly used threshold is 0.9. Additionally, features with a low variance across the different conditions are deleted. Some studies are doing further feature selection or dimensionality reduction afterwards. Some do a principal component analysis (PCA) for dimensionality reduction, others try to pick the data with the most information. Rohban et al. use a regression that starts with essential features, and then each feature is added to the set, and the feature that adds the most information to it is kept[135]. The replicate correlation measures the contribution. This process is repeated until the replicate correlation of the residue drops to less than 0.3. The use of the replicate correlation is commonly used in

feature selection. The Carpenter lab developed the Cytominer package for image data processing[140]. It also includes the option to analyse the feature importance by its contribution to the reduction of data entropy. Caicedo et al. wrote a review about the data analysis in 2017, where they mention further methods for feature selection[141]. They mention the minimum redundancy–maximum relevance method, and a method where a vector machine is used to give specific weights to the features that represent its usefulness. Then, the feature with the lowest weight is iteratively removed until the classification drops. Recently, progress was made with using machine learning for dimensionality reduction. Siegismund et al. were able to select only 20-30 features that were enough for a successful classification[142].

Correcting for batch effects requires a delicate balance between removing the batch effect and preserving the biological variance. Sphering is the most commonly used method for batch correction of Cell Painting data, as it is part of the Cytominer package. The sphering batch correction transforms the negative control of each batch with the assumption that variation between them is purely technical noise. A sphering transformation, which does the transformation, is also called whitening. It is a linear method that converts the initial vector in such a way that the new covariance matrix is the identity matrix. That means that the data is decorrelated. Usually, a zero-phase component analysis (ZCA) transformation is done to perform the sphering with Cell Painting data. The unique feature of the ZCA sphering transformation is that the resulting whitening matrix is symmetric. After obtaining the whitening matrix for the negative controls, this whitening matrix is used to correct the profile of the whole data set and remove the batch effect[143].

Arevalo et al. compared the sphering method with 10 other batch correction methods across different levels of batch effect, using the JUMP dataset. This dataset was chosen as it was collected in a variety of labs, resulting in a significant batch effect. The comparison was conducted in five different scenarios, ranging from single-laboratory, single-microscope data to data from multiple laboratories and multiple microscope types. Across these scenarios, the Seurat correction and Harmony correction consistently performed best in batch correction and

preservation of biological variance. An overview of their work is shown in Figure 2.4.

The Satija lab developed the Seurat method for the batch correction of scRNA-Seq data[144, 145]. It is a method based on nearest neighbour matching. Therefore, it does not require a negative control as an input, but it requires information about the batches. It first identifies anchors for the integration. Those are pairs of mutual nearest neighbours in a low-dimensional space across batches. Arevalo et al. tested the Seurat method with canonical correlation analysis (CCA) and reciprocal principal component analysis (RPCA). Both methods got similar scores in batch correction and retention of biological information. RPCA is faster than CCA and therefore preferable for massive datasets. It also supports greater heterogeneity between the datasets. The pairs are used to correct for the batch effect based on differences between them.

***Figure 2.4**: Batch effect correction for Cell Painting datasets. Arevalo et al. evaluated batch correction methods for the Cell Painting method, by evaluating a varied of scenarios of increasing complexity from the JUMP dataset (A). They performed a standard Cell Painting feature extraction and then used different batch correction methods and evaluated them for their effectiveness in batch correction and biological preservation (B). Scenario 5 shows the highest effectiveness in batch correction and biological preservation (Bio metrics) for the Seurat methods and Scanorama (C). Reprinted with permission of Arevalo et al.[139].*

Even after feature selection, the resulting dataset often contains more than 200 dimensions. To extract valuable insights from the data, further processing is necessary. This typically involves hierarchical clustering to identify similarities between different perturbations. Dimensionality reduction methods are then used to visualise the data in 2D and 3D space. The most commonly used reduction methods are t-distributed stochastic neighbour embedding (t-SNE)[146] and uniform manifold approximation and projection (UMAP)[147]. While principal component analysis (PCA) is the most well-known and historically most used method, the newer non-linear dimensional reduction methods, t-SNE and UMAP,

outperform it in separating clusters in a low-dimensional space. PCA preserves the global distances, while t-SNE and UMAP focus on a preservation of the local distances over the global distance. In a comparison between t-SNE and UMAP, UMAP is faster and preserves more of the global structure[148].

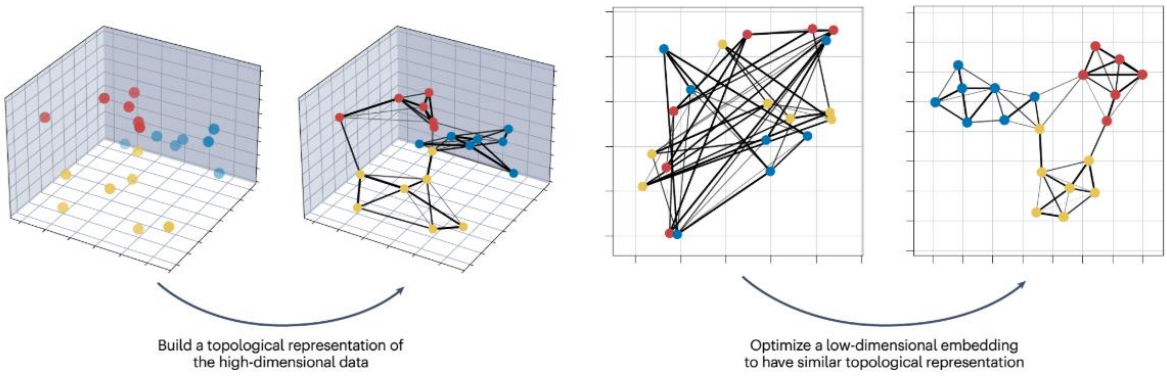

***Figure 2.5**: Representation of the UMAP dimensionality reduction process. The uniform manifold approximation and projection (UMAP) works by first building a topological representation of the high-dimensional data. This representation is then used to find a low-dimensional representation with similar topological properties. Reprinted with permission of Healy et al.[149].*

PCA can reduce the dimensions of a dataset by computing principal components, which are new, uncorrelated variables. The new principal components are used as dimensions for the dimensionality reduction, where the first principal component carries the most information, the second principal component carries the second most information and so on. Thus, the first two principal components can be plotted in a 2D scatter plot that contains most of the variation of the high-dimensional dataset[150].

T-SNE works by attracting and repulsing the nearest neighbours in a 2D space. For that, each data point is first plotted randomly in a 2D space and the attraction by similarity to the nearest neighbour is calculated. Based on this similarity, the data points are either attracted or repelled from each other. A Gaussian kernel calculates the similarity between data points. The perplexity defines its width. The perplexity is an important parameter for a good t-SNE plot. Since the initial placement in a 2D space is random, the final position of the clusters relative to each other is also arbitrary. It does not visualise the global geometry of the data[151].

UMAP works similarly to t-SNE, projecting high-dimensional data into a 2D space and adjusting the positions of individual data points based on their high-dimensional similarity. It first creates a fuzzy high-dimensional graph by calculating the probability that two data points are connected. If two data points are connected, is determined by checking if they are within a defined radius of each other. This radius is an important parameter for the UMAP construction, which is defined by the distance to the *n*th nearest neighbour of each point. A low-dimensional graph is constructed from it by finding a representation that shows the highest similarity to the high-dimensional graph (Figure 2.5). While t-SNE has one critical parameter, the perplexity, UMAP uses two parameters: the n-nearest neighbours and the minimum distance. The n-nearest neighbours parameter says how many neighbours each data point has. This parameter is adjusted to find a balance between the local and global structure. The global structure is more represented in high values, while low values focus on the fine details in the local structure. The minimum distance is important for the visualisation in a low-dimensional space. A high value results in broadly distributed data points in a cluster, while a low value results in tightly packed clusters. While UMAP provides a better representation of the global structure, it is not to be fully trusted either, as the distance between clusters lacks meaningful interpretation[148].

UMAP and t-SNE are stochastic methods and, therefore, one must keep in mind that each run with the same parameters gives different graphs. Furthermore, the range of the parameters can be guessed from the datasets nature. However, different sets of parameters need to be tested to gain a comprehensive understanding of the data. One also must be cautious with the interpretation of clusters, as the algorithm forces clusters; false clustering is possible and can be random noise. Thus, when interpreting the results of a UMAP projection, it is always advised to test multiple runs over a variety of parameters to obtain a good picture of the true nature of the data.

2.4. Traction Force Biology

The above-described mechanotransduction is well understood to influence cellular traction forces, as these forces are closely linked to key steps in the mechanotransduction pathway that respond to nanotopography. Cellular traction forces are determined by factors such as adhesion[19], cytoskeletal contractility[152], and nuclear displacement[153]. The motor protein myosin II plays a crucial role in generating these traction forces by facilitating intracellular contractions[152, 154]. Furthermore, nuclear mechanotransduction alters chromatin structure in response to different nanotopographies[9, 44, 46], which, in turn, affects traction forces based on the localisation of the nucleus and the arrangement of chromatin. Additionally, the stiffness of materials influences cell responses through similar pathways[155-157]. Therefore, analysing traction forces in relation to nanotopography and material stiffness is essential for gaining a comprehensive understanding of how cells respond to their biomechanical environment.

The cellular traction forces can be analysed by measuring the forces that a cell exerts on its surroundings, as this is an indicator of the cell state[158, 159]. Different approaches exist for measuring traction forces. The most used methods are based on elastomeric micropillars and polyacrylamide gels with fluorescent beads. The traction force can be measured by microscopically tracking the displacement of the beads when the cells apply forces to the gel and deform the gel[160, 161]. Micropillars are analysed similarly. The movement of the top of the pillars is tracked by a microscope when the cells bend the pillars due to their traction force (Figure 2.6)[156, 162-164].

This work focuses on micropillars, which were introduced for force tracking biology in 2003 by Tan et al. and are widely used[165]. An advantage of the micropillar platform is its compatibility with a broad range of cell types, as well as the possibility of additional measurements, such as fluorescent staining of the cells[166, 167]. The micropillars can mimic a wide range of pillar stiffness from 1-200 nN/µm. Another advantage is the localised analysis of traction forces, as each deflection of a pillar comes only from the force on that pillar. The stiffness of the

pillars depends on the geometry and arrangement of the pillars(Figure 2.6C); therefore, topographies with varying stiffness but the same adhesion area and chemical and mechanical material properties are possible[156, 157]. This way, the traction force, depending on substrate stiffness, can be measured without another effect like a different adhesion area or strength due to chemical differences in the substrate affecting the forces.

The mechanical properties of the micropillars can be adjusted by changing height, diameter and centre-to-centre spacing according to the equation for the shear modulus *G* of micropillars (equation 1) with the bulk young modulus E_{Bulk}, the diameter *D,* the height *H*, the centre-to-centre spacing *L,* and the fill factor *f*[156, 168, 169].

$$G = \frac{3}{16}\left(\frac{D}{H}\right)^2 f E_{\text{Bulk}} \tag{1}$$

$$f = \pi\left(\frac{D}{2}\right)^2 L^{-2} \tag{2}$$

$$F = k\,\Delta x \tag{3}$$

The traction force *F* (equation 3) can be calculated from the pillar deflection from equation (3) with the pillar displacement Δ*x* and the spring constant *k* shown below in equation 4.

$$k = \frac{3}{64}\pi E_{\text{Bulk}}\frac{D^4}{H^3} \tag{4}$$

PDMS with a bulk Young's modulus of 1-3 MPa is mainly used for micropillars, as it is biocompatible, flexible, transparent and easy to handle in soft lithography. The parameters of a micropillar array must be carefully designed. Limiting factors include the aspect ratio, cell adherence space, and gap between the pillars. If the aspect ratio is too high (often clearly more than 1:3 diameter:height ratio), the soft pillars tend to collapse. The centre-to-centre spacing needs to be chosen in a way that leaves a gap that is big enough that the pillars do not collapse due to attractive forces between the pillars, but close enough that the cells stay on top of the pillars and do not attach to the side of the pillars[170]. The size of the

studied cell type is of high importance for those design choices. Furthermore, the pillar diameter needs to be sufficiently large for the cells to adhere well to the pillars, allowing them to pull on them. Common pillar dimensions are a diameter of 1-5 µm and a height of 3-12 µm[162]. The centre-to-centre spacing is most often chosen between double and triple of the pillar diameter.

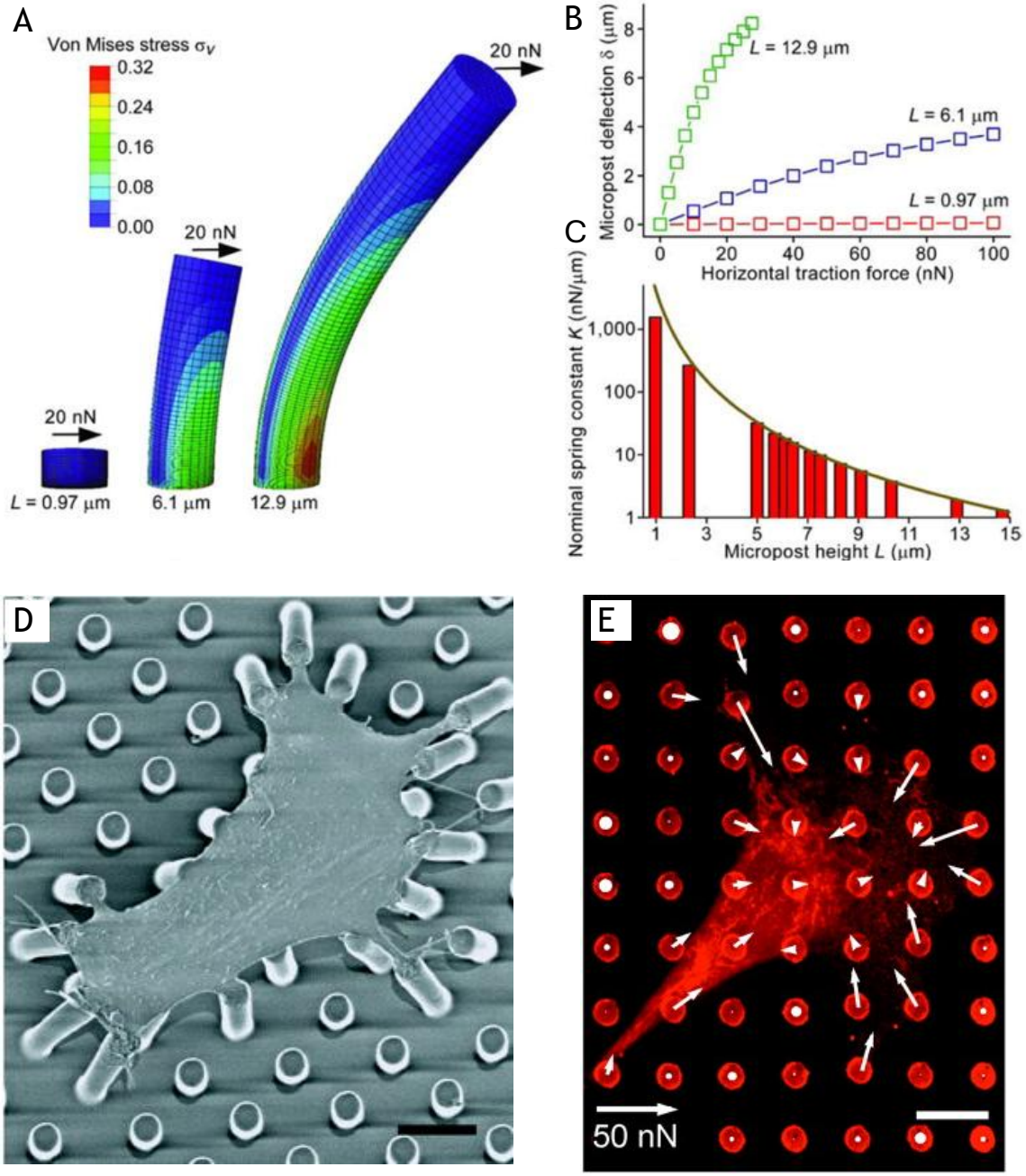

(caption for figure on previous page) ***Figure 2.6****: Overview of pillar based traction force microscopy. Finite element model of pillar deflection of pillars with varying heights under a horizontal traction force of 20 nN (A). The deflection of the pillar is plotted against the applied force, where a higher change in deflection is visible at larger pillars (B). The spring constant k calculated by the Euler-Bernoulli beam theory (yellow curve) follows the calculated spring constants from finite element modelling (C). Scanning electron microscopy image (D) and fluorescent image of cells on micropillars. The arrows visualize the deflection of the pillars due to cellular traction force. The scale bars represent 10 µm. Reprinted with permission of Fu et al.(A-C),[157] and Tan et al.(D,E)[165] (Copyright (2003) National academy of Sciences).*

The micropillar fabrication process is often a multi-step process, where a master mould is fabricated by photolithography or photolithography plus deep reactive ion etching (DRIE). This mould is then directly used for soft-lithography with PDMS or to make a PDMS master mould, which is then used to create the final PDMS micropillars. A silanisation step is necessary for every master to ensure a good demoulding of the PDMS micropillars from the pits. For good micropillars, a master with straight sidewalls is essential to avoid the pillars being stuck in the master[162].

For an accurate readout of the traction force, the cells must attach only to the top of the pillars and not the sidewalls. PDMS, being a hydrophobic and soft substrate, is not preferred by cells for attachment. To enhance adhesion, the surface is coated with fibronectin. A common technique is fibronectin contact printing, where a stamp is coated with fibronectin and then pressed against the top of the pillar. This ensures that the cells only attach to the top of the pillars. This process can be further optimised by coating the rest of the substrate with Pluronic[171] or bovine serum albumin (BSA)[169] to passivate the surface and inhibit cell binding in the areas without fibronectin.

Traction force microscopy with micropillars has a wide range of applications. It is especially interesting for contracting cells or migrating cells like muscle cells, cardiomyocytes, and cancer cells[158, 162, 164, 169, 172-174]. The cellular traction force depends on the stiffness of the substrate, cell-cell signalling, and adhesion strength. It has been shown in multiple studies that the cellular traction force is greater at higher pillar stiffness[157, 172]. Liu et al. showed that the focal adhesion force depends on the cell-cell adherence force[175]. It has further been shown that the cell-cell communication is an important factor for the single cell focal adhesion forces, as the main forces are visible at the edge of cell assemblies.

Cheng et al. created micropillars with different surface coatings to study the dependence of traction forces of MC3T3 cells on the cell-surface adhesion(Figure 2.7)[19]. The top of the pillars was coated with silicon oxide, titanium oxide or nanopillars, which are 500 nm tall and have a diameter of 280 nm. The silicon and titanium oxide surface coatings are hydrophilic, while the nanopillars are hydrophobic. The cells on hydrophilic surfaces exhibited a smaller normalised traction force, slower migration speed, and fewer filopodia compared to those on micropillars. Thus, they could conclude that the surface energy correlates with the migration speed and cellular traction forces.

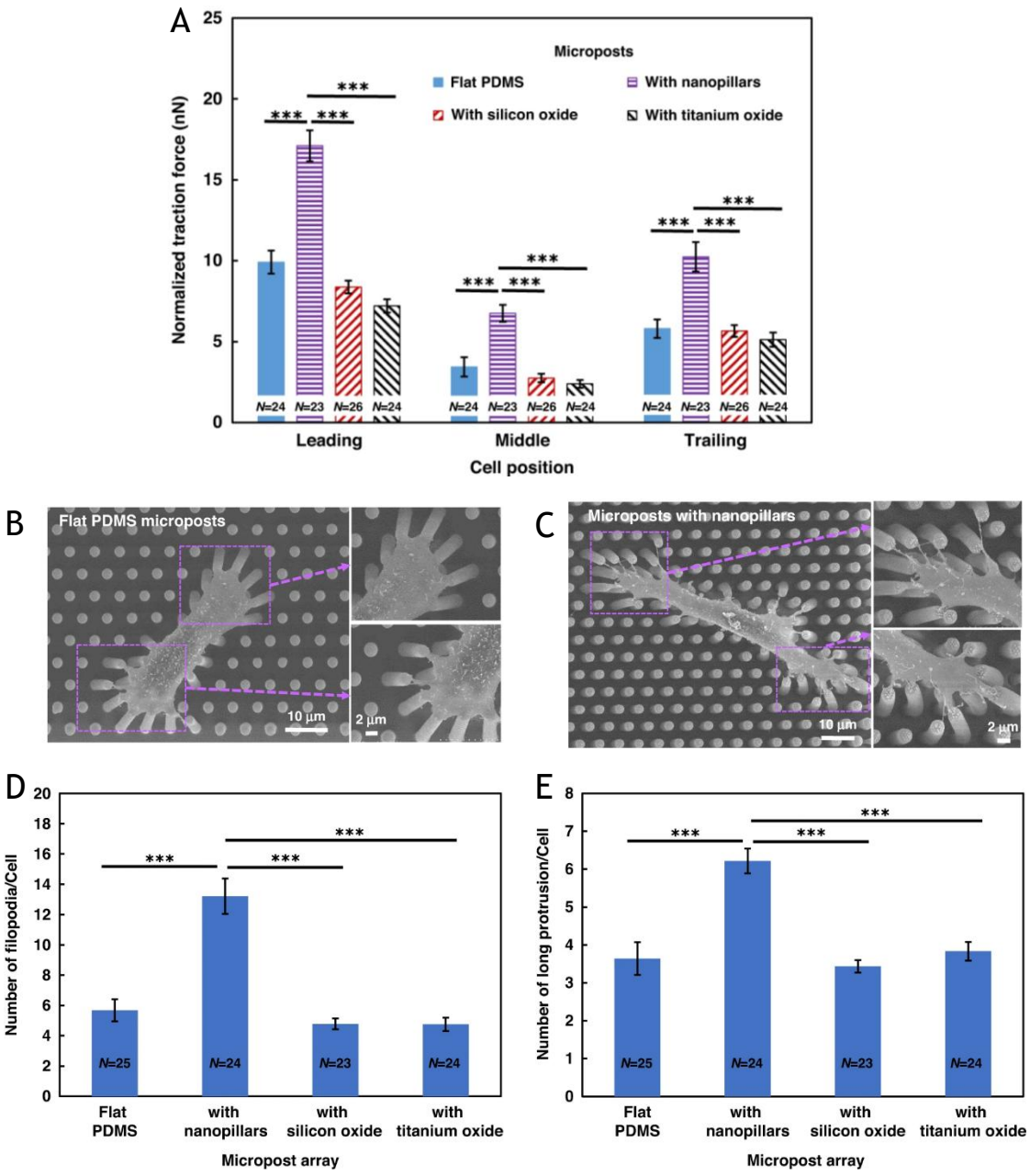

(caption for figure on previous page) ***Figure 2.7****: Traction force dependence on surface energy. Nanopillars on top of micropillars lead to an increased cellular traction force of MC3T3 cells in leading, middle and trailing position of the cell (A). The nanopillars also increase the number of filopodia/cell (D) and long protrusions/cell (E), as also shown in scanning electron images of MC3T3 cells on flat micropillars (B) and micropillars with nanopillars atop (C). Reprinted with permission of Cheng et al.[19].*

2.5. Hierarchical micro-/nanostructures

Microtopographies and nanotopographies have unique properties and effects on biological organisms. To study how different nanotopographies affect cellular traction forces, as well as how the mechanical properties of a substrate affect the cellular response to nanotopographies hierarchical micro-/nanostructures are needed. Several attempts have been made to create topographies like this, that incorporate both microscale and nanoscale features[176]. The fabrication of ordered nanofeatures with microfeatures is a complex task, requiring the interplay of various nanolithography techniques. Most of these hierarchical features consist of nanotopographies atop micro-sized features. Alameda et al.[177] are an exception as they created topographies with the nanofeatures between the microfeatures, as well as on top of the features, through a combination of maskless photolithography, nanoimprint lithography (NIL), and photolithography. The fabrication process is illustrated in Figure 2.8. First, a layer of nanostructures is printed at the bottom of the substrate using NIL. Next, a positive photoresist is spin-coated on the nanostructures, and another layer of nanostructures is imprinted on top of the photoresist. Then, the photoresist is exposed by maskless photolithography and developed. Maskless photolithography is using a laser instead of a mask to write the desired pattern into the photoresist. The micro-/nanostructure is then replicated in a PDMS mould. The mould can be used for further replications as a stamp for the NIL. That way, a higher level of hierarchy can be achieved. This approach enabled the creation of hierarchical micropillars with nanocones on four different levels. Specifically, 2x2 μm pillars were placed on top of 15x20 μm pillars with nanocones located between and on top of each level. These hierarchical materials were used to have a substrate that is bactericidal due to the nanocones, as well as favourable for cell proliferation and differentiation[18].

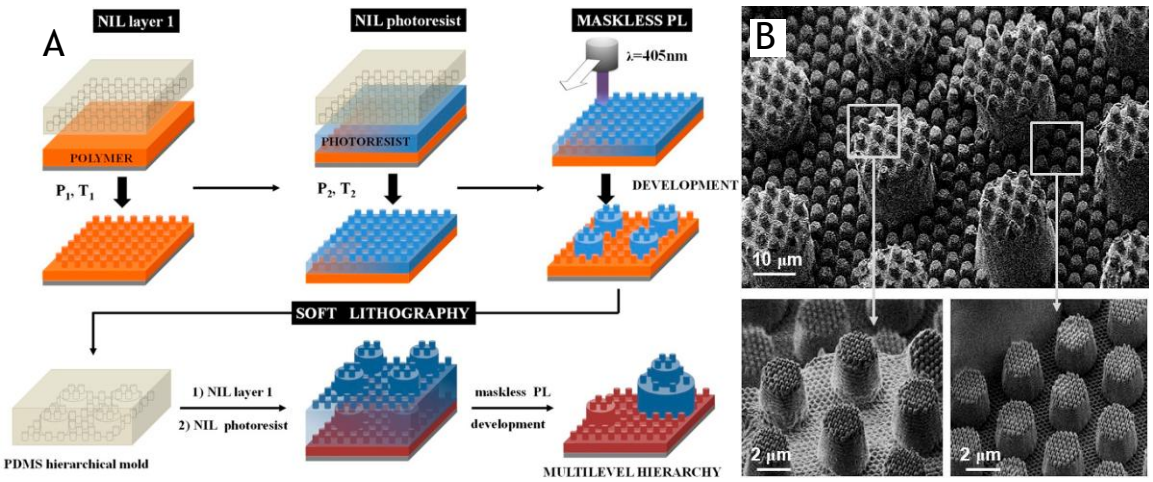

***Figure 2.8**: Fabrication process of hierarchical micro-/nanotopographies by subsequent NIL of nanocones and maskless photolithography of microposts. The final structure can be replicated by soft lithography(A). SEM images of the final structure show nanocones on 4 different levels. In between the microposts and on top of large microposts and on top of smaller microposts that are on top the large posts (B). Reprinted with permission of Alameda et al.[177].*

Another example of hierarchical micro-/nanotopographies is the work mentioned previously by Cheng et al.[19] which aimed to study the effect of cellular traction forces depending on cellular adhesion to nanopillars(Figure 2.9). They fabricated 2.7 µm diameter and 12 µm height micropillars by nanoimprinting, photolithography, reactive ion etching, and soft lithography. First, a thin layer of SU-8 is spun onto a silicon wafer, and nanopillars with a diameter of 280 nm and a height of 500 nm are nanoimprinted. Next, a 4 µm thick layer of photoresist was spin-coated on top of the nanopillars. The micropillars are created by photolithography. The micropillars are etched by reactive ion etching, and the remaining photoresist is removed, leaving silicon micropillars with SU-8 nanopillars on top. The nanopillars are then etched into the top of the micropillars by reactive ion etching, and a double cast of PDMS creates the PDMS micropillars. The master for the soft-lithography process is coated with Trichloro(1H,1H,2H,2H perfluorooctyl)silane (FOTS) to ensure good demoulding.

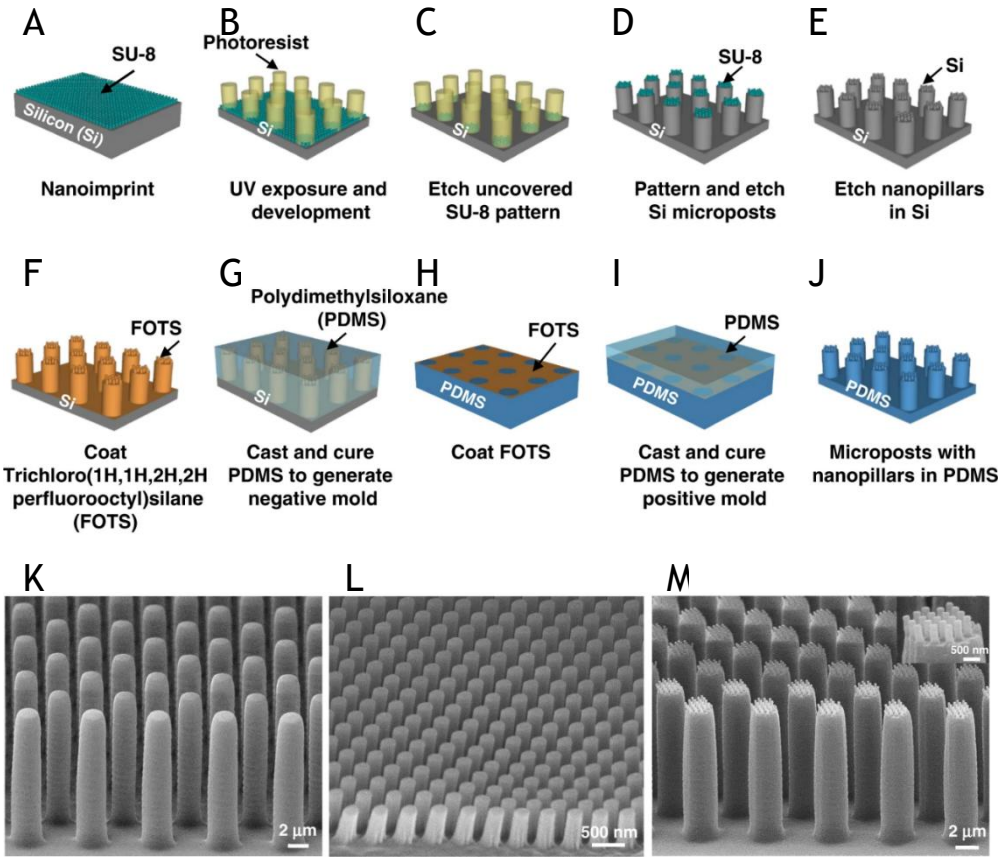

***Figure 2.9**: Fabrication of micropillars with a diameter of 2.7 µm and a height of 12 µm by nanoimprinting of nanopillars (A), photolithography of micropillars (B), and two etching steps for the final micro- and nanopillars (C-E). The final PDMS micropillars are achieved by a double casting of PDMS (F-J). The scanning electron images show flat PDMS micropillars (K), Nanopillars (L), and micropillars with nanopillars on top (M). Reprinted with permission of Cheng et al.[19].*

3.General methodology:

This chapter describes the used methodologies across the chapters. Variations and additional methods are described in detail in the corresponding chapters.

3.1. Cell culture:

We use the osteogenic progenitor cell line mouse MC3T3 (ATCC) in all cell experiments as a well-studied cell line with a strong known response to nanotopographies. The MC3T3 cells are cultivated in a growth medium of MEM α (no ascorbic acid, with nucleotides, Gibco A10490) with 10 % fetal bovine serum (FBS) and 1 % penicillin/streptomycin. They are incubated in an incubator at 37° C, 5% CO_2 and 95 % humidity.

3.2. Cell Painting staining and imaging

The fluorescence imaging follows the cell paint protocol with some minor adjustments. We adjust the protocol to our imaging setup and the MC3T3 cells. We use the Image-iT™ Cell Painting Kit (Thermo Fisher, I63000). We stain the actin cytoskeleton with phalloidin - Alexa Fluor 568 [5 µl/ml], the DNA with HOECHST 33342 [1 µg/ml], the ER with concanavalin A – Alexa Fluor 488 [15 µg/ml], and the Golgi and plasma membrane with wheat-germ agglutinin (WGA) – Alexa Fluor 555 [1.5 µg/ml]. We exclude the RNA stain because it struggles to stain the cell branches of the MC3T3 cells and overlaps with the fluorescence of the ER stain. Thus, we exclude the RNA stain for sharper ER staining. The focus of the mitochondria stain is inconsistent in our confocal laser scanning microscope and is therefore excluded. The live staining period of the mitochondria also gives cells enough time to recover from the prior perturbations by inhibitors and activators. We also increase the concentration of the phalloidin actin stain from 8.25 nM to 33 nM because the initial concentration gave a weak actin staining next to the background of the plasma membrane staining by WGA. The actin cytoskeleton is an essential part of the mechanotransduction pathway, and, therefore, we want to have a strong staining of it to see the actin stress fibres in the staining. We do not include additional stains for focal adhesions or osteogenic expression in place

of the discarded mitochondria and RNA stain because we want to keep the staining process as simple as possible, using a one-step staining process to enable processing across many different conditions. The focal adhesions are also a direct response to the nanotopography feature arrangement and will therefore replicate the architecture of the different topographies well. However, we are more interested in the overall cell state and the cell's indirect response to different nanotopographies.

***Table 3.1**: Required materials for the staining solution of the adjusted Cell Painting protocol.*

	Phalloidin	Concanavalin A	Hoechst	WGA	Triton X-100	BSA	HBSS
Solvent	Methanol	0.1 M sodium bicarbonate	RO water	RO water			
Stock	6.6 µM	2 mg/mL	1 mg/mL	0.15 mg/mL			
Desired Concen-tration	33 nM/ 5 µl/mL	0.005 mg/mL	1 µg/mL	1.5 µg/mL	0.1 %	1 %	
10 mL staining solution	50 µL	25 µL	10 µL	100 µL	10 µL	100 mg	9.805 mL

The staining is done by cell fixation with 4% paraformaldehyde for 20 minutes at room temperature without a previous wash to avoid washing cells off. Next, the cells are washed twice with 1x HBSS (Hanks' Balanced Salt Solution) and the cells are incubated in the staining solution for 30 minutes in the dark at room temperature. The staining solution consists of phalloidin - Alexa Fluor 568 [5 µl/ml], HOECHST 33342 [1 µg/ml], WGA – Alexa Fluor 555 [1.5 µg/ml], concanavalin A – Alexa Fluor 488 [15 µg/ml], 1% bovine serum albumin (BSA), and 0.1% Triton X-100 in 1x HBSS. WGA is centrifuged for 30s at 10 000g before addition to the staining solution to avoid taking protein aggregates. The amount of stains required to make up 10 mL of the staining solution is shown in Table 3.1. It also

specifies the stock concentrations and solvents. After staining, the cells are washed twice with 1x HBSS and kept in HBSS for imaging.

The imaging is done on a ZEISS LSM 800 confocal fluorescence laser scanning microscope (LSM). All imaging parameters are kept constant across samples. The fluorescence is imaged in three tracks. The first track excites the WGA and phalloidin at 561 nm. It detects the emission of WGA between 410 and 580 nm, and of phalloidin between 593 and 700 nm. The second track excites concanavalin A at 488 nm and detects the emission between 450 and 550 nm. The third track excites HOECHST 33342 at 405 nm and detects the emission between 410 and 546 nm. A 10x objective (Zeiss, EC Plan-Neofluar 10x/0.3 Ph1) is used, and 20 images are collected per replica with a pixel size of 291x291 nm. Three biological replicas are collected per condition. This accumulates to around 300 cells per condition with 5 cells per image. The imaging takes around 4.5 minutes per image.

The fluorescence images are analysed in CellProfiler[178] after image acquisition. The analysis is done in computer cluster with over 100 cores. The whole analysis of a dataset of 60 image sets takes around 60 to 90 minutes until the spreadsheet of the CellProfiler analysis is created. As a first step, the images are transformed into grayscale images and saved as those for the further measurements. We measure the granularity, area shape, intensity, intensity distribution, colocalization, texture, and image quality of the whole cell, nucleus and cytoplasm. CellProfiler is a powerful image analysis tool developed by the Carpenter lab[179, 180]. As a first step, the nucleus is segmented into the primary object and the cell as the secondary object. The segmentation process and used CellProfiler modules are shown in Figure 3.2. The Golgi and plasma membrane are used for cell segmentation since it stains the whole cell. Usually, the RNA stain is used for segmentation, but it struggles to stain the cell protrusions. We test the three different thresholding methods Otsu, minimum cross-entropy and robust background for its performance in cell segmentation.

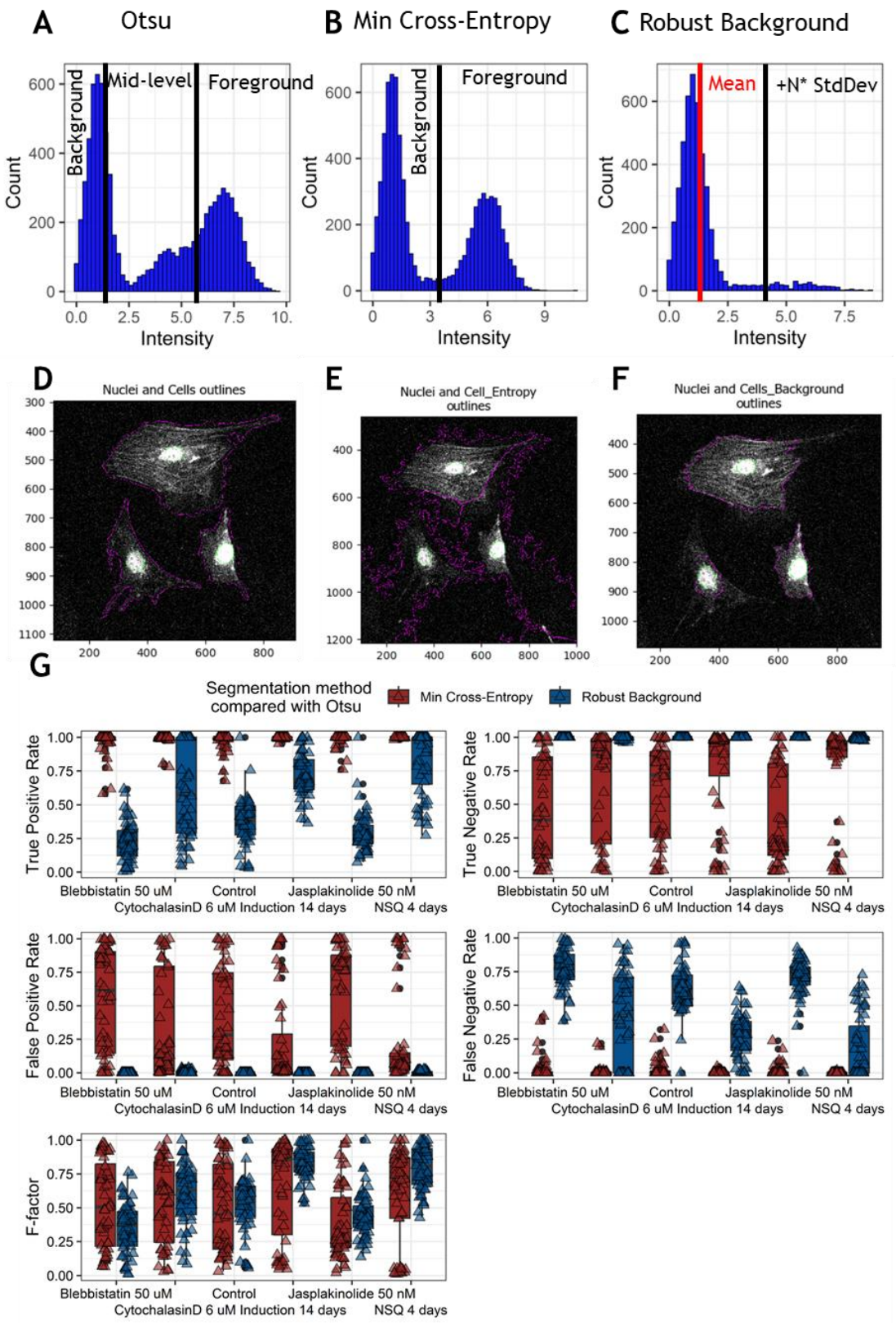
A Otsu
Background
Mid-level
Foreground
Count
Intensity
B Min Cross-Entropy
Background
Foreground
Count
Intensity
C Robust Background
Mean
+N* StdDev
Count
Intensity
D
Nuclei and Cells outlines
E
Nuclei and Cell_Entropy outlines
F
Nuclei and Cells_Background outlines
G
Segmentation method compared with Otsu
Min Cross-Entropy
Robust Background
True Positive Rate
True Negative Rate
False Positive Rate
False Negative Rate
F-factor
Blebbistatin 50 uM
Control
Jasplakinolide 50 nM
CytochalasinD 6 uM Induction 14 days
NSQ 4 days

(caption for figure on previous page) ***Figure 3.1****: An overview about the cell segmentation using Otsu, minimum cross-entropy and robust background method. The thresholding based on the intensity histograms is shown on arbitrary histograms of intensity distributions. The three class Otsu thresholding divides the histogram in three classes based on variance (A). The minimum cross-entropy method separates the histogram in two classes based on entropy between the classes (B). The robust background method calculates the mean of the intensity distribution and sets the threshold value as the mean plus N times the standard deviation (C). Example images of the cell segmentation for the three methods are shown below (D: Otsu, E: Minimum cross-entropy, F: Robust background). The cells are example images of MC3T3 cells after one hour incubation in 50 nM jasplakinolide, which is an actin stabiliser. The dimensions are given in pixels at the side of the images. One pixel unit is 291x291 nm. The colocalization of the cell segmentation using the Otsu method compared with the minimum cross-entropy and robust background method is shown in G. The true positive/negative rate, the false positive/negative rate and the F-factor is plotted. The F-factor is calculated by 2*(precision*recall)/(precision + recall), with the precision being the number of true positive pixels/(number of true positive pixels +number of false positive pixels) and the recall being the number of true positive pixels/(number of true positive + number of false negative pixels).*

The Otsu method calculates a histogram of intensities of the image and divides it into three classes (background, mid-level and foreground) for the used three class method(Figure 3.1A). The classes are defined by finding the minimizing the intra-class variance and maximizing the variance between the classes. The minimum cross-entropy method separates the intensity distribution in two classes, the foreground and the background(Figure 3.1B). The two classes are defined by calculating the cross-entropy between the two classes for every possible thresholding value. The value with the lowest cross-entropy is chosen for the thresholding. The robust background method calculates the thresholding value in a different way than the Otsu and the minimum cross-entropy method and works well for data that is mostly background and does not have two intensity peaks in the histogram that need to be separated but only one peak at low intensities (Figure 3.1C). It first removes the outliers of very high and low intensities and calculated the mean of the background intensities and its variance. The thresholding value is set as N times the standard deviation from the mean intensity.

We use the Otsu method because it yields the most consistent segmentation among the available methods, as shown in Figure 3.1. It is also recommended to use with image sets with a varying percentage of foreground coverage between images like we have with varying number of cells in the images. The rate of true and false positive and negative pixel rates between the Otsu method, the minimum cross-

entropy, and the robust background method is analysed to find the best segmentation method. Additionally, the F-factor is calculated following equation 5 with N_{TPos} as the number of true positive pixels, N_{FPos} as the number of false positive pixels, and N_{FNeg} as the number of false negative pixels.

$$\text{F-factor} = 2 * \frac{precision * recall}{precision + recall} \tag{5}$$

$$precision = \frac{N_{TPos}}{N_{TPos} + N_{FPos}} \tag{6}$$

$$recall = \frac{N_{TPos}}{N_{TPos} + N_{FNeg}} \tag{7}$$

The minimum cross-entropy method tends to overestimate the cell size, while the robust background method tends to underestimate it. We adjusted the cell segmentation parameters so that they can segment the extreme case of cells with 6 µM cytochalasin D as well as less extreme conditions. The Otsu method gave the best consistency across the different methods. We included a quality control measure, as the segmentation only tends to largely overestimate the cell size when it has a false segmentation. Thus, we exclude huge cells from the analysis since we expect them to be falsely segmented. Additionally, we are only interested in single cells. If we have more than 20 cells in one image, we exclude it because the cells are too crowded, which strongly affects the cell morphology.

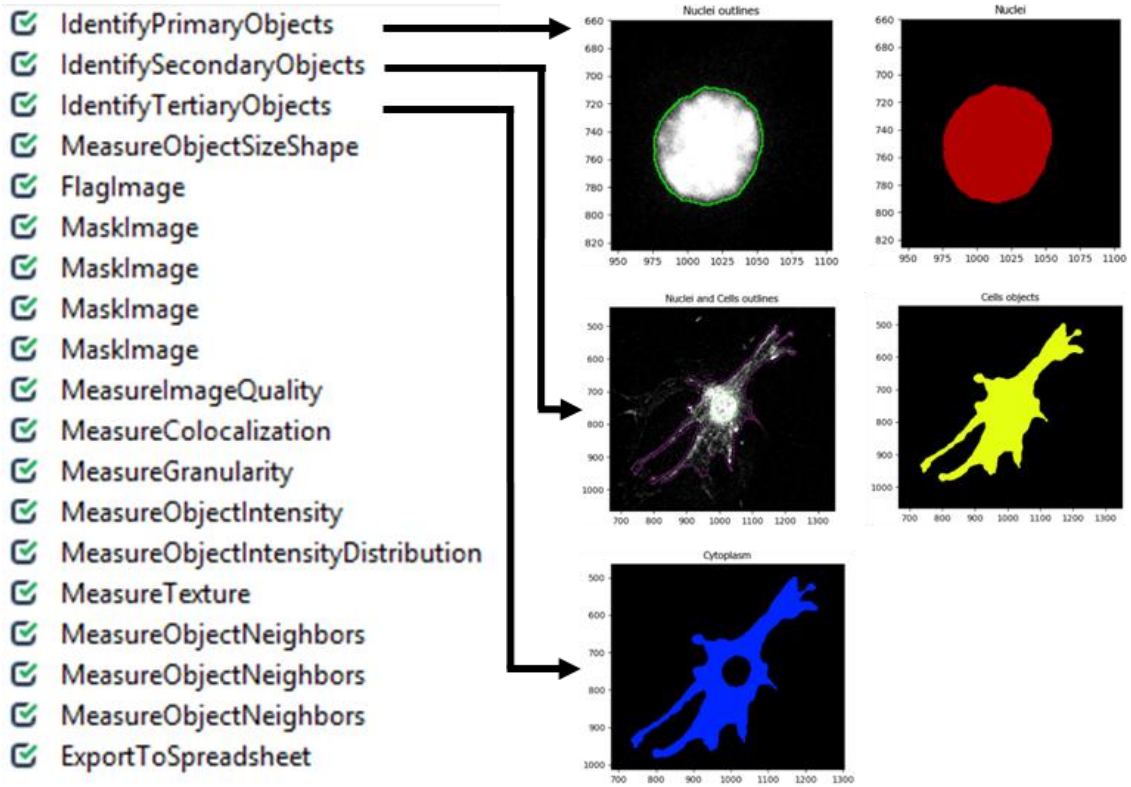

***Figure 3.2**: CellProfiler Pipeline and examples for the identification of primary, secondary and tertiary object. The dimensions are given in pixels at the side of the images. One pixel unit is 291x291 nm. The image analysis in CellProfiler starts with the cell segmentation and creation of masks for the ImageQuality measurements. Afterwards, the object measurements are performed and finally, the results exported to a spreadsheet.*

The optimisation of the primary object identification is first done by setting the size of the object to be identified. All sizes given in CellProfiles are in pixels, as it cannot convert the pixel units into SI units. We select a size range of 30 to 160 pixels, which excludes small particles like protein aggregates that are stained or large dirt particles. We also discard objects that touch the border of the image because we are only interested in complete cells. A global threshold strategy is employed because it provides even illumination with a low background. Therefore, a slower adaptive threshold strategy that calculates the threshold based on the local surroundings is not needed. The image quality of the nucleus staining is so high that little optimisation is needed. A minimum cross-entropy thresholding method is used, as it has shown good thresholding performance in tests. A slight smoothing with the factor 2 is beneficial since the LSM images have jagged edges. The most important parameters for the threshold are the lower and upper bounds. They provide a range of intensities for the object. To define the lower bound, example images are opened in CellProfiler, and by hovering over the image, one

can read the intensity in the location. The intensity of the background can be used to define the lower bound so that no background is detected as the object. This is necessary, even with strong fluorescence, as observed in the nucleus. Without a lower bound set to a reasonable value, the program will threshold random effects in the background if no cell is present in the image. When two nuclei are close together, we want to declump them by their shape since a nucleus always has a round shape and is therefore a good measure for the declumping. Finally, holes should be filled in the object because a nucleus does not have holes.

The thresholding of the cells, which are the secondary objects, is performed next. The plasma membrane staining that we use for the cell segmentation is not as strong as the nucleus staining and has a higher background. Thus, a good segmentation is more challenging, and additional adjustments are needed. The cell is defined around the nucleus by the propagation method, which finds the lines between clumped objects by identifying a brighter or darker line between them. The thresholding method is identified as described above by testing various methods under extreme conditions and determining which method yields the most consistent thresholding. The thresholding is smoothed with a factor of 7 because an LSM image is not smooth at the edges due to the line scanning method. Smoother edges are easier to threshold, and, therefore, we use a strong smoothing. The minimum and maximum bound is defined as above. A key difference in identifying the secondary object compared to the primary object is the application of a log transformation before thresholding. The log transformation increases the difference between the brighter objects and the background, which helps with thresholding. The holes in the identified object are filled again. The optimisation of both thresholding steps is an iterative process by changing the parameters with a focus on the lower and upper bounds until a good segmentation is achieved.

Next, the tertiary object is defined as the cytoplasm by subtracting the nucleus from the whole cell. Afterwards, the measurements for the quality control of the thresholding are performed. We measure the size and shape of the nuclei and cells with the *MeasureObjectSizeShape* module. This module measures size, orientation, and eccentricity. Those measurements include different types of minimum, maximum and average diameters, different measurements for the

shape and solidity of the cell. The Zernike features in the object are also calculated. The Zernike features calculate the Zernike polynomials, which are polynomials of sine and cosine that have an increased number of maxima with increased indices[181, 182]. The Zernike polynomials up to the sixth radial order are shown in Figure 3.3. A feature has an even distribution across the object, while a feature has a maximum on one side of the object and a minimum on the other side. With increasing radial order, the distribution is getting increasingly complex; thus, it is recommended to compute them only to an order of 9 because high orders provide little information. The Zernike features are a measure of the detailed intensity distribution across an object; as the order increases, the complexity increases, and it is important to ensure that enough pixels are analysed to reproduce the number of Zernike polynomial peaks. Therefore, one should be cautious when analysing smaller objects, such as the nucleus, if sufficient resolution is provided. In our case, the nucleus has a diameter of more than 50 pixels, which is sufficient to reproduce the Zernike features up to a high order. However, one should still be cautious when interpreting high-order Zernike features, as they may not be biologically relevant. The low-order Zernike features are to be considered more insightful.

The advanced features that calculate additional statistics for object moments and inertia tensors are not calculated as they add many columns, and we do not believe that they add significant additional information. The maximum diameter calculated by the module is used to flag images with bad thresholding. Due to the high background in some images, the cell size is largely overestimated. We exclude images where this happens by excluding any images that have cells with a maximum radius larger than 150 pixels. This value was tested to work well in only excluding faulty thresholding and not large cells.

In the next step, we measure the image quality, but only in the areas of the cells. Thus, we do not obtain per object, but per image measurements. As preparation for the measurement, we mask the images of each channel with the identified cell objects. Thus, we have per image measurements but only fluorescence in the cell and ignore the background fluorescence. The image quality measurement is interesting to us as it calculates the blur metrics in a range of 5, 10, 20 and 40 pixels, as well as on a global scale. The blur metrics calculate a focus score that

measures the intensity variance and the correlation of each pixel to the neighbouring pixel in the given scale. A blurred image has a high correlation, and a sharp image has a low correlation. That means that a well-defined actin stress fibre has a low correlation. In contrast, the lack of actin stress fibres results in a more even intensity distribution and a higher pixel correlation. The saturation is also computed and provides the percentage of the minimum and maximum pixel intensities.

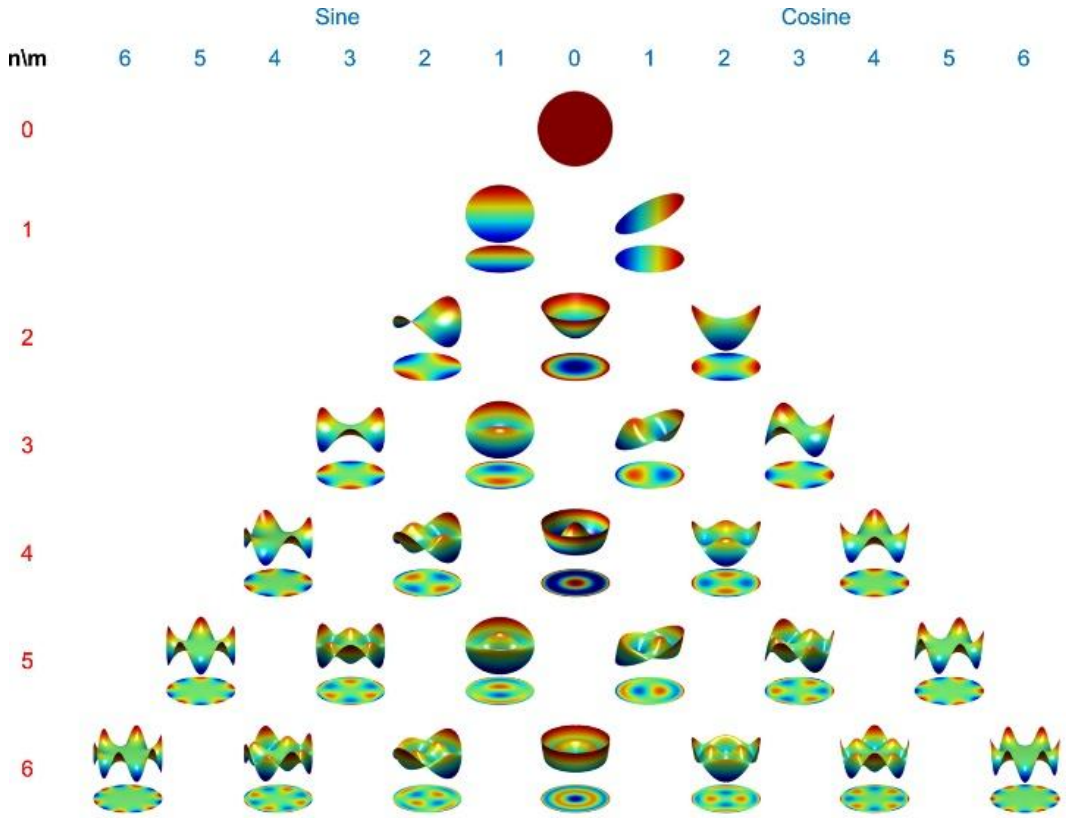

***Figure 3.3**: A visualisation of Zernicke polynomials up to the 6th order. Reprinted with permission of Niu et al.[182].*

Next, the colocalization measurement measures the correlation between the different channels. The correlation is measured by computing the Manders, Costes and Rank Weighted Colocalization (RWC) coefficients, as well as the overall correlation by Pearson correlation[183]. The correlation is measured between all channels in the cells, nuclei and cytoplasm. The only parameter that needs to be modified is the threshold for the intensity to be considered in the calculation. One wants to compare the staining of the different channels, not the background, between the channels. Therefore, only pixels with an intensity of at least 20 % of the maximum intensity are considered. The correlation is only measured within

objects and not across the whole image. *Faster* is selected as the Costes thresholding method to speed up the computation.

Afterwards, the *MeasureGranularity* module is used, which measures how big the granules in the image are. Granularity measurement involves defining a size for the granules, and any granules larger than this size are removed. The measurement reports the percentage of signal that is lost due to the removal. This process is repeated with increasing granule sizes to gain information about the granule sizes in the image. The measurement is performed in all four channels and in the cells, cytoplasm and nuclei. The subsampling factors are left at the default value of 0.25 to speed up the computation, as we have high-resolution images and the resolution is higher than needed for the granularity measurement. The radius of the structuring element is defined as 5, which corresponds to a feature size with a radius of 20 pixels with the subsampling factor of 0.25. The range of granular spectrum is determined in an iterative process with example images. The range starts at a high value like 50, and one checks until which value we observe measurements, and when they all turn to 0. This information is used to select a granular spectrum range that includes all information in the picture without doing unnecessary calculations without information.

Additionally, the intensity and intensity distribution are measured. The *MeasureObjectIntensity* module measures the intensities at the edge of the objects and the whole object. The mean, maximum, minimum, and standard deviation intensity across the object are measured. No adjustment of parameters is made in this module. The intensity is measured across all channels in cells, cytoplasm and nuclei. The distribution of intensities across the object is analysed mainly by the Zernike features in the *MeasureObjectIntensityDistribution* module. The magnitude and phase of the Zernike features are measured up to a Zernike moment of 9. The object is defined in 4 bins, and the Zernike magnitude and moment, as well as the total and mean intensity of each ring, are calculated. The cell is fractured into 4 bins with the centre of the nucleus as the centre for the binning. For the binning in the cytoplasm and nuclei, the centre of the corresponding object is taken as the centre for the binning. An example of the binning with the mean fraction intensities for each channel is shown in Figure 3.4.

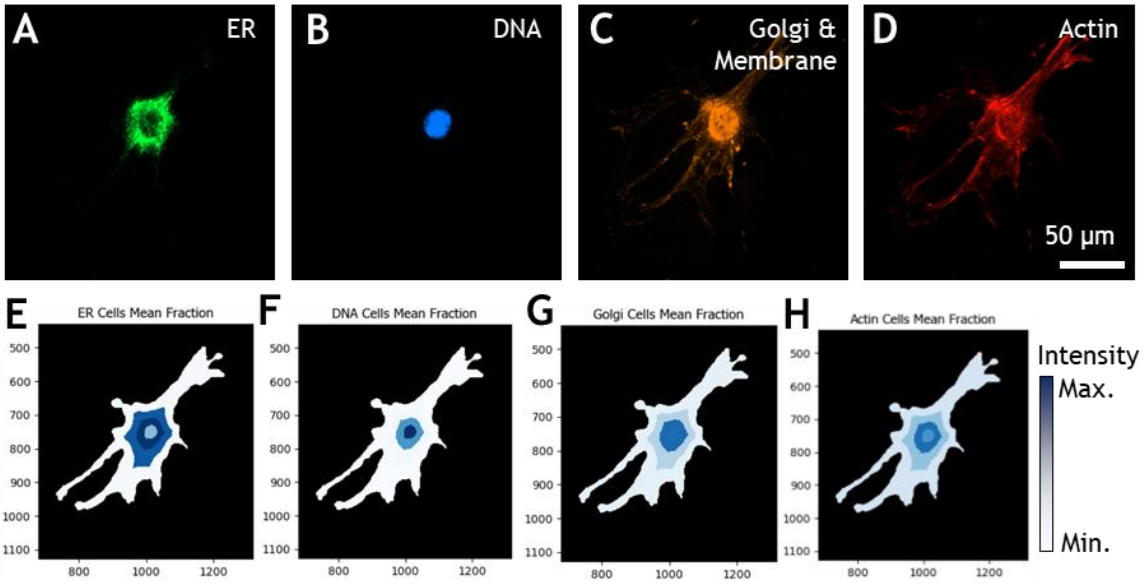

***Figure 3.4**: Example of binning by MeasureObjectIntensityDistribution module. Four bins are created with the centre of the nucleus as the centre of the binning. In each bin the mean intensity across the bin is visualised in a heatmap with a darker blue indicating higher intensity and lighter blue a smaller mean intensity. The fracturing is performed in all four channels of the Cell Painting assay. The fluorescence images of the corresponding MC3T3 cells after 30 minutes in 6 µM cytochalasin D are shown above (A-D). The dimensions are given in pixels at the side of the images. One pixel unit is 291x291 nm.*

The neighbour measurements report how many neighbours each cell has, their distance, and if they are touching. A cell is considered a neighbour if they are within 10 pixels of the neighbouring cell. During and immediately after mitosis, the nuclei of the cells are closely packed together. This is defined by measuring if the nuclei are 5 pixels close to each other. The number of touching cells is also determined by checking if they are adjacent, which means that they have adjacent boundary pixels. The texture of an object is measured by computing the Haralick features that are calculated from a grey-level co-occurrence matrix that describes how the image intensities of pixels occur in relation to each other. CellProfiler compares pixel values to determine intensity variations over a user-specified number of pixels to the right[184, 185]. Each measurement is taken in four directions: horizontally, vertically, and in two diagonal directions, NW-SE and NE-SW. It measures the contrast, variance, homogeneity, entropy and information in the specified region of pixels in the image. The maximum of grey levels is measured with 256 grey levels on a scale of 3 pixels. The small scale is used to observe localised patterns of texture. The measurements are performed in all four channels in the cells, cytoplasm, and nuclei.

The measurements are exported in a CSV file for further analysis. During the export, all measurements that include coordinates of the cells or object numbers are excluded because it does not carry any useful information. All the exported data is further analysed in R. The CellProfiler analysis produces 2246 different features for each cell, which are then further reduced by feature selection methods. The feature selection methods vary between the chapters and are further explained in the corresponding chapters. Before feature selection, the images that are flagged for faulty thresholding are deleted from the dataset. An error in the export can occur, so that not all the features are exported. Thus, it is checked that the same measurements are used. Next, the data is checked for images that have more than 20 cells. Those images are considered too crowded, with the cells tightly packed, which strongly affects cell morphology. Thus, they are excluded from further analysis. Next, the median and standard errors are calculated for each measurement and condition. An overview of the whole described Cell Painting process is shown in Figure 3.5.

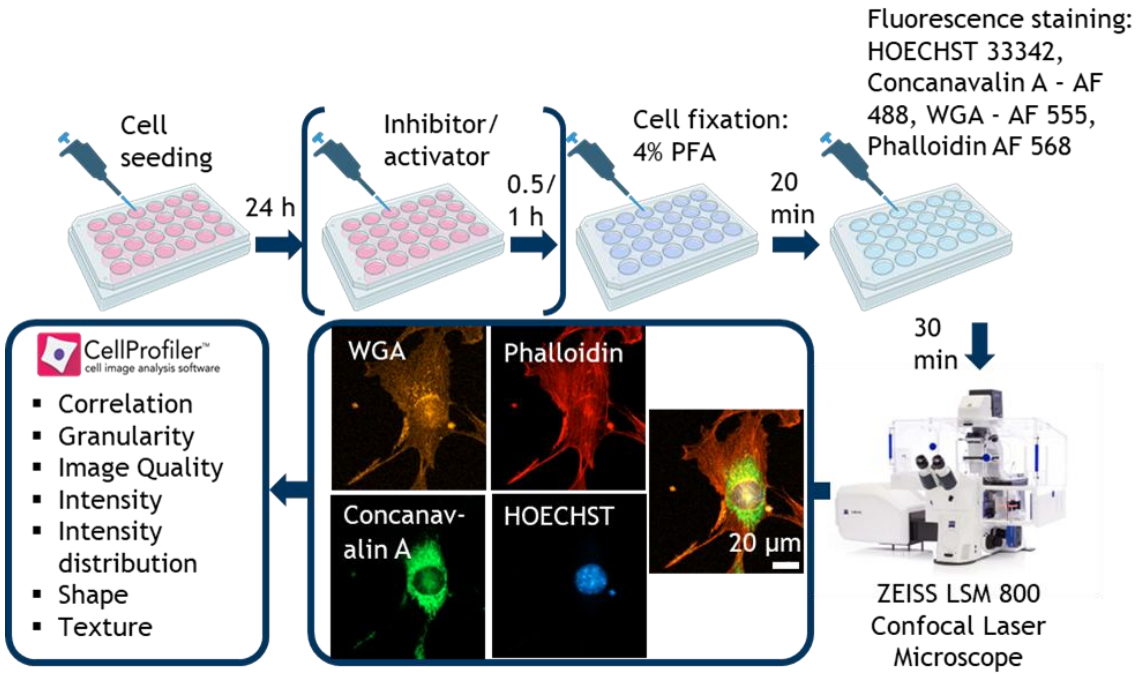

***Figure 3.5**: Cell Painting process from cell seeding to image analysis using CellProfiler. First, MC3T3 cells are seeded into a well plate and after overnight incubation they are perturbated with an activator or inhibitor for 0.5 to 1 hour. Next, the cells are fixed with 4% PFA, stained with the Cell Painting staining solution and imaged with a ZEISS LSM 800 confocal laser microscope. The images are analysed in CellProfiler. Schematic created in BioRender.*

3.3. Nanotopography preparation

The nanotopographies are prepared in self-made polystyrene (PS) well plates that have the size of a quarter of 96 well plates. This means that the well plates have 24 wells, where each well is the same size as a conventional 96-well plate. Figure 3.6 shows the fabrication process of the well plates with nanopatterns. The nanopatterns are injection moulded into a PS slide from nickel shims as previously reported[186]. The nickel shims are available in the lab and were previously fabricated by electron beam lithography of a 100 nm thin poly(methyl methacrylate) (PMMA) resist on a silicon wafer that was electroplated with nickel by Temicon (Germany). The nickel was removed from the silicon wafer by a lift-off process and cut into shape as a nickel shim with nanopillars. The injection moulding was performed on an Engel Victory 28 (ENGEL GmbH, Austria) injection moulding tool by Alysha Hunter. The injection moulded PS slides are ultrasonically welded onto the self-made 24-well plates by Dr Duarte Menezes using a Rinco Ultrasonics AG Standard 3000 (Rinco Ultrasonics AG, Switzerland) ultrasonic welding tool. The standard nanotopographies used are nanopits with a diameter of 120 nm, depth of 100 nm and centre-to-centre spacing of 300 nm. They are arranged in a square (SQ), hexagonal (HEX) and near-square (NSQ) array. In the NSQ array, each pit is randomly displaced by 50 nm from the ideal square lattice. More variations of the nanotopographies used in Chapter 4 are explained in the chapter. Before cell seeding, the well plates are treated for 30 seconds with oxygen plasma at 60 W to activate the surface for good cell adhesion. After plasma activation, the well plates are sterilised in a biological safety cabinet by UV light for 20 minutes and 10 minutes in 70 % ethanol. After Ethanol treatment, the wells are washed at least three times with phosphate-buffered saline (PBS).

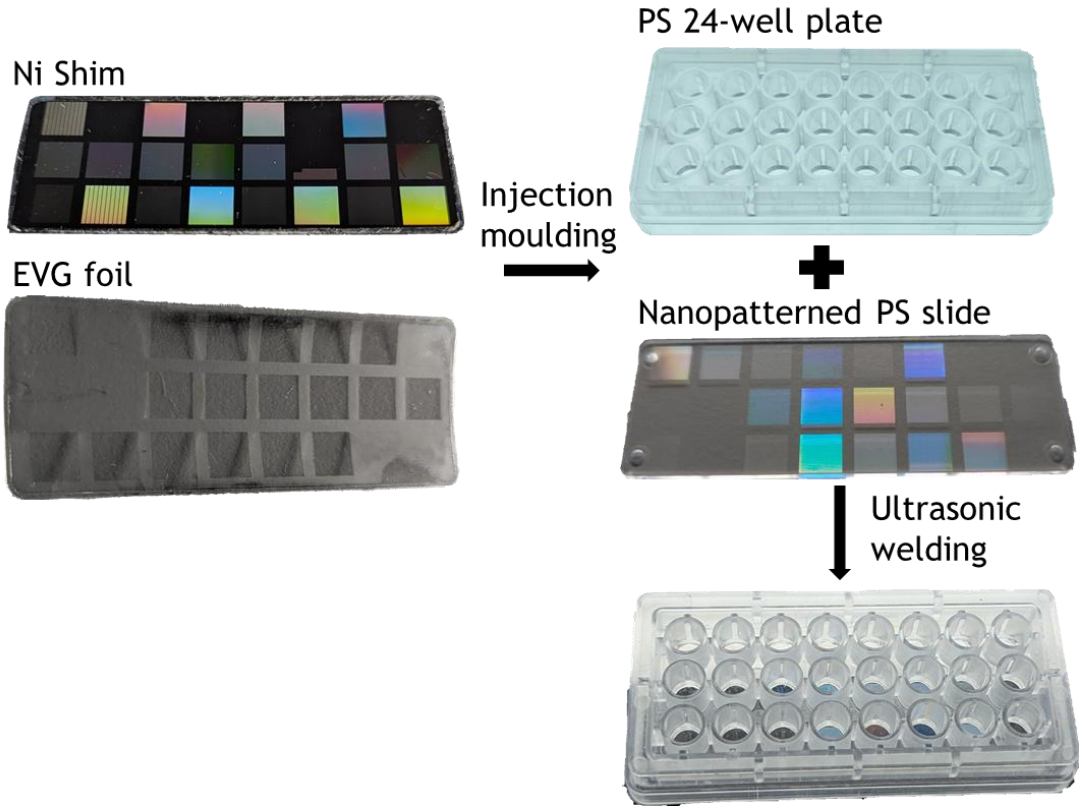

***Figure 3.6**: A representation of the fabrication of polystyrene 24 well plates with nanotopographies. A nickel shim or EVG foil is used as a master for an injection moulding process. The injection moulded nanopatterned PS slides are ultrasonically welded to self-made PS 24 well plates to have custom made well plates with nanotopographies.*

3.4. Scanning electron microscopy

All scanning electron microscopy (SEM) images are taken on a scanning electron microscope of the Hitachi SU8200 series (Hitachi, Japan). The samples are sputter-coated before imaging to ensure high-quality imaging and to prevent damage to the sample. A charging effect on the samples was best avoided by clamping the samples on specimen holders with metal clamps, rather than using adhesive and conducting carbon taps from Agar Scientific (UK). The sputter coating was performed depending on the sample type. Large features are sputter-coated with an Agar auto sputter coater (Agar Scientific, UK) with an 80/20 Au/Pd target. The sputter coating is performed at 20 mA for 40 seconds, which gives an Au/Pd layer of 6 nm. The sputter coating is relatively coarse, and, therefore, an even Pt sputter coating is performed for nanofeatures. The Pt sputtering is done on a Quorum Q300TT Plus (Quorum, UK) with a Pt target. An even layer of Pt is deposited by sputter coating the sample at 2 mA for 114 seconds. This produces a 2 nm thin layer of Pt with low grain size, enabling high-quality SEM images of small

features. A working distance of 8 mm is used as a standard while imaging. A shorter working distance below 4 mm with a small voltage of 2 kV or smaller and a probe current below 2 nA is also helping in obtaining high-quality, high-resolution images with a good contrast.

4. Visualising mechanotransduction pathways during differentiation using Cell Painting

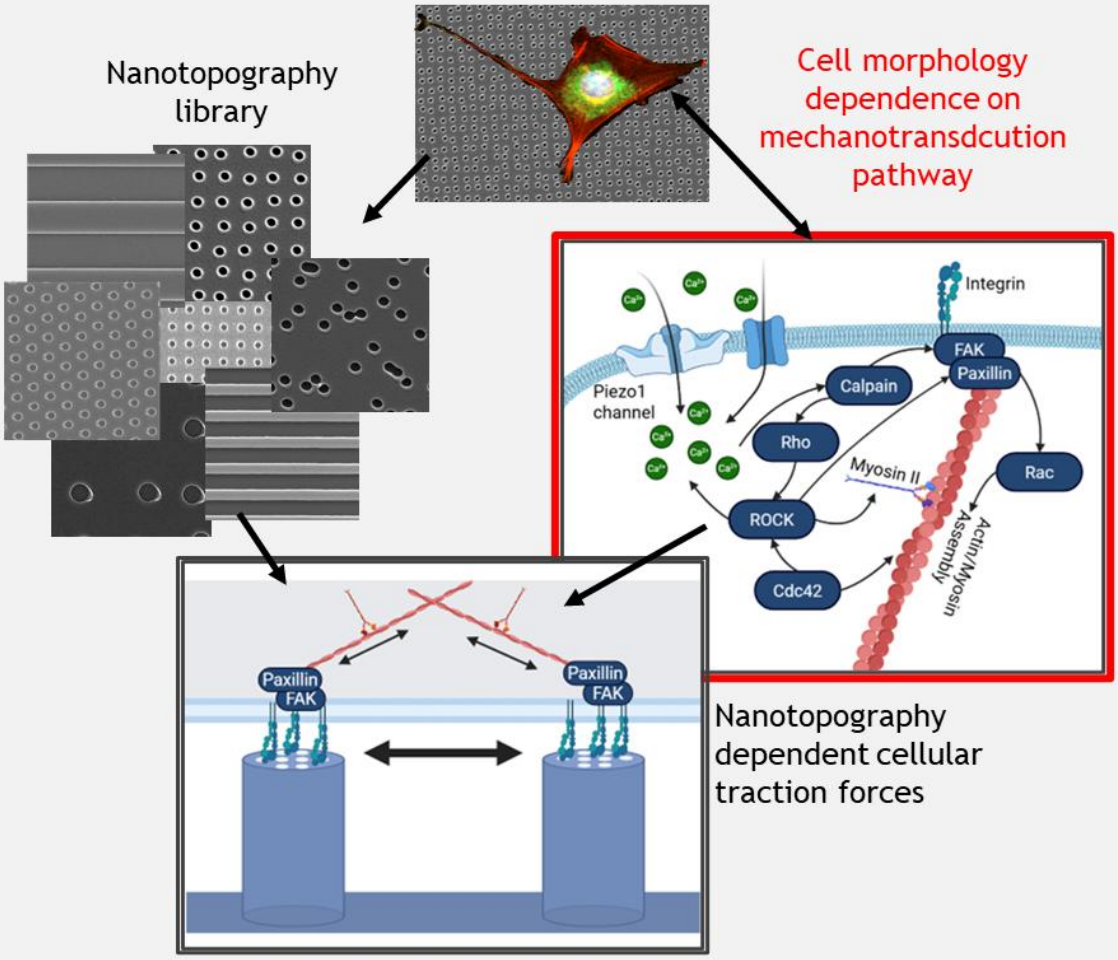

Methods: Morphological profiling with **Cell Painting**

- **11 inhibitors** and **activators** of the mechanotransduction pathway with **3** concentrations each
- **SQ**, **NSQ**, **HEX** topography after 1,4, and 7 days
- **Metabolites** and **osteogenic induction** after 1, 3, 5, 7, 9, 14 days

→ **53** different conditions → **>3200** fluorescence images

Results:

- The morphome reflects the mechanotransduction pathways
- Nanotpography response changes over time

→ Ca^{2+} signalling after **1 day**

→ decreased intracellular **tension** and **adhesion** after **4 days**

→ **senescence** and commitment to **differentiation** in osteoblasts after **7 days**

4.1. Introduction:

Differentiation pathways are often studied using omics techniques[12-14, 103-105], cell migration studies[106, 107], cellular traction forces[70, 108, 109], or protein localization[48, 60]. The omics methods are time extensive, need large cell numbers, and fail to report heterogeneity in the cell populations as they do not offer single-cell spatial resolution. There are current advances in DESI mass spectrometry[126-128] and other omic techniques like scRNA-seq and spatial transcriptomics [187-191] to achieve single cell resolution in isolated cells and tissue. We propose an alternative to the classic ways of pathway analysis by studying the cell morphology changes due to perturbations through drugs, inhibitors, activators, metabolites, and nanotopography using Cell Painting. In contrast to omics techniques, which need 10^5 cells, this approach only needs a few hundred cells per experiment and one hour of experimental preparation, as no time-consuming and error-prone lysing step is needed.

The phenotype of a cell is reflected in its morphology. Cell Painting [15, 138] has become a highly efficient method where simple reagents fluorescently stain the organelles of cells for morphological profiling. This versatile technique has been widely applied in various conditions, such as drug discovery[192-194], genetic modifications[133, 135], and diseases[134, 135, 195, 196]. It is a valuable tool for drug testing and for creating genetic and chemical perturbation libraries[133, 137]. Its ability to identify the mechanism of action of these perturbations and group them based on similar mechanisms of action makes it a versatile and powerful method in cell biology research.

In this work, we apply Cell Painting to elucidate relevant pathways relevant to the interactions of biomaterials. As an example, we focus on the mechanotransduction pathway of osteogenic differentiation. The Gadegaard group has shown in a previous work that the cell morphome of MC3T3 cells on nanopits correlates with osteogenic gene expression[20]. By using different inhibitors and activators of key parts along the mechanosensitive differentiation pathways, we can correlate the cell response to the response to nanotopographies. Figure 4.1 shows an overview of the used activators and inhibitors in the mechanotransduction pathway. Each

drug is used at three concentrations to demonstrate that Cell Painting is sensible enough to pick up concentration-dependent responses and to see if the pathways have a binary on/off state or if they can be modulated by the concentration.

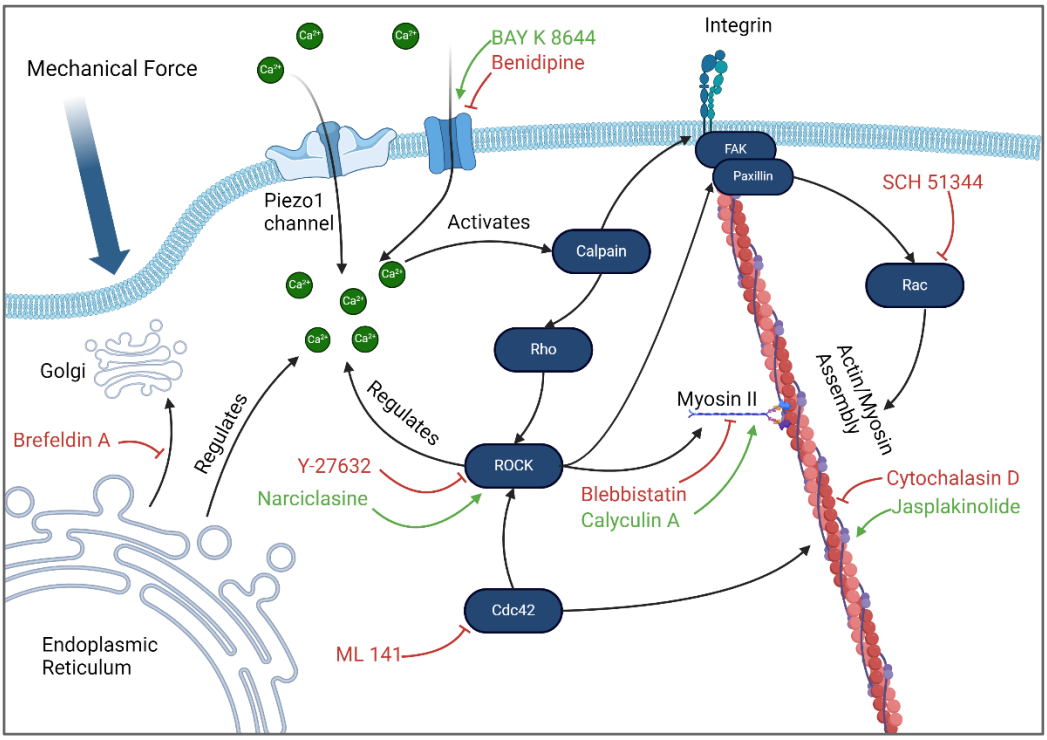

Figure 4.1: *A schematic representation of the mechanotransduction pathway and the influence of the used activators (green) and inhibitors(red) on the different parts of the pathway. Schematic created in BioRender.*

As cells undergo differentiation, different pathways are activated, depending on the signals that induce the differentiation process[11, 30]. The ROCK pathway, an important early stage in the mechanotransduction pathway, has been shown to affect the actin cytoskeleton and myosin-II activity. Actin polymerisation and organisation are crucial for cell morphology and play an important role in the differentiation process. The Ras/Rac transformation and Cdc42 also affect the cytoskeleton arrangement by promoting lamellipodia and membrane protrusion formations. Thus, we are using inhibitors and activators for those pathways[10, 22, 32].

Calcium signalling, a key player in osteogenic differentiation, plays an important role. It has been shown that nanotopographies affect the activity of calcium channels as the L-type calcium channel activity depends on the cytoskeletal arrangement[197]. On the other hand, calcium signalling is also essential for the

cytoskeletal arrangement[66]. Therefore, we also inhibit and activate the L-type Calcium channel. As an alternative, one could use the Piezo1 activator Yoda1[198] and Piezo1 inhibitors such as GsMTx4 or Dooku1[199]. Both Calcium channels are known to be active in MC3T3 cells. Piezo1 functions as a mechanosensor[200] and is involved in the osteogenesis process[201, 202]. The L-type Calcium channel in MC3T3 is partially inhibited by microgravity[203] and is regulated by the actin cytoskeleton[197]. Furthermore, the L-type Calcium channel promotes filopodia stability in cancer cells[66]. Since both Calcium channels play an important role, and we have L-type Calcium channel activators and inhibitors available, we choose those activators and inhibitors. Additionally, we use the Golgi inhibitor brefeldin A, which inhibits the build-up of the Golgi apparatus. This results in an aggregation of unfolded proteins at the ER that induces cell stress and the depletion of intracellular calcium storage[204].

We are comparing the differentiation induced by nanopits with chemical induction through dexamethasone, ascorbic acid and ß-glycerophosphate. Dexamethasone induces osteogenic differentiation via the MAPK and Wnt signalling pathway[205, 206]. Benidipine, cytochalasin D, and Y-27632 are also known to induce osteogenic differentiation. While those conditions induce osteogenesis, they do not necessarily wholly represent the cell response to nanotopographies, as they focus on one part of a pathway, and we expect the response to nanopits to be more complex than that.

Nanopits used in this work are arranged in square, hexagonal and near-square arrangements as they are well-characterised and known to induce the osteogenic differentiation of MC3T3 cells[20, 25, 95]. It has also recently been discovered that the intracellular tension and adhesion of MSCs on nanopits can be replicated by a metabolite mix consisting of niacinamide, adenine, citrate, and L-glutamic acid. This metabolite mix, which mimics the cellular response to nanopits, plays a crucial role in our research as it can be used as a model system for validation to ensure our findings' accuracy[207].

Here, we use morphological profiling by Cell Painting to analyse the mechanotransduction pathway of the progenitor osteoblast MC3T3 cells on nanopits. We prove that it is a viable high-throughput alternative to classic omics

techniques pathway analysis. The UMAP projection, a powerful tool for visualising high-dimensional data, replicates known relationships and pathways of the activators and inhibitors, thereby validating our approach (Figure 4.7). We, furthermore, highlight the importance of calcium signalling in the early stages of topography-driven osteogenesis. Thus, morphological profiling shows excellent potential for better understanding the effect of different nanotopographies on cells as a fast and efficient method.

4.2. Methodology:

4.2.1. Cell Painting:

We use the osteogenic progenitor cell line MC3T3 in this work. Different inhibitors and activators perturbate the cells before fixation and staining for fluorescence imaging. The different inhibitors and activators with their corresponding concentrations and incubation times are listed in table 4.1. Control images are taken after 1 and 3 days, and with 0.5 and 1 % dimethyl sulfoxide (DMSO) as the carrier of some of the used drugs. Extending the control to longer times is impossible because no single cells can be identified after longer incubation times. Longer incubation times are possible for nanopits, osteogenic induction, and metabolite mix since they decrease the proliferation rate.

The osteogenic induction media comprises the growth media with 10 nM dexamethasone, 10 mM ß-glycerophosphate, and 50 µg/ml ascorbic acid[208]. The induced MC3T3 cells are imaged after 1, 3, 5, 7, 9, and 14 days. The effect of the SQ, HEX and NSQ nanopits is imaged after 1, 4, and 7 days.

Niacinamide and a metabolite mix are used as controls for the nanopits as they show a similar cell response[207]. The cells are incubated with 10 mM niacinamide for 3 days and then for an additional 3 days with the metabolite mix. The mix is made up of 2.5 mM adenine, 2.5 mM citrate, 2.5 mM L-glutamic acid, and 5 mM niacinamide. The cells are imaged after 3 days with niacinamide and after 3+3 days niacinamide with following metabolite mix. Each condition is performed in three biological replicas. A detailed list of all used activators and inhibitors with

their corresponding incubation time, solvent and concentrations is shown in table 4.1.

***Table 4.1**: Concentrations and incubation times of used inhibitors and activators.*

Inhibitor/Activator	Incubation time	Concentration	Solvent	Inhibition
Y-27632	1 h	5, 10, 20 µM	DMSO	ROCK inhibitor
Narciclasine	1 h	25, 50, 100 nM	DMSO	ROCK activator
Blebbistatin	1 h	12.5, 25, 50 µM	DMSO	Myosin II inhibitor
Calyculin A	1 h	0.25, 0.5, 1 nM	DMSO	Myosin II activator
Cytochalasin D	30 min.	1.5, 3, 6 µM	DMSO	Actin inhibitor
Jasplakinolide	1 h	12.5, 25, 50 nM	DMSO	Actin activator/stabiliser
ML141	1 h	2.5, 5, 10 µM	DMSO	Cdc42 inhibitor
SCH51344	1 h	12.5, 25, 50 µM	DMSO	Ras/Rac inhibitor
Benidipine	1 h	25, 50, 100 µM	DMSO	L-type calcium channel inhibitor
BAY K 8644	1 h	0.25, 0.5, 1 µM	DMSO	L- type calcium channel activator
Brefeldin A	30 min.	17.5, 35, 70 µM	Methanol	Golgi inhibitor

4.2.2. Data analysis:

The fluorescence images are analysed in CellProfiler after image acquisition. We measure the granularity, area shape, intensity, intensity distribution, colocalisation, texture, image quality, and neighbours of the whole cell, nucleus and cytoplasm. All the data analysis is performed in R. The CellProfiler analysis produces 2246 different features for each cell, which are reduced to 112 features for the final analysis of the data (Figure 4.2). The data reduction is done by identifying significant data first. Any feature where two times the mean of the

standard error is larger than the difference between the highest and lowest mean value is considered noise and is excluded. In the next step, we exclude all features with a fold change smaller than 75 % between the maximum and minimum value to include all data with a clear change. Afterwards, the data is reduced by Pearson correlation. Redundant data is removed with a cutoff value of 0.95, and all features with an absolute correlation of less than 0.15 are excluded. The final data is projected into a 2D space by a UMAP projection with nine neighbours and a minimum distance of 0.1. An overview of varying parameters for the UMAP projection is shown in the appendix (Figure A4.1). All sensible parameters show the same trends and prominent clustering of perturbations. We chose the final parameters since those separate the clusters enough from each other to quickly identify the different groups while maintaining a proper global structure.

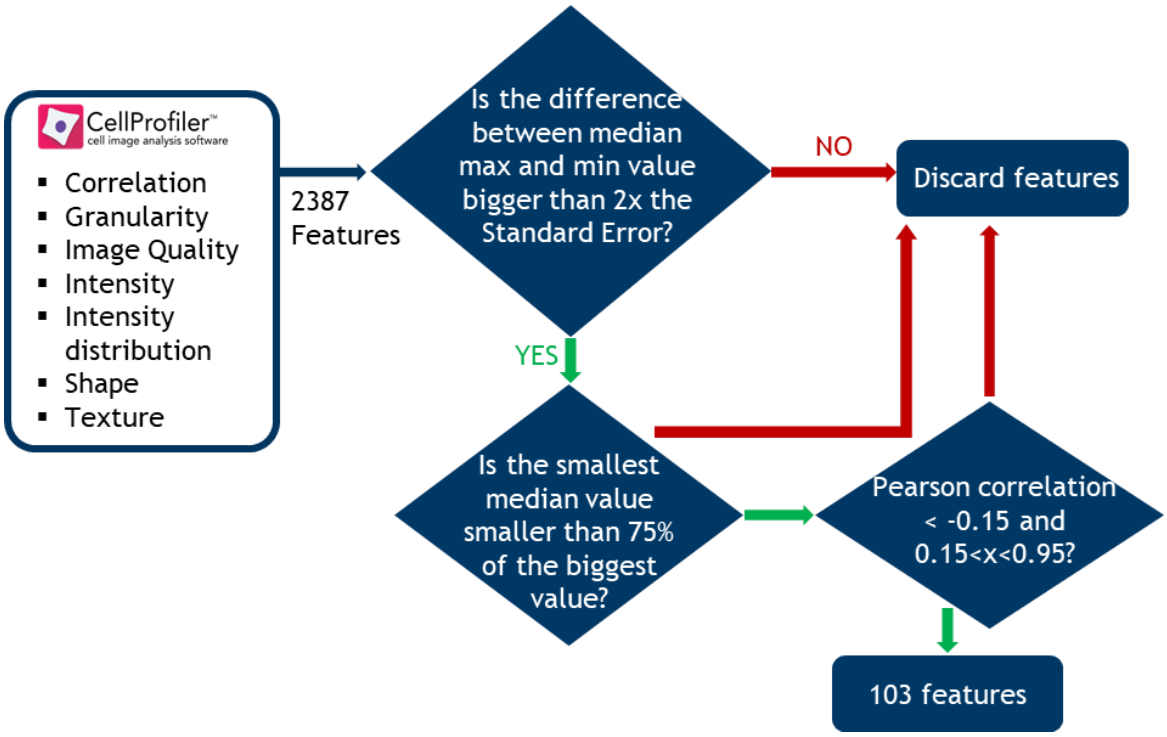

***Figure 4.2**: A schematic representation of the feature selection process. The CellProfiler features are first reduced by their significance, secondly only the features with a large enough between the conditions are picked. Lastly the features without any correlation between the conditions and redundant features are excluded.*

4.3. Results

4.3.1. CellProfiler parameters reflect cell morphology changes through perturbations

The fluorescence imaging of MC3T3 cells clearly shows the impact of the different perturbations (Figure 4.3B and Figure A4.2+A4.3). Surprisingly, WGA is also staining the nucleus of the cells. This is a staining artifact and not due a response of the Golgi to the perturbations. Blebbistatin and cytochalasin D have the most substantial impact on cell morphology, which can be easily observed by the eye. Blebbistatin induces the dissolution of actin stress fibres, which results in the cells blebbing[209, 210]. Cytochalasin D inhibits the actin polymerisation, which results in the replacement of actin filaments by local aggregates[211, 212]. As the cell loses its actin cytoskeleton, it also loses its typical shape.

The Golgi inhibitor brefeldin A mostly affects the Golgi's morphology. While the Golgi is visibly bright and sharp next to the nucleus in the other condition, we observe only a weak fluorescence with 20 µg/ml brefeldin A. The Golgi also looks less sharp than in the other conditions.

The metabolite mix and nanopits after 4 days are both producing a more elongated cell shape. This is expected as the metabolite mix recreates the intracellular tension and cell adhesion on those nanotopographies[207]. Therefore, the overall cell shape is expected to be similar between those two conditions. The metabolite mix is also showing a weaker fluorescence of the ER. Even though both conditions promote osteogenesis, the cells look very different after 9 days of osteogenic induction. The forming of many long cell protrusions dominates the morphology of the mature osteoblasts, which is represented in the solidity measurement of the cell shape. The solidity measures the amount of pixels of the convex hull in the object. A low solidity is an indicator for many protrusions, and MC3T3 cells after 9 days of induction have a solidity of 0.567±0.009; the control got a solidity of 0.669±0.009 and the nanotopography after 4 days of 0.697±0.01.

Those differences are clearly visible, but a fluorescence image offers much more data than one can see at first glance. Image processing software like CellProfiler can extract all the information a fluorescence image has to offer. A thorough analysis of the image parameters, such as shape, granularity, texture, intensity, and intensity distribution, quantifies image data to reveal the changes in the organelles under varying conditions.

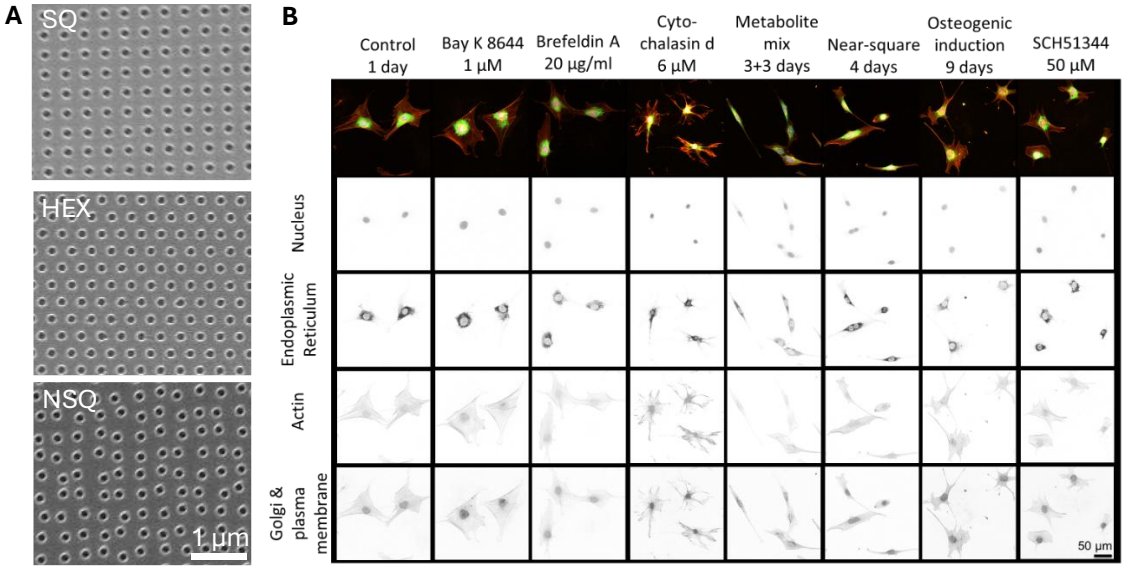

***Figure 4.3**: Images of nanopits and MC3T3 cells after Cell Painting under various conditions. A: Scanning electron microscope (SEM) images of polystyrene slides with 120 nm diameter nanopits in a square (SQ), hexagonal (HEX), and near-square (NSQ) arrangement. B: Cell Painting images of MC3T3 cells stained for the Nucleus with HOECHST 33342 (blue), Endoplasmic reticulum with concanavalin A – Alexa Fluor 488 (green), actin cytoskeleton with phalloidin - Alexa Fluor 568 (red), and the Golgi and plasma membrane with wheat-germ agglutinin (WGA) – Alexa Fluor 555 (orange). An overview of conditions with a control after 1 incubation day, L-type calcium channel activator Bay K8644, Golgi inhibitor brefeldin A, actin inhibitor cytochalasin D, Ras/Rac inhibitor SCH51344, the metabolite mix after 3+3 days, near-square nanopits after 4 days, and the osteogenic induction after 9 days.*

4.3.2. Morphology change due to activators/inhibitors is concentration dependent

After a detailed analysis of the image features with CellProfiler and a data reduction to the relevant and unique features, one can see in the heatmap in Figure 4.4 that all organelles, as well as the cell shape, contribute to the morphological identity of the cell phenotype. The total amount that each organelle represents must be interpreted with caution. When removing redundant features, we remove 258 of 370 features, and we are left with only 112 features.

Those removed measurements give helpful information for the classification of the conditions, but they give the same information as other measurements. The decision on which measurement of several redundant measurements is kept is not closely monitored. It does not matter for the further analysis which measurement is kept. However, when we, for example, have four redundant measurements, where one is from the Actin and the three other measurements are from the Golgi. We keep the measurement of the Actin, and it does not correctly represent the importance of the organelle for the cell classifications. However, we can confidently say that each organelle contributes unique features that help identify the phenotypes.

The heatmap not only visualises a first impression of similarities between conditions but also shows that the readout is not binary. The cell morphology shows the effect of the perturbation and its strength. We can see the concentration dependency of the cell response. Some features are selected as an example in Figure 4.5. The features show high variability, which makes the observed trends insignificant. However, even though the features exhibit substantial variation, concentration-dependent trends are observable in the heatmap in Figure 4.4. Thus, the observed trends can only be considered potential, since the data uncertainty does not yield a significant difference in the measured features across varying concentrations.

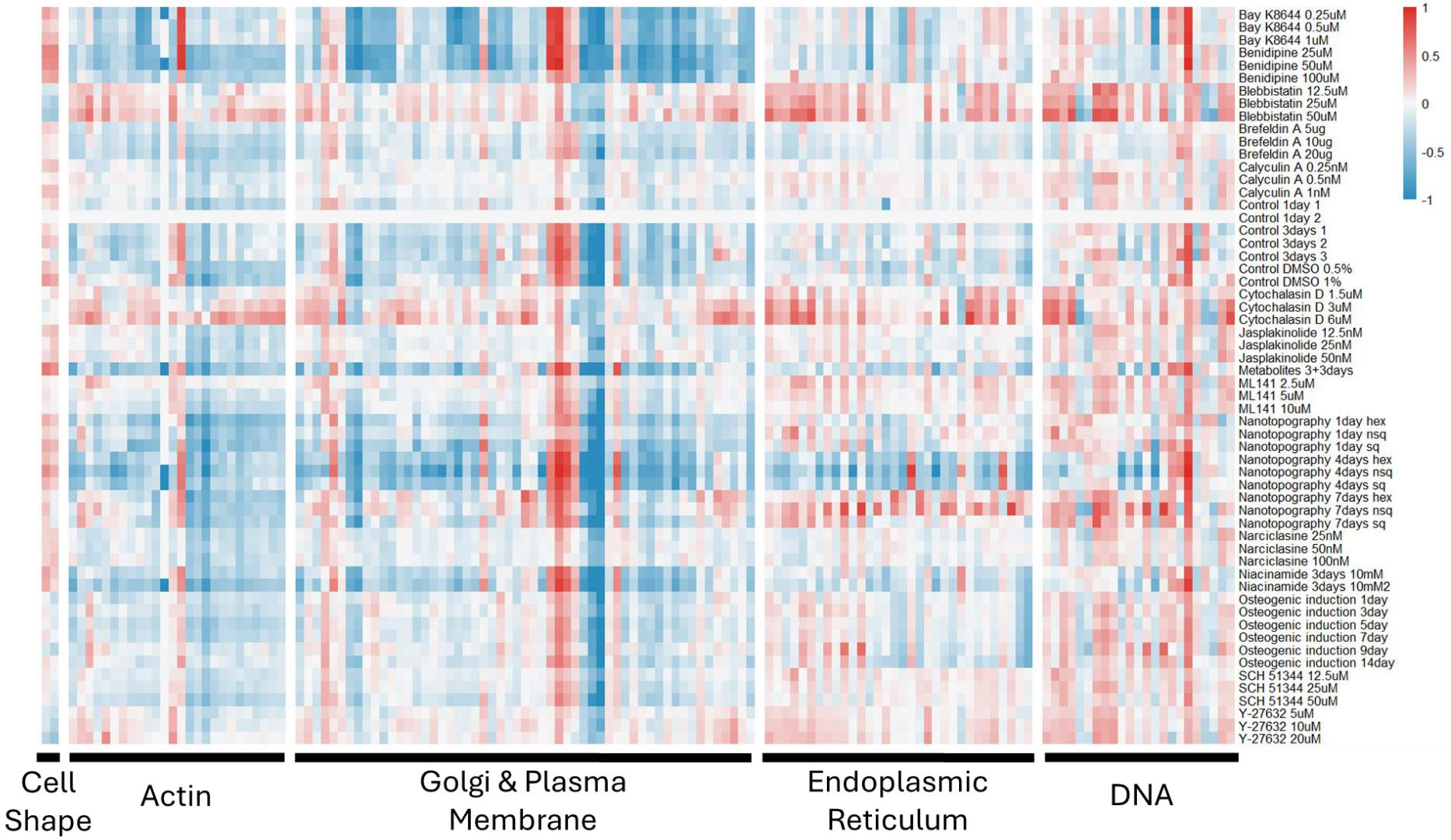
Bay K8644 0.25uM
Bay K8644 0.5uM
Bay K8644 1uM
Benidipine 25uM
Benidipine 50uM
Benidipine 100uM
Blebbistatin 12.5uM
Blebbistatin 25uM
Blebbistatin 50uM
Brefeldin A 5ug
Brefeldin A 10ug
Brefeldin A 20ug
Calyculin A 0.25nM
Calyculin A 0.5nM
Calyculin A 1nM
Control 1day 1
Control 1day 2
Control 3days 1
Control 3days 2
Control 3days 3
Control DMSO 0.5%
Control DMSO 1%
Cytochalasin D 1.5uM
Cytochalasin D 3uM
Cytochalasin D 6uM
Jasplakinolide 12.5nM
Jasplakinolide 25nM
Jasplakinolide 50nM
Metabolites 3+3days
ML141 2.5uM
ML141 5uM
ML141 10uM
Nanotopography 1day hex
Nanotopography 1day nsq
Nanotopography 1day sq
Nanotopography 4days hex
Nanotopography 4days nsq
Nanotopography 4days sq
Nanotopography 7days hex
Nanotopography 7days nsq
Nanotopography 7days sq
Narciclasine 25nM
Narciclasine 50nM
Narciclasine 100nM
Niacinamide 3days 10mM
Niacinamide 3days 10mM2
Osteogenic induction 1day
Osteogenic induction 3day
Osteogenic induction 5day
Osteogenic induction 7day
Osteogenic induction 9day
Osteogenic induction 14day
SCH 51344 12.5uM
SCH 51344 25uM
SCH 51344 50uM
Y-27632 5uM
Y-27632 10uM
Y-27632 20uM
1
0.5
0
-0.5
-1
Cell Shape
Actin
Golgi & Plasma Membrane
Endoplasmic Reticulum
DNA

(caption for figure on previous page) ***Figure 4.4****: Heatmap of the morphological features for all conditions after feature reduction by Pearson correlation and removal of redundant and non-significant data. The features are grouped by the cell shape and the organelles actin, DNA, endoplasmic reticulum, and the Golgi and plasma membrane. The features are normalized by bringing the data to a 0 to 1 scale by subtracting the minimum value and dividing by the maximum. Afterwards, the data is standardized to the control by subtracting each value by the control.*

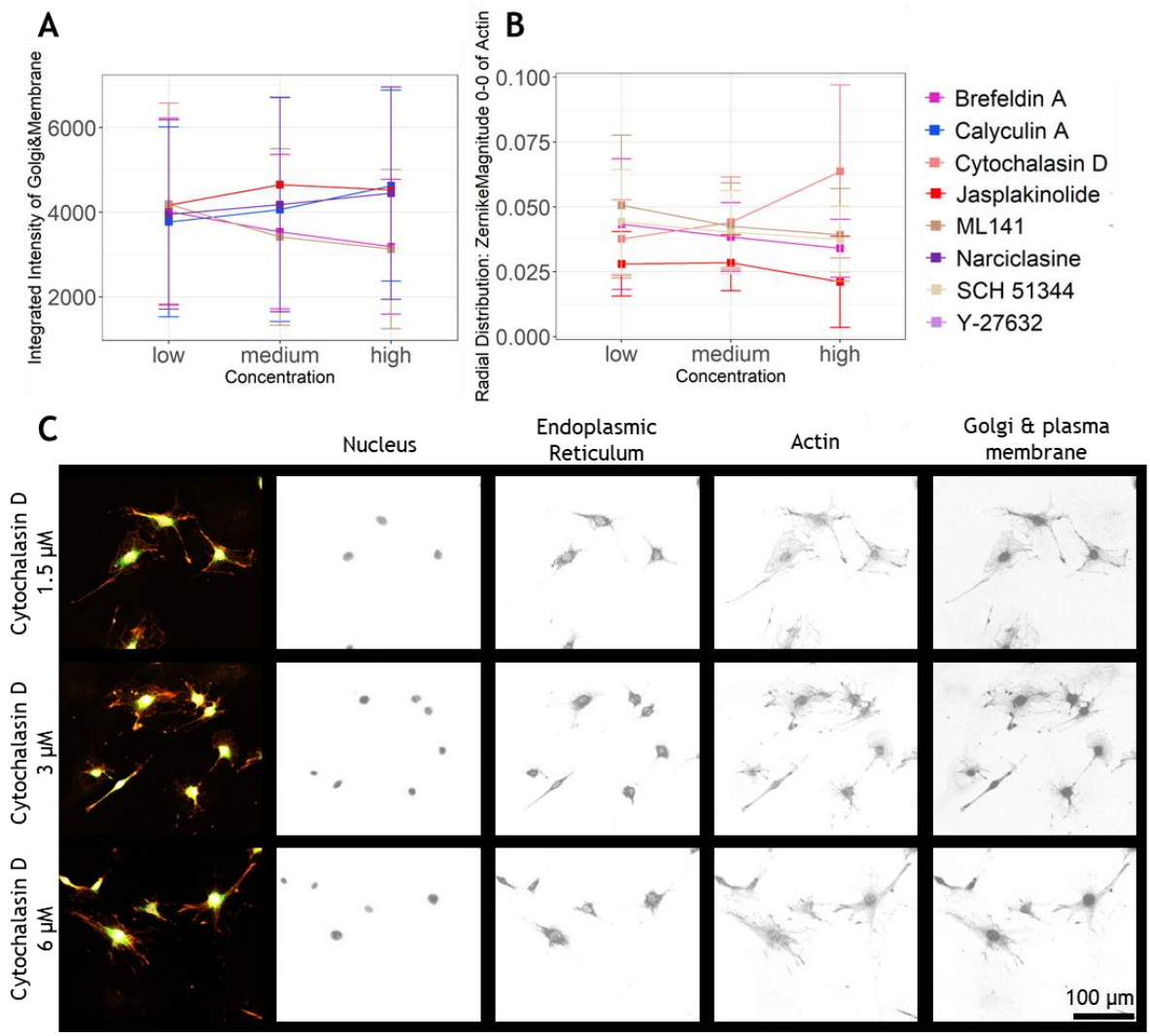

Figure 4.5*: Assorted examples of the concentration dependency of measured featured by CellProfiler. The different concentration of the activators and inhibitors are grouped into low, medium and high concentration for simplification. An increase in brefeldin A as well as ML141 results in a decreased Golgi intensity as the Golgi build up is inhibited (A). An increase in cytochalasin D concentration increases the Zernike$_{00}$ Magnitude of Actin as the intensity distribution gets more evenly distributed when the actin filaments are destabilised. In the same sense decreases the Zernike$_{00}$ Magnitude with increasing jasplakinolide concentration (B). The change of MC3T3 cell morphology with increasing cytochalasin D concentration from 1.5 µM to 6 µM is shown in (C).*

The Zernike Magnitude is a measure of the intensity distribution across an area. A high Zernike$_{00}$ Magnitude represents a uniform intensity distribution. This is a good measure of actin stability. A cell with prominent and stable actin fibres has an

uneven intensity distribution since it has high-intensity values where the fibres are and low values between the actin fibres. Thus, it has a low $Zernike_{00}$ Magnitude. We can pick up this concentration-dependent effect. The highest concentration of jasplakinolide, which stabilises the actin filaments and can result in a patchy appearance of cortical actin, has the lowest $Zernike_{00}$ Magnitude. The F-actin inhibitor cytochalasin D has the highest $Zernike_{00}$ Magnitude, as it disrupts the actin filaments, and no fibres are visible anymore. Thus, one has a much more uniform intensity distribution across the cells with local actin aggregates.

The intensity of the Golgi decreases with increasing brefeldin A concentration as the Golgi build-up is blocked off more and more. A very similar effect can be observed for the Cdc42 inhibitor ML141. It has been shown before that ML141 can also induce changes to the Golgi structure[213]. The lung epithelial cells BEAS-2B observed more dispersed staining of the Golgi apparatus under 20 µM ML141.

4.3.3. Morphology changes reflect function of inhibitors and activators

When reducing the dimensions of the high-dimensional feature map to 2D using a UMAP projection, one can identify different groups that cluster together. Those groups follow the known mechanisms of action of the perturbation. The cell morphology change on nanopits over time gives us insight into the underlying intracellular signals by fitting the morphology into the map of perturbations. Based on the UMAP projection in Figure 4.7, one can divide the perturbations into four groups.

The first group are the Actin, Myosin-II and ROCK inhibitors cytochalasin D, blebbistatin and Y-27632. Those inhibitors are all on the same pathway, which results in an actin destabilisation. Blebbistatin and cytochalasin D have the most potent effect on the overall cell shape and morphology disruption. The cell loses its typical shape under both conditions. While blebbistatin disintegrates actin stress fibres, which results in a blebbing of cells, cytochalasin D completely disrupts the actin cytoskeleton, resulting in a complete loss of shape and just small patches of actin. ROCK is known to stabilise actin filaments. Thus, the inhibition of ROCK by Y-27632 also destabilises the actin cytoskeleton[53]. This

results in more elongated cells with neurite-like elongations. The collapse of the cell shape under cytochalasin D leaves elongations similar to this morphology.

The second group consists of jasplakinolide, calyculin A, and narciclasine, which are the corresponding activators for actin, myosin-II, and ROCK. The actin stabiliser jasplakinolide and the Myosin II activator calyculin A induce actin aggregates while having a prominent actin cytoskeleton[214-217]. The ROCK activator narciclasine also promotes the stabilisation of F-actin through the ROCK pathway and promotes actin stress fibres[218, 219]. The Golgi inhibitor brefeldin A not only prevents the build-up of the Golgi apparatus but also affects the F-actin distribution as a consequence[220]. This can lead to actin patches. Jasplakinolide also affects the Golgi by fragmenting it[221]. The normal controls lay in this group, too, as those morphology changes are not as drastic as those due to the other perturbations.

The third group comprises the L-type Calcium channel activator BAY K 8644 and the Calcium channel inhibitor benidipine. Little is known about the morphology changes induced by those. Curiously, the inhibitor and activator of the same channel lie together. A disruption in calcium signalling mainly triggers the intracellular control mechanisms, which involve similar pathways regardless of whether they must counteract an increase or decrease of calcium ions through the L-type calcium channel.

The fourth cluster includes the Cdc42 inhibitor ML141 and the Ras/Rac inhibitor SCH51344. Both inhibitors affect the cytoskeleton's organisation[54]. ML141 inhibits filopodia formation[222], and SCH51344 inhibits lamellipodia formation and blocks membrane ruffling[223]. Thus, both inhibitors create relatively static cells without cell elongations.

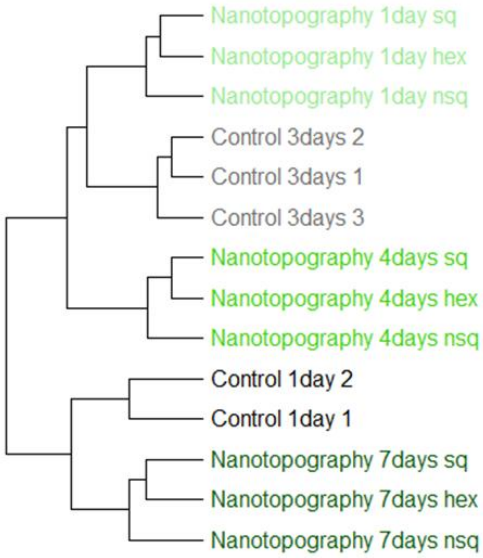

***Figure 4.6**: Hierarchical clustering of Nanotopography data. The different time points cluster together and a higher similarity between SQ and HEX topographies is found. NSQ topographies separate from them following previously found osteogenic marker expression profiles.*

The impact of nanotopographies on cell morphology and differentiation is a significant finding in our research. The fluorescence images of the Cell Painting on the different topographies is shown in Figure A4.3. Over time, cells react to the topography, and this reaction is clearly visible. The different nanopit arrangements in SQ, NSQ, and HEX play a crucial role. Cutiongco et al.[20] demonstrated that an NSQ arrangement has the most prominent effect, with MC3T3 cells showing the highest expression of the early osteogenic markers RUNX2 and SP7 on it. The SQ and HEX arrangements, on the other hand, have a smaller and similar expression to each other. This grouping is also evident in our data through hierarchical clustering, with distances calculated using a normalised Euclidean method (Figure 4.6). For one, four, and seven days, the SQ and HEX nanopits cluster closer together than the NSQ nanopits, indicating the correctness of our morphological clustering. Thus, the morphology of cells on SQ and HEX shows more similarities between each other than to cells on NSQ nanopits, underscoring the significance of our research in understanding cell behaviour. However, all types of nanotopographies are known to induce osteogenesis and have a similar effect on MC3T3 cells, with reduced tension and decreased proliferation over time. The NSQ nanopits are known to have the most prominent effect and are therefore separating from the other nanopit arrays. All nanopits still produce a similar morphology in comparison to the drastic changes through the activators and inhibitors.

4.3.4. Response of MC3T3 cells to nanopits changes over time

When adding the cell response to SQ, NSQ, and HEX nanopits over time into the UMAP projection of the inhibitors and activators, we can see how the cell changes over time and how the corresponding influences on the cells change over time (Figure 4.7). The control lies with the above-noted second group of ROCK, Myosin-II and Actin activators since they have the smallest effect on the cell morphology and are, therefore, most similar to the control. After 1 day on the nanopits, the morphology is similar to the morphology change through the L-type calcium channel inhibitor and activator. This hints at an important role of calcium signalling in the early stages of differentiation, which aligns with current research. The mechanosensitive calcium channel piezo 1/2 regulates osteoblasts differentiation by increasing the early osteogenic marker Runx2[224], which is known to have an increased expression nanopits. Therefore, one can expect the calcium signalling to drive the early stages of osteogenesis on nanotopographies.

After 7 days on SQ, NSQ, and HEX nanopits, the MC3T3 cells show a substantial increase in the osteogenic markers RUNX2, SP7, BGLAP, and SPP1 expression[20]. At this stage, the cells group with the Cdc42 and Ras/Rac inhibition, highlighting that the cells are more static. We expect the cells to be less mobile as they have been sitting on the nanopits for 7 days. The filopodia formation decreases during differentiation into osteoblasts due decreased motility and increased intracellular tension. It is well known that nanopits and, especially, NSQ nanopits increase the cellular tension by the formation of integrin clusters[26, 207]. The increase in cellular tension decreases the lamellipodia formation[225, 226].

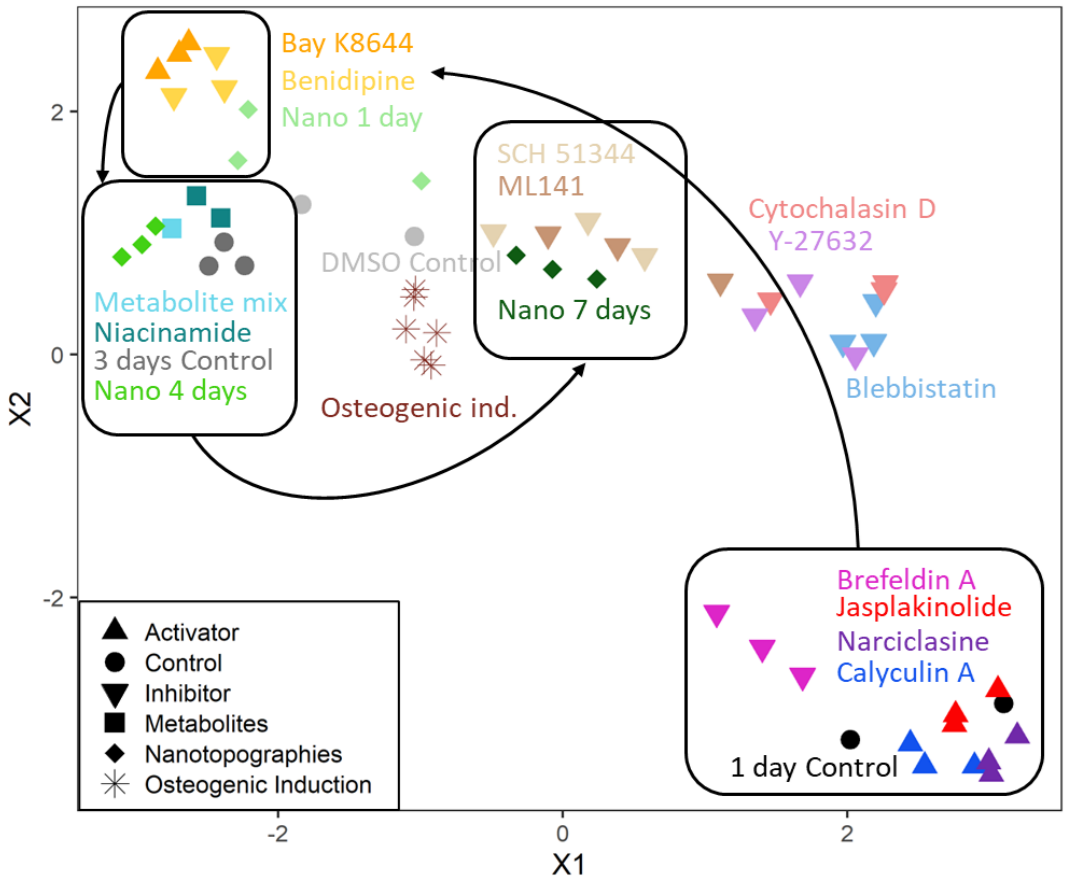

***Figure 4.7**: UMAP projection of the activators, inhibitors, metabolites, nanotopography and osteogenic induction. Each data points represents the median features of each concentration or condition. The UMAP projection is performed with 9 neighbours and a minimum distance of 0.1. The arrows show the journey of the cell response to nanopits over time as the morphology clusters with the L-type calcium channel inhibition and activation. After 4 days on nanopits they cluster with the niacinamide and metabolite mix, which replicate the intracellular tension and adhesion of the nanopits. Finally, they are with the Ras/Rac and ML141 inhibitors that inhibit the filopodia and lamellipodia formation. The osteogenic induction through dexamethasone, ß-glycerophosphate, and ascorbic acid form their own group. The inhibitors of the actin cytoskeleton (cytochalasin D), myosin II (blebbistatin), and ROCK (Y-27632) cluster together just like their activators.*

The metabolite mix verifies the grouping in the UMAP projection. Niacinamide and the metabolite mix increase the oxidative glycolysis and, as a result, the intracellular actin cytoskeleton tension and cell adhesion decreases. The same effect is observed on the NSQ, SQ and HEX nanopits. The cells on nanopits after 4 days group together with the niacinamide and the metabolite mix in the UMAP projection as expected. The control after 3 days clusters in the same group, which shows the strong effect the culturing time has on cell morphology.

The osteogenic induction through the induction media does not group up perfectly with the other conditions but forms its group. The osteogenic induction shows

many similarities as well as some differences in its gene array compared to the induction through nanopits[95]. Therefore, it can be expected that we can also see a difference in morphology during nanotpography-driven differentiation and benidipine[227], cytochalasin D[212], and Y-27632[53] promote the osteogenic differentiation of MC3T3 cells. None of those perturbations cluster together with the osteogenic induction. The chosen perturbations are involved in the mechanotransductional differentiation pathway, which differs from the differentiation through the drugs dexamethasone and glycerophosphate. Therefore, the mature osteoblasts on the nanopits also cluster with the inhibitors and not the mature osteoblasts through osteogenic induction. Many different pathways can lead to osteogenic differentiation. The cell morphology changes accordingly depending on the dominant pathways triggered by drugs or topography.

4.3.5. Feature analysis of clustering

A UMAP projection, a powerful tool in high-dimensional data analysis, effectively visualises similarities in cell morphology data. However, it does not provide information about the formation of the 2D representation, or which features are primarily responsible for the small distance between the different conditions within one group. The different groups in Figure 4.7 can be grouped into six clusters. The four previously discussed clusters are highlighted in the UMAP plot. Additionally, in addition to those four clusters, two more clusters are formed: osteogenic induction through the differentiation media and inhibitors of Actin, Myosin, and ROCK. The clusters are numbered as follows: The first cluster consists of cells in the initial state with minimal morphological changes. It consists of controls after one day, as well as the activators jasplakinolide, narciclasine, and calyculin A, along with the Golgi inhibitor brefeldin A. The second cluster represents the first response to the nanopits after one day, as well as the response to Calcium channel activators and inhibitors. The third cluster is the response to nanopits after four days, and the metabolites. The fourth cluster represents the response to nanopits after seven days, as well as the inhibition of Cdc42 and Ras/Rac. The fifth cluster consists of inhibitors that produce the strongest

morphology changes, particularly with ROCK, Actin, and Myosin inhibitors. The sixth cluster are the cells after osteogenic induction.

A heatmap plot ordered by the different clusters reveals clear differences between them (Figure 4.8). Clusters two and three exhibit many similarities, indicating that the cell's initial response to the nanopits changes relatively slowly until the morphology undergoes significant changes after 7 days, revealing apparent differences from the other clusters. Cluster five, which consists of the cytoskeleton inhibitors that have the strongest impact on the cell morphology, is also clearly separated from the other clusters. To gain a better understanding of the morphological differences between the clusters, we manually reviewed the features. We selected those with clear and understandable meanings from the entire heatmap, which provides insight into the morphological differences between the clusters (Figure 4.9).

The area shape measurements are the easiest to understand and give an overview of the general cell shape. After feature selection, we are left with the form factor and solidity as measures of cell shape. The form factor is a measure of the roundness of the cell and is calculated as $4*\pi*Area/Perimeter^2$, where a value of one is a perfectly round cell. The solidity calculates how much of the object is also in the convex hull. The convex hull is created by connecting the outer points of the object. One can imagine it as a band that is stretched around the object. A round cell without many protrusions has a high solidity, while a cell with many protrusions, such as filopodia, has a lower solidity. The form factor decreases as the time on the nanopits increases. This reflects the observed increase in cell elongation over time as the cells settle on the nanopits and cease forming lamellipodia and filopodia in different directions to sense the substrate. Surprisingly, the solidity also decreases over time, as we would expect it to increase with the presence of missing filopodia. The differences in solidity between the clusters are relatively small, so that the decrease might have an unknown cause (Figure 4.9).

The location of the nucleus in the cell and the chromatin organisation are measures of the cell state. Those factors can be calculated from the radial distribution of DNA staining intensity in the nucleus as well as in the whole cell.

The granularity and radial distribution measurement FracAtD, which measures the fraction of total staining from the inner area 1 to the outer area 4 in the nucleus. It measures the chromatin distribution in the nucleus. A difference is visible primarily for clusters two and three compared to the other clusters. The Zernike magnitude of the DNA in the whole cell measures the amount of intensity in different parts of the cell and is therefore a measure of the localisation of the nucleus inside the cell. We observe a high error in each cluster, indicating that the nucleus localisation varies within a cluster and is likely not a reliable measure to highlight the differences between the clusters.

The Golgi and plasma membrane staining can provide significantly different information, as they stain distinct organelles. That makes it harder to interpret, too. The Golgi has a higher intensity than the membrane; thus, bright dots in the cells are the Golgi and can be identified by granularity measurements. The granularity changes between clusters two and three, whereas clusters 1, 4, 5, and 6 have a similar level of granularity. The integrated intensity can be a measure of how strong the Golgi staining is, as well as how bright the intensity of the Golgi staining is, and also how large the cell is. We observe significant differences in Golgi and membrane intensity across the different clusters, with clusters two and three having the lowest intensity. In contrast, the other clusters have a higher integrated intensity, with cluster one exhibiting the highest intensity.

Correlation measurements with Golgi and plasma membrane, as well as actin, can also be seen as an indicator of how much of the cell is filled out by the organelle, since their staining fills out most of the cell. The correlation between the ER and the organelle changes between the clusters, with the smallest correlation observed in cluster three for the metabolites and nanopits after four days. The other clusters are in a more similar range. The integrated ER intensity at the edge of the cytosol is clearly the highest in cluster four of the Cdc42 and Ras/Rac inhibitor, as well as the nanopits, after seven days. As the cell settles with decreased filopodia and lamellipodia formation, the cell body gets narrower and smaller, and the ER reaches the edge of the cell. Thus, the fluorescence intensity of the cell increases.

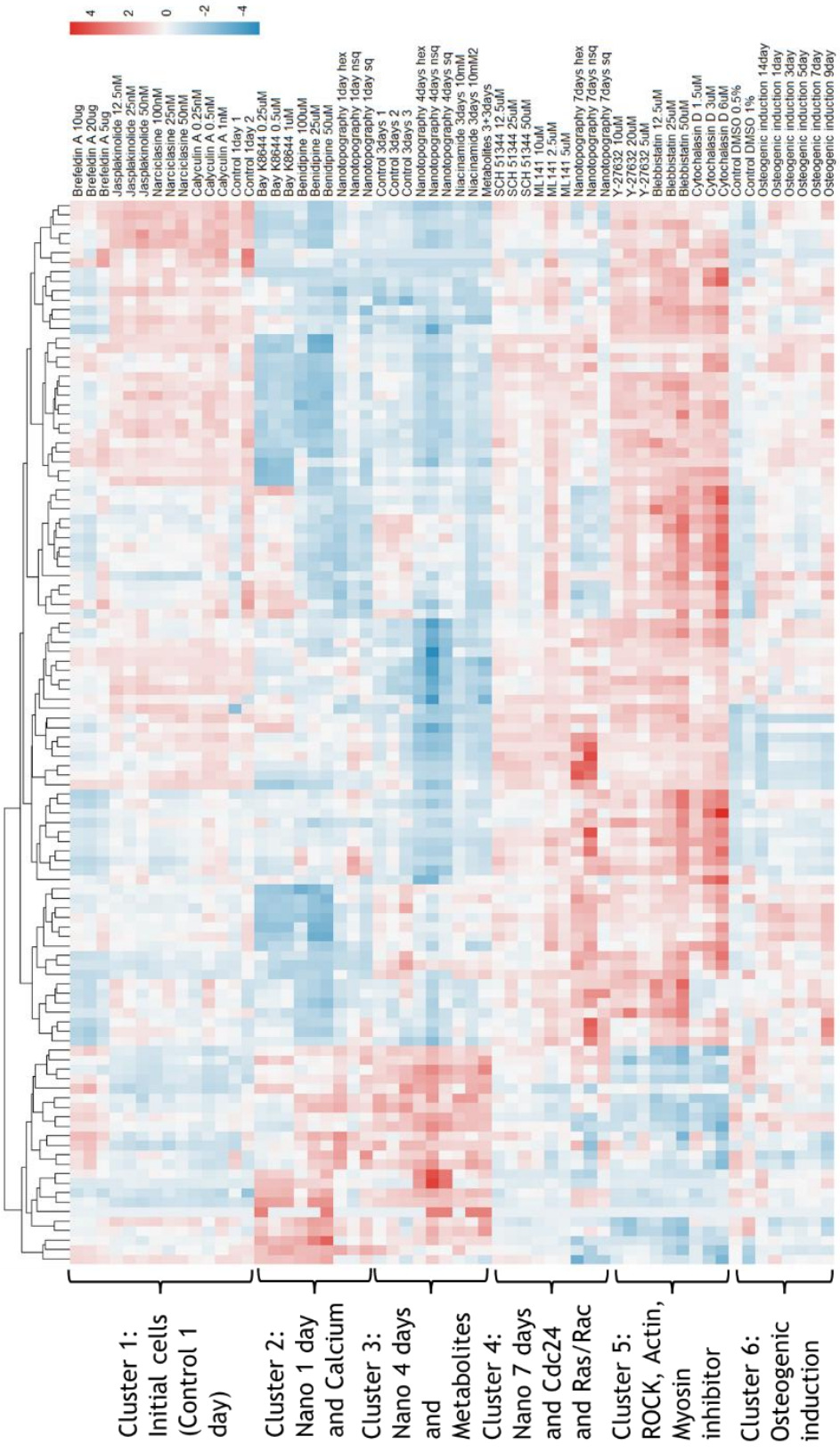

***Figure 4.8**: A heatmap of all the analysed conditions ordered by the clusters identified from the UMAP in Figure 4.7. The features replicate the found clusters. The clusters number 2 and 3 are relatively similar to each other as well as the clusters number 4 and 5. The separation between the other clusters is clearly visible from the heatmap.*

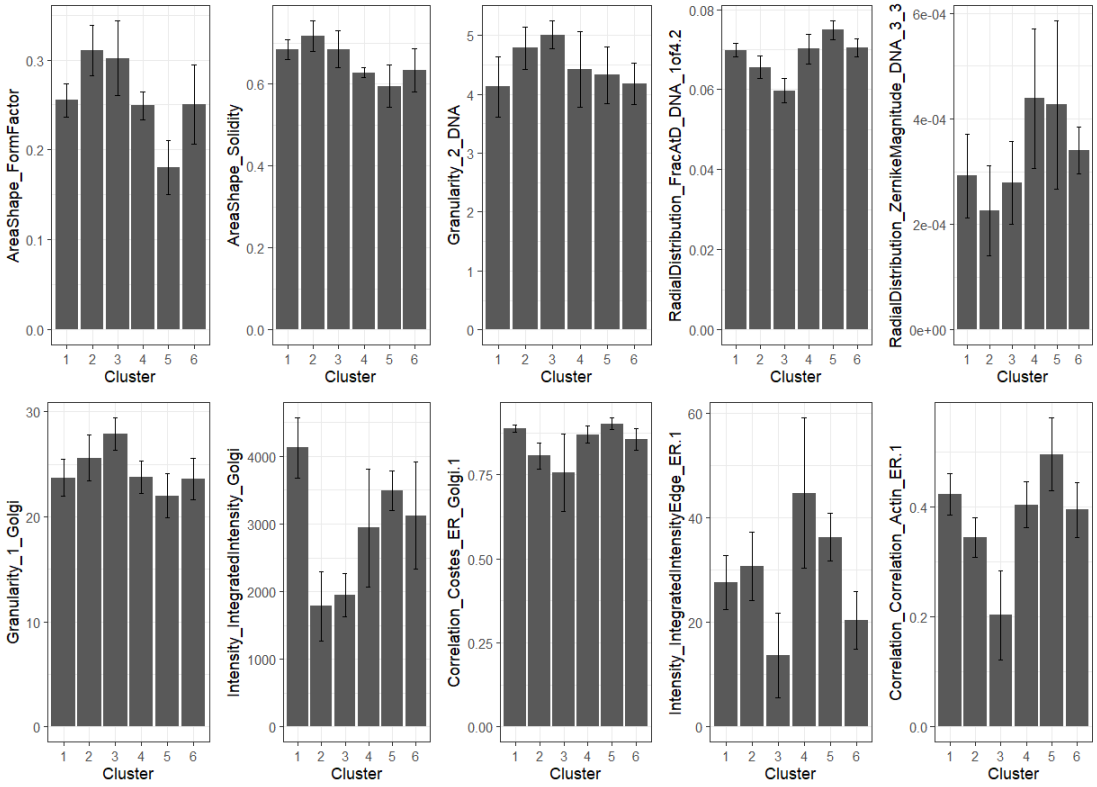

***Figure 4.9**: A barplot of selected features that highlights the morphological differences between the clusters. It shows that the clusters clearly differ for some features like the integrated intensity of the Golgi and membrane or the FormFactor, which shows smaller values for cluster 5 then for the rest. Other features as the DNA Granularity of 2 or the solidity show a more even distribution. A '1' behind the measurement means that the measurement is in the cytosol. A '2' means that the measurement is in the nucleus.*

The above-mentioned features provide an overview of the morphological changes between the clusters. However, we do not know the importance of these features in distinguishing the conditions within the observed clusters. To obtain an idea of feature importance, we have employed an entropy-weighted k-means clustering (wskm package in R)[228]. It works by assigning a weight to each feature for each cluster and adjusting those weights until it converges to obtain a clustering into a specified number of clusters. We chose six clusters based on our observations in the UMAP projection and attempted to select parameters for the weighted k-means clustering in a way that would replicate our initial clusters as closely as possible. The clustering is plotted in a 2D PCA space in figure 4.10A. The change in clusters for the different conditions is shown in table 4.2. While there are some differences in the clustering, the most important clusters for the change in cell morphology over time in response to the nanopits are very similar to those from the UMAP projection. The nanopits, after four days, cluster with the metabolites, and the nanopits, after seven days, cluster with the Ras/Rac and Cdc42 inhibitor.

The nanopits after one day do not fully cluster with the calcium channel activator and inhibitor. Only the SQ nanopits are in one cluster with it, and the NSQ and HEX nanopits form their own clusters after one day. The difference in clustering cannot be fully explained. We expect that the SQ, NSQ, and HEX nanopits have slightly different morphologies, as NSQ nanopits have the strongest positive impact among those topographies on osteogenic differentiation. However, all nanopits promote osteogenic differentiation of MC3T3 cells. The weighted k-means clustering starts by randomly assigning weights to the features, making the method stochastic. We chose weights that produce a similar clustering to the UMAP clustering in Figure 4.7. While we achieve a good agreement between the clustering methods, a perfect overlap of clusters is not possible. The most important findings of the UMAP clustering are also shown in the weighted k-means clustering as discussed above.

We collected the features with the highest weight for each cluster and plotted them in a heatmap in Figure 4.10B. Cluster 5, with cells on nanopits after seven days, ML141, and SCH 51344, clearly has the highest weight for the radial distribution of actin. However, no apparent differences from other conditions are visible in the raw data. Cluster 1, with the nanopits after 4 days and metabolites, has the highest weight for a texture measure of the ER. This feature has relatively low values for the conditions in these clusters. The conditions with stronger cytoskeletal disruptions have a higher value in this feature. Cluster 6, with calcium activator and inhibitor, and SQ nanoparticles, after one day, has the highest weight for the correlation of DNA and ER, as well as the percentage of maximum intensity in Golgi and membrane staining. There is also no clear difference visible in the raw data that supports these features for clustering within the observed groups. Generally, the differences in weight are minimal between the features, with a few exceptions. Thus, the overall picture formed by the different features is more important than any single feature for clustering. The heatmap of the selected features displays clear blocks of similar measurements within the different groups, which support this barcode mechanism (Figure 4.11). The cytoskeletal inhibitors cytochalasin D, blebbistatin, and Y-27632 generally exhibit high feature values in the heatmap (red) and can be clearly distinguished by their similar morphological profiles.

***Table 4.2**: The differences in clustering between UMAP projection and entropy weighted k-means clustering. The clustering shows a lot of similarities with only some minor differences. The main clustering by function is represented in the UMAP as well as entropy weighted k-means clusters.*

Condition	UMAP Cluster	Entropy weighted k-means cluster
Control 1 day	1/1	1/3
Brefeldin A 5/10/20 µg/ml	1/1/1	3/1/1
Jasplakinolide 12.5/25/50 nM	1/1/1	5/5/5
Narciclasine 25/50/100 nM	1/1/1	5/3/3
Calyculin A 0.25/0.5/1nM	1/1/1	3/3/3
Bay K 0.25/0.5/1 µM	2/2/2	6/6/6
Benidipine 25/50/100 µM	2/2/2	6/6/6
Nanotopography 1 day SQ/NSQ/HEX	2/2/2	6/4/4
Control 3 days	3/3/3	1/1/1
Nanotopography 4 days SQ/NSQ/HEX	3/3/3	1/1/1
Niacinamide 3 days 10 mM	3/3	1/1
Metabolites 3+3 days	3	1
SCH 51344 12.5/25/50 µM	4/4/4	5/5/5
ML141 2.5/5/10 µM	4/4/4	5/5/5
Nanotopography 7 days SQ/NSQ/HEX	4/4/4	5/5/5
Blebbistatin 12.5/25/50 µM	5/5/5	2/2/2
Cytochalasin D 1.5/3/6 µM	5/5/5	3/2/2
Y-27632 5/10/20 µM	5/5/5	3/5/3
Control DMSO 0.5/1 %	6/6	1/1
Osteogenic induction 1/3/5/7/9/14	6/6/6/6/6/6	5/5/5/5/5/5

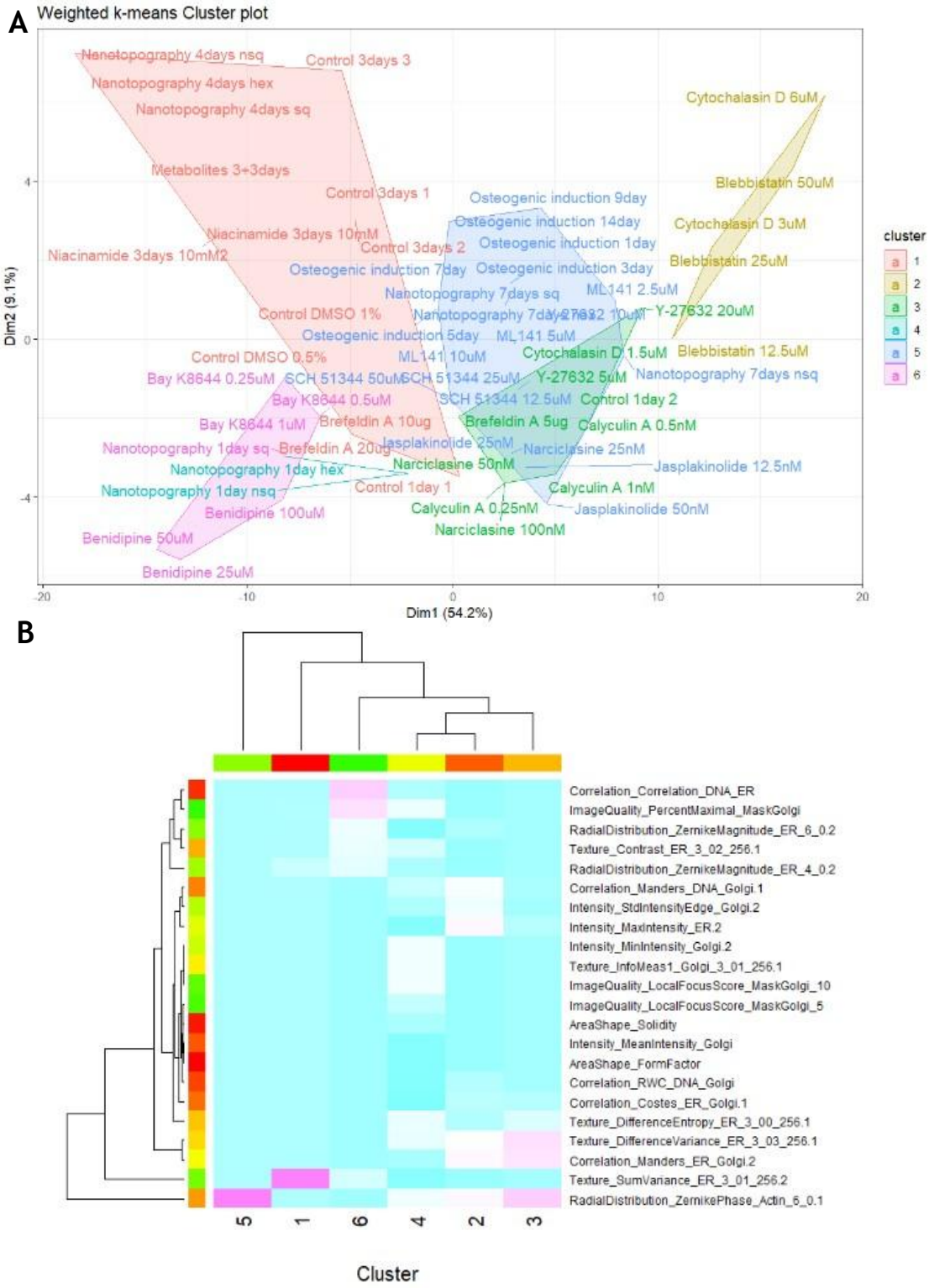

***Figure 4.10**: Entropy weighted k-means clustering for analysis of feature importance. The clustering visualized in a 2D PCA projection using the first 2 dimensions visualizes the formed clusters (A). Similar to the UMAP clustering in Figure 4.7, the activators and inhibitors cluster together by their function. The weight of the handpicked most important features for the formation of each cluster is plotted in a heatmap with pink being the high values and blue the low values (B). The clusters are ordered according to a hierarchical clustering to enhance the visibility of differences between the clusters. Most weights are in a similar range with a few outliers of high importance for the clustering as the Zernike$_{50}$Phase for Actin, the SumVariance texture measurement of the ER or the Correlation of DNA and ER.*

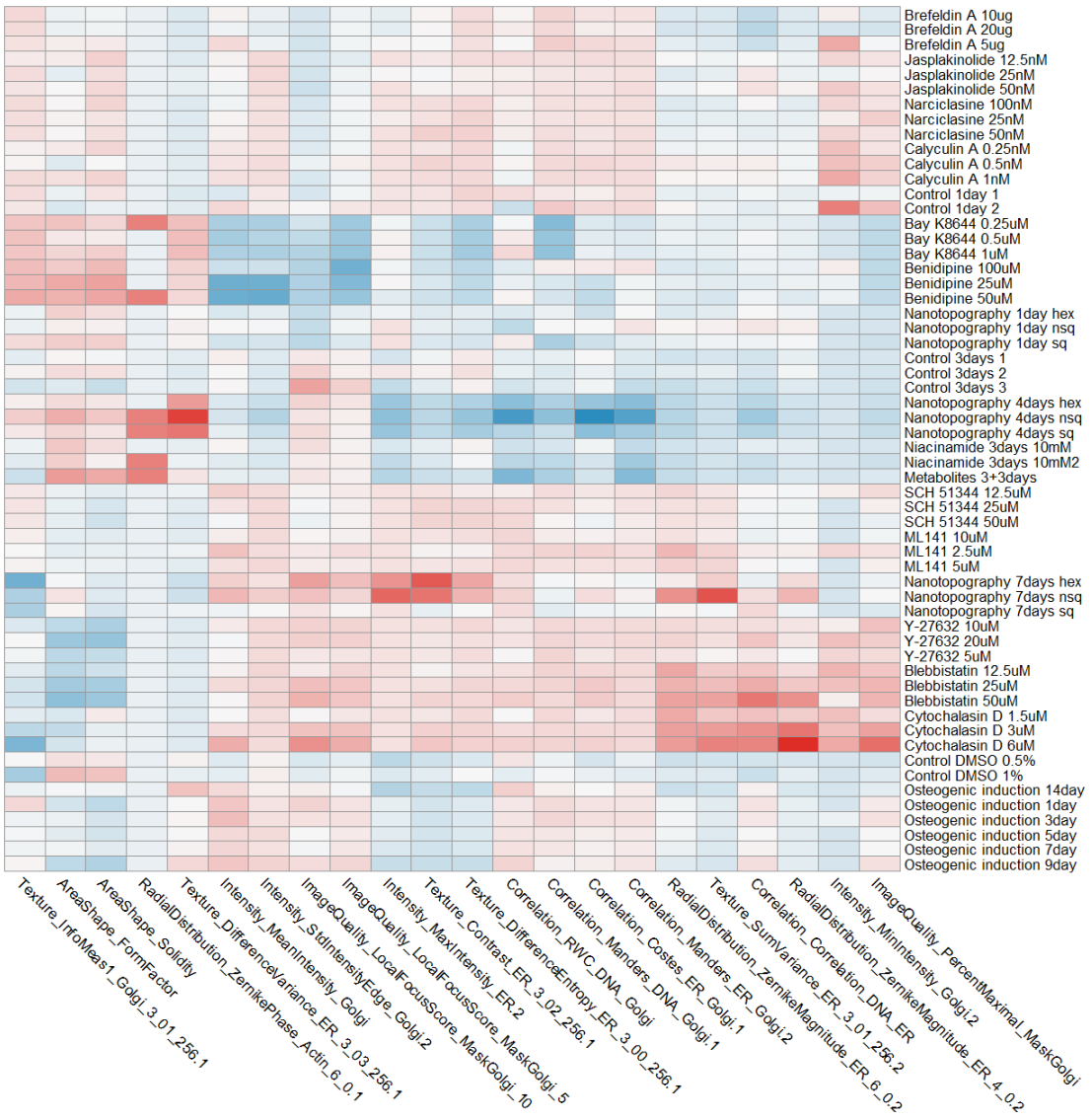

***Figure 4.11**: A heatmap of the selected most important features with the highest weights in the entropy weighted k-means clustering. The conditions are ordered by the clustering done by the UMAP projection. This clustering is also visible in the blocks of similar morphology by the selected features. It shows a similar picture as the large heatmap in Figure 4.8 with all features, however the selection of the most important features enables a visualization of the changes in single features, which is not possible with too many features.*

The 103 features selected from the complete data set are distributed across all four channels/organelles (Table 4.3). The Golgi and plasma membrane stand out with 55 features that are selected from that channel. When selecting the top features in the weighted k-means clustering, we observe an unexpectedly strong drop in actin features, with only one feature remaining. One would typically expect that the actin cytoskeleton is more important for the morphological

profiling of cells in the mechanotransduction pathway, which is very focused on cytoskeleton organisation. On the other hand, it highlights the potential and importance of the cell painting method for morphological profiling. In the complex process of mechanotransduction, it is essential not only to examine the known cell compartments involved but also to take a comprehensive view of the cell to capture its morphological phenotype fully.

All CellProfiler measurement categories are also well represented in the full dataset. Most features are from the intensity distribution and correlation measurements. The selected features from the entropy-weighted k-means clustering are also distributed across all measurements, except for the granularity. That highlights that, similar to the different stains, all measurements also provide helpful information for identifying the morphological phenotypes. When interpreting those numbers, especially the importance of single measurements, one must be cautious not to overestimate the significance of the feature. Many features are excluded from the final analysis due to high correlation with other features. Thus, many features that represent different morphological changes give the same information about the grouping of the different conditions.

***Table 4.3**: An overview of the feature distribution based on different stains/organelles and on the CellProfiler measurements. The full dataset consists of the 103 selected features by our feature selection method. Those features are compared with the selected features from the entropy weighted k-means clustering.*

Organelle	**Full dataset**	**Weighted k-means: Selected Features**
Actin	26	1
Golgi & plasma membrane	55	10
Endoplasmic Reticulum	32	11
DNA	23	3

CellProfiler Measurement	**Full dataset**	**Weighted k-means: Selected Features**
Correlation	29	5
Granularity	7	0
Image Quality	9	3
Intensity	16	4
Intensity distribution	34	3
Shape	2	2
Texture	18	5

4.4. Discussion

We successfully imaged MC3T3 cells with 11 different inhibitors and activators and three concentrations each, as well as SQ, NSQ, and HEX nanopits after 1, 4, and 7 days. We also incubated them with metabolite mix after 3 days and osteogenic induction media for 1, 3, 5, 7, 9, and 14 days. This accumulates to 53 different conditions and more than 3200 fluorescence images. An image has an average of 5 cells, which means that we have more than 16000 cells. An imaging time of 4.5 minutes per image means a constant imaging time of 240 hours. This highlights the magnitude of data collected and analysed.

Our research has revealed that cell morphology is a powerful tool for studying the mechanotransduction pathway of MC3T3 cells on SQ, NSQ and HEX nanopit surfaces. By employing Cell Painting with activators and inhibitors of the pathway, we have been able to demonstrate a UMAP projection that clusters inhibitors and activators based on their function. Notably, inhibitors and activators of the ROCK-Myosin II pathway cluster in their respective groups, providing a significant insight into the mechanotransduction process. Additionally, we can also pick up the different strengths in cell response to the different nanopits arrangements in SQ, NSQ and HEX arrangements as the similarity of cells on SQ and HEX nanopits compared to cells on NSQ nanopits reflects the previous reported differences in osteogenic marker expressions on the same topographies.

From the clustering in the UMAP projection, we propose that calcium signalling dominates the first cell response to the nanopits after one day. This aligns with the current state of research that calcium signalling promotes the early osteogenic genic marker RUNX2[224]. Furthermore, we expect that membrane proteins like calcium channels in direct contact with the nanotopography will have a significant impact in the first response to nanotopographies as it is the most direct influence of the topography on the cell. The intracellular actin cytoskeleton tension and cell adhesion are reduced due to increased oxidative glycolysis in the following differentiation process over the following days[207]. After seven days on the nanotopographies, the mature osteoblasts are in senescence and lack lamellipodia and filopodia since they are in a static and settled state with decreased mobility.

Our data show the above-mentioned mechanotransduction responses in MC3T3 cells to nanotopographies. However, other known involvements of the studied mechanotransduction pathway are not picked up. The ROCK pathway is known to regulate osteogenic differentiation of primary rat osteoblasts on titanium nanotopographies. Inhibition of ROCK with Y-27632 suppresses osteogenesis[229]. The known promotion of osteogenesis by cytochalasin D[212] is also not visible in the data. The response to nanotopography is more complex than a simple inhibition or activation of a single factor. Therefore, the morphomes of ROCK pathway inhibition and activation do not match those from the nanotopographies. Thus, the morphological profiling can only guide to interesting interactions, but does not exclude conditions that do not cluster with the nanotopographies.

We must be careful when interpreting results from the cell morphology of cells with different incubation times. Naturally, the incubation time has a significant effect on the cell morphology. Thus, the control after four days lies with the perturbations for three, four and six days and not the control after one day. After four days on flat surfaces without perturbations, the overall cell shape will be different to a cell after one day as it has settled down and built up a more excessive extracellular matrix. A UMAP projection tries to group every point into a group, where the group size depends on the chosen number of neighbours. Consequently, it will move a point to the most similar points, which does not necessarily mean that they are the same. They are just more similar than the other conditions.

We still believe in the UMAP projection as a truthful representation of similarities between phenotypes because of the observed grouping of the different inhibitors and activators, which aligns with known mechanotransduction pathways, and the morphology changes described in detail above. Furthermore, the observed grouping of the metabolites with the nanotopographies provides additional validation of our method.

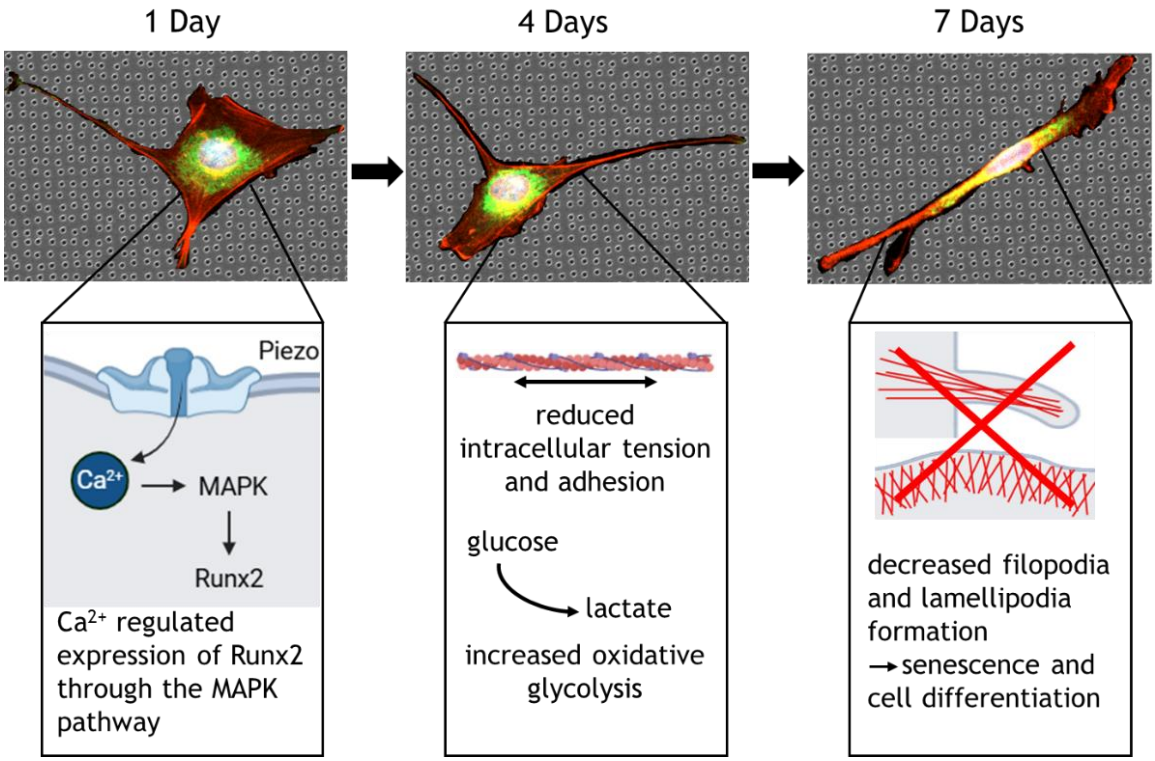

(caption for figure on previous page) ***Figure 4.12****: Visualization of the cell response to nanopits over time. After one day the calcium signalling is increasing the Runx2 expression through the MAPK pathway to start the osteogenesis. After four days the intracellular tension and adhesion decrease, and oxidative glycolysis increases. After seven days the cell goes into senescence and cell differentiation. In that state the cells have a decreased filopodia and lamellipodia formation. Schematics created in BioRender.*

The cell morphology is not only able to cluster different perturbations together, but it can also reflect their strength. Increasing concentrations of activators and inhibitors increases the strength of responses across many features, even though the features exhibit high variability. Even with the high variability, the median shows clear trends throughout many features. Willis et al. showed that Cell Painting can capture concentration dependence by performing a concentration-response screening of 14 phenotypic compounds in U2OS, A549, ARPE-19, HepG2, HTB-9, and MCF7 cells[230]. This could be used for dose tests in future work. It can be especially interesting for the use of nanotopographies as the dose dependence of the drugs can be compared with the different orientations of nanopits. The strength of the effect of the nanopits varies with the orientation, represented by the morphology. One can use the varying responses to different topographies to identify an ideal nanotopography to elicit a desired response. Another advantage of morphological profiling is the possibility of capturing the immediate reaction to the topography, while other techniques like transcriptomics have a delay until enough noticeable changes in transcription are observable. We can follow the adaption of the cells to the nanotopographies in real-time and can even analyse the early-stage cell-surface interactions, which refer to the initial contact and response of the cell to the nanotopography. By predicting Cell Painting images from brightfield images[231], one can study the adaption of live cells to different nanotopographies.

This study is the first study to use Cell Painting in combination with nanotopographies. The closest comparable study is the work of Tuvshindorj et al.[232] that tested 2176 arrays of unique geometries coated with Arginine-Glycine-Aspartic acid/polyethylene glycol for guided cell adhesion. They discovered that the morphome correlates with YAP nuclear translocation. However, they have not tried correlate the morphome to the patterns. Conventionally, Cell Painting is used to study drugs, especially for drug discovery. It is used in a wide area of applications, for example, to create a library of

morphomes for a large number of perturbations, such as 30,000 small molecules[133] or the famous JUMP dataset[137] with 116,750 different small-molecule compounds, over-expression of 12,602 genes and knockout of 7,975 genes in U2OS cells. Cell Painting is applied to identify 258 impactful variants of lung cancer variants by overexpressing 375 genes in A549 cells[134], novel gene functions discovered in U2OS cells by successfully clustering genes and alleles[135], and potential targets and drugs to treat intestinal fibrosis were identified by screening 5,000 compounds[233]. It has also been successfully employed to study the cytoskeleton and to identify compounds that target tubulin[234]. Cell Painting can also be used to identify chemical hazards[235].

These studies correlate newly identified chemical compounds or gene expression with known genes and chemical compounds to identify mechanisms of action, compound targets, and cytotoxicity. In contrast to those studies, our work uses the drugs not for drug discovery, but rather utilises their known effects to correlate cellular functions with nanotopographies. This is a new concept, and this work functions as a proof-of-concept for the method and for the work in the following chapter using a library of nanotopographies. Our work involves only a few perturbations compared to previous Cell Painting applications. Thus, it serves as a proof-of-concept and might yield new significant insights into mechanotransduction by upscaling the number of perturbations. Cell Painting profiling also only provides correlations between components by screening across many perturbations and topographies. To fully understand the biological connections, more in-depth studies of the identified connections are necessary.

5. Nanotopography prediction from the morphome using a nanotopography library

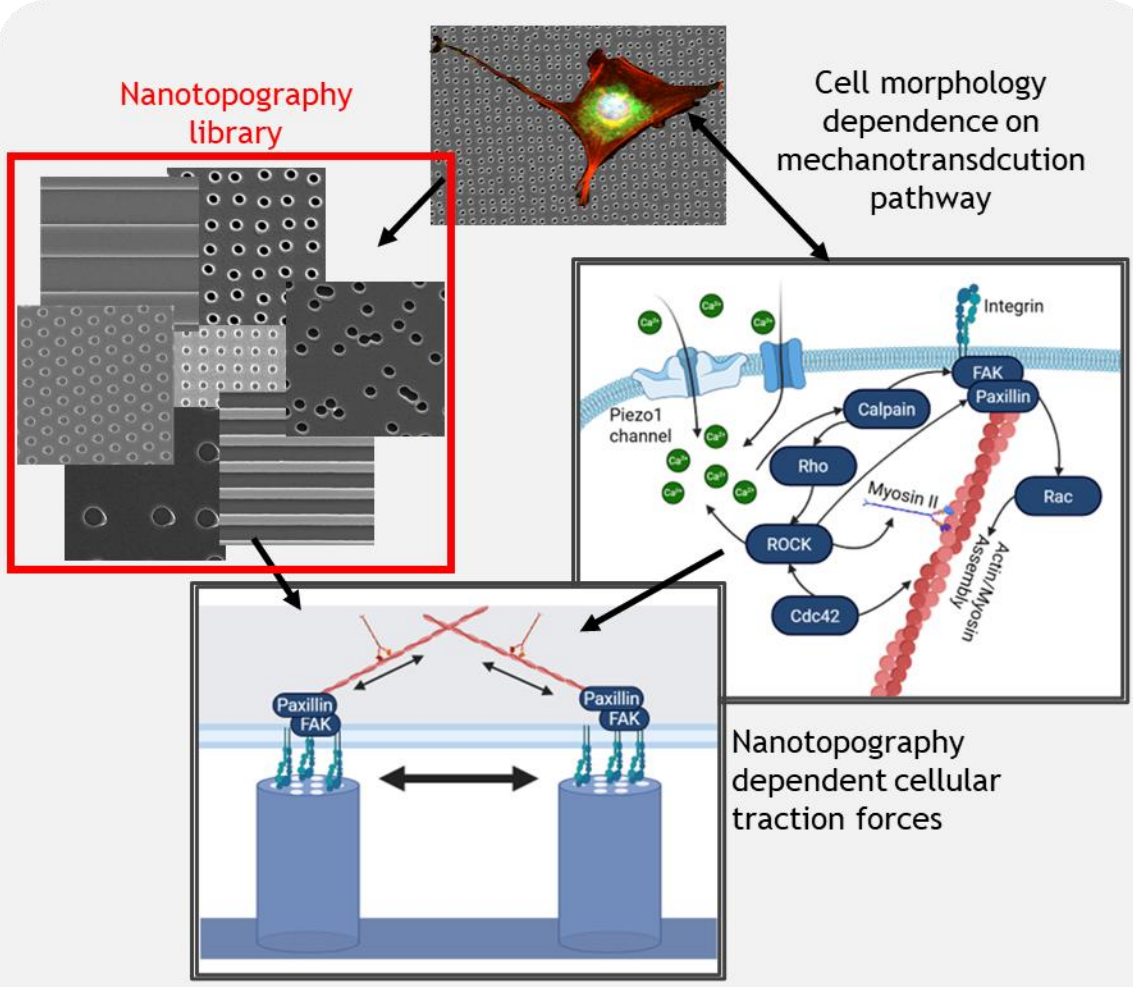

Methods: Morphological profiling with **Cell Painting**

- **84** different nanotopographies are prepared in **polystyrene**
- **78 nanopit** in **SQ**, **NSQ**, **HEX**, and **NHEX** arrays with varying **diameter**, **pitch**, and **disorder** are used
- **6 gratings** of varying widths are used

  ⟶ **>5340** fluorescence images

Results:

- Batch correction necessary ⟶ **Seurat** performs best
- Prediction of new topography not possible
- **Disorder** shows **highest correlation** with morphome
- Nanofeatures of **<5 µm** necessary for cell response
- Cell **alignment** at 200 nm grating depth is **adhesion driven** and not confinement driven

5.1. Introduction

The cell response to nanotopographies is strongly influenced by the geometry of the topography. The overall geometry of the topography, whether they are pits, pillars, gratings or other shapes, as well as the fine parameters of the topography, such as its size, organisation and distance between features, play a crucial role. These topographies influence the behaviour of cells by guiding the adhesion areas of the cells[3]. The size and orientation of the adhesions affect the cell's response[57, 101, 102].

The search for the ideal topography by testing a wide range of nanotopographies is challenging and limited by the fabrication of large enough arrays of these nanotopographies, as well as by time-consuming analysis to obtain a detailed picture of the cell's state. Few micro-/nanotopography libraries have been tested so far[17]. The most well-known and extensive libraries are the Micro-/NanoTopoChip by de Boer[77, 236] and the BioSurface Structure Array (BSSA) by Foss[237]. The MicroTopoChips consist of 2176 unique microtopographies created from random combinations of squares, triangles, and circles that overlap to form new shapes[236]. The features of the NanoTopoChip are created in the same way, just at smaller dimensions. UV lithography, DRIE and hot-embossing fabricate 1246 unique topographies. The cell morphology of U2OS cells is analysed on the topographies[77]. The BSSA library consists of 169 topography designs of squares, circles and rectangles of varying organisation, size and spacing. The 169 topographies are produced at heights of 0.6, 1.6, and 2.4 µm[238]. The feature size ranges from 1 to 8 µm. It is used to study the mineralisation and expression of osteogenic markers in MC3T3 cells[238] and the response of human fibroblasts by analysing changes in focal adhesion morphology and cytoskeletal organisation[237]. Kim produced a smaller feature library in the form of the MultiARChitecture (MARC) plate, which consists of up to 30 patterns[239]. The used patterns vary depending on the applications. They include gratings, wells, pillars, and lenses, with sizes ranging from 250 nm to 10 µm. It is used to study the response of pluripotent stem cells[240, 241] and murine neural progenitor cells[242]. The integrated mechanobiology platform (IMP) that bonds PDMS with nanotoporgraphies on bottomless 96 and 384 well plates[243]. They use gratings

with 500 nm to 3 µm spacing and square grids with trenches of 100, 200, and 300 nm. All nanotopography libraries identified the spacing between features as a key driver of cell response.

The screening of micro-/nanotopographies is performed mainly by immunofluorescence staining, as it does not require large cell numbers. The de Boer redesigned the Micro-/NanoTopoChip into a TopoWellPlate to achieve a sufficient number of cells per array for cytokine measurements of mesenchymal stromal cells[244]. Another benefit of the new TopoWellPlate is the physical separation of the different topographies into their own wells. This prevents the cross-talk between cells and enables the study of secretion profiles. However, this results in a reduction to 76 unique topographies. The MARC ship is used for RT-qPCR to study the differentiation of pluripotent stem cells[240]. This is only feasible due to the relatively small number of 30 different topographies. The BSSA chip is used with actin, focal adhesion, and osteogenic marker staining[110, 237, 238]. The effect of the topographies of the NanoTopoChip U2OS cells was analysed through the cell shape and actin morphology[77]. We believe that morphological profiling using Cell Painting can improve screening by providing a more in-depth view of cell state.

A similar screening is performed with the Galpagos chip by the de Boer group[232]. Instead of microtopographies, a chemical pattern library identical to that of the MicroTopoChip is fabricated with a binary Arginine-Glycine-Aspartic acid/polyethylene glycol coating. Human mesenchymal stem cells are studied by Cell Painting and YAP protein localisation. The adhesion pattern and the material affect the cells. The group of Daniel Anderson developed a screening platform to study the chemical composition of the surface, containing 1,728 different polymer spots[245]. In another device, they have created a platform of 496 polymer surfaces that differ in wettability, stiffness, and surface roughness by combining 22 monomers at varying ratios[246]. All those factors have proven important for cell response, but in our work, we focus on the nanotopography library.

Gratings create adhesion areas in a line. Thus, the cell morphology follows the grating, and one observes elongated, parallel-oriented cells along the gratings. This effect is especially of interest in the work with neuronal cells[91, 92]. Pits

and pillars create adhesion areas depending on the size of the features and the spacing between the pillars and pits. The slight differences in topography, as well as the features of height, size, and disorder, affect the response of the cell[26, 31, 96, 97]. When choosing a topography for an application, the fine details of the topography geometry are rarely considered when identifying the ideal topography. The conventional analysis is done with expensive and time-consuming omics techniques, so that an in-depth analysis of various topographies is not feasible[12-14]. We believe that morphological profiling using the Cell Painting method is a viable technique for studying a large library of topographies. As we have shown in the previous chapter, the Cell Painting method can detect the cell response to nanotopographies, with the ability to differentiate between nanopits in square (SQ), near-square (NSQ), and hexagonal (HEX) arrays.

When studying the morphological profile of cells on nanotopographies, the differences in morphology will be relatively small. Thus, a good feature selection and batch correction are necessary. The morphological profiling has a large number of features compared to the number of variables. This curse of dimensionality is a well-known problem in machine learning with omics data, highlighting the importance of feature selection[247]. Additionally, the Capenter lab studied the feature selection and batch correction for the Cell Painting method in detail[141]. For an optimised and standardised data processing of Cell Painting data, they developed the Cytominer package for Python and R[140]. A study of batch correction methods for data of varying complexity, from single-laboratory, single-microscope data to multiple-laboratory, multiple-microscope data, showed good performance of Seurat correction and Harmony correction. The Seurat batch correction method is the state-of-the-art method for scRNA-Seq data[139].

We aim to use the morphological profile of MC3T3 cells on various topographies to compare the morphology of the cells on the topographies with the morphology from the activators and inhibitors of the previous chapter to design new nanotopographies that replicate the effect of the activators/inhibitors. In machine learning, the prediction of a variable from a dataset is widely done[248, 249]. However, the prediction of new variables, which are a new topography in our case, is rare and much more challenging[250, 251].

The expression of osteogenic markers can be predicted from the morphome of MC3T3 cells on 100 nm diameter nanopits in a square, near-square and hexagonal array using Bayesian linear regression[20]. An in-depth literature analysis was done to identify the optimal parameters for osteoinductive biomaterials via machine learning[251]. They found that a porous calcium phosphate ceramic with micropores between 2.5 and 10 µm and macropores of 250 to 1300 µm. A fabricated material based on the found optimal parameters, featuring macropores of 300 to 760 µm, micropores of 10 to 100 µm, as well as pores of 2 to 10 µm, with a porosity of 76.7%. The new bone formation surpassed the database average of 10.97 % with 14.7 ± 7 %. Thus, it has been shown that new materials can be predicted from a database of different biomaterials. However, the prediction of new parameters has many limitations due to varying data quality and non-standardised experimental procedures, the difficulty of comparing materials, and small dataset sizes[250, 251]. This work is the only one so far to predict new biomaterials from a library of different biomaterials. Other work has only been able to predict already known biomaterials from the cell morphome or identify the optimal biomaterial for a defined application from a library of tested biomaterials. Thus, we aim to take this work further by predicting new topography designs that match a cell morphome that does not come from a topography. That means we have the cell morphome of a cell in one state, for example, after osteogenesis induction, on the one hand, and, on the other hand, the cell morphomes from a library of systematically different nanotopographies. Now we want to make up a new topography that produces the morphome after osteogenic induction.

Our approach with Cell Painting on injection-moulded polystyrene slides in well plates is designed to overcome these challenges of screening a large library of nanotopographies. The type of 24 well plate was used before by Huethorst et al.[186] for the screening of cardiomyocytes on grooves, chondrocytes on nanopillars and MC3T3 cells on high aspect ratio nanopillars. A comprehensive amount of data can be collected under well-controlled experimental conditions across a wide range of topographies by changing one parameter at a time and maintaining consistent material properties. The employed nanotopographies will be nanopits with varying pitch in a square and near square array, varying

diameters, varying disorder of hexagonal and square arrays, and gratings of different sizes.

5.2. Methodology

The staining and imaging procedures using the Cell Painting method are performed as described in Chapter 3. The staining is performed after four days of incubation on the nanotopographies, since it has been shown in Chapter 4 that we see an effect on the cell morphology after four days, while the control is not yet overcrowded.

5.2.1. Nanotopography fabrication

The polystyrene well plates with nanopatterns are fabricated using injection moulding and ultrasonic welding, as detailed in the general methodology section. These plates feature five distinct types of arrays of nanotopographies, each with its unique characteristics. Four of the five arrays consist of nanopits with a standard diameter of 120 nm, depth of 100nm, and centre-to-centre spacing of 300 nm. The NSQ pitch array introduces a disorder of 50 nm from the ideal square lattice and a varying pitch from 250 to 350 nm (Figure 5.1A). The arrays with a pitch of 265 and 285 nm are missing due to a writing error in the master. The SQ pitch array, on the other hand, presents the nanopits in a square lattice with a varying pitch from 250 to 350 nm (Figure 5.1B). The array with a pitch of 290 nm is missing due to a writing error. Both arrays also include a well with a flat surface, nanopits in a HEX lattice, and a standard SQ and NSQ lattice for comparison. The sizes array offers varying nanopits with diameters from 150 nm to 5 µm in a SQ, NSQ, HEX, and near-hexagonal (NHEX) lattices (Figure 5.2A). The NSQ array with a diameter of 150 nm is missing due to a writing error in the master. These arrays are injection moulded with a previously made nickel shim as a master. The disorder array introduces nanopits in an NSQ lattice with varying disorder from 0 to 150 nm and in an NHEX lattice with a disorder of 0, 10, 20, 50, and 80 nm (Figure 5.3). The grating arrays, 200 nm in depth and with a size of 200 nm, 500 nm, 1 µm, 2 µm, 5 µm, and 10 µm (Figure 5.2B), are injection moulded from EVG PDMS foils.

The master is fabricated using the EVG nanoimprinting tool, a crucial step in our process, which is described in detail below.

First, a master for the nanoimprint must be fabricated. A four-inch silicon wafer is solvent cleaned in methanol, acetone, and isopropanol in an ultrasonic bath for 5 minutes per solvent. After oxygen plasma cleaning for two minutes at 150 W in YES G-1000 plasma asher and a dehydration bake for at least one hour in a 180 ºC oven, a PMMA layer of 200 nm is spun on the wafer at 2000 rpm for one minute. A Allresist AR-P 632.09 PMMA with 9 % weight in anisole and a molecular weight of 50k is used. After spinning, the wafer is baked on a vacuum hotplate for 5 minutes at 180 ºC to evaporate the solvent. Next, the desired pattern is written in the resist using electron beam lithography with a Raith EBPG 5200.

The pattern is developed in a 2.5:1 isopropanol:methyl isobutyl ketone (IPA:MIBK) developer for 25 seconds at 21 ºC under constant agitation. The nanopattern is then etched into the silicon wafer using reactive ion etching with an SPTS Omega LPX 200 Rapier (SPTS, UK). The wafer is etched for 55 seconds to obtain a 100 nm depth. The etch parameters are as follows: C_4F_8 flow rate: 90 sccm, SF_6 flow rate = 30 sccm, pressure = 20 mTorr, average platen HF power = 28 W, pk platen HF power = 280 W, platen HF duty = 10 %. The remaining resist is removed in a solvent cleaning process, as before when preparing the wafer. Afterwards, it is plasma cleaned again in a YES G-1000 oxygen plasma asher at 150 W for two minutes.

Next, the wafer is prepared for the EVG UV-nanoimprinting. The EVG nanoimprinting is performed with the kind help of Dr. Iliyana Samardzhieva. First, an anti-sticking layer (2-Methoxy-1-Methylethyl Acetate) is spun for 60 seconds at 800 rpm on the wafer and baked on a hotplate at 200 ºC for 75 seconds. After letting the wafer cool for 60 seconds, a propylene glycol monomethyl ether acetate solution is dispensed on the wafer while spinning at 500 rpm for 30 seconds and afterwards at 3000 rpm for 20 seconds. This step cleans the wafer and removes the edge bead. Next, the EVG PDMS soft stamp material is applied to the wafer and spun for 300 seconds at 4000 rpm.

In the EVG Nanoimprinting tool, the prepared wafer is placed on a vacuum chuck, and a Polyethylene Terephthalate (PET) foil is spanned into the machine. First, the PET foil is preconditioned for 10 seconds with UV exposure. After removing the protective foil from the PET foil, the wafer is moved below the PET and brought into contact with the foil using a roller to ensure good contact without bubbles. The sample is exposed to UV light for 300 seconds while holding a pressure of 1250 mbar. A 1000-Watt UV lamp is used for the UV exposure. After exposure, the foil is separated from the wafer, and one obtains the PET foil with the EVG PDMS with nanotopography on top. The foil-PDMS dual layer can then be cut into the desired shape by laser cutting and is ready for injection moulding.

5.2.2. Data integration of Cell Painting data

The morphome on the nanotopographies shows a smaller variety than the data with activators and inhibitors in the previous chapter. Thus, two different feature selection methods are tested. The first method, consistent with the previous chapter, involves the identification of significant data. Any feature with a difference between the highest and lowest mean values exceeding twice the mean standard error is deemed noise and excluded. Subsequently, all features with a fold change less than 75% between the maximum and minimum values are excluded to capture all data with an observable change. The data is then refined using Pearson correlation, with redundant data removed at a cutoff value of 0.95, and all features with an absolute correlation of less than 0.15 are excluded.

In the second feature selection method, we leverage the advanced capabilities of the R Cytominer package. The package was developed by the Carpenter lab for the optimal data processing of Cell Painting data. So far, each study uses its own methods for feature selection, which makes the comparison difficult. A standardized data processing with an optimized package as Cytominer can improve the comparability of studies. This feature selection method begins by excluding data with near-zero variance, followed by the removal of redundant data. The latter is identified by Pearson correlation, and all data with a correlation higher than 0.95 is removed. The remaining features are then analysed for their importance by their contribution in decreasing the information entropy. The *svd_entropy* function is employed, providing values for each feature, where higher

values indicate that the feature contains more information. The features with the most information are then selected, showcasing the power of the R Cytominer package in our research.

A strong batch effect is observed in the data set. Therefore, different batch correction methods are used with increased complexity. As a simple batch correction method, the data is normalized by centring the data to the median of the control using equation (8) with $\tilde{x}$ as the median and MAD, the median absolute deviation.

$$\frac{x-\tilde{x}_{Control}}{MAD_{Control}} \tag{8}$$

When the data is not normalised by centring to the control, the data is normalised by subtracting the single cell value from the mean and dividing by the standard deviation. A cube root transformation is also tested, which normalises the data similar to a log transformation. A log normalisation of the data is not possible since we have negative and very small values. A log(x+1) normalisation can be used instead, and the data can be shifted in a positive range. The cube root transformation has the benefit that it remains the special case of having zero values.

As a more advanced batch correction method, we employ the Seurat method. This method follows the adaptation of the Seurat batch correction for the Cell Painting data of Arevalo et al. who demonstrates its adaptability and applicability[139]. The batch correction is performed using the Seurat package developed by the Satija lab[144, 145]. We utilise the Seurat method with reciprocal PCA as a dimensionality reduction method. To find the anchor points, the nearest neighbours are searched by reciprocal projections onto the PCA space. After finding the integration anchors based on mutual nearest neighbours, the data is integrated to perform the batch effect correction.

The quality of batch effect correction is analysed in UMAP projections. Those high-dimensionality reduction methods must be used with caution, as it is known that they can distort data. However, it has also been proven to be a valuable tool to visualise the analysis. The controls on the different batches, as well as the

standard SQ, NSQ, and HEX nanopits in each batch, serve as an indicator to visualise whether a batch effect is visible or not.

5.2.3. Linear Regression and canonical correlation analysis

To test whether the morphome of the cells on the topographies of the nanotopography library correlates with the geometry of the topography, we use a multivariate multiple linear model[252, 253]. In conventional linear regression models, one single variable is predicted from a set of predictors. In the multivariate multiple linear regression (equation 10), multiple variables are predicted. Thus, the model appears as shown below, with ***Y*** representing the responses, ***X*** the predictors, and ε a random vector.

$$\begin{pmatrix} Y_{11} & \cdots & Y_{1q} \\ \vdots & \ddots & \vdots \\ Y_{n1} & \cdots & Y_{nq} \end{pmatrix}_{n\times q} = \boldsymbol{Y} \tag{9}$$

$$\boldsymbol{Y} = \begin{pmatrix} X_{11} & \cdots & X_{1p} \\ \vdots & \ddots & \vdots \\ X_{n1} & \cdots & X_{np} \end{pmatrix}_{n\times p} \begin{pmatrix} \beta_{11} & \cdots & \beta_{1q} \\ \vdots & \ddots & \vdots \\ \beta_{p1} & \cdots & \beta_{pq} \end{pmatrix}_{p\times q} + \begin{pmatrix} \varepsilon_{11} & \cdots & \varepsilon_{1q} \\ \vdots & \ddots & \vdots \\ \varepsilon_{n1} & \cdots & \varepsilon_{nq} \end{pmatrix}_{n\times q} \tag{10}$$

With more predictors *p* than conditions *n,* we encounter a dimensionality problem, and a regression model is not possible. Thus, the number of features selected needs to be reduced. So far, we have always selected the features independently of the variables. To ensure a good regression, we use a maximum correlation minimum redundancy method. We calculate the correlation of the features to each of the geometry parameters. The geometry of the topographies can be fully explained by the x-pitch, y-pitch, diameter, noise, and offset. The features with the highest correlation to the features, and a correlation cut-off of 0.7 for the correlation between the features.

To determine if the activator and inhibitor data from the previous chapter correlate with the data from the nanotopography library, we employ CCA[254]. CCA works similarly to PCA as it is also a dimensionality reduction method. However, it is not creating new variables with the highest variability, but it finds the linear combination of variables that has the maximum correlation to the

parameters of the dataset. We use the *CCA* R package and follow González et al.[255]. We use a regularised CCA to avoid dimensionality problems. The regularisation parameters are first computed by estimating them with a leave-one-out cross-validation process. The optimal parameters are identified by first using a large grid and then refining it in the area with the highest cross-validation criterion. Since a CCA is similar to a PCA, both are dimensionality reduction methods based on matrix algebra and eigen analysis, and they can be visualised in a similar way. In the same way that we obtain a specific number of principal components from PCA that can be plotted in a 2D plot as the dimensions, we obtain canonical variates that can be plotted as the dimensions of the data.

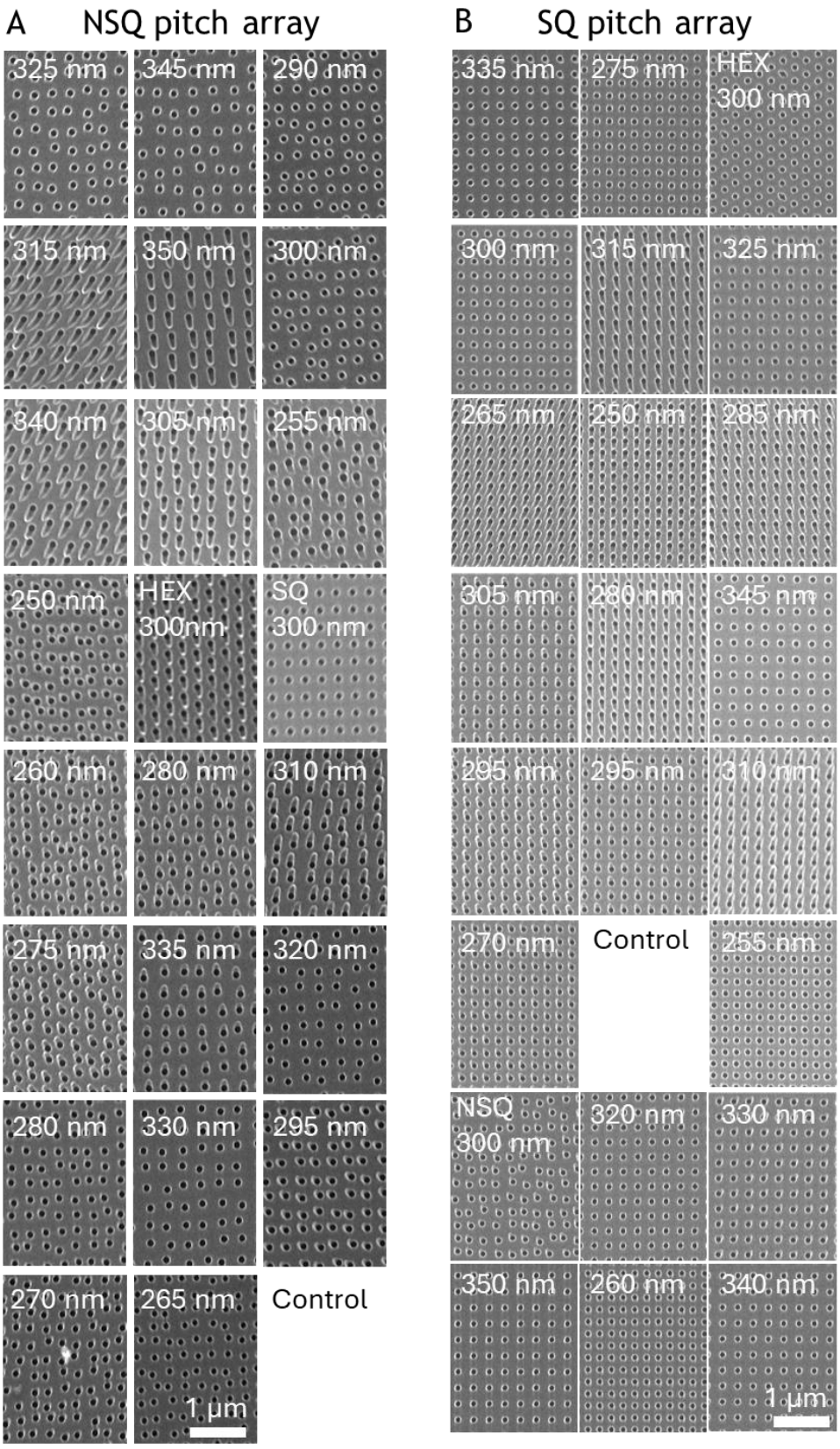

***Figure 5.1**: SEM images of nanopits in a NSQ pitch array (A) and SQ pitch array (B). The NSQ pitch array has nanopits with 100 nm diameter, and a varying pitch from 250 nm to 350 nm. The pits randomly vary by 50 nm from the ideal square lattice. The SQ pitch array has nanopits with 100 nm diameter, and a varying pitch from 250 to 350 nm in a square lattice. The SEM images are organized in the same way that they are organized on the used polystyrene slides with a flat control area. All SEM images are taken with a Hitachi scanning electron microscope of the SU8200 series. The scale bar shows 1 µm.*

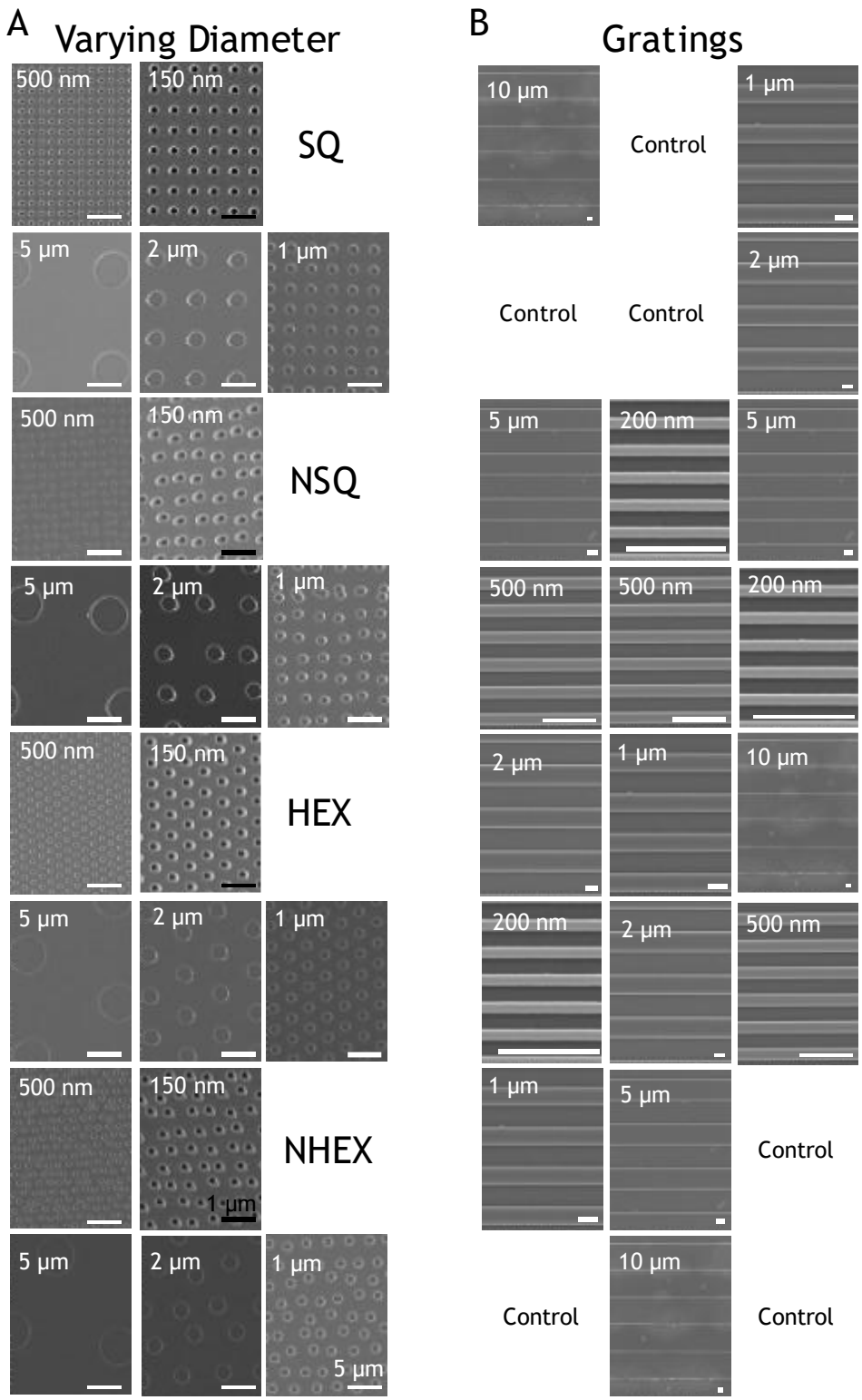

***Figure 5.2**: SEM images of polystyrene slides with nanopits with varying diameter (A) and gratings (B). The slide with varying diameter has nanopits of 150 nm, 500 nm, 1 µm, 2 µm, and 5 µm diameter. They are arranged in a square lattice (SQ), near square lattice (NSQ), hexagonal lattice (HEX), and near hexagonal lattice (NHEX). The nanopits in a disorder always differ by 50 % of the diameter. The centre-to-centre pitch is always three times the diameter. The gratings are in a 1:1 ratio of pitch and grating with a size of 200 nm, 500 nm, 1 µm, 2 µm, 5 µm, and 10 µm. The SEM images are organized in the same way that they are organized on the used polystyrene slides with a flat control area. All SEM images are taken with a Hitachi scanning electron microscope of the SU8200 series. The scale bars in A show 5 µm (white), and 1 µm (black). All scales bars of B are 1 µm.*

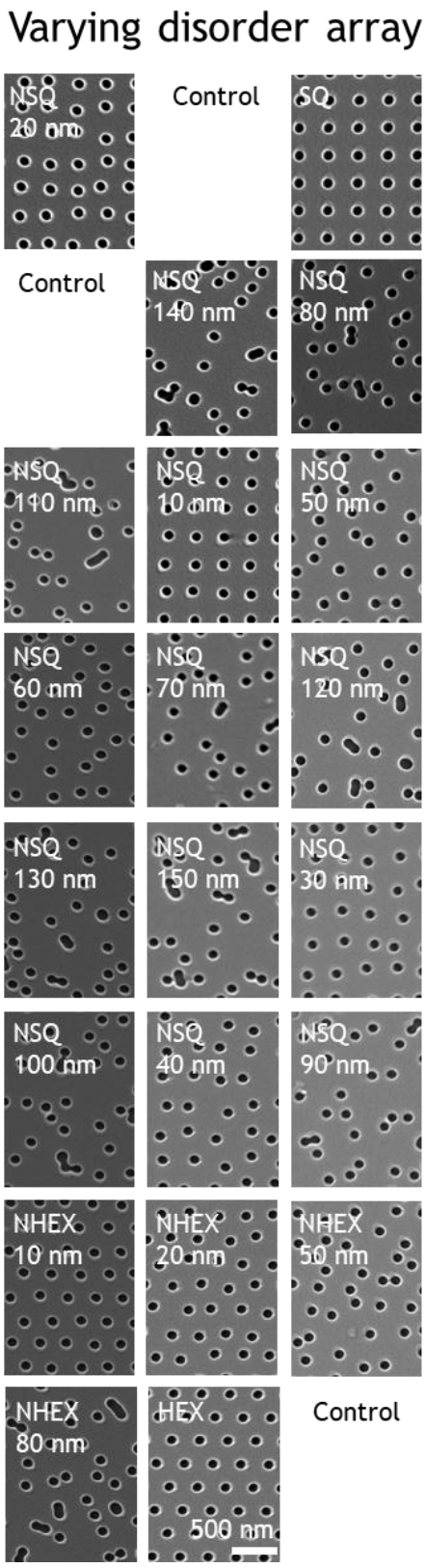

***Figure 5.3**: SEM images of nanopits in a square array and hexagonal array with varying disorder. The nanopits have a diameter of 100 nm, centre-to-centre spacing of 300 nm, and a varying disorder from the ideal lattice by 0 to 150 nm for the square lattice (NSQ) and 0 to 80 nm for the hexagonal lattice (NHEX). The SEM images are organized in the same way that they are organized on the used polystyrene slides with a flat control area. All SEM images are taken with a Hitachi scanning electron microscope of the SU8200 series. The scale bar shows 1 µm.*

5.3. Batch correction of nanotopography library data

The MC3T3 cells are successfully stained and imaged on all five different nanotopography arrays. When handling the CellProfiler data the same way as in Chapter 4, with a feature selection based on correlation and significance, we observe a strong batch effect. The UMAP in Figure 5.4 shows that the SQ pitch array data is especially separated from the other data. This is to be expected from the fluorescence images shown in Figure A5.3-A5.6, which show that the SQ pitch array has a weaker ER fluorescence throughout all topographies. The controls visualised by circles are not clustering together as they should, but they remain in their respective batches. The same effect can be observed for the standard SQ, NSQ, and HEX patterns that are present in every batch, except for the gratings. The batches of varying sizes and NSQ pitch are more connected. A clear trend based on the different topographies is still not visible in those batches.

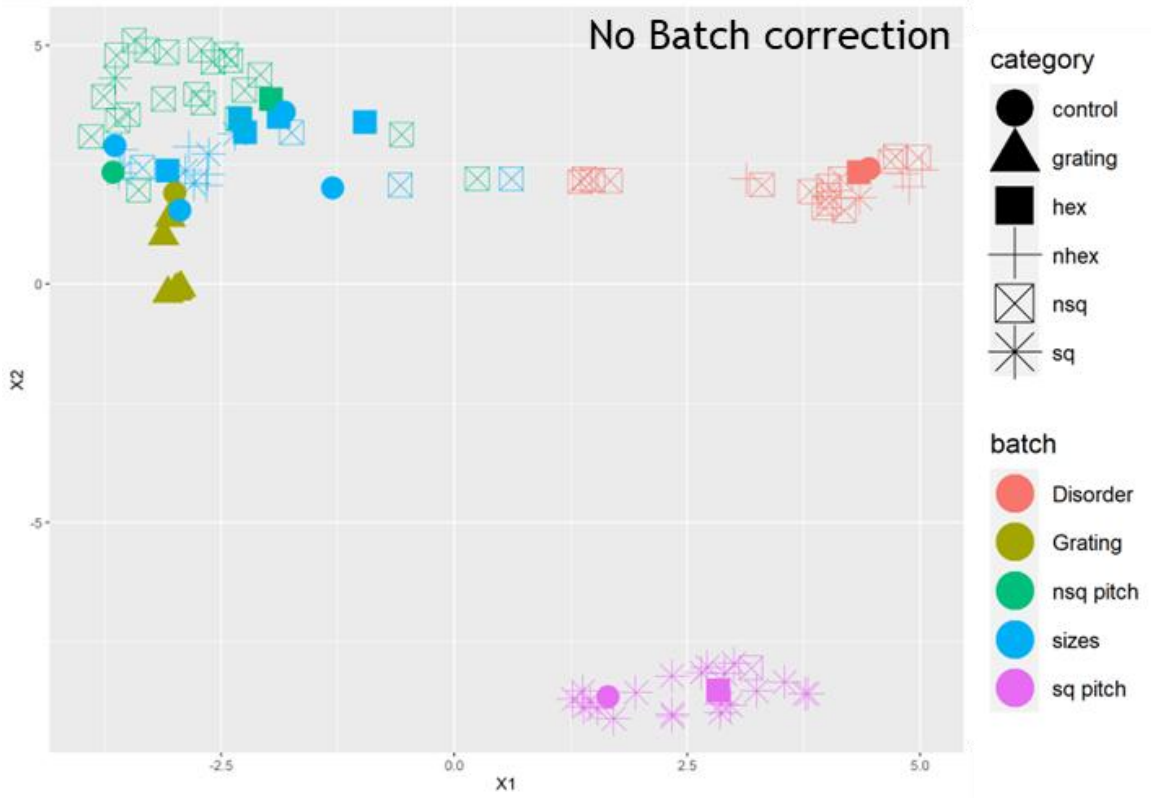

***Figure 5.4**: UMAP of nanotopography library data without batch correction. The datapoints are coloured by their batch and a clear clustering by the batches is visible. Especially, the array of SQ with varying pitches and the one with varying disorder are in a separate cluster. The control (circles) and standard HEX (square) as a reference topography stay in their batch and do not cluster with the same or similar topographies.*

Due to the strong observed batch effect, a correction is necessary that should correct for the difference in staining intensity we see for the SQ pitch array. A first attempt at batch effect correction is done by centring the data to the median of the control of each batch. We assume that the morphome in the controls is the same across the different batches. Thus, an observed change is due to the batch effect. By centring the data to the median of each batch, we pick up the change for each condition in relation to the control of the corresponding batch (Figure 5.5A). This batch correction method is the least invasive used, as it implies a minimum modification to the raw data. Naturally, the controls of the different batches cluster together in UMAP plot. However, the standard SQ, NSQ and HEX topographies of the different batches are still in their corresponding batch and not close to the same topographies. Thus, we change the feature selection from before the centring to after the centring, because if we select features before centring the data, we select the features that responsible for the batch effect. The feature selection after centring only improves the batch effect slightly. The UMAP plot continues to show a clear batch effect (Figure 5.5B).

To improve the correction, we first change the normalization method to a cube root transformation from normalizing the data to a mean of 0 and standard deviation of 1. The cube root transformation improves the normality of the data set that should help with the later statistical analysis that works best for normal distributed data. Instead of centring the data to the control of the corresponding batch, we now choose the control of the gratings batch as the reference control. All data is centred using the median and median absolute deviation of the gratings control. We choose the control from this batch because we have three controls in each batch and, therefore, a large dataset for of good reference images. This batch effect correction method improves the correction again, but a clear batch effect is still visible in the UMAP plot (Figure 5.5C). Especially, the SQ pitch array data is still clustering almost completely together. The remaining data is also still clustering together mostly by the batches and not the categories.

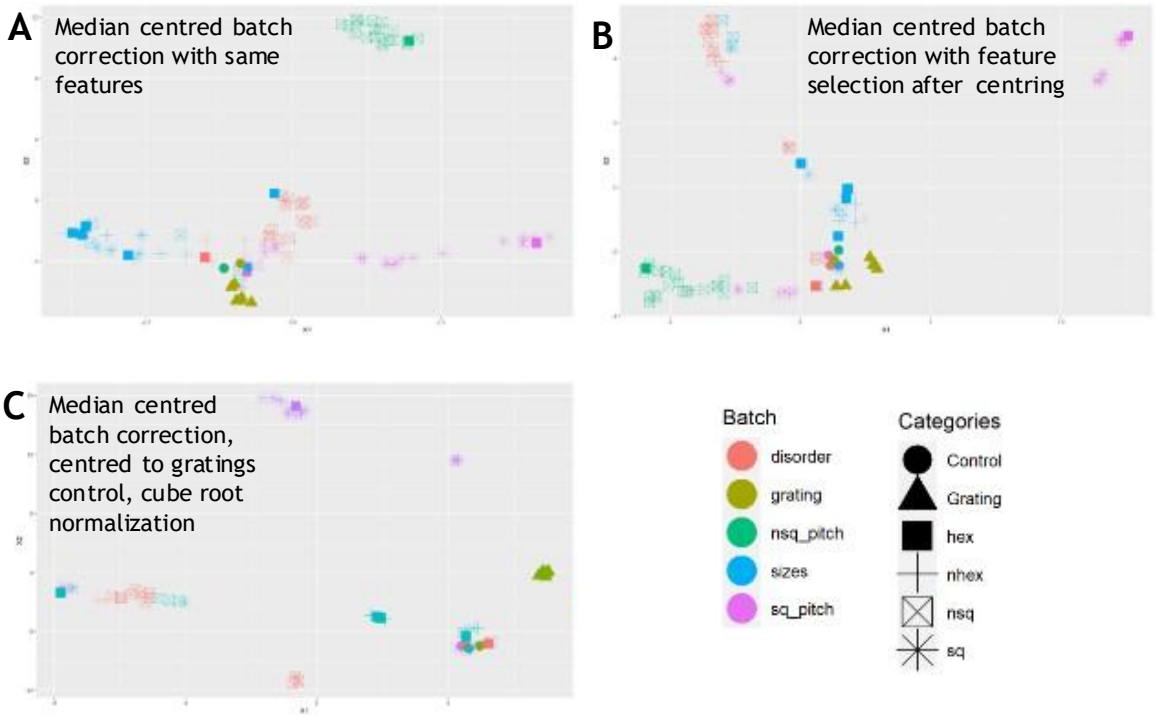

***Figure 5.5**: UMAP of nanotopography library data with median centred batch correction. The data is median corrected to the control of each batch and the same feature as in the initial feature selection are used (A). A feature selection after centring the data improves the distribution in the UMAP (B). An additional cube root formation for normalization further improves the batch effect correction (C). The median centring forces the controls together, which improves the batch effect. However, the reference topographies of standard SQ, NSQ and HEX arrangement are still clustering in their corresponding batch and not with similar topographies.*

All the above-mentioned batch effect correction methods are not able to reduce the batch effect enough. Thus, we use a more invasive method with the Seurat method. Seurat is a state-of-the-art batch correction method for scRNA-Seq analysis. It has also proven to work well with Cell Painting data, as it can successfully remove the batch effect while conserving the biological significance. Initial attempts at the Seurat correction using the old feature selection method, which involved removing redundant data and selecting significant data, did not sufficiently improve the batch effect correction. Therefore, we also have to consider the feature selection method. The Cytominer package developed by the Carpenter lab, which are also the creators of the Cell Painting method and CellProfiler, is the best possible toolbox for the analysis of morphological profiling data. This toolbox also includes a function to measure feature importance based on its ability to reduce data entropy. The features with the highest importance are selected after the removal of redundant features and features with near-zero variance. In contrast to previous methods, we do not have a cutoff value for

feature selection; instead, we must specify how many features are needed for a good representation of the data. A first test showed that a feature number of at least 200 is necessary.

Finally, we observe the best batch effect correction with the RPCA Seurat correction, where the data is normalised by centring it on the median of the controls for each batch before the Seurat correction. Then, the top 300 features with the highest importance for the reduction of data entropy in the dataset are selected after removing features with near-zero variance and redundant features with a cutoff value of 0.95. The data is combined with the activator and inhibitor data from the previous chapter for the Seurat correction. However, for feature selection, only the nanotopography library data is used, as we are interested in the features that describe changes across the topographies. The UMAP plot shows a good distribution of the data and no strong batch effect as before (Figure 5.6A+B). The topographies still do not cluster perfectly by their category, but it is a significant improvement compared to the initial data. With 84 different nanotopographies and 13 different activators and inhibitors, each with three concentrations per condition, this plot includes too much information to be easily comprehended. To better understand the clustering, we break down the plot into each batch and plot it separately.

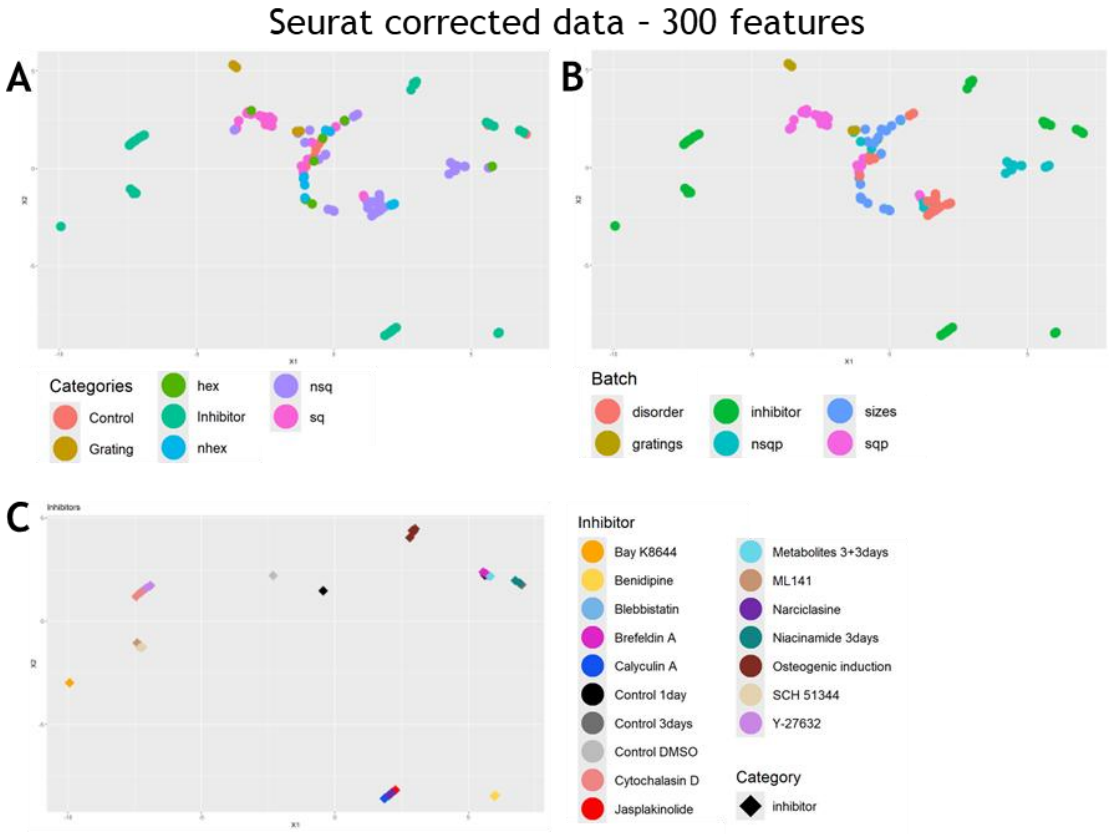

(caption for figure in previous page) ***Figure 5.6****: UMAP of nanotopography library data after Seurat correction. The nanotopography library data is plotted together after a Seurat correction with the top 300 features selected by information entropy based selection. The UMAP is coloured by the topography categories (A), and the batch (B) to visualize the batch correction. The data does not cluster together only by the batches, but the batches are spread across the plot. However, no obvious relation between the categories of topographies is visible. The activators and inhibitors do not cluster with any of the other data. Thus, a change in topography is not triggering other parts of the mechanotransduction pathway. The isolated activator/inhibitor data of the full UMAP show a good grouping by the different activators and inhibitors (C).*

It is noticeable in the full UMAP plot that the activators and inhibitors are clearly separated from the nanotopography library data. Only the control lies with the other controls. This does not support our hope that the changes in the nanotopography might trigger different responses in the cell. When examining the isolated activator and inhibitor data, similarities to the distribution of the activator and inhibitor data from the previous chapter are visible (Figure 5.6C). The Ras/Rac and Cdc42 inhibitors SCH51344 and ML141 cluster together as well as the cytoskeletal activators jasplakinolide, narciclasine, and calyculin A. The cytoskeletal inhibitors cytochalasin D, Y-27632, and blebbistatin also cluster together. This shows that the clustering is working well and that we can trust the distribution in the UMAP plot.

An isolated look at the batches of the nanotopography library data reveals that no clear trends based on geometry are observable; however, the topographies group into three clusters per batch for the NSQ pitch array, SQ pitch array, and varying disorder array (Figure 5.7). We did not necessarily expect a continuous relationship between the pitch distance or disorder and cell morphology. However, it has been shown that sweet spots in adhesion areas exist. Thus, we expect ranges of topographies to have a similar response. We plot the observed clusters against the pitch as well as the disorder (Figure 5.9). While we observe some signs of periodicity in the SQ pitch array and NSQ pitch array, no clear pattern is visible. Additionally, the disorder array is mostly together in one big cluster, with the topographies with the largest disorder of 140 nm and 150 nm separated. At very high disorder, nanopit placement is entirely random, and the pits often overlap. At such a high level of randomness, we expect the topographies to be more similar. Surprisingly, they lay together with the standard SQ topography.

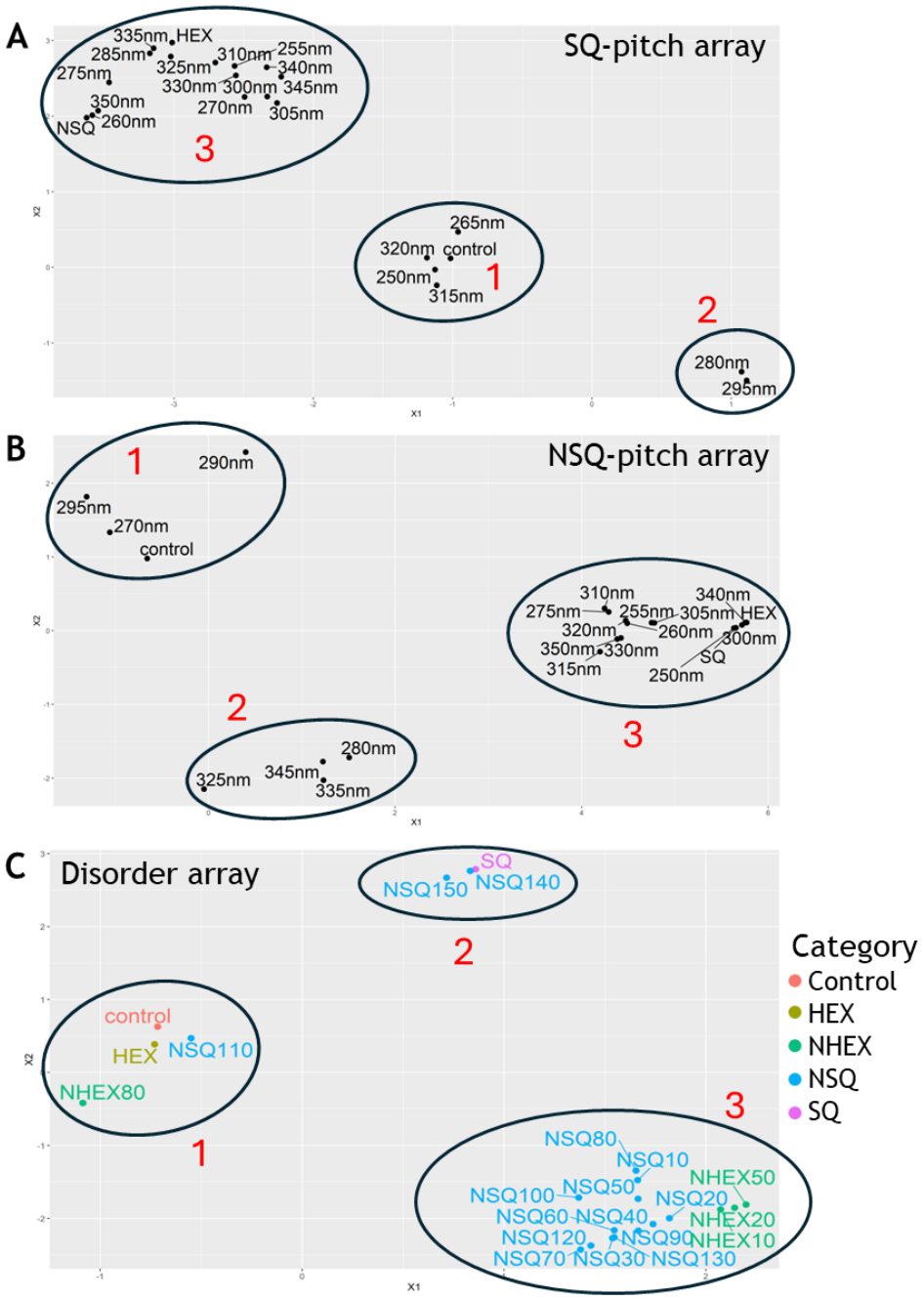

***Figure 5.7**: UMAP of isolated nanotopography library batches. The projection is from the full UMAP and the UMAP coordinates of the SQ-pitch array batch (A), NSQ-pitch array (B), and varying disorder batch (C) are plotted independently for better visibility. The formed clusters are highlighted by circles and numbered. No underlying pattern in the in the clustering of the topography parameters is visible for any of the arrays.*

The batch with varying diameters and gratings does not have enough data with one changed parameter to analyse the cluster in the same way. For both batches, the topographies that are 5 µm or larger in size are close to the control as visible in Figure 5.8. With a feature size that large and a depth of only 100 nm, the nanotopographies no longer affect the cell. The cell can adhere to the whole surface, and the small 100 nm step does not affect the cell enough to have a

visible effect. The topographies of a large diameter also have a large spacing in between. That spacing is likely to be too large to form localised integrin clusters. Additionally, the cell feels the shape of the nanopits only in a few places, and has a curved membrane only in those areas due to the topography. This will not be enough to create a significant influence on F-BAR protein binding due to membrane curvature. In the batch with varying diameters, the hexagonal pattern and near-hexagonal pattern primarily cluster together. The hexagonal and square arrays with pits of 500 nm are close to the nanopits, which have a high disorder of 140 and 150 nm. The high disorder might produce large adhesion areas that are similar in size to those patterns with 500 nm diameter nanopits, which have a distance of 1 µm between the nanopits.

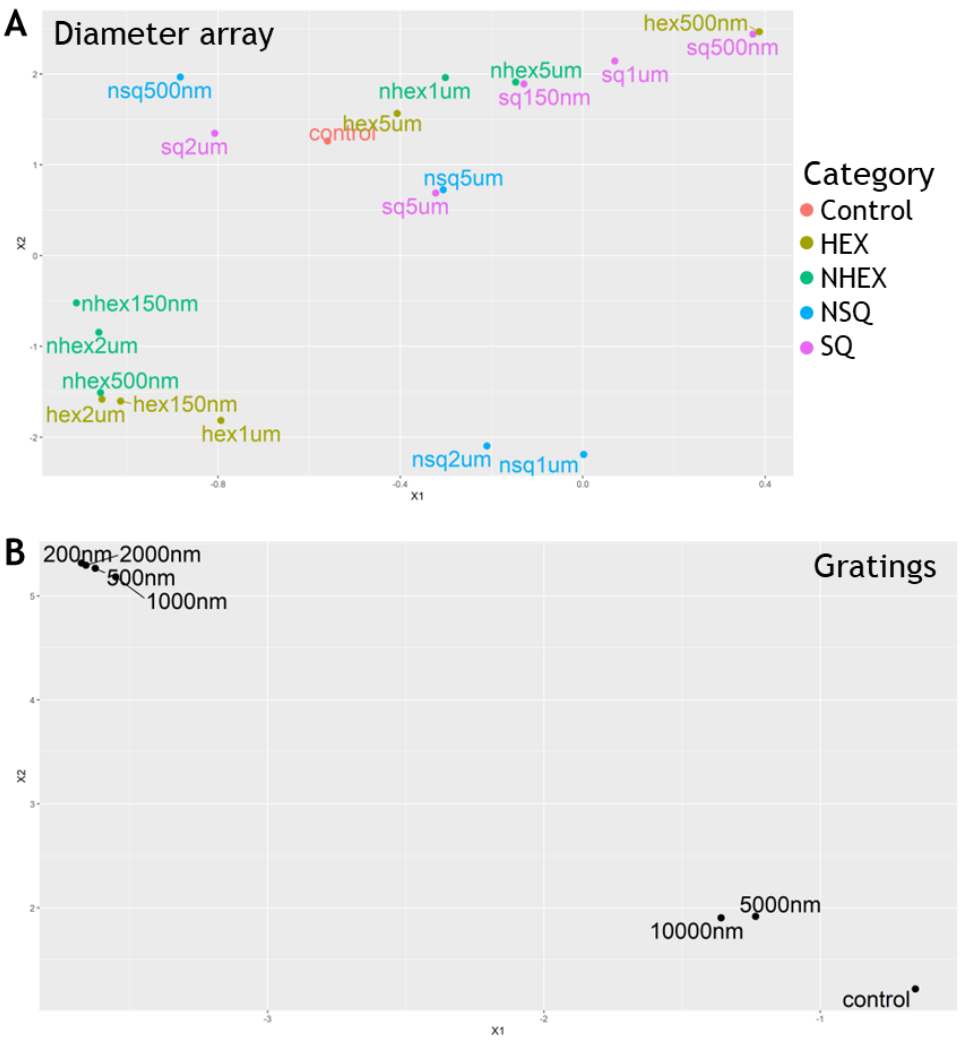

(caption for figure on previous page) ***Figure 5.8****: UMAP of isolated nanotopography library batches with varying diameter (A) and gratings (B). For both arrays the large features of 5 µm and above are close to the control because the extremely low aspect ratio makes the topography not noticeable to the cells. Many of the NHEX and HEX nanopits are close to each other, however, not all of them are located in one cluster. Thus, it is not clear if the topography arrangement or nanopit sizes drive the cell morphology changes. The projection has the dimensions from the UMAP of the full nanotopography library data.*

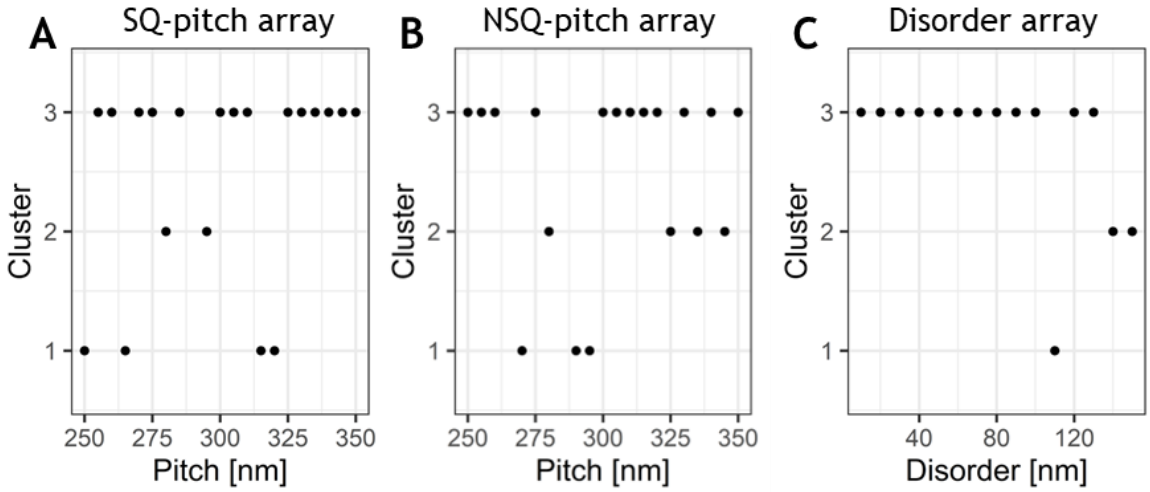

Figure 5.9*: Plot of the different clusters depending on the pitch for the SQ pitch array (A), and for the NSQ-pitch array (B), and depending on the disorder for the disorder array (C). The clusters are taken from Figure 5.7. No trend that is depending on the pitch or disorder is visible. The clustering seems mostly random.*

5.4. Linear regression and canonical correlation analysis of nanotopograpy library data

To design new topographies from the cell morphome, we need to ensure first that the geometry of the topography correlates with the morphome. The nanotopographies need to be parameterised to be in a comparable format. Five parameters can fully describe them: the x-pitch, y-pitch, diameter, noise/disorder, and offset. The x- and y-pitch are the same for the nanopit arrays. For the gratings, the x-pitch is the same value as the diameter because it is a constant line, and there is no space between them. The y-pitch is two times the diameter. The offset defines whether the nanopits are in a hexagonal array. A hexagonal array has an offset of half of the centre-to-centre pitch. Those parameters are used with the morphome to check for a linear relationship between the morphome and topography parameters. A multivariate multiple linear regression is employed for it.

The features with the highest correlation to the topography parameters are selected. For each batch, we select the features with the highest correlation to the corresponding geometry parameter. For the SQ and NSQ pitch array, we look at the correlation to the pitch; for the batch with varying disorder, we look at the correlation to the disorder, and for the batch with varying sizes and gratings, we look at the correlation to diameter. For each batch, the 10 features with the highest correlation are picked. For the gratings batch, only the three highest features are selected because it has fewer different conditions, with only six different grating sizes. We need a smaller number of features than conditions to be able to check if the regression works just for the isolated data from one batch.

Combining the different batches into a complete data set presents its own set of challenges. With increasing diameter, the raw absolute pitch and noise values also change, while the relative value remains constant. The pitch arrays have a varying pitch in 5 nm steps in a range of 100 nm, and the disorder array has a varying disorder in 10 nm steps in a range of 150 nm. However, the pitch changes for an increased nanopit diameter of 500 nm by 1200 nm, a massive change that a linear relationship of the morphome cannot explain. This skewness of the whole dataset makes a linear regression of the raw absolute data impossible. As a result, we only consider the SQ and NSQ pitch batch and the batch with varying disorder when examining the raw absolute data (Figure 5.10). For the whole dataset, the geometrical parameters are calculated relative to the diameter.

The linear regression of the pitch and disorder against the morphome shows a good linear relationship for the batches with the changed parameter (Figure 5.10). The pitch can be predicted well for the NSQ and SQ pitch arrays, and the disorder can be predicted well for the batch with varying disorder. However, the batches with a constant pitch or disorder are not predicted correctly through the linear regression. The linear regression of the pitch for the raw data of the SQ and NSQ pitch batch show an adjusted R^2 of only 0.012 and a p-value of 0.466, while the linear regression of the absolute disorder shows a much better linear regression with an adjusted R^2 of 0.647 and a p-value of $3.81\ 10^{-6}$. The linear regression of the pitch improves with the use of relative data with an adjusted R^2 of 0.098 and a p-value of 0.271. However, the performance of the linear regression of the disorder decreases with an adjusted R^2 of 0.52 and a p-value of 0.00017. The

problem is that while the pitch stays the same, the adhesion area and therefore also the morphome still change across the differently disordered topographies of the batch with varying disorder. The adhesion areas are known to be a driving factor in the cell response to nanotopographies. We expect that across nanopits arrays with varying pitch and disorder, we will have topographies with very similar distributions and sizes of adhesion areas. So that the cell response will also be similar, a simple linear regression cannot replicate this similarity in morphome on clearly different topographies. More advanced models would be necessary to describe it. The linear regression of the disorder is better than the regression of the pitch. We believe that the disorder is a more important factor in the cell response than the pitch. The disorder is likely to have a higher impact on the cell and the morphome, and with more substantial changes in the morphome, the linear regression works better.

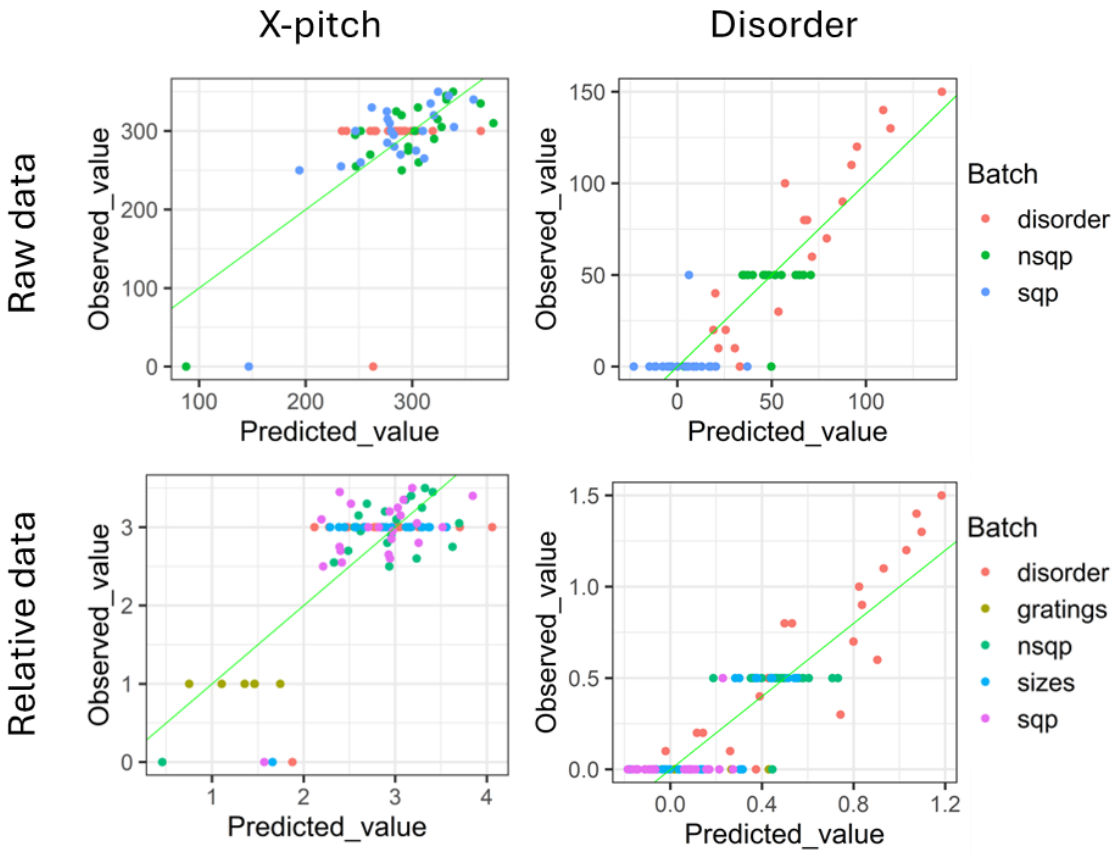

***Figure 5.10**: Linear regression calculated by multi variant linear regression for the centre-to-centre pitch and disorder of nanopitches. The raw data values for the pitch and disorder are only calculated for the disorder, NSQ-pitch array (nsqp), and SQ-pitch array (sqp) since the high values of the large diameter pits as well as large gratings skew the data too much. The pitch and disorder relative to the diameter can be calculated for the whole nanotopography library.*

The newly selected features for the linear regression are selected to describe the changes in the relevant batches well. Thus, they are also not performing as well in correcting a batch effect. Especially, the raw absolute data of just the NSQ and SQ pitch and the disorder batch cluster together just by their batch in a UMAP plot (Figure 5.11A). The full dataset, including the relative geometric parameters, improves it. Unfortunately, there are no novel trends in the UMAP plot visible (Figure 5.11B). For the SQ pitch, NSQ pitch and varying diameter batch no trends are visible. The batch with varying disorder has the nanopits with high disorder above 120 nm separated from the other nanopits of the batch. Surprisingly, the disorders of 60 and 70 nm are close to the topographies with high disorder. As mentioned earlier, the highly disordered nanopits are entirely random, with many overlaps, and therefore, they are also expected to elicit a different cell response. The gratings show again that we need features of less than 5 µm to have a visible response to the topography. Furthermore, the controls cluster in their respective batches again rather than together, indicating a batch effect. That might be because we select features with the highest correlation with the topography parameters. The controls have a value of zero for all topography parameters and, therefore, are outliers in the feature selection. The correct classification of the control is not prioritised in the feature selection, and therefore, the features are unlikely to highlight similarities between the controls.

The multivariate multiple linear regression shows that the morphome correlates with the geometrical parameters of the nanotopographies, even though not the whole topography can be predicted from the morphological features. A CCA analysis is used to check the correlation between the activator and inhibitor data and the nanotopography library data (Figure 5.12). The activators and inhibitors do not cluster in the CCA plot of the first two dimensions in a way that would make sense based on the function of the activators and inhibitors, as well as the previously discovered relationship to the response to the standard SQ, NSQ, and HEX topography. The CCA plot does not show any systematic relationship between the activators and inhibitors and the nanotopography library data.

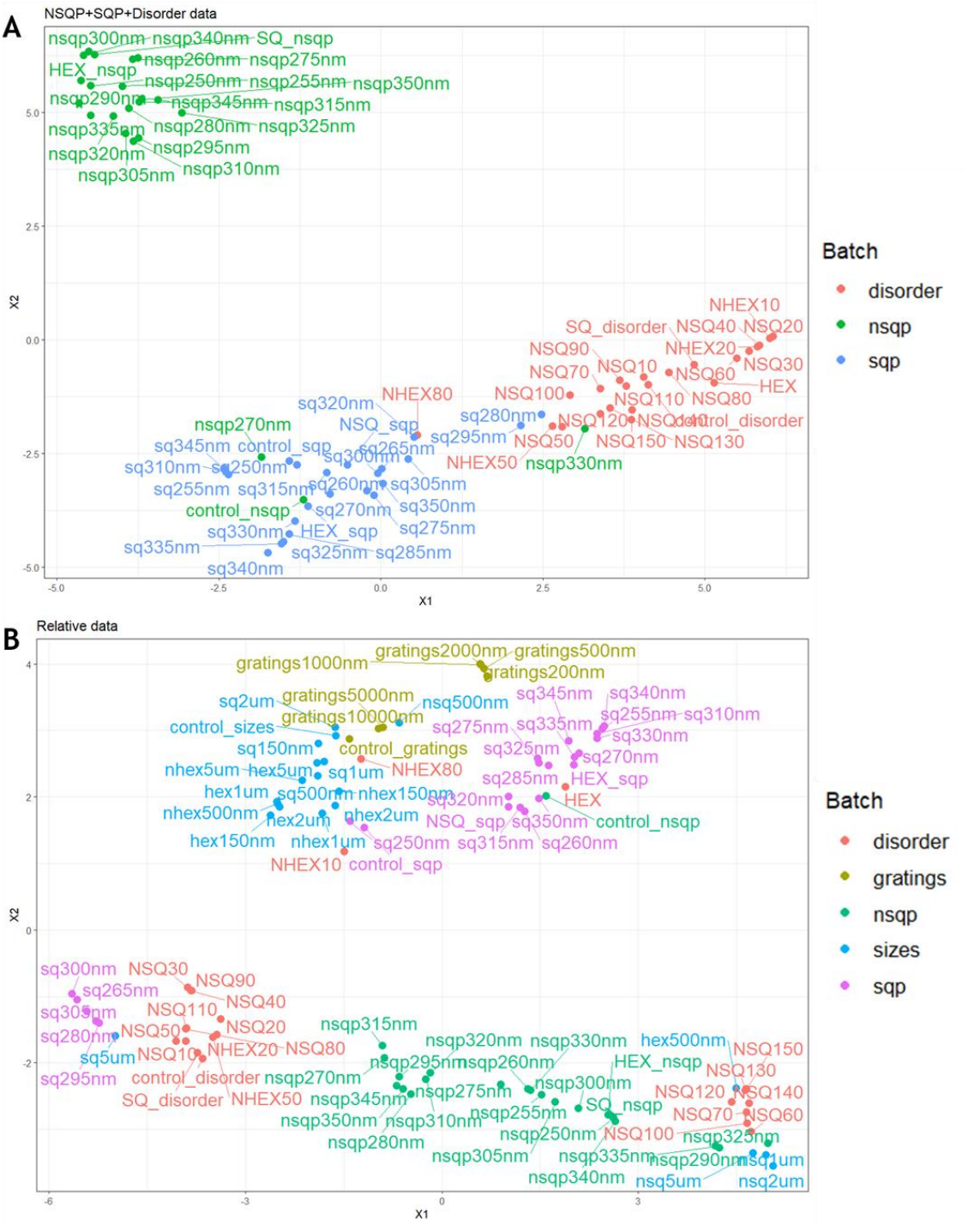

***Figure 5.11**: UMAP of nanotopography data after feature selection for linear regression of raw absolute data (A) and relative data (B). The relative data takes the disorder, pitch and offset relative to the feature diameter to avoid the skewing of the data because of the large features. The use of the relative data improves the clustering in UMAP. The raw absolute data shows a clear clustering by the batch while the relative data have more separation in the batches.*

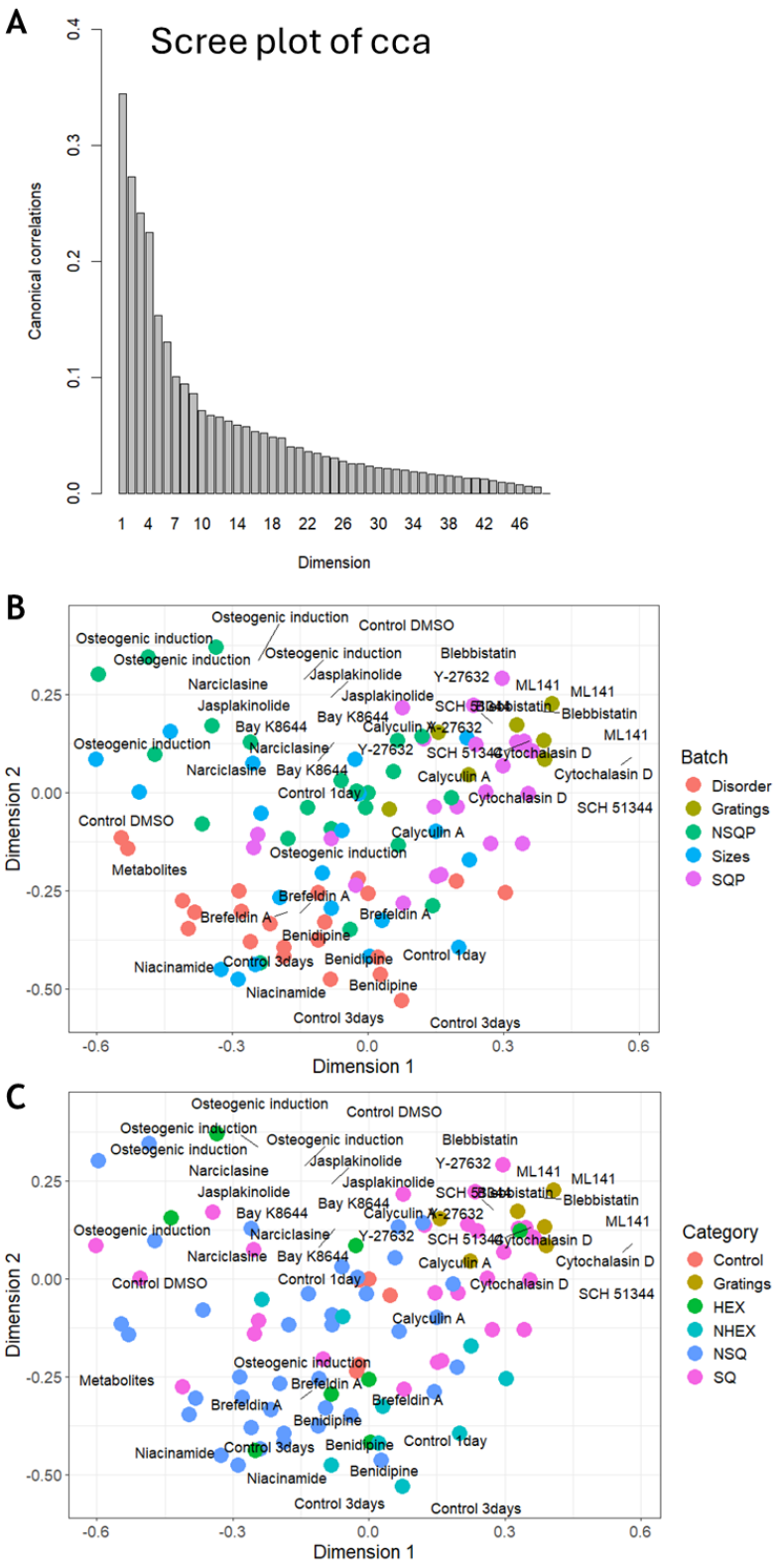

***Figure 5.12**: Canonical correlation analysis (cca) of nanotopography data to activator and inhibitor data. The Scree plot shows the canonical correlation of the computed dimensions (A). The canonical correlation of the variables is plotted in the first two dimensions by the batch (B) and category of topography (C). No clear correlation between topography parameters and mechanotransduction pathway activators and inhibitors are visible in the cca.*

5.5. Influence of topography parameter on cell morphome

As described above, a combined analysis of the topography parameters is not possible due to the interplay in cell response between the geometrical parameters. Thus, we change our approach to analysing topography parameters, which is characterised by a systematic separation of the data into four groups. Each group represents a unique aspect of the cell response, with only one parameter being altered at a time. The first group examines the disorder batch, the second group explores the variation in pitch by combining the NSQ and SQ pitch arrays, the third group investigates the varying diameters, and the fourth group studies gratings with different widths. This systematic approach allows us to gain a comprehensive understanding of the cell response. We then visualise the cell response by plotting heatmaps of the corresponding groups and subjecting them to a hierarchical clustering of the variables. The distances for the hierarchical clustering are calculated using the Euclidean method. The selected features are chosen in a manner similar to the feature selection process for multivariate multiple linear regression. The features are batch corrected using RPCA Seurat correction, and redundant and zero-variance features are removed. Next, the features with a Pearson correlation of more than 0.5 to the topography are selected.

5.5.1. Nanopits of varying disorder

The nanopits of varying disorder exhibit a high correlation with morphological changes, as indicated by 132 features with a Pearson correlation above 0.5. The most prominent clustering we observe is the high disorder above 120 nm. They show a clearly different morphome from the other topographies as visible in the heatmap in Figure 5.13. The fluorescence images are shown in Figure A5.3. Interestingly, the disorder of 60 and 70 nm is grouped in the same cluster. The high disorder creates an entirely random topography that no longer follows the square array. Additionally, we observe many nanopits that overlap at high disorder. Among the other disorders, no clear trend is observable, except for the separation between NHEX topographies and NSQ topographies. This highlights that even in a disorder, the controlled aspect of the disorder is important for the cell response.

Furthermore, the underlying organisation of nanopits, whether in a square or hexagonal array, is important for the cell response. That we can pick up those fine differences in the topography by the morphome supports again the potential of morphological profiling using the Cell Painting method.

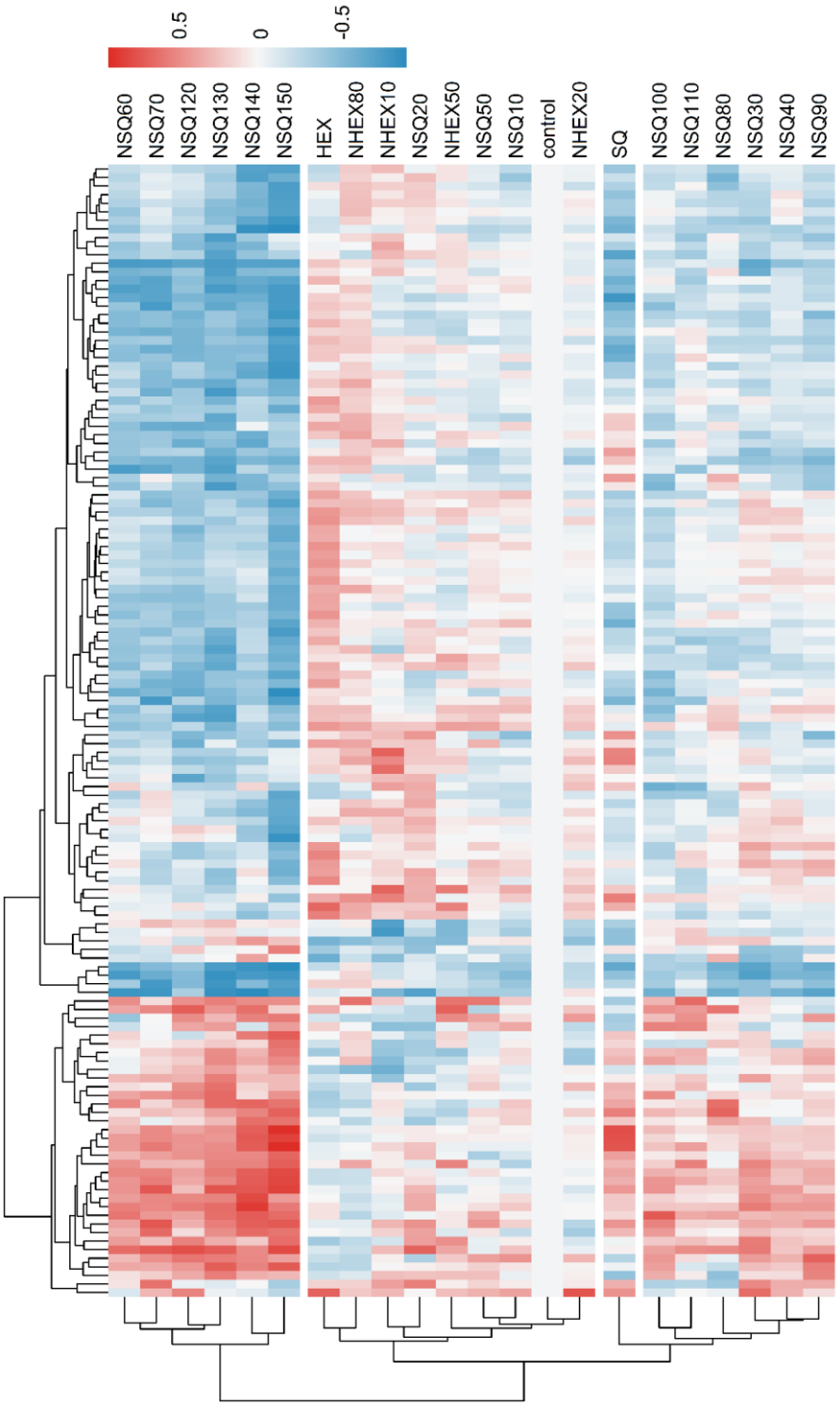

(caption for figure on previous page) ***Figure 5.13****: Heatmap of the morphome depending on the disorder of nanopits. The heatmap is ordered by hierarchical clustering using Euclidean distances. The features are normalized between 0 and 1. Each feature is corrected against the control by dividing it from the control. The topographies are labelled by the array geometry if it is square (SQ), near square (NSQ), hexagonal (HEX), or near hexagonal (NHEX). The number behind the geometry describer corresponds to the disorder in nanometer. The NSQ patterns with a disorder above 120 nm cluster together as the nanopatterns are more randomly distributed. Surprisingly, the NSQ of 60 and 70 nm have similar features. The features mostly depend on the NHEX and NSQ arrangement.*

5.5.2. Nanopits of varying pitch

The pitch does not correlate with the morphome as strongly as the disorder. When examining the individual NSQ pitch and SQ pitch batches, the NSQ pitch batch contains 54 features with a Pearson correlation of over 0.5 to the pitch, while the SQ pitch array comprises 17 features with high Pearson correlations. When combining both datasets into a single dataset of varying pitches, no feature has a Pearson correlation coefficient higher than 0.5, and only three feature has a correlation above 0.4. 49 features have a higher correlation than 0.3 with the pitch and are used for the heatmap (Figure 5.14). The fluorescence images of the NSQ pitch array are shown in Figure A5.4 and the images of the SQ pitch array in Figure A5.5. The correlation values are calculated with the control set as a pitch of 0 nm. We believe that this drop to 0 for the control compared with the pitch from 250 to 350 nm disturbs the correlation too much since a feature needs to be higher or lower than the control for all pitches to be correlated. Thus, we also calculate the Pearson correlation excluding the control. Surprisingly, it does not change the number of correlated features a lot. We observe 19 features that have a correlation larger than 0.5 for the NSQ pitch array, and 22 features that have a correlation larger than 0.5 for the SQ pitch array. The combined dataset shows a Pearson correlation to the pitch that is larger than 0.4 for five features, and 37 features have a Pearson correlation larger than 0.3. We believe that those features still replicate the morphome depends better than the features that are calculated including the control and use them for the analysis. Since the correlation is low, the clustering in the heatmap seems random as well. No trend depending on the pitch is visible. The SQ and NSQ batches mostly separate, indicating that the disorder has a more substantial effect on cell response than the pitch differences. This is also supported by the substantial decrease in correlation of the morphome

to the x-pitch when combining the SQ and NSQ datasets. The NSQ and SQ pitches also do not exhibit a pitch dependent trend when viewed separately (Figure A5.1 and A5.2).

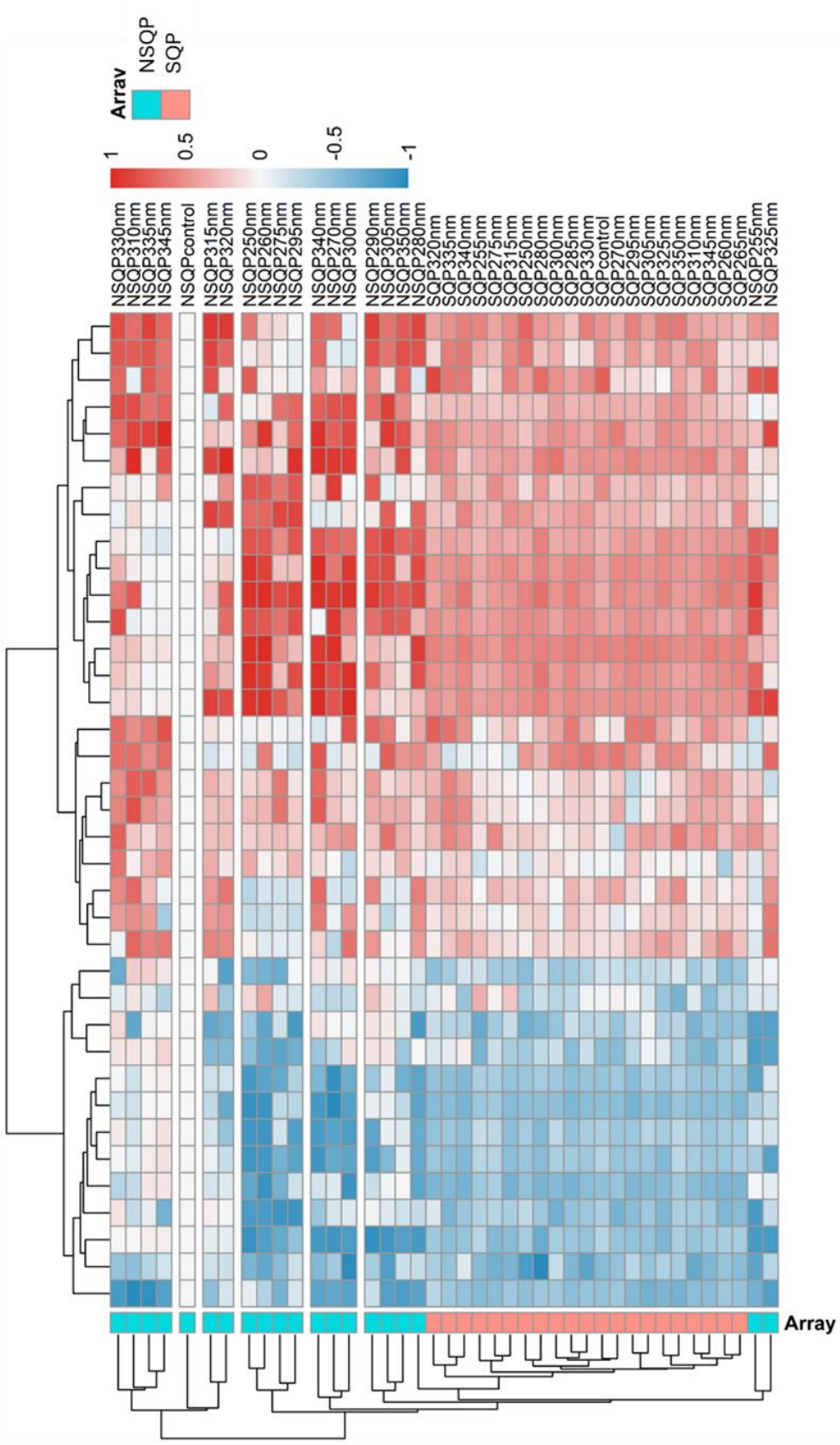

(caption for figure on previous page) ***Figure 5.14****: Heatmap of the morphome depending on the pitch of nanopits. The heatmap is ordered by hierarchical clustering using Euclidean distances. The features are normalized between 0 and 1 and corrected against the control by dividing the control from the other substrates. The topographies are labelled by the array geometry if it is square (SQP), or near square (NSQP). Additionally, the corresponding batches are labelled in red (SQP) and blue (NSQP). The number behind the describer of the geometry (SQP/NSQP) corresponds to the centre-to-centre spacing. The features show most similarities in their own batch. Especially, the SQ array nanopits show little variation with varying pitch.*

5.5.3. Nanopits of varying diameter

The dataset of varying diameters has the smallest correlation to the morphome of all individual datasets. Only four features have a Pearson correlation of more than 0.5 with the morphome, and 26 features show a correlation of over 0.4. Those 26 features are used for analysing the diameter dependence (Figure 5.15). The fluorescence images are shown in Figure A5.6. The hierarchical clustering reveals a separation of the HEX, NHEX, NSQ, and SQ arrays, with a diameter of 5 µm, from the remaining data. Surprisingly, the SQ array with nanopits of 1 µm diameter falls into the same cluster. Overall, the nanopits are close to topographies of the same diameter. Thus, the cell response to the diameter, independent of the array geometry, can be detected. However, the low number of features with high correlation to the nanopit diameter suggests that it does not have a substantial effect on the morphome, and that the geometrical arrangement may play a more significant role in the cell response than the diameter of the nanopits. The separation of the high diameter nanopits is expected because, at a depth of 100 nm and a diameter of 5 µm, cell adhesion will not be limited to the areas without pits but will adhere to the whole surface and will only feel the 100 nm deep edge of the nanopits. With smaller adhesion guidance through the large nanopits, we expect it to be similar to a flat surface. However, curiously, the control clusters closed with the 500 nm nanopits, which cannot be explained by the previously found clustering in the UMAP (Figure 5.8A), where the control clustered with the 5 µm nanopits as expected. The correlation between nanopit size and morphome is weak; therefore, we expect the selected features may not be well-suited to describe the cell response, depending on feature size.

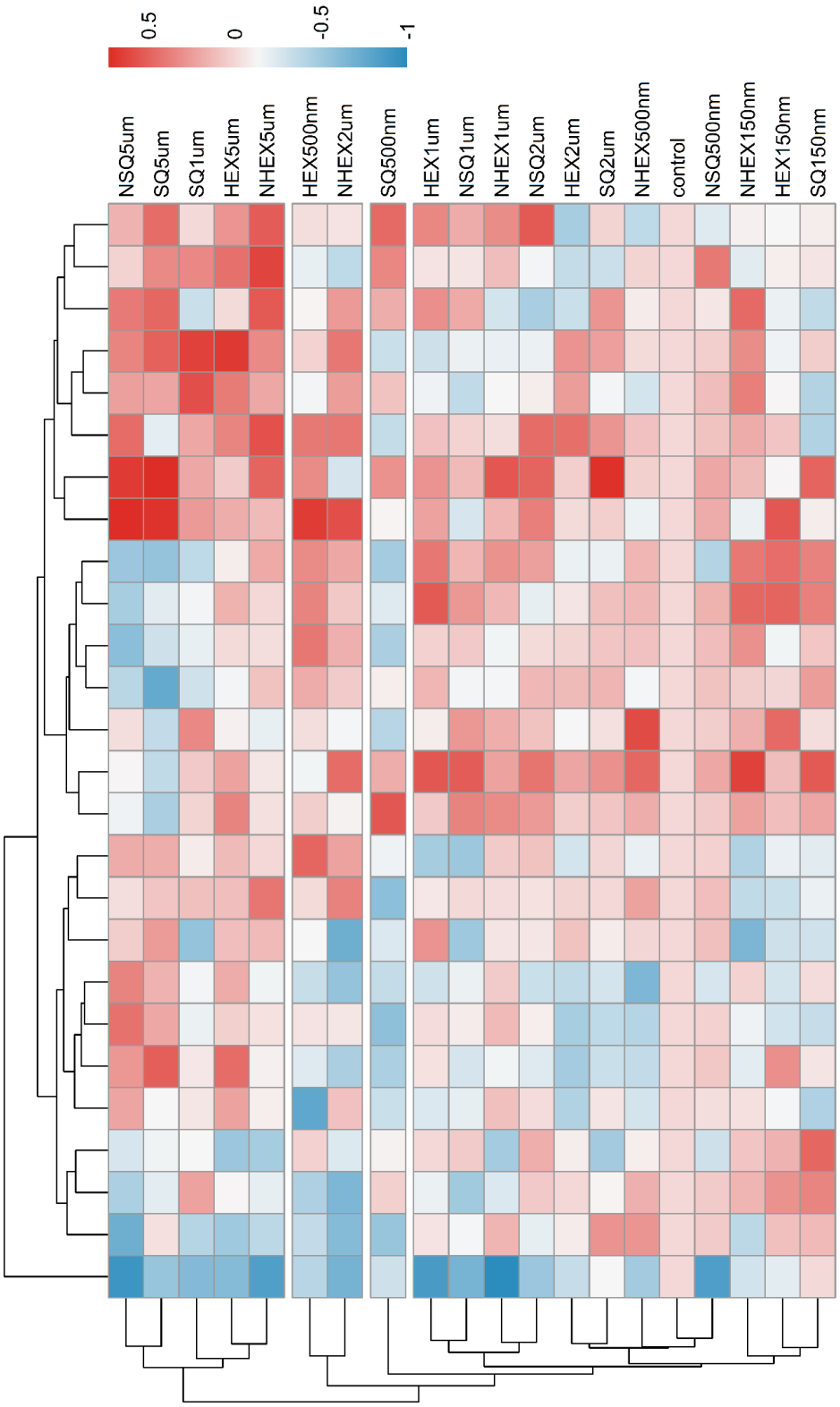

***Figure 5.15**: Heatmap of the morphome depending on the diameter of nanopits. The heatmap is ordered by hierarchical clustering using Euclidean distances. The features are normalized between 0 and 1 and corrected against the control by dividing the control from the other substrates. The topographies are labelled by the array geometry if it is square (SQ), near square (NSQ), hexagonal (HEX), or near hexagonal (NHEX). The diameter of the nanopits is mentioned after the array category. The large nanopits of 5 µm show a similar morphology that separates them from the other topographies. The clustering is mostly driven by the nanopits diameter and not the geometrical arrangement in a SQ, NSQ, HEX, or NHEX array.*

5.5.4. Gratings of varying widths

The gratings show the most prominent effect on cell morphology. Therefore, it comes as no surprise that a strong correlation between the widths of the gratings and the morphome can be observed. 295 features have a Pearson correlation coefficient greater than 0.5 with the pitch of the gratings. The gratings direct cell alignment, causing highly oriented and elongated cells along the direction of the gratings. The morphological change is more pronounced than the change through nanopits. On nanopits, the MC3T3 cells maintain their typical shape, with slight changes in protrusions and elongation depending on the geometry. The elongation on the gratings decreases with increased widths, as can be clearly seen in the fluorescence images of the Cell Painting staining (Figure 5.16B). This is also reflected in the heatmap and hierarchical clustering, where the gratings cluster together by their size. The largest gratings, 5 and 10 µm, exhibit the most significant difference in the morphome, as the gratings do not align the cells. The remaining grating sizes have a similar morphome with the smaller 200 and 500 nm gratings clustering together and the 1 and 2 µm gratings clustering together.

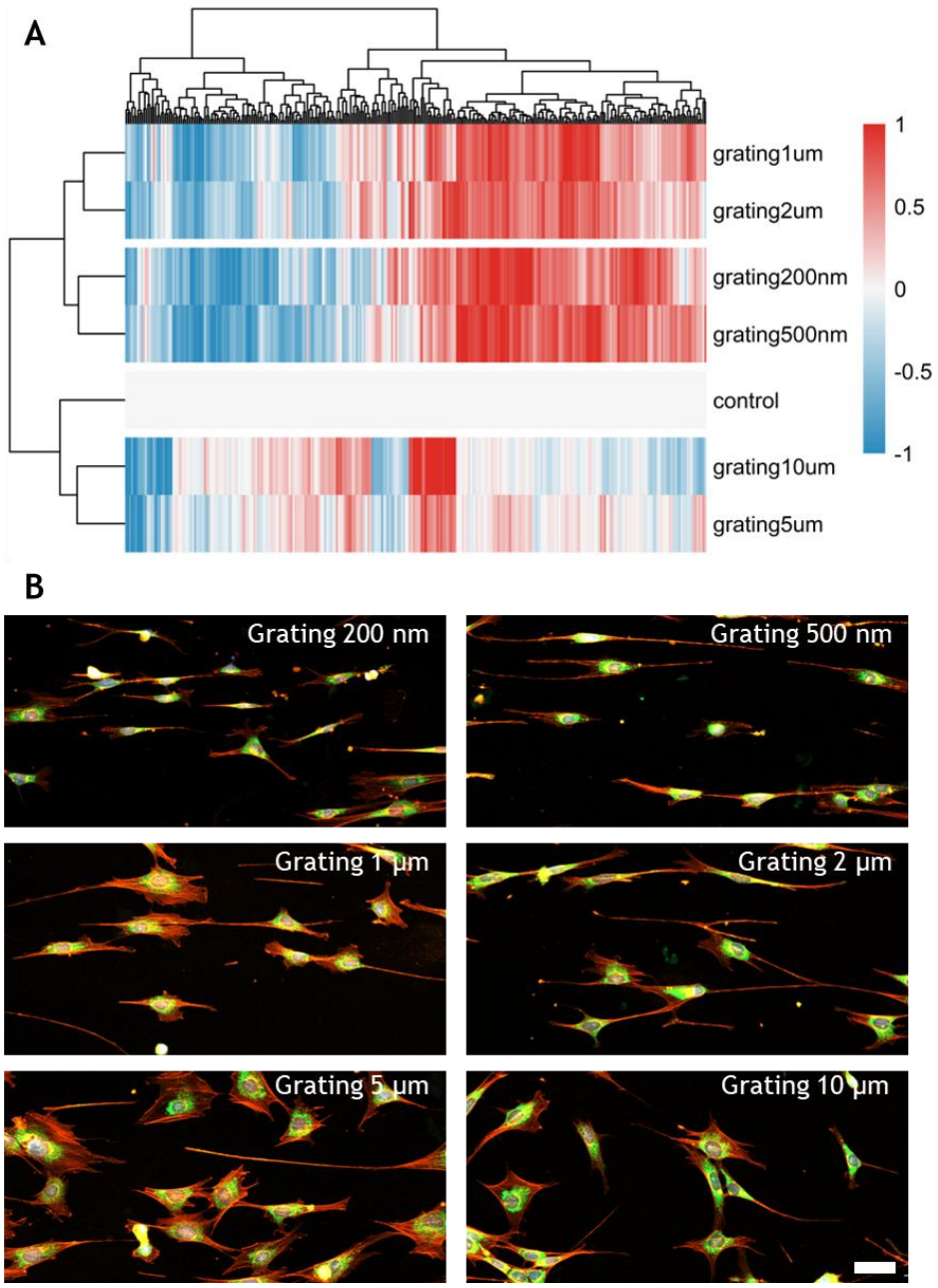

***Figure 5.16**: The morphome dependence on grating width is plotted in a heatmap (A) and shown in fluorescence images (B). The heatmap (A) is ordered by hierarchical clustering using Euclidean distances. The features are normalized between 0 and 1 and corrected against the control by dividing the control from the other substrates. The large gratings of 5 and 10 µm show a different feature expression to the smaller gratings and show a higher similarity with the flat control. The Cell Painting fluorescence images (B) show the alignment of MC3T3 cells with the gratings for a width of 200 nm to 2 µm, while the 5 and 10 µm gratings do not produce a cell alignment. The scale bars shows 50 µm.*

The control is more similar to the large gratings, as they resemble the typical MC3T3 cell shape. It shows that the alignment to nanotopographies is an adhesion driven effect, rather than an effect driven by physical confinement, as observed on gratings with heights above 1 µm[256, 257]. Refaaq et al. demonstrated that PDMS gratings with 6 µm ridges and 4 µm grooves confine MC3T3 cells at grating

depths of 1 µm and 4.5 µm. At high heights, the alignment is driven by cell protrusions that sense the walls of the ridges and make contact with them, which in turn drives cell elongation along the gratings[258]. At a low grating height of 150 or 200 nm, the gratings do not provide enough area for the protrusions to make contact with. However, at small gratings with a width of a few hundred nanometers, the focal adhesion clusters are aligned along the gratings, which produces cell elongation and alignment along the gratings. The size dependent effect of the gratings is similar to the size dependent effect of the nanopits. Features of 5 µm and larger are too large to direct focal adhesion formations in a way that visibly affects cells.

5.6. Conclusion

We successfully imaged fluorescently stained MC3T3 cells on 84 different nanotopographies, consisting of 78 nanopits in SQ, NSQ, HEX, and NHEX arrays with varying diameters, pitches, and disorder, as well as 6 gratings with varying widths. We take 20 images in three biological replicas per condition, which accumulate to more than 5340 images taken and 26700 cells analysed, with an average of 5 cells per image. The imaging of the fluorescence images takes approximately 400.5 hours of continuous imaging for the entire dataset. This represents the large magnitude of data collected and how extensive the used nanotopography library is.

The analysis of the morphome of MC3T3 cells on a library of nanotopographies has proven more complicated than expected. A first challenge is the relatively small difference in responses between different topographies. Due to the slight differences, careful feature selection and batch correction are needed. The Seurat batch correction, known for its effectiveness in scRNA-Seq and Cell Painting data batch correction, has proven to remove a significant portion of the batch effect while retaining the biological information. We can separate the controls of the batches and get the batches mixed. However, we still do not observe a perfect correction, as the standard SQ, NSQ, and HEX topographies that are in all nanopit batches do not cluster together.

Additionally, we found that the feature selection method must be suitable for the purpose. To study the relationship between different topographies, a metadata-independent feature selection method is most effective. A feature selection method that measures the feature importance based on its ability to reduce the data entropy works best. When we want to study the relationship between the morphome and the geometry of the nanotopography, a feature selection approach based on the correlation between morphological features of the cells and geometrical features of the nanotopographies works best. In general, the complexity of the relationship makes the analysis difficult. The high dimensionality of the data poses another challenge. Usually, over 100 different features are used, which means that we have more variables than observations, which causes dimensionality problems in a linear regression. The reduced number of features selected for the multivariate multiple linear regression helps to overcome the dimensionality problems, thereby reducing the risk that it does not describe the full effect of the topographies on cell morphology and, consequently, does not reveal the full relationship. In general, one must be cautious not to overfit the data with normalisation, Seurat correction and feature selection.

The nanotopography library shows that the nanotopography features need to be smaller than 5 µm to influence the cell. Larger topographies do not create designated adhesion areas. This is especially visible in the gratings of different sizes. The small gratings create highly oriented and elongated cells along the gratings, whereas the large gratings of 5 and 10 µm do not significantly affect cell morphology. In general, the morphome differs a lot on the gratings compared to the nanopits. In comparing the different nanopit topographies, we find that disorder has the most substantial impact, next to the diameter of the nanopits. For the diameter, the dependency is similar to the gratings with the nanopits of 5 µm, having a smaller impact. The disorder exhibits a better linear relationship with changes in the morphome than the pitch. Additionally, a clear trend is observable, where the high disorder separates from the other disordered topographies as the placement becomes completely random, and we see many overlaps of pits. However, we are unable to explain why we observe a change in morphology at the transition from a disorder of 110 nm to 120 nm. In particular, the similar morphology of the 60 and 70 nm disorder to the high disorder nanopits

is not explainable. The high disorder and overlap between pits might create larger areas without adhesions, since integrins need to be closer than 70 nm to form integrin clusters, and the adhesion area needs enough space to form a cluster of several adhesions[259-261]. For the formation of stable focal adhesions, at least 4 integrin attachments are needed with an interspacing distance of 60 nm or less. However, the cluster size does not affect cell spreading above 4 integrins[262]. We would assume from this that the organisation of the integrin clusters we find on our topographies is more important than the adhesion sizes, as they are mostly large enough to facilitate their formation. When the nanopits are extremely close due to high disorder, the space between them might not be large enough for the formation of integrin clusters, even when the nanopits do not overlap. On the other hand, it also creates relatively large adhesion areas when the nanopits are far apart due to disorder, with a maximum of 150+150 nm of additional spacing between two nanopits. It is known that the cell response to nanotopographies depends on the available adhesion areas. We believe that the nanopits of the NSQ pitch batch, SQ pitch batch, and batch with varying disorder in an NSQ and NHEX arrangement should have topographies with similar adhesion areas between the different topographies. We do not find any support for this claim in the data.

Cell alignment has been widely studied across different cell types and grating dimensions. Alignment properties vary strongly by cell type. It is known to depend on grating height and spacing. Dual gradient chips with gradients in height and spacing showed the highest elongation and orientation along the gratings for the highest (0.85 – 1 µm) and widest (8 – 30 µm) gratings in human-induced pluripotent stem cell-derived cardiomyocytes[263]. The endothelial LE2 cells and fibroblast hTERT cells show the strongest alignment with the narrowest gratings (8 µm) and the largest height (1 µm)[264]. Fibroblasts show greater alignment than epithelial and endothelial cells. At wide gratings with a width of 1 µm or larger, a large height of around 1 µm is needed for the cells to align with the gratings. With high gratings, the cells feel the sidewalls through cell elongations, such as filopodia[257, 258]. Gratings with a smaller height at 350 nm showed the highest alignment and elongation in narrow 350 nm gratings for human mesenchymal stem cells[241]. The alignment is still visible up to a width of 2 µm. The alignment drastically drops at a width of 10 µm. Those findings align with our data. However,

for neurons, only 2 µm wide and 2 µm high gratings cause alignment. 250 nm wide and 250 nm high gratings do not produce any alignment[242]. Thus, the cell line must be considered when designing the biomaterial. Due to the observed difference in alignment between microgratings and nanogratings, we believe that two distinct alignment mechanisms exist. At microgratings, the cells sense the gratings' sidewalls and align along them. The alignment on nanogratings is probably adhesion-driven, with an arrangement of focal adhesions along the gratings that elongates and aligns cells.

A detailed study of the response to varying topographies has proven challenging in general. One big challenge is that the change of different topography parameters has a similar effect on the cell. A reduction of the pitch of an SQ array may similarly change the adhesion areas as an increase in disorder. Thus, it is challenging to correlate specific changes in the morphome to a change in one parameter, but the interplay between the different topographical parameters needs to be considered. We are also assuming a linear relationship between topographical parameters and morphome. However, the analysis of clusters shows a hint of possible periodicity, and it can very well be that sweet spots of topographies exist for the cell response. Thus, more work is needed to fully understand the influence of the different topography parameters on the cells. However, an analysis not assuming linearity and considering the relationship between the different topography parameters is much more challenging.

We also see that the response to nanotopographies is more complicated than the response to activators and inhibitors in the previous chapter. The morphome of the inhibitors and activators does not cluster with any specific group of topographies. The CCA showed some correlation between topographies and activators and inhibitors, but no trend is observable. The activators and inhibitors strongly affect one part of the mechanotransduction pathway, while the nanotopographies affect the complete mechanotransduction pathway. The cell response changes in nuances to the changes in the topography, and not as extreme as to changes in activators and inhibitors. For example, a slight change in disorder will not completely change the differentiation of the MC3T3 cell from differentiating into mature osteoblasts to not differentiating at all. Depending on the topography, the differentiation is slightly stronger or weaker. Thus, we will

likely see changes in the strength of the response, not see different responses and different mechanotransduction pathways. Those nuances are obviously much more challenging to pick up; however, we believe that we can pick them up. It can be compared with the different concentrations of the activators and inhibitors in the previous chapter. Only the gratings with a completely different topography compared to the nanopits show a clearly different cell morphology, which is captured by our analysis.

While a machine learning based approach for predicting new topographies is a promising option, it would require a significant amount of work and optimisation. Additionally, the use of a polytomous variable class analysis (poLCA)[265] could provide intriguing insights into the similarities between topographies. While poLCA is not designed for predicting topographies, it excels in identifying sources of cofounding between variables and constructing clusters based on this information. It can uncover hidden subgroups in the dataset that may reveal similarities between different topographies with similar available adhesion areas.

In contrast to other large nanotopography libraries, our library is highly systematic, with only five parameters needed to describe all topographies. The BSSA chip of the Foss group also uses a systematic approach. However, it shows greater variation in its patterns due to different combinations of circles, squares, and rectangles, whereas ours with nanopits shows only variation in pitch, size, and disorder[237, 238]. The NanoTopoChip[77] primarily focuses on the variance in feature shape resulting from the random combination of squares, triangles, and circles into unique shapes. Our nanotopography library also differs in the size range of topographic variations from those of the BSSA chip library. We study the difference in pitch at steps of 5 nm and in disorder at steps of 10 nm, whereas the BSSA platform steps in 1 µm increments and larger. The NanoTopoChip has a very detailed variation of features and pitch sizes. However, distinct values for possible adhesion areas are challenging to name due to the complex shapes. We believe that our systematic approach can be beneficial for predicting new topographies, even though it has a smaller range of topographies than the BSSA and NanoTopoChip platforms.

Even though our library and the NanoTopoChip and BSSA platform differ significantly in the topographies used, screening methods, and plate design, we face the same challenges and achieve similar results. We identified the size and, therefore, the large difference in feature spacing as the main driving factor for the cell phenotype. At the same time, small changes in pitch and disorder did not significantly affect cell morphology. The NanoTopoChip showed that U2OS cell spreading depends on the ratio of patterned to non-patterned area. Additionally, they found that few large, patterned areas give rise to small cell areas, whereas many small adhesion areas give rise to large cell areas. No influence of feature shape was observed[77]. The BSSA platform identified that the inter-pillar gap size is the most important factor in promoting osteogenesis[110]. The highest osteogenic marker expression was observed at a gap size of 4 µm, whereas larger gap sizes strongly reduced differentiation. Pillars with a size of 1 and 2 µm exhibit the strongest response in osteogenic marker expression. In comparison, pillars with diameters of 4 and 6 µm exhibit significantly lower expression of osteogenic markers. This observation matches our results, which show that cellular morphology changes decrease at larger adhesion areas with larger nanopits. A similar effect was observed for the BSSA platform on fibroblasts, where the inter-pillar distance also drives proliferation. At the same time, the shape of the pillar does not affect the cells significantly[237].

The Galapagos chip, which used the MicroTopoChip design to create unique adhesive areas, found similar limitations to us[232]. They found no correlation between YAP nuclear translocation and adhesion patterns. However, they were able to correlate cell morphology to YAP nuclear translocation. Adding a factor such as YAP nuclear translocation could also be an approach to improve our nanotopography library screening.

6. Cellular traction force dependency on nanotopography - the challenge of hierarchical micro-/nanostructure fabrication

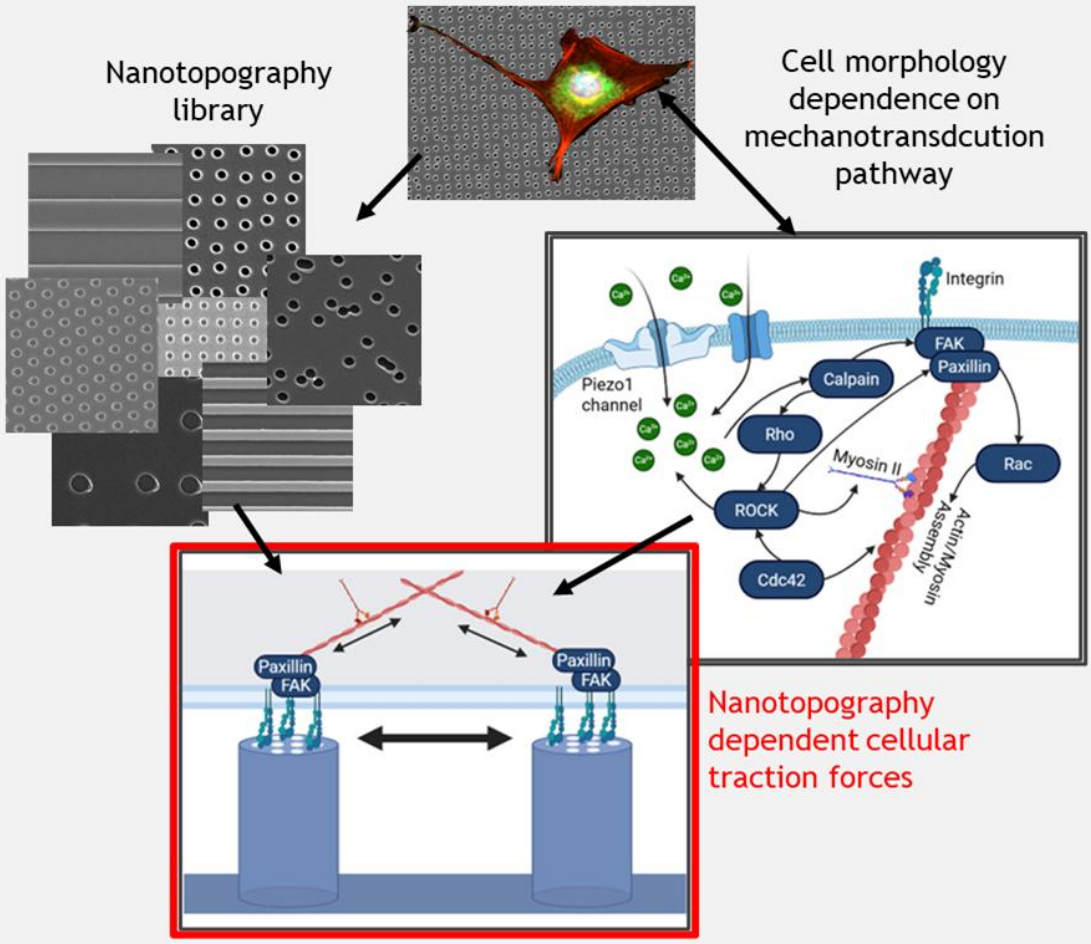

Methods: Traction force microscopy with MC3T3 cells on **hierarchical micropillars** with nanopits on top

Challenge: Fabrication of master for soft lithography replication in PDMS

Results:

- **H-PDMS** needed for replication of nanotopography **<200 nm**
- Protocol for **e-beam lithography** in **10 µm thick PMMA** resist
- **Photolithography** with **SU-8** resist most promising
- **UV-light interaction** with **nanopillars** hinders fabrication of hierarchical micropillar by photolithography
- **Traction force** microscopy with flat PDMS micropillars with **5.93±0.15 µm** diameter and **18.61±0.28 µm** height ⟶ **~10 nN**

6.1. Introduction

In the previous chapters, we discussed the effect of nanotopographies on cells in detail with the example of the osteogenic progenitor cell line MC3T3. In vivo, the cell is responding to the topography of its surroundings as well as the stiffness of the environment[4, 33, 34]. Engler et al. have shown that the mechanical properties of the surrounding biomaterial dictate the differentiation of MSCs[5]. In vivo different tissue has a wide range of stiffness. Brain tissue is one of the softest tissues, with a Young's modulus of 0.1-1 kPa. Muscle tissue has a modulus of 8-17 kPa, and bone tissue is the hardest, with a modulus of 25-40 kPa[34]. Thus, the stiffness of the environment is an important indicator for the cell response. The stiffness of the tissue is also of interest in wound healing as scarred tissue is stiffer than healthy tissue[6]. Furthermore, tumours are stiffer than the healthy surrounding tissue and cancer cells are known to migrate towards the stiffer tissue. This effect is known as durotaxis[7, 35]. Those effects are also observable due to nanotopographies. Nanotopographies are used in various applications, including directing cell differentiation and guiding cancer cell migration[8, 24]. The early reviews of Curtis and Wilkinson[266, 267] and others[268, 269] already show the vast impact of nanotopographies across a wide range of cell types and applications. As nanolithography methods improved, the field expanded, and a great number of topographies of different materials and geometries were created, and the understanding of cellular response grew as well[270-272]. Some examples include guided cell movement along adhesive tracks[273], alignment of epithelial cells along grooves and ridges[274], differentiation into neurons on gratings[92, 242], and into osteoblasts on nanopits[31].

Cellular adhesions are an essential part of mechanotransduction, since biomechanical extracellular cues are sensed, among others, by focal adhesions and translated into the cell through the cytoskeleton[11]. Material stiffness affects cell adhesions and the cellular response[275]. Zhou et al.[276] have shown that increased material stiffness increases vinculin recruitment at focal adhesion sites and traction forces. The focal adhesion area also increases with material stiffness. Nanotopographies locally limit the adhesion sites for cells. The

size[277], organisation[95, 278] and spacing[77] between adhesion sites affect the cell response.

We are interested in studying the interplay between those two effects. Only a few studies have examined material stiffness and nanotopography simultaneously [279]. Gratings or waves are synthesized in PDMS and hydrogel [280], polyacrylamide gels from 3 to 145 kPa[281], and polyurethane-based surfaces from 1.8 MPa to 1.1 GPa[282] and 11 MPa to 1.1 GPa All those studies have the disadvantage that changes in stiffness are accompanied by changes in the material's chemical composition. To overcome this problem, we need to create a biomaterial that differs in only one parameter at a time, either topography or stiffness. Nanotopographies with different stiffness, achieved by using varying materials or PDMS compositions, differ not only in stiffness but also in chemical composition, which in turn affects the cell response. Hierarchical micropillars are a good solution for it. Different nanotopographies can be fabricated on top of the micropillars, and by varying the dimensions of the micropillars, the mechanical properties of the biomaterial are changed while keeping the chemical composition constant. The micropillars can also be well used for traction force microscopy[159, 162].

Cellular traction forces are a good measure of the cell response to varying stiffness. Micropillar arrays are widely used to study the effect of different stiffness materials on cellular functions[156, 157]. For many cell types, cellular traction forces are also a reliable measure of the cell’s state. Traction forces are studied in a broad range of applications. They are of high interest in highly contractile cell types, such as cardiomyocytes[283, 284] and smooth muscle cells[285]. They are also widely used in cancer research and show great promise for drug discovery[173, 286]. Those varying cell types are in tissues of different mechanical properties. The micropillars used for traction force microscopy can be fabricated with different dimensions, replicating the stiffness of the different tissues. The micropillars of different stiffness have also been used to study the effect of biomaterial stiffness on MSCs. Rigid micropillars direct the MSC differentiation towards osteogenesis, while soft micropillars direct the differentiation towards adipogenesis[157].

The cellular traction force is adhesion-dependent, and nanotopographies affect the adhesion. Thus, the fabrication of micropillars with nanotopographies is of high interest for studying the effect of nanotopographies on cellular traction forces and, consequently, adhesion. It was recently shown by Cheng et al.[19] in 2013 that 280 nm diameter and 500 nm tall nanopillars on top of micropillars with a 5 µm diameter increase the cellular traction force of MC3T3 cells. Furthermore, they have shown that the nanopillars increase the migration speed and filopodia number. The higher amount of actin-rich protrusions produce larger cellular traction forces[287]. A silicon oxide and titanium oxide coating of the micropillars produces the opposite effect. Therefore, the surface energy correlates with traction forces[19]. It is further known that nanotopographies change intracellular tension and contractibility. Mechanotransduction, the process by which cells convert mechanical stimuli into biochemical signals, plays a key role in these changes[11]. Myosin II is an important protein in the mechanotransduction pathway and is essential for the traction forces as it is responsible for the contractile forces in cells[70, 108, 152, 154]. Nanotopographies also affect the nuclear structure and chromatin formation through nuclear mechanotransduction, translating extracellular forces and nanotopographies into cytoskeleton rearrangement toward the nucleoskeleton. Changes in the nucleoskeleton enable the transport of signalling proteins like YAP and a chromatin rearrangement[9, 44, 46]. The nucleus location and chromatin structure are, in turn, correlated with the traction forces[153]. Those examples highlight the importance of studying the interplay between the topography and the mechanical properties of biomaterials to achieve a comprehensive understanding of the cellular response to its environment, as the mechanotransduction of topography and material stiffness shares the same pathways.

We aim to take this further by including a variety of nanotopographies in the form of nanopits in a square, near-square and hexagonal arrangement. Additionally, we want to use micropillars of varying dimensions to study the effect of material stiffness on the cellular traction forces on nanopits. The used nanopits have the advantage over the nanopillars that the response will be mainly based on the adhesion. The nanopillars used by Cheng et al.[19] result in a stiffer material on top of the micropillars, which can be sensed by the cells and can change the cell

response[288-290]. The nanopillars on top of the micropillars have a spring constant of 7 nN/µm, and the micropillars have a spring constant of 12.16 nN/µm. The nanopits are not significantly affecting the material properties. Therefore, we believe that the nanopits will mainly impact the adhesion sites of the cells, with the changes to the mechanical properties due to the nanopits being negligible.

The fabrication of hierarchical micropillars with nanopits on top has proven to be highly challenging. Thus, this chapter focuses mainly on the attempted fabrication of those micropillars. The general fabrication process starts with a master fabrication by electron beam lithography or photolithography. Next, the micropillars are replicated by soft lithography from the master using PDMS. This process has several challenges. For a good replication in soft lithography, the master needs straight sidewalls in the micropits to avoid the pillars getting stuck in the master. Another challenge is the replication of nanofeatures in PDMS. The conventionally used soft Sylgard PDMS is not able to replicate nanotopographies of 100 nm. For the replication of nanotopographies, hard PDMS (h-PDMS) formulations are used, which have a tuneable stiffness in a range exceeding that of Sylgard PDMS by more than twice[291-293]. However, the usage of hard PDMS causes challenges in the micropillar fabrication. Due to the higher stiffness, one would need micropillars with a higher aspect ratio, which in turn makes the master fabrication more challenging again. The h-PDMS is also more brittle, which makes the replication of microfeatures challenging.

Several factors limit the design of the micropillar dimensions. First of all, the diameter needs to be large enough to have sufficient space for the nanotopography. Then, the aspect ratio needs to be high enough that the pillar is soft enough to pick up the pillar deflection with the microscope. The used Zeiss Observer with a 63x objective has a pixel unit of 103 nm/pixel, and 1/5 of a pixel unit can be picked up by the traction force microscopy. Thus, a deflection of 20.6 nm can be seen. Common traction forces are in the range of 10s of nN for MC3T3 cells[19, 294]. That means that a micropillar needs to have a spring constant of less than 485 nN/µm to have an observable deflection, following Hooke's law $F=k*\Delta x$.

6.2. Methodology

This Chapter 6 is mainly focused on the fabrication of hierarchical micropillars with nanopits on top. Thus, the detailed methodology is explained in the corresponding sections below. We will describe the methodology that is uniform across the different tested methods in this subchapter first. The osteogenic progenitor cell line MC3T3 is used in this chapter as in the previous chapters and is maintained as described in the general methodology section. The general outline of the fabrication stays the same across the different fabrication methods. The design of all e-beam lithography patterns is done using L-edit software. The designed GDS file is then converted into a GPF file in BEAMER (GenISys), where the resolution, beam step size, and field sizes are set. Depending on those parameters, the pattern is fractured into mainfields and subfields, and the location of beam shots is calculated. It is essential to have the shape detection of circles enabled to obtain round objects. We also have an overlap of the beam shots, as this helps to obtain a smooth, round object. Next, a cjob file is created in the Cjob software of Raith to bring the patterns into the correct format for the e-beam lithography tool. The exposure dose is also set in this step. All electron beam lithography is performed on a Raith EBPG 5200.

The fabrication of the micropillars follows the schematic in Figure 6.1. First, HSQ nanopillars are fabricated on a silicon wafer piece by electron beam lithography. Next, the micropits are fabricated using e-beam lithography or photolithography. The resist is spun on top of the nanopillars after a short oxygen plasma cleaning in YES G-1000 oxygen plasma asher for 30 seconds at 80 W and dehydration bake at 180° C for 30 minutes. After development, the master stamp is ready for the soft lithography step. The master is silanised by adding 3 µL of Trichloro(1H,1H,2H,2H-perfluorooctyl)silane in a desiccator with the master. It is kept in the vacuum desiccator for 1 hour with the vacuum pump on and is then kept overnight in the vacuum. Next, the micropillars are replicated from the master using the Sylgard 184 PDMS or h-PDMS.

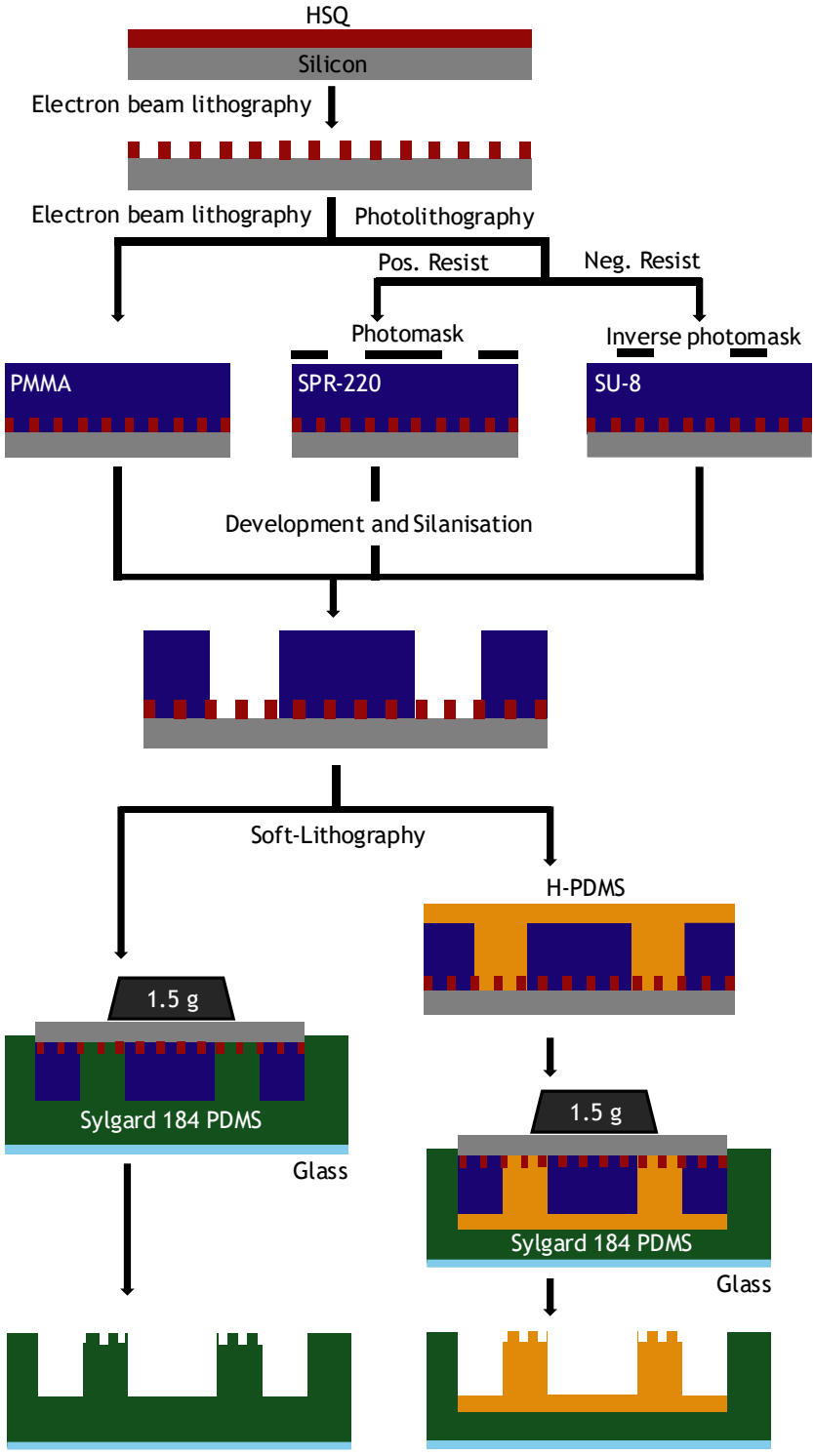

***Figure 6.1**: Schematic drawing of different fabrication approaches of PDMS micropillars with nanopits on top. First, the master stamp is fabricated on a silicon wafer piece. The nanopillars are produced in HSQ by e-beam lithography. Next, the micropits are fabricated either by e-beam lithopgraphy and PMMA resist or photolithography and SPR-220 as a positive photoresist or SU-8 as a negative photoresist. After development and silanisation the micropillars are fabricated by a soft-lithography process with either a combination of h-PDMS and Sylgard 184 PDMS or only Sylgard 184 PDMS.*

6.2.1. HSQ nanopillar fabrication

First, a master for the soft lithography process is fabricated, which begins with the fabrication of nanopillars. For the fabrication of the nanopillars, a silicon wafer piece is solvent cleaned in an ultrasonic bath with methanol, acetone, isopropanol (IPA), and reverse osmosis (RO) water for 5 minutes each. Afterwards, the silicon piece is dried with a nitrogen gun. Next, it is dehydration baked for 1 hour at 180° C in an oven and oxygen plasma cleaned for 3 minutes at 150 W. A 1:3 hydrogen silsesquioxane:methyl isobutyl ketone (HSQ:MIBK) solution is spun at 2000 rpm for 1 minute for a thickness of 100 nm. For a thickness of 200 nm, a 1:1 HSQ:MIBK is spun for 1 minute at 3000 rpm. The backside of the silicon piece is cleaned with acetone to remove any resist, and it is then baked at 90° C on a vacuum hotplate for 2 minutes. The e-beam lithography is performed with a beam step size of 30 nm and an 8 nA beam that has a spot size of 36 nm. Dose tests define the optimal dose; 100 nm diameter and 100 nm height nanopillars are written with a dose of 1350 μC/cm2. The nanopillars of 200 nm diameter and 200 nm height are written with a dose of 2100 μC/cm^2. The nanopillars are developed in 25 % tetramethylammonium hydroxide (TMAH) for 1 minute at 23° C under constant agitation. Next, it is washed twice in RO water for 30 seconds and in IPA for 15 seconds. Finally, the silicon piece is dried with a nitrogen gun. Before further processing for an additional e-beam resist or photoresist layer, the silicon piece with the HSQ nanopillars is oxygen plasma cleaned at 80 W for 30 seconds and dehydration baked at 180° C for 30 minutes.

6.2.2. PDMS softlithography of micropillars

The replication of the micropillars from the master in Sylgard 184 PDMS follows the same procedure, independent of the master composition. The Sylgard 184 PDMS is prepared in a 10:1 monomer:curing agent ratio and thoroughly mixed. The PDMS mixture is degassed in a vacuum desiccator for 30 minutes until no air bubbles are visible in the PDMS mixture. Next, a glass cover slip is solvent cleaned in acetone and IPA in an ultrasonic bath for 5 minutes per solvent. After solvent cleaning, the glass coverslip is dried with a nitrogen gun and oxygen plasma cleaned in a Henniker Plasma HPT-200 plasma oven (Henniker Scientific, UK) for

1 minute at 80 W. Next, the PDMS is spun on the glass cover slip. Two to three drops of PDMS are placed on the centre of the glass, and it is spun in a five-step process. In a first step, the cover slip is spun at 500 rpm and 100 rpm/s for 3 seconds. Next, the spin speed is increased to 1000 rpm and 100 rpm/s for 3 seconds. In the third step, the cover slip is spun at 2500 rpm and 100 rpm/s for 60 seconds. The spinning is then slowly stopped by decelerating to 1000 rpm and 100 rpm/s for 3 seconds, and 500 rpm for 3 seconds at the same acceleration. Afterwards, the spin is fully stopped, and the silicon master is placed on top of the PDMS with the face down. A 1.5 gram weight is placed on top of the master to press it down, and it is then placed in a vacuum desiccator for at least 1 hour, until no air is trapped between the master and the glass cover slip. The PDMS is cured in an oven for 10 hours at 70° C. After curing, the master is carefully demoulded from the glass cover slip by cutting along the edge of the master with a scalpel to separate the PDMS from the master. Next, the master is carefully pried off the glass cover slip, and the replication is checked in an optical microscope as well as in a SEM. Instead of a glass coverslip, a 35 mm MatTek glass-bottom dish is also used for the cell experiments. The fabrication process using a MatTek glass-bottom dish is the same as with the glass cover slip. Only the solvent cleaning is not necessary.

6.3. Micropillar fabrication by electron beam lithography

The fabrication of highly controlled nano- and microfeatures can be achieved using various nanofabrication techniques, depending on the feature sizes. For features as small as 3 nm to a few micrometres, electron beam lithography is primarily used[74, 75, 295-298]. Conventionally, a resist is spun on a silicon wafer, cured and then exposed in an electron beam lithography tool. PMMA and HSQ are among the most commonly used resists. PMMA is a positive resist, which means that the exposed resist becomes soluble by the electron beam, as the electrons damage the cross-linking in the resist. Thus, the exposed area can be washed off with a fitting developer. Usually, IPA:water or IPA:MIBK mixtures are used for the development. HSQ is a negative tone resist, which means that the electrons cross-link the resist, and the remaining unexposed resist is washed off with a developer. Typically, tetramethylammonium hydroxide (TMAH) based developers are used for

HSQ resist[296, 299]. PMMA can turn into a negative resist at high doses above 50-70 C/m^2[300].

We utilise the properties of the different types of e-beam resists to fabricate nanopatterns from the thin, high-accuracy negative resist HSQ, as described above. The micropits are fabricated in the thick positive e-beam resist PMMA. The exposure of the positive tone in the second e-beam exposure should not affect the previously developed negative tone HSQ resist. We use PMMA widely in our lab to fabricate the masters for the micropillar fabrication of micropillars with a diameter of 1 µm. They can be easily fabricated with different stiffness by varying the PMMA layer thickness.

The fabrication of the master for 1 µm diameter micropillars starts by spinning Allresist AR-P 642.15 PMMA with 15 % weight in anisole and a molecular weight of 200k on top of the oxygen plasma cleaned and dehydrated silicon wafer piece with the HSQ nanopillars. If the micropits are fabricated without HSQ nanopillars, the silicon wafer piece is always solvent cleaned in methanol, acetone, and IPA in an ultrasonic bath for 5 minutes per solvent and dried with a nitrogen gun afterwards. Then, the silicon wafer piece is dehydration baked for 1 hour at 180° C in an oven and oxygen plasma cleaned for 3 minutes at 150 W. The PMMA layer is spun for 1 minute at a speed determined by the desired thickness. The spin speeds are shown in Table 6.1. For a single PMMA layer, the silicon wafer piece with PMMA is baked at 180° C in an oven overnight. A bilayer of PMMA is needed for a thicker layer of resist. For this, the thicker layer is spun at a lower spin speed first and then baked at 180 °C for 4 hours in an oven. Afterwards, the second thinner layer is spun on top of the first layer and baked at 180° C overnight in an oven. After baking, the e-beam lithography exposure is performed using a 100 nA beam and an aperture of 300 µm that has a beam spot size of 52 nm. A beam step size of 30 nm is used. Afterwards, the development is performed in 2.5:1 MIBK :IPA developer at 25° C and the silicon piece is constantly agitated while developing to ensure an even development. The development time depends on the PMMA layer thickness and is written in Table 6.1. After development, the development process is stopped by

rinsing the substrate in IPA for 10 seconds. The PMMA microtopography is then dried again with a nitrogen gun.

To obtain a thicker PMMA resist for the master of 4 μm micropillars, a PMMA resist with higher viscosity is needed. A smaller anisole percentage in the resist achieves a higher viscosity. We use the same Allresist AR-P 642.15 PMMA resist that is to 85 % anisole. To reduce the anisole percentage, we place 1 mL of PMMA resist in an open 1.5 mL Eppendorf tube in a laminar flow cabinet for 5-6 hours until the weight is reduced by 10%. In the laminar flow cabinet, the anisole evaporates, while the absolute PMMA content remains constant. Thus, the relative PMMA content increases and the viscosity increases. That way, a 10 μm thick PMMA layer can be spun on a silicon piece by spinning three layers at 1000 rpm for 1 minute per layer.

After the first layer, the PMMA is baked at 180° C for 30 minutes in an oven, and the next layer is baked on a vacuum hotplate for 5 minutes at 180° C. The third layer is baked in an oven at 180° C overnight. Afterwards, Electra 92 is spun on top of the PMMA layer at 2000 rpm for 1 minute and baked at 90° C for 2 minutes on a vacuum hotplate. The Electra 92 layer serves as a thin charge dissipation layer, preventing charging in the resist, which can cause it to crack. The e-beam lithography is performed using a 100 nA beam and an aperture of 300 μm that has a beam spot size of 52 nm. A beam step size of 40 nm is used. After e-beam lithography exposure, the Electra 92 layer is rinsed off with RO water for 1 minute. Next, the sample is developed with 7:3 IPA:water developer for 5 minutes at 23° C. After development, the sample is rinsed in IPA for 10 seconds and dried with a nitrogen gun.

***Table 6.1**: Spin, development and electron beam lithography conditions for the fabrication of micropits in PMMA with varying height.*

PMMA	Rpm	Height in µm	Development time	Dose in µC/cm^2
AR-P 642.15	4000	1.23	30 s	1000
AR-P 642.15	2000	1.75	30 s	1100
AR-P 642.15	1500	2.03	30 s	1200
AR-P 642.15	1000	2.478	40 s	1350
AR-P 642.15	2000+4000	3.0175	40 s	1400
AR-P 642.15	1000+4000	3.728	50 s	1800
AR-P 642.15 (-10 % weight)	3x 1000	10	5 min	1050

A

1 µm Diameter – PMMA master

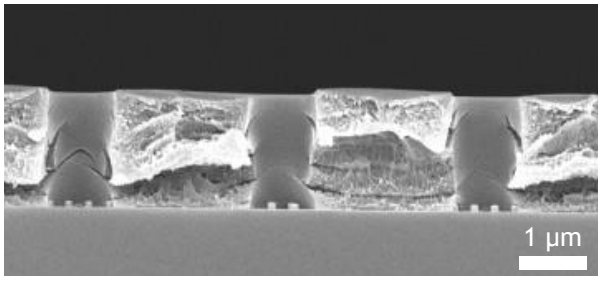

B PDMS replica

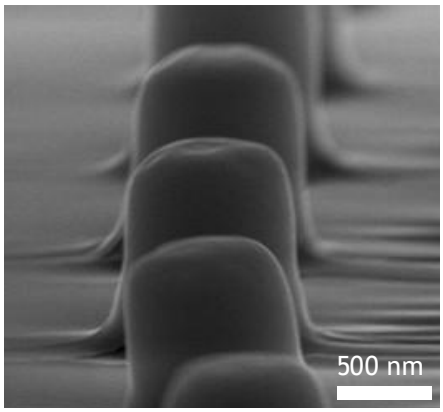

C

4 µm Diameter – PMMA master

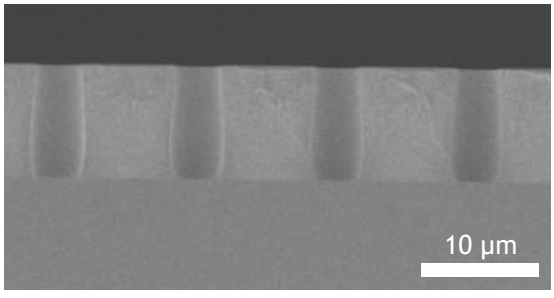

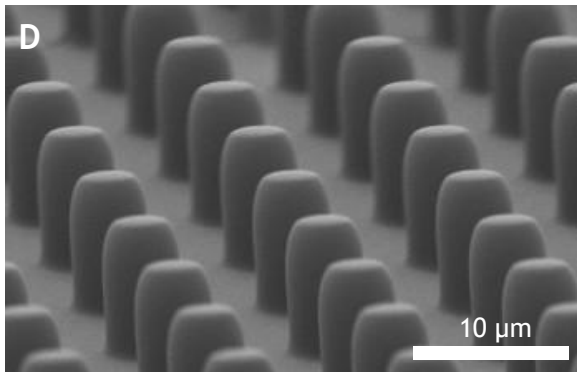

(caption for figure on previous page) ***Figure 6.2****: SEM images of PMMA masters for micropillar fabrication and PDMS replica. PMMA masters for micropillars with 1 µm diameter and a height of 3 µm are successfully fabricated with HSQ nanopillars at the bottom by electron beam lithography (A). The replication of 1 µm diameter micropillars using Sylgard PDMS replicates the micropillars, but not the nanotopography (B). 4 µm diameter holes in 10 µm thick PMMA resists are fabricated by electron beam lithography (C) and successfully replicated with Sylgard PDMS (D). All SEM images are taken with a Hitachi scanning electron microscope of the SU8200 series.*

The micropits of 1 µm diameter are successfully fabricated, and micropillars can be fabricated in PDMS (Figure 6.2A+B). However, a diameter of 1 µm does not provide sufficient space for 100 nm diameter nanopits with a centre-to-centre spacing of 300 nm. Only three nanopits would fit in a row on one micropillar at a time, with two of them being at the edge of the micropillar. So, no proper topography is formed on top of the micropillar. Therefore, larger-diameter micropillars are required. The height of the micropillars must grow with the diameter to ensure a 1:3 aspect ratio for flexible pillars. Conventionally, e-beam lithography is not used for this thick resist since it is at the limit of its capabilities[301]. We are able to spin a reliable layer of 10 µm thick PMMA resist by decreasing the anisole content by 10 % by evaporation. The micropits without nanopillars are fabricated well, and a replication in PDMS is also successful. However, no straight sidewall could be achieved (Figure 6.2C+D). This is due to the electron scattering as well as the shape of the electron beam with the focus point on top of the resist. The electrons scatter forward in the resist, backwards from the substrate and backwards within the resist. The electrons collide with the atoms of the resist and are inelastically scattered by them. This results in a conical shape of the electron beam in the resist, as well as the proximity effect, which means that scattered electrons also expose the resist in proximity to the exposed area[302, 303]. Therefore, it is essential to consider the electron path in the resist when fabricating high-quality nanotopographies, particularly when a straight sidewall of the features is required. The scattering effect is especially strong in thick resist. The longer the electron path, the more it scatters. The proximity effect is negligible for our topographies, as it remains constant throughout the entire area. Only at the edges is a difference in dose. Since we measure the micropillar diameters at the centre of the array and not at the edge, a slide difference in micropillar diameter sizes at the edge is negligible.

Additionally, the electron beam is focused on the top of the PMMA layer, which means that the beam is diverging in the resist. This effect is negligible for thin resists but has an effect in thicker resists. Due to those two effects, an undercut is observed. With the non-straight sidewalls, the Euler-Bernoulli beam theorem to calculate the applied forces from the pillar deflection does not hold anymore. However, the sidewall profile can be approximated by a Bézier curve to adjust for the wider top of the pillar[304]. We test an offset of the electron beam focus to the bottom of the resist to compensate for the undercut, but it does not improve the sidewall profile. While the replication of PDMS micropillars with an undercut in the master is sometimes successful, it is highly unreliable, depending on the strength of the undercut. With a just slightly higher undercut than shown in Figure 6.2C, the PDMS pillars get stuck in the master, and no replication is achievable.

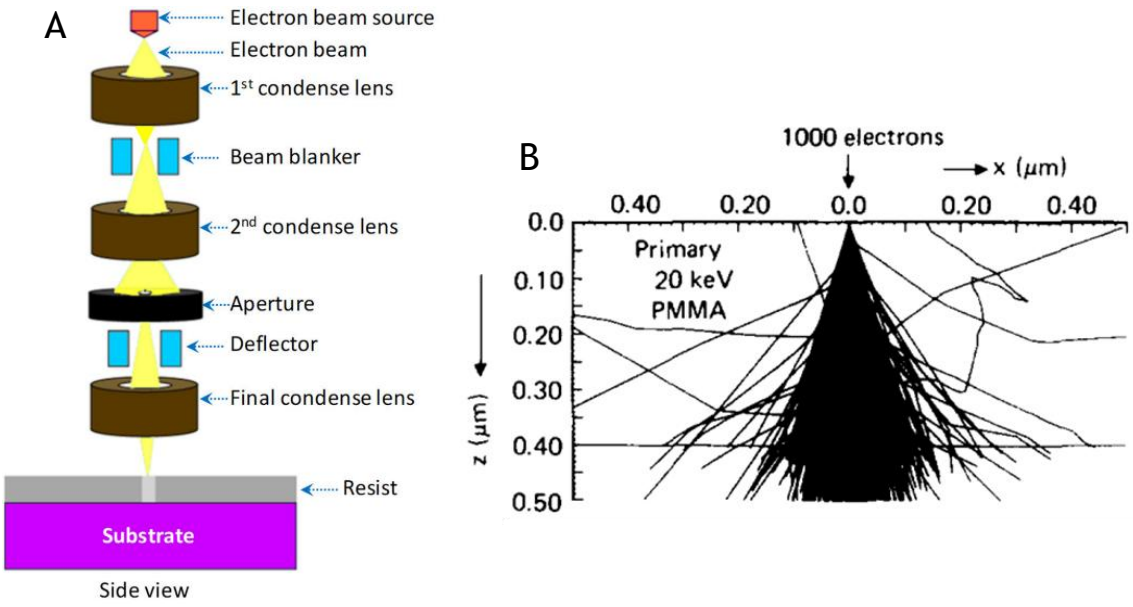

***Figure 6.3**: Schematic diagram of a typical electron beam lithography tool, where the electron beam is focused through condense lenses to write with an electron beam into resist with nanometre precision(A). (B) shows a Monte Carlo simulation of the primary electron scattering in PMMA. Adapted from Sharma et al.,[299] and Murata et al.[303].*

The observed undercut is not the only issue that is noticed in the fabrication process of micropillars with nanopits on top. Figure 6.2B also shows that the replication of the 100 nm diameter nanopits in Sylgard 184 PDMS is not working well. It is known that the soft Sylgard 184 PDMS struggles with the replication of features in the range of less than 200 nm. Hard types of PDMS have been developed that can replicate features as small as 50 nm. The hard PDMS (h-PDMS) recipes

consist of more copolymer than the standard PDMS recipe. That way, the number of crosslinks can be tuned more effectively, and a PDMS that is up to 5 times harder can be obtained[291-293, 305-308]. The h-PDMS consists of two copolymers and shorter curing agents than the Sylgard 184 PDMS. This results in the more rigid material. Additionally, it is a four-component mixture which provides a larger variety of stiffnesses than the two-component Sylgard 184 PDMS mixture. However, a downside of the use of h-PDMS is the brittle nature of the h-PDMS. A bilayer of h-PDMS and soft Sylgard 184 PDMS is used, where a thin h-PDMS layer replicates the nanostructures and a thick Sylgard 184 PDMS layer gives the h-PDMS layer the needed stability. This bilayer of different stiffness will be challenging for us as we will have h-PDMS micropillars on top of soft PDMS. This changes the behaviour of the pillars and how the cell traction forces can be calculated from the measured pillar deflection. As shown by Schoen et al. does the pillar deflection also depend on the material stiffness that the pillars are sitting on[309].

The soft-lithography fabrication process of h-PDMS nanopits or micropillars with nanopits is performed by preparing the h-PDMS first. The h-PDMS consists of the four components (7.0-8-0 % Vinylmethylsiloxane)-dimethylsiloxane copolymer (trimethysiloxyl terminated) (VDT-731, Gelest), Platinum-divinyltetramethyldisiloxane complex in xylene (SIP 6831.2, Gelest) in a 1:2 SIP 6831.2:toluene solution, 2,4,6,8-Tetramethyl-2,4,6,8-tetravinylcyclotetra-siloxane (SIT 7900, Gelest), and (25-35% Methylhydrosiloxane)-dimethylsiloxane copolymer, trimethylsiloxane terminated (HMS-301, Gelest). First, 1.7 g VDT-731, 0.5 g HMS-301 and 9 µL SIP 6831.2 in a 1:2 solution in toluene are mixed. 25 µL of SIT 7900 is mixed into it last. Next, the h-PDMS solution is poured onto the silicon piece with either the PMMA micropits with HSQ nanopillars, or on a piece only with nanopillars. The silicon piece is left for 30 minutes to let the h-PDMS sink into the cavities. Next, we spin the silicon piece in a two-step process. In the first step we spin it at 500 rpm for 1400 seconds to ensure a good spreading of the h-PDMS, and then at 1500 rpm for 60 seconds for the final thickness. After spinning, a first curing step is performed at 80° C for 10 minutes in an oven. In the meantime, Sylgard 184 PDMS is spun on a glass coverslip as described before. The partially cured h-PDMS on the silicon wafer piece is placed on the glass cover slip with the h-PDMS contacting the soft PDMS. A 1.5 g weight is placed on top of the silicon

wafer piece, and it is placed in a vacuum desiccator for 1 hour until no air is trapped under the silicon wafer piece. The sample is then cured for 10 hours at 70° C in an oven. During curing the Sylgard 184 PDMS crosslinks with the h-PDMS that makes it strongly connected. After curing, the silicon master is carefully demoulded in the same way as described above.

To test the replication of nanopits, we created nanopillars with a diameter of 200 nm and a height of 100 nm, spaced 600 nm apart in a square array. We replicated them in Sylgard 184 PDMS and h-PDMS. The replication in the soft Sylgard 184 PDMS is not working for just the nanopillars (Figure 6.4B) and the micropits with nanopillars (Figure 6.4A). Interestingly, the micropillars with nanopits have a platform at the top. Typically, the PDMS does not entirely fill the undercut and forms a drop shape at the bottom of the micropit. When the PDMS touches the nanopillars, it spreads over the nanopillars to form the observed platform. The h-PDMS replicates the nanopillars well (Figure 6.4D), but it fails to replicate the micropits. Due to the higher stiffness and brittleness of the h-PDMS, the micropillars become stuck in the master mould during demoulding. The softer Sylgard 184 PDMS can probably deform enough while demoulding to negate the negative effect of the undercut in the master.

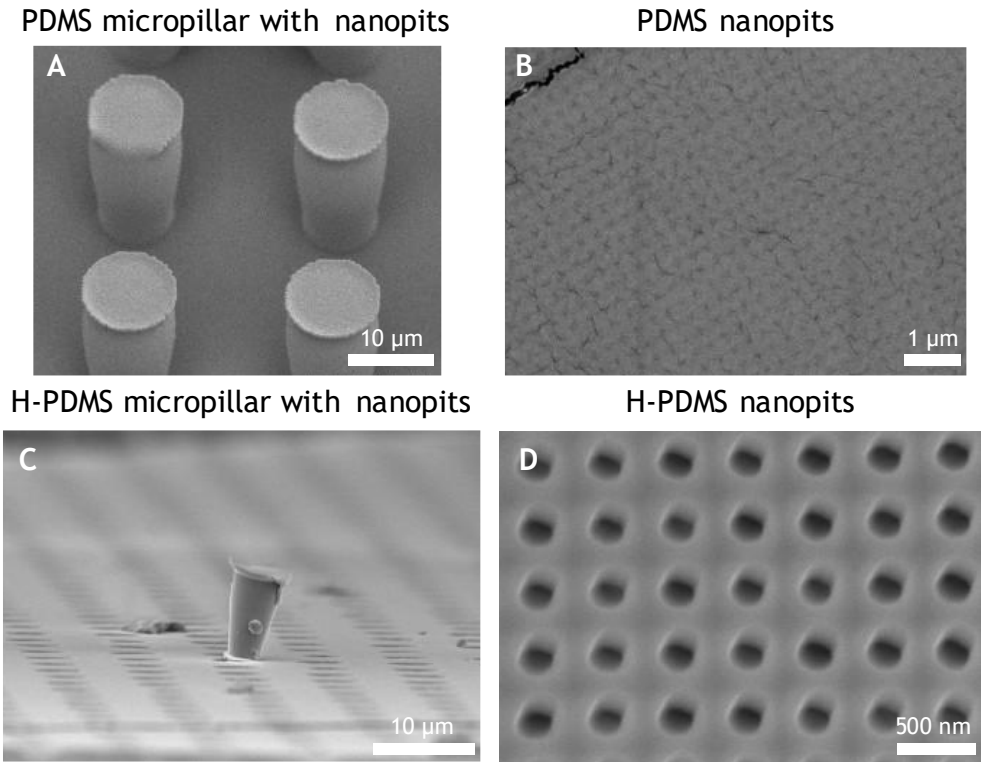

(caption for figure on previous page) ***Figure 6.4****: SEM images of large micropillar replication with nanotopography from PMMA masters. The replication of the micropillars works well for Sylgard PDMS (A), but no replication of 200 nm diameter nanopits is possible (B). H-PDMS can replicate the nanotopography (D), but not the Micropillars, as they get stuck in the PMMA master (C). All SEM images are taken with a Hitachi scanning electron microscope of the SU8200 series.*

6.4. Micropillar fabrication by photolithography

Micropillar fabrication using e-beam lithography is not working well enough to establish a reliable process. The main issue is the produced undercut that is unavoidable due to the beam shape and electron scattering in the resist. Photolithography is an alternative lithography technique for the fabrication of micron sized features[310-312]. The photons do not scatter in the resist like the electrons; therefore, it can be used with thick resist and still provides straight sidewalls. This reduces the formation of an undercut. The light path and the resist properties define the sidewall. In photolithography, using a mask aligner, the quality of lithography strongly depends on the contact with the mask. The wavelength of the light defines the resolution of photolithography and has a typical minimum feature size of 2 µm. UV light is mainly used for photolithography and operates in a manner similar to EBL. Positive resists are cured before exposure, and the cross-linking is broken up by the photons, allowing the developer to wash it out. The negative resists are cross-linked by photon activation, and the developer washes away the unexposed areas.

We test SPR220-7.0 as a positive tone photoresist and SU-8 as a negative tone photoresist. We only tested resist without a nanopillars on the silicon wafer piece. The silicon wafer piece is at least 25x25 mm large to ensure a good spinning of the thick resist. The silicon wafer piece is prepared by solvent cleaning in methanol, acetone, and IPA for 5 minutes per solvent in an ultrasonic bath. It is dried with a nitrogen gun afterwards and dehydration baked at 180° C for minutes on a vacuum hotplate. Next, it is oxygen plasma cleaned at 150 W for 3 minutes. The SPR220 sample is prepared with a MicroChem Primer 80/20 (MCC 80/20) that is made up of 20 % Hexamethyldisilazane (HMDS) and 80 % propylene glycol monomethyl ether acetate (PM acetate) that aids the adhesion of the photoresist. The MCC 80/20 is poured on the silicon wafer piece to cover the surface. After waiting for 20 seconds, the sample is spun dry and nitrogen purged to remove

remaining ammonia on the surface. Next, the SPR220-7.0 is spun in a 3-step spinning process. The resist is puddle dispensed on the silicon piece and spun at 500 rpm for 5 seconds with an acceleration of 100 rpm/s to spread the resist. In the second step, the resist is spun to its final thickness for 30 seconds at 3000 rpm and 2000 rpm/s. Finally, the sample is slowed to a stop at a deceleration of 1000 rpm/s. After spinning, the sample is left standing for 30 minutes so that the solvent can evaporate. After the solvent evaporation, the soft bake is performed on a vacuum hotplate at 118° C for 90 seconds. Next, the sample is transferred to a watch glass that has been heated to 120° C in an oven to ensure slow cooling. The slow cooling prevents cracking of the resist. Next, the sample is left standing for 1 hour to rehydrate before exposure. The photolithography process is performed on a SUSS Mask Aligner MA6 with a 365 nm UV-mercury lamp with a lamp power of 350 W that has a light intensity of 7.2 milliwatts/cm2 constant power. The used mask has arrays of 2 μm diameter holes and 5 μm holes with centre-to-centre spacing of 3 times the diameter. The mask is a chrome on quartz glass photomask received from Compugraphics. The sample is exposed for 28 seconds in the hard contact mode and a wedge edge correction of 0.4 bar. After exposure, the sample is left standing for 1 hour to rehydrate. Then, the post exposure bake is performed at 118° C for 90 seconds. The sample is cooled slowly again by placing it on a watch glass that comes out of a 120° C oven. The development is performed after a 20 minute delay to ensure the sample is completely cooled down. It is developed in Microposit MF CD-26 developer that contains 1-5 % TMAH for 2 minutes under constant agitation. The sample is rinsed in RO water for 5 minutes after development. Finally, a hard bake process is performed on a vacuum hotplate at 120° C for 10 minutes.

SU-8 is a negative-tone photoresist and one of the most used thick resists for high-aspect ratio microtopographies[313-315]. Amato et al.[316] fabricated micropillars with an aspect ratio of 11, with a diameter of 1.8 μm and a height of 20 μm. They have a straight side wall at this height. For larger structures, an aspect ratio of more than 20 is achieved. Thus, we use it as a negative tone photoresist to fabricate micropits with straight sidewalls. Since SU-8 is a negative-tone photoresist, we cannot use the same photomask for it but need the negative of it. The JWNC lab technicians, Linda Pollock, Sarai Diaz Romero and Archie

McIver, prepared a negative copy of the available mask on a soda lime glass plate with a titanium and nickel-chromium pattern. A soda lime glass plate with a thin iron-based coating that is UV-light blocking, and a layer of the AZ1518 photoresist is exposed with the mask we used above. The plate is developed, the iron-based layer is etched away, and titanium and nickel-chromium are deposited on the plate. Next, a lift-off process of the remaining resist is performed, and the remaining iron-based layer is etched away. Thus, only the titanium and nickel-chromium are left in the exposed areas. That way, a good negative copy of the photomask is fabricated, even though the copy is not perfect, as it has missing dots in the arrays.

We use 30x30 mm silicon wafer pieces for the fabrication of SU-8 micropits. The SU-8 layer is prepared in two different thicknesses for 2 μm diameter micropits and 5 μm micropits. We describe the fabrication of 2 μm diameter micropits in SU-8 photoresist first. The silicon wafer piece is solvent cleaned, dehydration baked, and oxygen plasma cleaned the same way as described above for the SPR220-7.0 samples. SU-8 3005 is dispensed on the silicon piece and spun for 5 seconds at 500 rpm and 100 rpm/s to spread the resist. Next, it is spun for 30 seconds at 3000 rpm and 300 rpm/s for a final thickness of 6 μm. After spinning, the soft bake is performed by placing the sample on a 65° C hotplate for 30 seconds, 95° C for 2 minutes and again 65° C for 30 seconds. The slow ramp helps to prevent a cracking of the resist. After the soft bake, the sample is exposed in the SUSS MA6 Mask Aligner with an i-line bandpass filter for 15 seconds. The i-line filter filters UV light by only allowing the desired 365 nm light to pass. This ensures a straight sidewall in photolithography of SU-8 resist. The photolithography is performed in hard contact mode. After exposure, the sample is baked at 65° C for 1 minute on a hotplate, followed by 3 minutes on a 95° C hot plate and again 30 seconds on a 65° C hotplate. The development is performed in ethylene carbonate (EC) solvent for 2 minutes in one beaker under constant agitation and 2 minutes in a second beaker with fresh EC solvent under constant agitation. The sample is washed with IPA first, by rinsing it with IPA. If no misty white residue is visible, it is fully developed and is washed in IPA for 1 minute. The sample is dried with a nitrogen gun after development.

For the 5 µm diameter micropits, we need a thicker resist. Thus, we use SU-8 3010. The fabrication procedure is the same as with SU-8 3005, just the spin speed and durations change. The SU-8 3010 resist is spun to its final thickness of around 18 µm at a spin speed of 1000 rpm. The soft bake is performed for 1 minute at 65° C, 9 minutes at 95° C, and 1 minute at 65° C. The thick resist produces a large edge bead that needs to be removed since good contact with the mask is essential for the lithography process. We remove the edge bead by cutting off the edges of the silicon wafer piece where the edge bead is visible. The sample is exposed for 15 seconds. The post exposure bake is made for 1 minute at 65 ° C, 4 minutes at 95° C, and 30 seconds at 65° C. The development is performed for 5 minutes per EC solvent beaker and 1 minute in IPA. We attempt to adjust the development by increasing the development time and using an ultrasonic bath. However, it does not improve the washing out of the resist. Too high a development time results in delamination of the resist.

The fabrication of 2 µm diameter micropits with SPR220-7.0 is not working. The observed pits are only 1-2 µm deep and around 5 µm wide (Figure 6.5B). A 100 µm broad line surrounds the arrays of microdots. This line shows that the sidewall is not nearly straight enough to be able to fabricate holes of 2 µm. Additionally, a lip that is overhanging is observable at the edge of the line. This lip would be problematic in the following soft lithography process. SU-8 is also not able to produce 2 µm diameter micropits with a depth of 6 µm. The light exposes the resist with straight sidewalls, but it is not possible to entirely remove the SU-8 resist from the holes (Figure 6.5C+D). A porous structure is left in the hole, which we believe to be partially cured resist. We expose the entire silicon wafer, except for the 2 µm dots, which are not exposed to light. That probably causes a strong proximity effect that partially cures the resist in the areas that UV-light does not directly expose. Another possibility is that the self-made negative copy of the photolithography mask does not have as good antireflective properties as the purchased photomasks from Compugraphics. That could cause a reflection of the light and standing light waves in the resist that partially cure the resist.

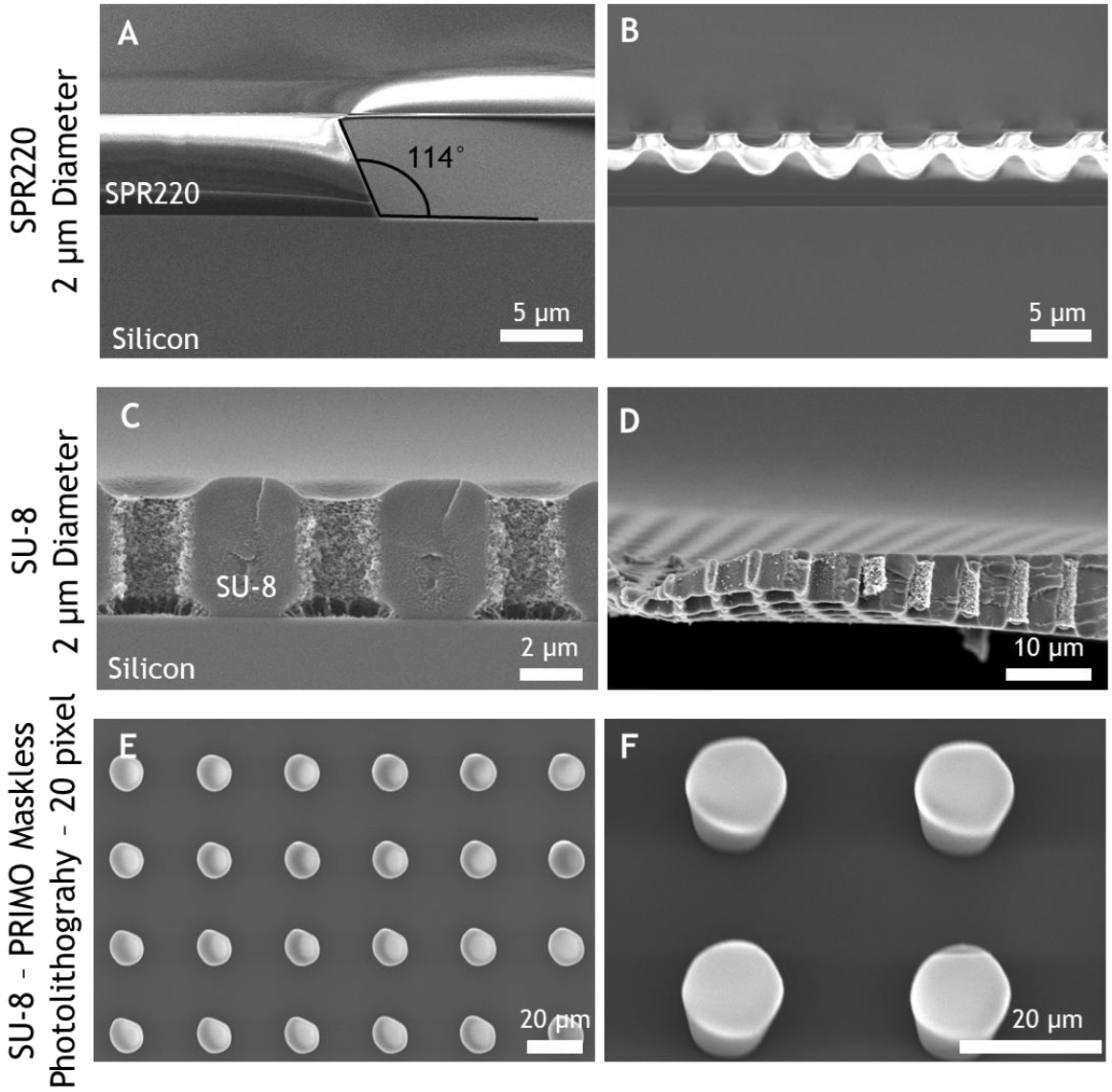

***Figure 6.5**: SEM images of photolithography tests using SPR220 and SU-8. Photolithogrpahy cannot create arrays of 2 µm holes. SPR220 does not have a straight enough sidewall to create as small features. Additionally, it has a lip at the top that prevents a good demoulding in soft lithography (A, B). SU-8 cannot fully expose the 2 µm diameter holes with a 1:3 aspect ratio. The holes are filled with partially cured SU-8 resist that is probably cured due to reflections from the wafer and mask (C, D). An alveole Primo maskless photolithography tool struggle to create round pillars of 20 pixel size which are more than 10 µm in diameter (E, F). All SEM images are taken with a Hitachi scanning electron microscope of the SU8200 series.*

Since we believe that the failed fabrication of 2 µm holes in SU-8 resist may be due to the mask, we attempt maskless photolithography using an alveole Primo maskless photolithography tool, which has a resolution of 1.2 µm and can replicate any grayscale image loaded into the software. However, initial tests indicate that when attempting to design 20 pixel diameter micropillars in 6 µm thick SU-8 3005 resist with a dose of 60 mJ, the pillars are not sufficiently round. A not perfect

roundness strongly affects the mechanical properties of the micropillars and would give different flexibilities depending on direction. This makes an analysis of pillar deflections due to cellular traction forces extremely challenging. The 20 pixel diameter corresponds to around 13 µm, which means that one pixel is 0.65 µm large and a 2 µm object is 3 pixels large. We do not believe that we can prepare micropits with the desired accuracy with this tool. Therefore, this route is not further followed.

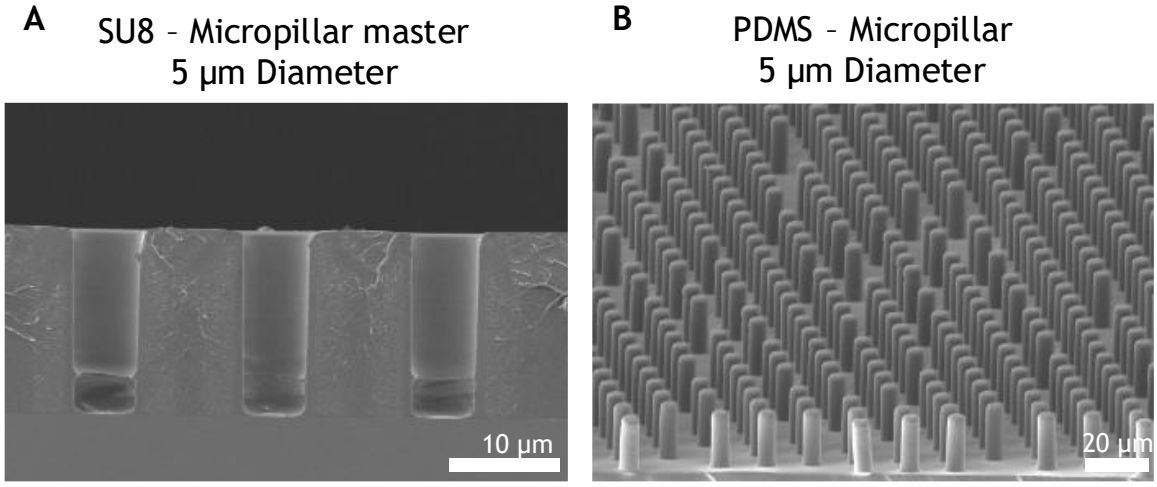

***Figure 6.6**: Micropillar fabrication with a diameter of 5 µm and height of 18 µm using SU-8 resist and photolithography. The SU-8 master show holes with straight sidewalls (A). With 6 µm, the diameter is one micron larger than designed. The micropillars replicated well in Sylgard 184 PDMS (B). All SEM images are taken with a Hitachi scanning electron microscope of the SU8200 series.*

Micropits of 5 µm diameter are successfully fabricated in 18 µm thick SU-8 3010 resist (Figure 6.6A). The diameter of the pits is one µm larger than designed, but we have straight sidewalls all the way to the bottom of the resist to the silicon wafer. A replication by soft lithography with Sylgard 184 PDMS is working well. We create high aspect ratio micropillars with a diameter of 5.93±0.15 µm and a height of 18.61±0.28 µm. However, it is worth noting that the fabrication is still not very reliable, but it is the best we can achieve at this time. A good contact between the photomask and the sample has proven to be highly crucial. Just a slight edge bead or contamination on the sample that prohibits a perfect contact and results in shallow and broad dips in the resist instead of deep and straight pits.

Thus, the edge bead removal is of utmost importance. Cutting off the edge of the silicon wafer piece that has the edge bead has proven successful. However, one

must take care that no particles from the cutting process land on top the sample. A good spin is the first important step to ensure a successful and reliable sample preparation. It has proven best to puddle dispense 1.5 mL from a syringe to the centre of a square 30x30 mm silicon piece and start the spinning immediately. That way, a consistent thickness can be achieved, and the edge bead can be minimised. When letting the resist spread before spinning, it touches the edge of the sample before the spin starts. During spinning, the resist follows that path, resulting in areas on the edge of the sample without resist, which leads to larger edge beads and a less uniform surface. A sample size of 30x30 mm provides sufficient space to cut off the areas with the edge bead.

Since the fabrication of large micropits in SU-8 3010 photoresist has proven to be the best fabrication method, we also use this method to create micropillars with nanopits on top. We prepared HSQ nanopillars with a height of 200 nm and a diameter of 220 nm in a square array with a centre-to-centre spacing of 600 nm (Figure 6.7A). We expect the larger nanopillars to be easier to replicate than 100 nm high nanopillars. However, the replication of the micropillars with nanopits on top does not work well with Sylgard 184 PDMS. The area of micropillars is larger than the area of nanopits, so that an area of micropillars without nanopits surrounds the area with nanopits. The micropillars surrounding the area with nanopits replicated well while the micropillars in the area of the nanopits are cut in half (Figure 6.7C).

A look at the master stamp after replication reveals that a narrowing occurs in the middle of the pit. This narrowing works as a breaking point to rip the micropillar in half. One can see in Figure 6.7D that the lower half of the micropit is filled with remaining PDMS, while the PDMS has demoulded at the top half. Since this effect is only observed in the area of the nanotopography, we believe that a light interaction of the nanopillars with the UV-light causes the effect. Nanopillars are known for their unique optical properties, and the light reflection can be expected to be significantly different to the light reflection from a flat silicon surface. Some pillars are still replicated well and show that the nanotopography is also replicated (Figure 6.7B). The remaining PDMS in the master stamp on top of the nanopillars shows that the PDMS covers the nanopillars. However, the nanopillars are not fully immersed in the PDMS, so they do not replicate nanopits with a sharp edge at the

top, but with a round edge. The replicated nanopits should still be replicated well enough to affect cell adhesion. It should also be noted that SEM imaging of the nanopits on top of the micropillars is challenging since the soft PDMS tends to melt under a high imaging current, and the contrast of the nanopits is low. Thus, one must find a compromise between a high enough current to be able to image the low contrast of the nanopits and a low enough current not to damage the PDMS too much.

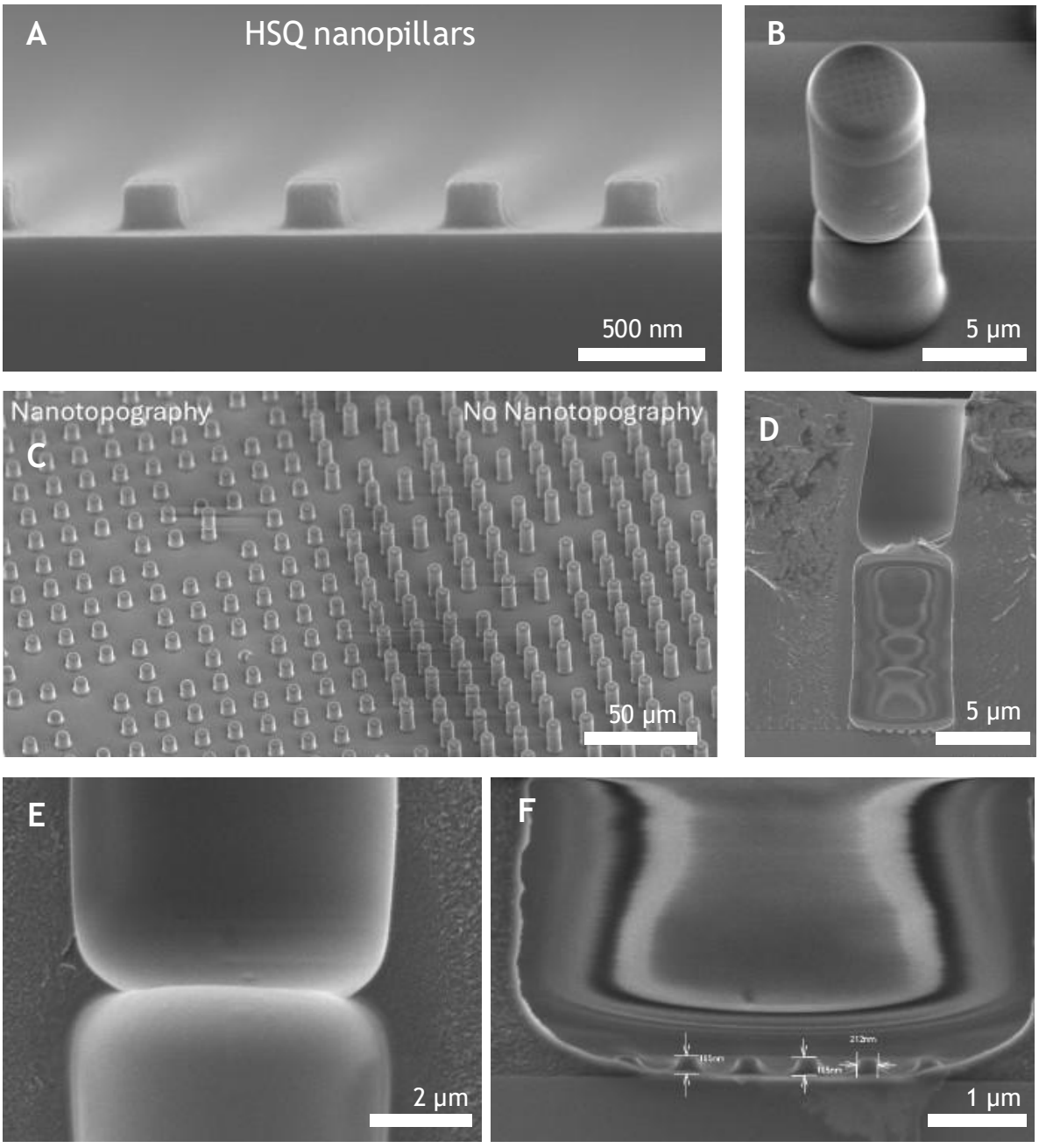

(caption for figure on previous page) ***Figure 6.7****: Fabrication of large micropillars with nanopits using SU-8 resist and photolithography. The used HSQ nanopillars are 200 nm high and 220 nm in diameter (A). When replicating 6 µm diameter micropillars in 18 µm thick SU-8 resist with nanopits on top in Sylgard PDMS, only the area without nanotopography replicates well (C). The nanopillars in the SU-8 master cause an interference with the light that create a narrowing in the centre of the hole (D,E). Thus, the top part of the PDMS pillars get stuck inside the SU-8 master mould. The few micropillars that are fabricated replicate the nanopits (B). The nanotopography replication does not work perfectly as the soft Sylgard PDMS surrounds the nanopillars but cannot create a sharp replication (F). All SEM images are taken with a Hitachi scanning electron microscope of the SU8200 series.*

6.5. Traction force microscopy of MC3T3 cells on 6 µm micropillars

The micropillars with nanopits on top do not replicate well, but the micropillars without nanopits with a height of 18.61±0.28 µm and a diameter of 5.93±0.15 µm, that are shown in Figure 6.6B, can be used for pillar-based traction force microscopy. 5 µm micropillars are widely used in pillar-based traction force microscopy, but they are often used with a spacing of 10 µm from centre-to-centre. Our micropillars have a centre-to-centre spacing of 15 µm. A simple pillar traction test with MC3T3 cells may not yield new biological information, but it will provide us with helpful insights. It will tell us if the design of 6 µm diameter pillars with a large centre-to-centre spacing provides enough adhesion area for the cells to adhere to the top of the pillars and not between the pillars. Additionally, it will show if the autofocus on top of the pillars for the cell traction works and if the pillar deflections can be detected for this type of micropillars.

6.5.1. Micropillar preparation for traction force microscopy

The micropillars are prepared in 35 mm MatTek glass bottom dishes. Cells do not like to adhere to PDMS. Thus, the surface needs to be treated to increase cell adhesion. Fibronectin is widely used to increase cell adhesion to non-adherent surfaces. We do a fibronectin contact printing to ensure that only the top of the pillars is fibronectin coated. A fibronectin-FITC (fluorescein isothiocyanate) (MERCK, F2733-1ML) is used to be able to visualize the fibronectin coating. For the fibronectin contact printing, the stamp is fabricated by first preparing a PDMS stamp. Sylgard 184 PDMS is prepared as described above and filled into a petri

dish at approximately 5 mm height. After curing in an oven at 70° C for 10 hours, the PDMS slabs are cut with a scalpel into the desired format. One wants the stamp to cover the array of micropillars, but not bigger than the array, to ensure good contact printing. In our case, the array is around 15x15 mm big. The PDMS slab is cleaned in ethanol in an ultrasonic bath for 5 minutes and dried with a nitrogen gun. The fibronectin-FITC is prepared at a concentration of 60 µg/ml in RO water. 100 µl of the fibronectin-FITC solution is placed on the PDMS stamp and incubated at room temperature in the dark for 1 hour. The fibronectin is carefully removed with a pipette from the side and blown dry with nitrogen. The PDMS stamp is now ready to use. The micropillars are activated by oxygen plasma treatment at 80 W for 1 minute. Next, the PDMS stamp with fibronectin-FITC is carefully placed on top of the micropillars and slightly pressed down for 30 seconds. The contact printing must be carried out extremely carefully to ensure that the micropillars are not damaged. Movement of the stamp while it is in contact with the pillars causes them to collapse.

After fibronectin contact printing, we passivate the rest of the pillar array by incubating the micropillars in 3 % BSA in PBS for 1 hour in the dark at room temperature. To only use the area in the MatTek dish with micropillars, we use ibidi 2-well culture inserts that are placed on top of the micropillars and create two wells on the micropillars with a culture area of 0.22 cm2. After incubation with BSA, the micropillars are washed 6 times with PBS. While washing, it is essential to ensure that the micropillars are always covered with liquid. When the pillars dry out they collapse due to surface tension forces. After washing with PBS, the pillars are washed at least three times with the culturing media to ensure that PBS does not dilute the culture media. 4000 MC3T3 cells/cm2 are seeded on the micropillars and incubated overnight at 37° C, 5 % CO2 and 95 % humidity.

The fluorescent fibronectin coating is imaged with Zeiss Observer with a Colibri 7 LED light source. The FITC is excited with a 475 nm LED at 100% light intensity and imaged with a Zeiss N-Achroplan 63x objective. The pillars are stained well, and one can clearly see the outline of the pillar tops (Figure 6.8A). To determine if only the pillar tops are stained, we perform a z-stack analysis using a Zeiss LSM 800 confocal microscope. The FITC is excited using a 488 nm laser and an EC Plan-Neofluar 40x objective. The z-stack is performed at 530 nm per step over a depth

of 22.26 µm and shows that the fluorescence is confined to the tops of the micropillars. It is not a perfect contact printing, since the side of the pillars is also coated at the top of the micropillars. No fluorescence is visible at the bottom of the pillars and between the pillars. Thus, the cells are expected to attach only to the top of the pillars (Figure 6.8B+C). Thus, we can assume that the MC3T3 cells will only attach to the top of the pillars.

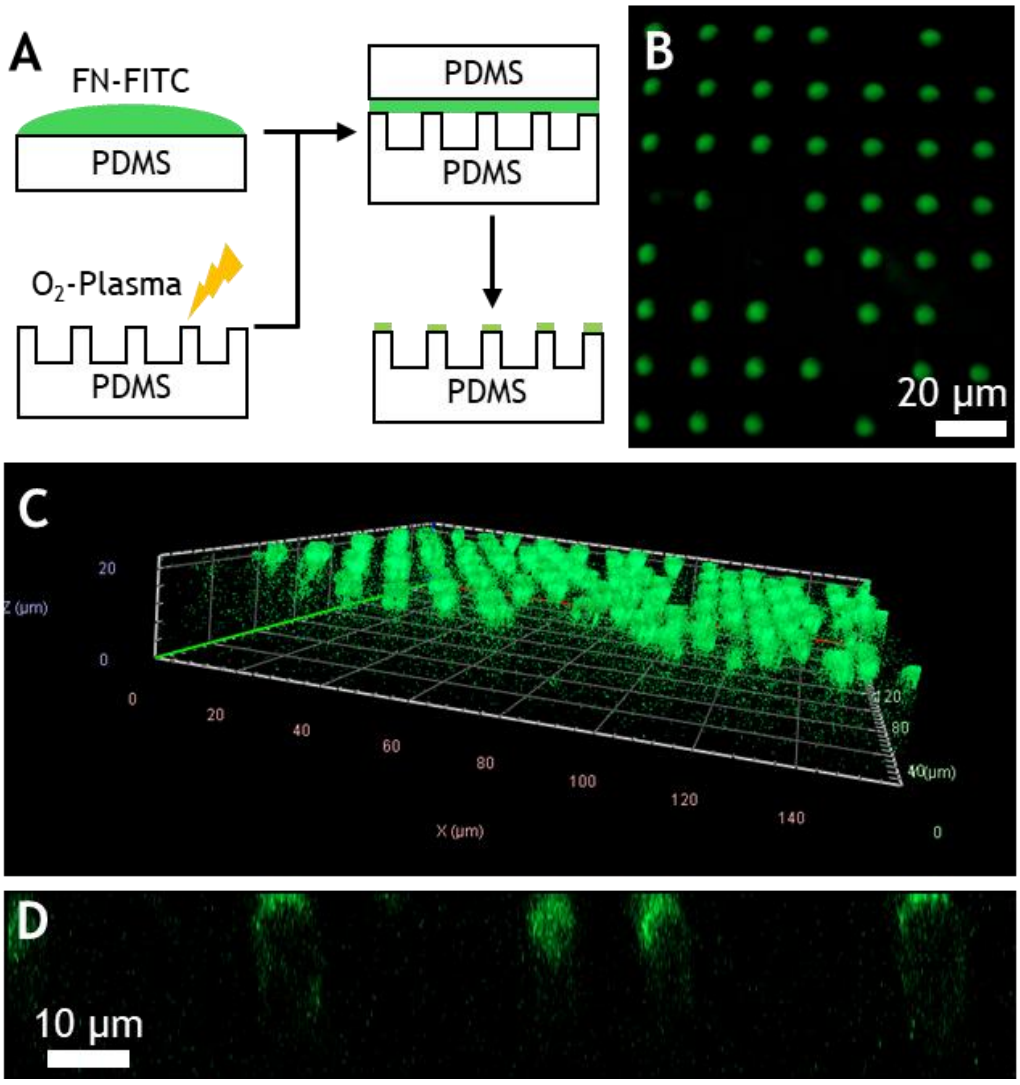

***Figure 6.8**: Contact printing of fluorescent fibronectin-FITC on 18.61±0.28 µm high PDMS micropillars. A PDMS stamp is incubated with fibronectin-FITC (FN-FITC) and broad in contact with oxygen plasma activated micropillars for the contact printing (A). Fluorescent images of flat micropillars coated with fluorescent fibronectin-FITC by contact printing. Fluorescent images taken from the top are taken with Zeiss Observer microscope and a 63x objective (B). A z-stack proves that the fibronectin-FITC coating is only around the top of the pillars (C). The cross-section of the staining shows that the first few micrometer on top of the pillars are coated with fibronectin (D). The z-stack is taken using a Zeiss LSM 800 confocal laser microscope.*

6.5.2. Performing pillar-based traction force microscopy

The pillar traction microscopy is performed on a Zeiss Observer with a Zeiss Colibri 7 LED light source and a Zeiss N-Achroplan 63x objective. An on-stage incubator that keeps the sample at 37° C, 5 % CO2 and 95 % humidity. Twelve positions are imaged per sample, and the tracking is done for 2 hours with an image every minute. After placing the sample on the incubated stage, we wait for 10 minutes to let the incubator and stage settle. The adjustment in temperature and humidity causes a drift of the stage. Even after the incubator has reached the working conditions and the stage has settled a slight drift is still visible over a time frame of 2 hours. Furthermore, is the micropillar surface never completely level. Therefore, an automated focus is needed. We use the in-build autofocus that finds the position of best contrast.

The images are collected in the CZI format of Zeiss and exported as TIFF images without compression. The pillar deflection is analysed in Fiji ImageJ[317]. An overview of the pillar traction analysis is shown in Figure 6.9. First, the time series is loaded into ImageJ as an image stack, and the image stack is checked for out of focus images that are deleted from the stack. Next, the image stack is rotated to make square array level in the image. The microscope stage is often drifting over time. Thus, it needs to be corrected for the stage drift. The correction is performed by the *MultiStackReg* function of the *Registration* plugin. The created stack is used as the only stack and *Align* is used as Action 1. The transformation is performed using the *Rigid Body* method. After checking if the registration is successful and the pillars are not drifting over time, the image stack is cropped to the interesting area, and the pillar traction is performed. The *PillarTracker GUI* function of the *MBI-PillarTracker* plugin is used for pillar traction.

First, the pixel size is set to 103 nm per pixel. Next, the pillar diameter is set to 59 pixels, the pillar spacing is set to 146 pixels, and the grid is set to 90 degrees as the micropillars are in a square array. First, a Gaussian curve fit for the pillars is defined by drawing a line across a representative pillar and calculating the Gaussian sigma in pixels. Make sure that the curve fit is fitting over the centre of the pillar and not a peak in intensity at the edge of the pillar. Different curve fits are tested by changing the drawn line until a good fit is achieved. Afterwards, a

fast Fourier transform (FFT) is performed, and maxima of the FFT are selected that are used to do an inverse FFT to create a mask. At the inverse FFT, the off-centre mask radius and centre mask radius are kept at 5. The inverse FFT is checked to ensure that it functions as a reference image, where the cells are not visible, and the pillars are clearly visible with a good contrast. If that is not the case, the number of maxima selected needs to be changed until a good inverse FFT mask is created. Next, pillars are detected by clicking on *Fast Detect Pillars*. The pillar detection is checked that the pillars are detected and that they are detected at the centre of the pillar and not the edge of the pillar. When the pillar detection was successful, the pillar traction can be performed by navigating to the *Tracking* tab and selecting the stabilised image stack. This step takes the calculated values from the previous steps, and therefore, no adjustments are needed here. By clicking on *Track & Optimise,* the pillar traction is performed, and the output is saved in a bin file as well as an Excel file. The Excel file is used for further analysis.

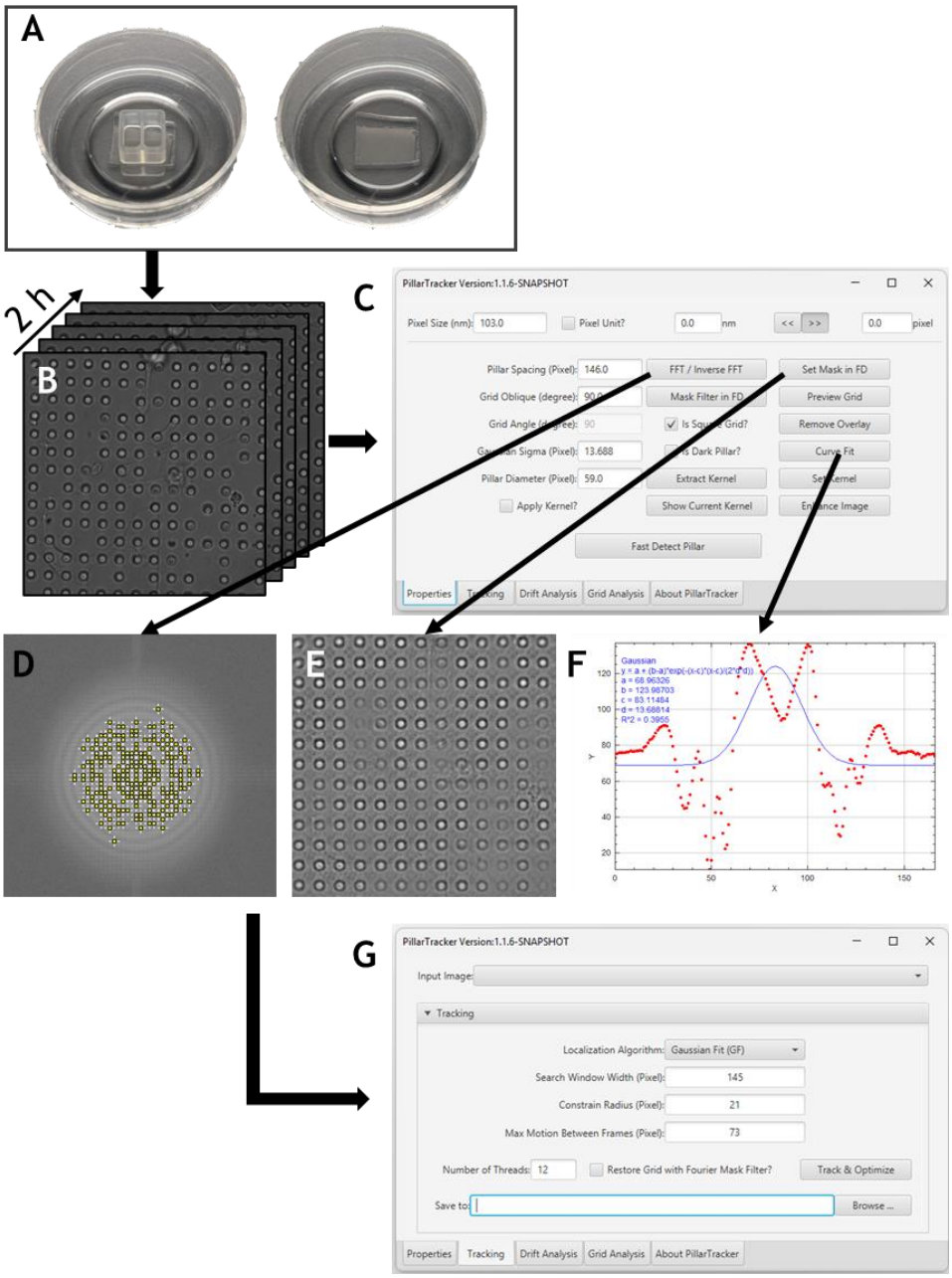

***Figure 6.9**: A schematic representation of the pillar based traction force microscopy process. The micropillars are prepared in a glass-bottom MatTek dish and an ibidi 2 well insert is used to confine the cells to the micropillar area. After traction force microscopy for two hours the images are analysed in ImageJ using the MBI-PillarTracker plugin. The pillar detection is prepared by a Gaussian fit to the micropillar (F), a FFT (D), and an inverse (FFT) to create a mask for the final pillar traction (G).*

In the output file, the pillar deflection of each pillar at each frame (time point) is given. The pillars are numbered, and we must select relevant pillars first before we can analyse the measured pillar deflection. The created bin file can be loaded into the *Grid Analysis* tab, and the pillar deflection is visualised with arrows and overlayed on the microscope images. We manually select pillars that touch the cell and where a change in deflection is measured over time, without extreme

deflection outliers that are due to traction errors. The pillar deflection is measured in the change of x and y coordinates. The length of that vector is calculated by using equation (11) with dx being the deflection in x direction, dy the deflection in y direction and Δxy the total deflection.

$$\Delta xy = \sqrt{dx^2 + dy^2} \tag{11}$$

The total deflection in pixels is then transformed into m using the pixel size of 103 nm of the used microscope. From that deflection the exerted cellular traction forces can be calculated using Hooks law. We use micropillars of 5.93±0.15 µm diameter and 18.61±0.28 µm height with Sylgard 184 PDMS with a Young's modulus of 2 MPa. Using equation (4) with those micropillar dimensions means that we have pillars with a spring constant of 0.0574 N/m. This corresponds to a shear modulus of 4.67 kPa using equation (1). We measure the deflection of the pillars over a time frame of 2 hours. We calculate the mean deflection of each pillar over the whole time frame to get the mean deflection over time. The standard deviation of the pillar deflection over time is also calculated and plotted.

6.5.3. Results of traction force microscopy of MC3T3 cells

While performing the pillar based traction force microscopy, we notice that the autofocus of the microscope focuses on two different focus planes (Figure 6.10A). It either takes the top of the pillar in focus, which results in pillars with a bright spot in the centre and a sharp border. Alternatively, it focuses on the pillars on top of the pillars. In that case, the pillars are slightly out of focus, have a more uniform dark appearance and a ring around the pillar. This makes the Gaussian fitting more challenging. It often tries to fit in the bright spot between the ring around the pillar and the dark pillar, rather than at the centre of the pillar. To ensure a good pillar detection we must force the Gaussian fit to be broad enough to detect the pillar and not the bright spot next to it. The focus on the pillars also presents its challenges in pillar detection. We are using the ibidi 2 well inserts to force cells onto the micropillar array. However, when imaging close to the wall of the well, it affects the light, and the bright spot is not in the centre of the pillar but instead at the side of the pillar, close to the wall. If the bright spot is too far at the edge the pillar detection detects the pillar at the edge of the pillar. When

the cells are moving along those pillars, the light at the edge of the pillars is affected, and we only pick that effect up and not the pillar deflection. Thus, it might be better not to use the ibidi 2-well inserts in the future to avoid those artefacts. Many more cells are needed in that case, but for the use of cells like the analysed MC3T3 cells that are available in abundance, it is no issue.

The cells spread on the micropillars and touch the micropillars. However, compared to smaller pillars and shorter centre-to-centre spacings, the cells pull on a few pillars, which may affect the cellular traction forces as the forces are combined at a few positions and are not spread evenly across the cell. The missing pillars due to errors in the negative photomask copy are also causing some challenges. It creates space that allows cells to spread, which is mostly avoided by passivation with BSA. The gap also restricts cell movement, as larger gaps between the pillars need to be bridged by the cells. Furthermore, the missing pillars impact the quality of the FFT. The FFT depends on periodicity, and we already have few pillars in one image with several bright spots due to their large size. The missing pillars are also breaking with that periodicity. The mask creation and pillar traction are still working well, but it could be improved by a complete micropillar array without gaps.

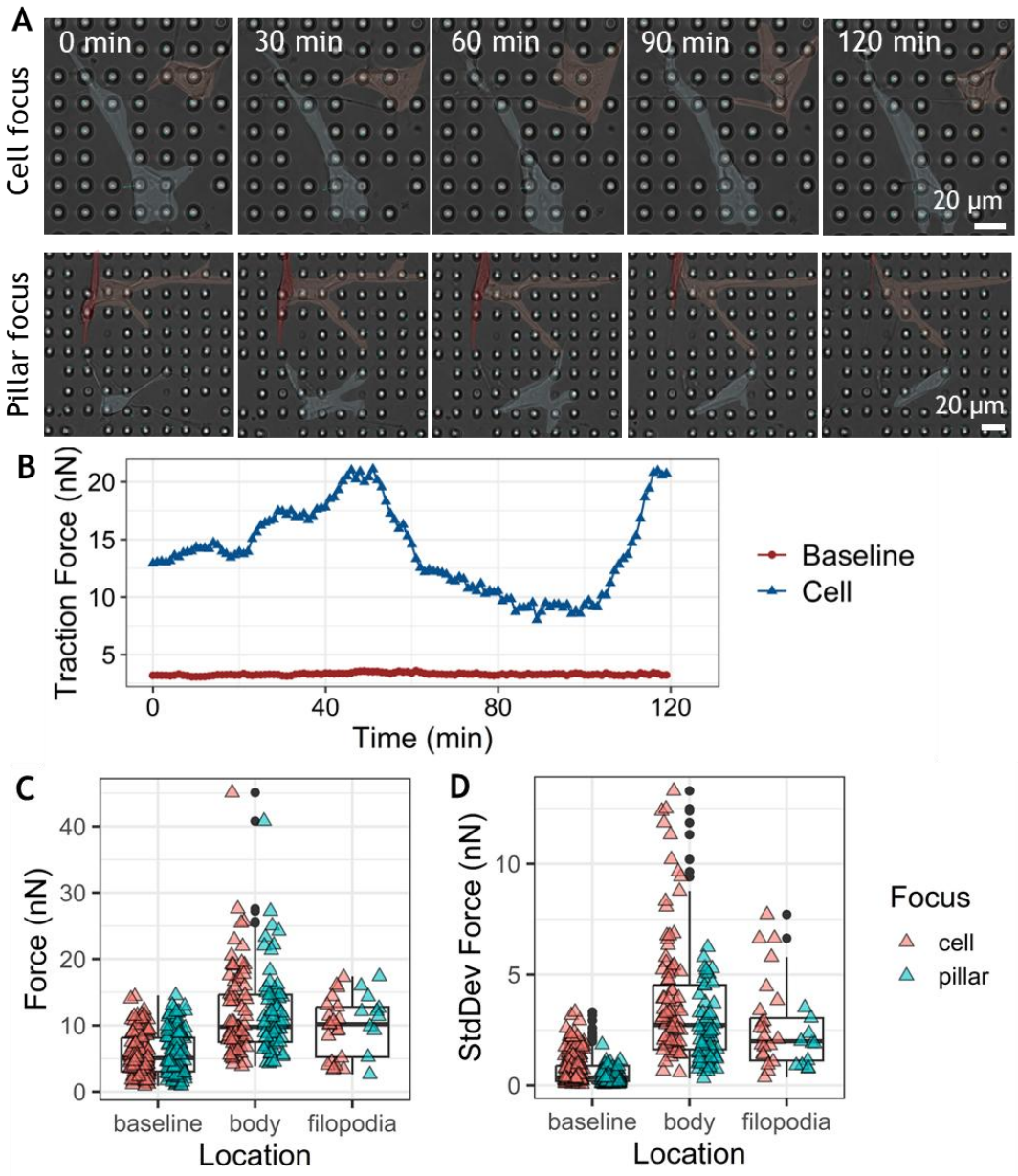

***Figure 6.10**: Force traction microscopy of MC3T3 cells on 6 µm diameter and 18 µm height micropillars. The cellular traction force is recorded over 2 hours using a Zeiss observer microscope and a 63x objective. The autofocus of the microscope focuses either on the pillars or the cells on top of the pillars (A). An example of the pillar traction force applied on a pillar touching a cell and not touching any cells (baseline) over 2 hours is plotted (B). The two pillars a selected from the same position that has a focus on the pillars. The measured traction force is divided in pillars touching the body of the cell, touching the filopodia and not touching the cells as a baseline (C). The cells are highlighted in the images for better visibility. The higher outliers are only visible in the pillars touching the cell body. Each data point is the mean force of one pillar over two hours. While the baseline still has strong reflections the reflections are more static as the plotted standard deviation of each pillar over two hours shows (D). A focus on the pillars improves the baseline and therefore the pillar tracking.*

When calculating the traction forces, we separate the pillars into three groups: pillars touching the body of the cell, pillars touching the filopodia of the cell and pillars not touching the cell, which we use as a baseline. Furthermore, we plot

the differences between the focus on the pillars and the focus on the cells to check if both focus points are working for the pillar traction. First of all, the measured mean cellular traction forces for the body of the MC3T3 cells and the filopodia are around 10 nN, which agrees with the reported traction forces of MC3T3 cells in the literature, as mentioned above[19].

However, the baseline of the mean pillar deflection reaches a similar force to that of a large part of the pillar deflections due to cellular traction forces. When examining the vector of the baseline pillar deflection, it becomes apparent that the measured pillar deflections are constant in one direction. This is reflected in the standard deviation of the pillar deflection over time. It is a measure about the activity of the pillar overtime, and the baseline shows clearly less changes over time than the pillars that are touched by the cell or filopodia. This means that we have a good baseline of pillar movement over time, and we do pick up the pillar deflections because of the pulling of the cells on the pillars.

When comparing the cellular traction forces of the cell body and the filopodia, we can see that the mean traction forces show no significant difference. The filopodia and the body of the cell exert the same average forces on the pillars. However, the outliers of large traction forces are only in the traction forces of the body of the cell, which means that the body of the cell can exert larger forces than the filopodia or more false pillar deflections are measured. When comparing the traction forces depending on the focus position, we can see that the focus on the cells has more outliers. Especially, the difference in the standard deviation of pillar deflection over time highlights the better performance of the pillar traction when the pillars are in focus. The baseline pillars have low activity, and the pillar deflections of pillars on the cell have fewer outliers and are closely packed. This means that the pillar detection is more accurate when the pillar is in focus and not the cells.

6.6. Conclusion

The fabrication of hierarchical micropillars with nanopits on top in PDMS has proven challenging. The best fabrication results are achieved using SU-8 resist with photolithography to produce the master stamp. High aspect ratio micropillars with a diameter of 5.93±0.15 µm and a height of 18.61±0.28 µm in a square array with centre-to-centre spacing of 15 µm are successfully fabricated and used for pillar-based traction force microscopy. The measured traction forces are in the area of 10 nN, which was reported before in literature for MC3T3 cells. Thus, we are confident that this pillar design and our setup can correctly measure pillar deflections due to cellular traction forces.

The fabrication of the hierarchical micropillars with nanopits is challenging because we are moving on the edge of what is possible at several steps during the fabrication process. The fabrication of nanofeatures of 100 nm in HSQ using e-beam lithography is widely done. However, the replication of those features is in the resolution limit of soft lithography processes using PDMS[293]. To replicate nanofeatures smaller than 200 nm, h-PDMS was developed, which can effectively replicate nanostructures. However, it comes with several disadvantages for our application. The fabricated micropillars in h-PDMS are brittle and tend to break more easily. Furthermore, they tend to be more impacted by an undercut in the master stamp as they are stiffer and cannot deform as much as the soft Sylgard 184 PDMS while demoulding. A composite stamp of h-PDMS and soft Sylgard 184 PDMS is also needed for the fabrication of the micropillars of h-PDMS. The soft underlayer of the micropillars affects the mechanics of pillar bending and complicates the calculation of the correct spring constant for force calculations. A simulation of the pillar bending with the material properties is likely necessary to obtain the correct spring constant. Thus, we need to consider if we want to replicate 100 nm large nanostructures and have more challenging micropillars to work with or have larger nanostructures and the simple Sylgard 184 PDMS micropillars. We have shown in the previous chapter that increasing the nanopit diameter from 100 nm to 500 nm does not have a significant impact on the cell response. Therefore, we decide that it is a better route to create 220 nm diameter nanopillars that replicate in soft PDMS and still affect the cell adhesion.

The fabrication of 10 μm deep holes in PMMA by e-beam lithography is clearly above the usual applications that are only up to a few microns deep. The fabricated holes for the creation of micropillars are not good enough for our application. The scattering of secondary electrons in the resist and the conical shape of the electron beam are affecting the side profile of the pits too strongly[302, 303]. However, we have shown that we can spin 10 μm thick PMMA resist and do e-beam lithography with it without cracking of the thick resist or resist swelling during development by developing in 7:3 IPA:water developer, that is known to improve the contrast and sensitivity compared to MIBK based developers[318], and using a charge dissipation layer of Electra 92. This is an entirely novel fabrication technique that overcomes the size limitations of conventional e-beam lithography procedures with PMMA. Even though, the sidewalls are not straight enough for our application it can be still a valuable method for the fabrication of high aspect ratio micropatterns of 2 or 3 μm width where photolithography can struggle.

The resolution limit of standard photolithography by contact and proximity printing is often mentioned to be around 2 μm sized features[310, 311]. The resolution can be largely improved by projection photolithography to few tens of nanometers[76]. However, it is challenging to achieve photolithography on that scale with a high aspect ratio in practice. Thus, our desired topography lies at the lower limit of the resolution limit of photolithography and above the resist thickness used in PMMA e-beam lithography. SU-8 performed best to create the needed micropits as it can produce straight sidewalls at high aspect-ratio. The contact between mask and resist is essential for a high-quality photolithography process in SU-8[313], especially for the fabrication of narrow trenches or pits. Zhang et al.[319] improved contact by applying a soft cushion beneath the sample to enhance resist-mask contact. This enabled the fabrication of 8 μm wide trenches in 145 μm thick resist. However, since it is a negative-tone photoresist, it makes the fabrication of micropits more challenging. Since photolithography of negative photoresists works by UV-light cross-linking the resist, and nanopillars have unique interactions with light and reflect light differently than flat silicon, we still struggle with fabricating a master stamp for the creation of hierarchical micropillars with nanopits at the top. Currently, we are attempting to use the

positive photoresist AZ4562 with a maskless laser beam lithography tool for fabrication, with the assistance of Yuyan Liu at the Technical University of Denmark. We hope that the lack of a mask reduces the effects of reflections. Furthermore, we expect a smaller effect of the light interference of the nanopillars in a positive photoresist as the UV-light exposes less area of the sample.

The successful fabrication of hierarchical micro-/nanostructures differs from our approach. Most applications have larger features and not as high aspect ratios as our application, like the work of Alameda et al.[177]. The work of Cheng et al.[19] has a similar application to our work and can therefore be well compared. They fabricate the high aspect ratio pillar master by reactive ion etching, which is widely used in high aspect ratio micropillar fabrication, as it can etch straight sidewalls with aspect ratios higher than 1:5. To use reactive ion etching for the fabrication of hierarchical structures, the nanotopography needs to be on the top of the surface and not the bottom. Thus, a double replication process is needed that involves a PDMS to PDMS replication step. We tested a PDMS to PDMS replication as well by fabricating 2 µm diameter SU-8 micropillars with a height of 6 µm and replicating them in PDMS that one obtains a PDMS mould with 2 µm diameter pits. The PDMS mould is silanised the same way we normally silanise our samples, and a PDMS replication is done. Replication is not possible because the PDMS samples are not demoulding well from each other. Cheng et al. used a critical point dryer after their demoulding process which is essential and not available to us. The PDMS to PDMS replication is also known to be challenging, as PDMS strongly binds to PDMS.

The combination of micropillars of varying heights and different nanopit arrays would enable us to combine the effects of material stiffness and nanotopography. Both are known to affect cell adhesion[102, 259, 275], and they have been rarely studied in combination[280-282, 320]. All studies so far have fabricated nanotopographies of varying stiffness by altering the material's chemical composition. However, the chemical composition of the biomaterial affects cell response, as shown by Anderson et al. in an extensive library of 1,728 different chemical compounds[245]. The hierarchical micro-/nanotopography platform enables the study of the interplay between stiffness and topography without

altering the chemical composition of biomaterials. Micropillars of varying height have already been successfully used to measure the stiffness-dependent cellular traction forces of human mesenchymal stem cells[156, 157]. The stiffness of the pillars affected cell morphology, traction forces, focal adhesions and differentiation. We aim to determine whether one of the two properties dominates the cell response and whether the cell response to the different topographies changes similarly across different material stiffnesses.

7. Summary and Outlook

We have collected and analysed an enormous amount of data in this work. We collected fluorescence images of 53 different conditions in Chapter 4 and 84 different conditions in Chapter 5. We have a total of 137 different conditions and more than 8540 fluorescent images with four channels. On average, we have five cells per image. Thus, we have analysed more than 42700 cells. To highlight the magnitude of the data collected, we can calculate the total continuous imaging time required, with an imaging time of approximately 4.5 minutes per image. We require 640.5 hours of continuous imaging for the entire dataset, which is approximately 64 working days, assuming a standard working day of 10 hours.

In this thesis, we have analysed the cell response of MC3T3 cells to nanopits and gratings using only fluorescence microscopy. Our unique approach involves the use of the Cell Painting method developed by Carpenter et al for the first time in morphological profiling of the cell response to nanotopographies. This work serves as a strong proof-of-concept, demonstrating that the clustering of mechano-transduction pathway inhibitors and activators in the UMAP plot accurately represents the known functions of these molecules in the pathways. The ROCK, myosin II, and actin inhibitors cluster together, as do the corresponding activators. Metabolites that mimic intracellular tension and adhesion on nanopits also cluster with the cells after four days on nanopits. These observations underscore the reliability of mapping morphological profiling data in a UMAP plot.

We successfully used the Cell Painting assay to observe the time-dependent response of MC3T3 cells to nanopits in SQ, NSQ, and HEX arrays. The first response to the nanotopography is dominated by the calcium signalling, which increases the expression of the early osteogenic marker Runx2 through the MAPK pathway. After four days, the cells have adapted to the nanopits and the intracellular tension and adhesion are decreased. The oxidative glycolysis is increased at this stage. After seven days, the cells are in senescence and have fully committed to the differentiation process into mature osteoblasts. The cells show decreased filopodia and lamellipodia formation as they cluster with the Cdc42 and Ras/Rac inhibitor.

Our morphological profiling using Cell Painting has also demonstrated high sensitivity, as well as a comprehensive understanding of the cell response to nanotopographies. We have not only differentiated between inhibitors and activators but also shown concentration dependency and differences in nanotopographies. We analysed the morphome of MC3T3 cells on 84 different nanotopographies, ranging from changes of 5 nm up to changes of micron size. Most topographies used in this work are nanopits that vary in size, pitch, and orientation to each other, as they are in ordered square and hexagonal arrays or with varying disorder. Additionally, we have used gratings with a size of 200 nm, 500 nm, 1 µm, 2 µm, 5 µm and 10 µm, providing a comprehensive view of the cell response to various nanotopographies.

The nanotopographies and especially the different geometries of nanopits produce a cellular response following the same mechanotransduction pathways. Only the details in the strength of the responses differ. Therefore, the change in the morphome is also minimal. The imaging and staining are performed in different batches on different days, which produces a batch effect. Compared to the slight differences in morphology due to minimal changes in topography, the batch effect is relatively large. Thus, a good batch correction is needed to analyse this dataset. The Seurat method, a state-of-the-art batch effect correction method developed for batch effect correction in scRNA-Seq[139, 144, 145], has proven to be most successful. We get rid of most of the batch effect while retaining the biological information, as the correct clustering of the activators and inhibitors shows.

Five parameters fully describe the topographies: the x-pitch, y-pitch, diameter, noise, and offset. Our goal was to create new topographies based on those parameters and their correlation with the morphome. This was an extremely ambitious goal because we want to pick up minimal changes in cell morphology systematically and correlate them to the geometry parameters, which are in turn correlated to each other. Typically, prediction in machine learning is achieved by training a dataset and using the trained model to predict to which category the new dataset belongs. We are not interested in categorising new data into one of the existing nanotopography categories but instead want to treat the geometrical parameters as continuous values. Suppose we have a cell that is altered, for example, by incubation in induction media. How must the nanotopography look to

obtain the same morphology without limitation to the observed topographies? We are not able to perform this prediction due to its complexity. Each topography does not cause a specific change in the morphome, but each parameter affects the whole morphome. Additionally, the cell response strongly depends on the available adhesion area, and changes in the parameters affect it similarly. For example, a decrease in pitch might decrease the adhesion area similarly to an increase in disorder. Thus, all topography parameters must be analysed simultaneously if we want to study the entire library. An addition of nanopillars in similar geometrical arrays would also improve the nanotopography library as it completes the topographies.

It is possible to separate the parameters and only study the datasets with changes in the separated parameters. The disorder has the strongest correlation to the morphological changes between the different nanopit arrays. Thus, we find that disorder is the decisive factor in the cell response. No distinct continuous trend in the disorder is observed. We only see that the high disorder of 120 to 150 nm clearly separates from the remaining cells. Curiously, the disorder of 60 nm and 70 nm produces a similar morphome. The pitch and size affect the morphome only slightly, and no similarities are observed between the pitch variations of SQ arrays and NSQ arrays. The gratings have a distinct effect on the cells as they align with the gratings. Thus, a high correlation is observed between the morphology and the width of the gratings. The gratings need to be smaller than 5 µm to affect the cells.

To overcome those challenges, much work must be done. A larger dataset would be beneficial for any machine learning approaches. The slow speed of the LSM currently limits our imaging. A change to a widefield microscope would be beneficial. First experiments with a Zeiss Observer with a Colibri 7 LED-Lightsource showed promising results with an imaging speed of less than 30 seconds instead of more than 4 minutes per image for the LSM. This offers the option of thousands of cells per condition instead of hundreds, which will be helpful for training in machine learning. However, it is not possible to separate the membrane and Golgi staining from the actin staining in this microscope setup, and they need to be in one channel, as in the original Cell Painting protocol. The

imaging of the mitochondria stain, MitoTracker Deep Red, worked well with that microscope and can be added to gain more information about the cell state.

We are confident in our results and the proposed mechanotransduction pathway over time. However, verifying our findings with conventional omic techniques, such as proteomics, would significantly enhance our work. It would be beneficial to obtain proteomics data for each identified group from one of the activators or inhibitors, as well as the nanotopographies at the corresponding time points. This data could validate the morphological profiling and provide more insight into the state of the cells at those time points.

The proteomic analysis could also be taken to the single cell level with DESI mass spectrometry. In this work, we have not taken advantage of the single-cell character of morphological profiling. A single-cell analysis, considering heterogeneities in the cell culture, can likely improve the analysis. Morphological profiling has already been used to predict gene expressions of MC3T3 cells on nanopits in SQ, NSQ, and HEX arrays. However, the mean of single-cell data is used to predict the batch gene expression. With DESI mass spectrometry, the single cell morphome can be matched with the protein expression of the corresponding cell[127]. This approach holds the potential to enhance our understanding of how intracellular processes influence cell morphology and to improve predictions based on the morphome.

Initial tests with the grating slides for DESI measurements have been conducted, but they have not been successful so far. The tool requires samples in a slide format that allows the nozzle for electrospray and the inlet to the mass spectrometer to be positioned close to the cells. Thus, the PS slides are not ultrasonically welded but taped to the bottom of the 24 well plates using an adhesive double-sided Microfluidic Diagnostic Tape 9965 (3M, US). After four days of cell incubation, the cells are stained using the Cell Painting protocol and then washed with RO water to remove any ions from the surface. The slides are pried off, dried by vacuum desiccation for 1 hour and kept in a -80° C freezer until use. We prepare slides with stained cells and with cells that are not stained. Mark Towers attempted the DESI analysis at Waters™ (UK). However, several challenges occurred. The adhesive tape leaves a glue residue on the slide that physically

hinders the sprayer and melts due to the heat from the source and inlet, contaminating the inlet and DESI spray. The stained cells have a high polymer signal that we believe comes from TritonX-100. Thus, to perform DESI measurements with the slides, they cannot be in the well plate format, and no staining is possible. The slides can be incubated in a well plate, but in that case, crosstalk between the cells on different topographies exists as they share the same media.

To avoid staining, the Cell Painting staining can be predicted from brightfield images. Cross-Zamirski et al. have proven that the Cell Painting staining of U-2 OS cells can be predicted using U-net and a generative adversarial network (GAN)[231]. The prediction of Cell Painting staining can also be helpful for analysing cell responses to nanotopographies over time. At the current approach, for every time point, a new sample is needed because the cells need to be fixed for the staining procedure. By using live cell images, one sample can be imaged at many time points and the time-dependent response to topography can be analysed in much more detail. It would even be possible to analyse the first response to the topography when seeding the cell and the dynamic adaptations to adapt to its surroundings, and how it affects internal processes by correlation to mechanotransduction pathway morphologies, and single-cell proteomics predictions.

It was not possible to obtain a complete understanding of the cellular response to the biomechanical environment because we were unsuccessful in fabricating hierarchical PDMS micropillars with nanopits on top. As a result, we could not study the effects of different nanotopographies on cellular traction forces or the interplay between material stiffness and topography. Despite not achieving our initial goal, we gained valuable insights into the lithography process at the resolution limits of e-beam lithography and photolithography.

We developed a novel protocol for performing e-beam lithography using a 10 µm thick PMMA resist to create micropits with a diameter of 4 µm. Although these micropits were not suitable for our specific application, the process may still be beneficial for other uses where a thick resist is necessary for fabricating micron-sized elements with high precision.

Photolithography using SU-8 resist has proven to be the most promising technology for creating high-aspect-ratio micropillars with nanopits on top. We successfully fabricated PDMS micropillars with a height of 18.61±0.28 μm and a diameter of 5.93±0.15 μm from a SU-8 master stamp through soft lithography. However, generating a master with nanopillars remains challenging due to their interference with UV light, which necessitates further investigation. A maskless photolithography approach using a UV laser writer and a positive-tone AZ4562 photoresist may reduce this light interference enough to create the desired mask. Additionally, using a maskless photolithography tool allows for easier changes to design parameters.

In our pillar-based traction force microscopy tests with micropillars of 6 μm diameter and MC3T3 cells, we found that tracking the forces would likely improve with a smaller diameter and a centre-to-centre spacing of twice the diameter instead of three times. This design would allow the cells to spread out over more pillars and exert force on them, thereby improving the statistical analysis per cell and enhancing cell adhesion. We observed that only a few cells had pillars located at their centres; most were only in contact with the pillars at their outer edges. Therefore, a denser pillar array would offer a larger area for the cells to attach to. The traction force on the pillars would also likely improve with a denser array, as it increases periodicity and, consequently, the FFT. Furthermore, a smaller diameter would enhance the identification of the pillar centre by the traction software.

8. Bibliography

1. Singla, R., et al., *Nanomaterials as potential and versatile platform for next generation tissue engineering applications.* Journal of Biomedical Materials Research Part B-Applied Biomaterials, 2019. **107**(7): p. 2433-2449.
2. Krishna, L., et al., *Nanostructured scaffold as a determinant of stem cell fate.* Stem Cell Research & Therapy, 2016. **7**.
3. Nguyen, A.T., S.R. Sathe, and E.K.F. Yim, *From nano to micro: topographical scale and its impact on cell adhesion, morphology and contact guidance.* Journal of Physics-Condensed Matter, 2016. **28**(18).
4. Discher, D.E., P. Janmey, and Y.L. Wang, *Tissue cells feel and respond to the stiffness of their substrate.* Science, 2005. **310**(5751): p. 1139-1143.
5. Engler, A.J., et al., *Matrix elasticity directs stem cell lineage specification.* Cell, 2006. **126**(4): p. 677-689.
6. Diegelmann, R.F. and M.C. Evans, *Wound healing: An overview of acute, fibrotic and delayed healing.* Frontiers in Bioscience-Landmark, 2004. **9**: p. 283-289.
7. Vasudevan, J., C.T. Lim, and J.G. Fernandez, *Cell Migration and Breast Cancer Metastasis in Biomimetic Extracellular Matrices with Independently Tunable Stiffness.* Advanced Functional Materials, 2020. **30**(49).
8. Chen, S., et al., *Actin Cytoskeleton and Focal Adhesions Regulate the Biased Migration of Breast Cancer Cells on Nanoscale Asymmetric Sawteeth.* Acs Nano, 2019. **13**(2): p. 1454-1468.
9. Dahl, K.N., A.J. Ribeiro, and J. Lammerding, *Nuclear shape, mechanics, and mechanotransduction.* Circ Res, 2008. **102**(11): p. 1307-18.
10. Hoffman, B.D., C. Grashoff, and M.A. Schwartz, *Dynamic molecular processes mediate cellular mechanotransduction.* Nature, 2011. **475**(7356): p. 316-323.
11. Martino, F., et al., *Cellular Mechanotransduction: From Tension to Function.* Front Physiol, 2018. **9**: p. 824.
12. Misra, B.B., et al., *Integrated omics: tools, advances and future approaches.* Journal of Molecular Endocrinology, 2019. **62**(1): p. R21-R45.
13. Ramanan, V.K., et al., *Pathway analysis of genomic data: concepts, methods, and prospects for future development.* Trends in Genetics, 2012. **28**(7): p. 323-332.
14. García-Campos, M.A., J. Espinal-Enríquez, and E. Hernández-Lemus, *Pathway Analysis: State of the Art.* Frontiers in Physiology, 2015. **6**.
15. Bray, M.A., et al., *Cell Painting, a high-content image-based assay for morphological profiling using multiplexed fluorescent dyes.* Nature Protocols, 2016. **11**(9): p. 1757-1774.
16. Seal, S., et al., *Cell Painting: a decade of discovery and innovation in cellular imaging.* Nature Methods, 2025. **22**(2).
17. Vermeulen, S. and J. de Boer, *Screening as a strategy to drive regenerative medicine research.* Methods, 2021. **190**: p. 80-95.
18. Alameda, M.T., et al., *Hierarchical micro-nano topographies to control Bacteria and mesenchymal stem cells biological responses.* Scientific Reports, 2025. **15**(1): p. 25405.

19. Cheng, Y.J. and S.W. Pang, *Effects of nanopillars and surface coating on dynamic traction force.* Microsystems & Nanoengineering, 2023. **9**(1).
20. Cutiongco, M.F.A., et al., *Predicting gene expression using morphological cell responses to nanotopography.* Nat Commun, 2020. **11**(1): p. 1384.
21. Janmey, P.A. and C.A. McCulloch, *Cell mechanics: Integrating cell responses to mechanical stimuli.* Annual Review of Biomedical Engineering, 2007. **9**: p. 1-34.
22. Goetzke, R., et al., *Why the impact of mechanical stimuli on stem cells remains a challenge.* Cell Mol Life Sci, 2018. **75**(18): p. 3297-3312.
23. Wolfenson, H., B. Yang, and M.P. Sheetz, *Steps in Mechanotransduction Pathways that Control Cell Morphology.* Annual Review of Physiology, Vol 81, 2019. **81**: p. 585-605.
24. Sun, X.Y., et al., *Cell Motility and Nanolithography.* Three-Dimensional Microfabrication Using Two-Photon Polymerization: Fundamentals, Technology, and Applications, 2016: p. 335-344.
25. Allan, C., et al., *Osteoblast response to disordered nanotopography.* Journal of Tissue Engineering, 2018. **9**.
26. Dalby, M.J., N. Gadegaard, and R.O.C. Oreffo, *Harnessing nanotopography and integrin-matrix interactions to influence stem cell fate.* Nature Materials, 2014. **13**(6): p. 558-569.
27. Dobbenga, S., L.E. Fratila-Apachitei, and A.A. Zadpoor, *Nanopattern-induced osteogenic differentiation of stem cells - A systematic review.* Acta Biomaterialia, 2016. **46**: p. 3-14.
28. Hamouda, M.S., C. Labouesse, and K.J. Chalut, *Nuclear mechanotransduction in stem cells.* Curr Opin Cell Biol, 2020. **64**: p. 97-104.
29. Chen, Y., et al., *Receptor-mediated cell mechanosensing.* Mol Biol Cell, 2017. **28**(23): p. 3134-3155.
30. Teo, B.K., et al., *Nanotopography modulates mechanotransduction of stem cells and induces differentiation through focal adhesion kinase.* ACS Nano, 2013. **7**(6): p. 4785-98.
31. Dalby, M.J., et al., *The control of human mesenchymal cell differentiation using nanoscale symmetry and disorder.* Nat Mater, 2007. **6**(12): p. 997-1003.
32. Huang, J.Y., et al., *The relationship between substrate topography and stem cell differentiation in the musculoskeletal system.* Cellular and Molecular Life Sciences, 2019. **76**(3): p. 505-521.
33. Brown, X.Q., K. Ookawa, and J.Y. Wong, *Evaluation of polydimethylsiloxane scaffolds with physiologically-relevant elastic moduli: interplay of substrate mechanics and surface chemistry effects on vascular smooth muscle cell response.* Biomaterials, 2005. **26**(16): p. 3123-3129.
34. Handorf, A.M., et al., *Tissue Stiffness Dictates Development, Homeostasis, and Disease Progression.* Organogenesis, 2015. **11**(1): p. 1-15.
35. Sunyer, R., et al., *Collective cell durotaxis emerges from long-range intercellular force transmission.* Science, 2016. **353**(6304): p. 1157-1161.
36. Kobayashi, T. and M. Sokabe, *Sensing substrate rigidity by mechanosensitive ion channels with stress fibers and focal adhesions.* Curr Opin Cell Biol, 2010. **22**(5): p. 669-76.

37. Chen, W., et al., *Observing force-regulated conformational changes and ligand dissociation from a single integrin on cells.* Journal of Cell Biology, 2012. **199**(3): p. 497-512.
38. Webster, K.D., W.P. Ng, and D.A. Fletcher, *Tensional Homeostasis in Single Fibroblasts.* Biophysical Journal, 2014. **107**(1): p. 146-155.
39. Bachmann, M., et al., *Phosphorylated paxillin and phosphorylated FAK constitute subregions within focal adhesions.* J Cell Sci, 2022. **135**(7).
40. Lachowski, D., et al., *FAK controls the mechanical activation of YAP, a transcriptional regulator required for durotaxis.* Faseb Journal, 2018. **32**(2): p. 1099-1107.
41. Schiller, H.B. and R. Fässler, *Mechanosensitivity and compositional dynamics of cell-matrix adhesions.* Embo Reports, 2013. **14**(6): p. 509-519.
42. Schiller, H.B., et al., *β- and a-class integrins cooperate to regulate myosin II during rigidity sensing of fibronectin-based microenvironments.* Nature Cell Biology, 2013. **15**(6): p. 625-+.
43. Zhou, J., et al., *Mechanism of Focal Adhesion Kinase Mechanosensing.* Plos Computational Biology, 2015. **11**(11).
44. Guilluy, C. and K. Burridge, *Nuclear mechanotransduction: forcing the nucleus to respond.* Nucleus, 2015. **6**(1): p. 19-22.
45. Shiu, J.Y., et al., *Nanopillar force measurements reveal actin-cap-mediated YAP mechanotransduction.* Nature Cell Biology, 2018. **20**(3): p. 262-+.
46. Uhler, C. and G.V. Shivashankar, *Regulation of genome organization and gene expression by nuclear mechanotransduction.* Nat Rev Mol Cell Biol, 2017. **18**(12): p. 717-727.
47. Nardone, G., et al., *YAP regulates cell mechanics by controlling focal adhesion assembly.* Nature Communications, 2017. **8**.
48. Elosegui-Artola, A., et al., *Force Triggers YAP Nuclear Entry by Regulating Transport across Nuclear Pores.* Cell, 2017. **171**(6): p. 1397-+.
49. Niethammer, P., *Components and Mechanisms of Nuclear Mechanotransduction.* Annu Rev Cell Dev Biol, 2021. **37**: p. 233-256.
50. Booth-Gauthier, E.A., et al., *Force-Induced Changes in Subnuclear Movement and Rheology.* Biophysical Journal, 2012. **103**(12): p. 2423-2431.
51. Darenfed, H., et al., *Molecular characterization of the effects of Y-27632.* Cell Motility and the Cytoskeleton, 2007. **64**(2): p. 97-109.
52. Carmena, A., *Non-muscle myosin II activation: adding a classical touch to ROCK.* Small GTPases, 2021. **12**(3): p. 161-166.
53. Galli, C., et al., *Actin cytoskeleton controls activation of Wnt/β-catenin signaling in mesenchymal cells on implant surfaces with different topographies.* Acta Biomaterialia, 2012. **8**(8): p. 2963-2968.
54. Samuel, M., Olson, Michael, *Rho-GTPases in Embryonic Stem Cells*, in *Embryonic Stem Cells - Basic Biology to Bioengineering*. 2011, IntechOpen.
55. Totsukawa, G., et al., *Distinct roles of MLCK and ROCK in the regulation of membrane protrusions and focal adhesion dynamics during cell migration of fibroblasts.* Journal of Cell Biology, 2004. **164**(3): p. 427-439.
56. Totsukawa, G., et al., *Distinct roles of ROCK (Rho-kinase) and MLCK in spatial regulation of MLC phosphorylation for assembly of stress fibers*

and focal adhesions in 3T3 fibroblasts. Journal of Cell Biology, 2000. **150**(4): p. 797-806.
57. Seo, C.H., et al., *The effect of substrate microtopography on focal adhesion maturation and actin organization via the RhoA/ROCK pathway.* Biomaterials, 2011. **32**(36): p. 9568-9575.
58. Bhadriraju, K., et al., *Activation of ROCK by RhoA is regulated by cell adhesion, shape, and cytoskeletal tension.* Experimental Cell Research, 2007. **313**(16): p. 3616-3623.
59. Liu, Z.S., et al., *The Mechanotransduction Signaling Pathways in the Regulation of Osteogenesis.* International Journal of Molecular Sciences, 2023. **24**(18).
60. Zhang, W., et al., *Curved adhesions mediate cell attachment to soft matrix fibres in three dimensions.* Nature Cell Biology, 2023. **25**(10): p. 1453-+.
61. Lou, H.Y., et al., *Membrane curvature underlies actin reorganization in response to nanoscale surface topography.* Proceedings of the National Academy of Sciences of the United States of America, 2019. **116**(46): p. 23143-23151.
62. Mim, C. and V.M. Unger, *Membrane curvature and its generation by BAR proteins.* Trends in Biochemical Sciences, 2012. **37**(12): p. 526-533.
63. Carman, P.J. and R. Dominguez, *BAR domain proteins-a linkage between cellular membranes, signaling pathways, and the actin cytoskeleton.* Biophys Rev, 2018. **10**(6): p. 1587-1604.
64. Su, M., et al., *Comparative Study of Curvature Sensing Mediated by F-BAR and an Intrinsically Disordered Region of FBP17.* Iscience, 2020. **23**(11).
65. Ho, H.Y.H., et al., *Toca-1 mediates Cdc42-dependent actin nucleation by activating the N-WASP-WIP complex.* Cell, 2004. **118**(2): p. 203-216.
66. Jacquemet, G., et al., *L-type calcium channels regulate filopodia stability and cancer cell invasion downstream of integrin signalling.* Nature Communications, 2016. **7**.
67. Xiao, B.L., *Mechanisms of mechanotransduction and physiological roles of PIEZO channels.* Nature Reviews Molecular Cell Biology, 2024. **25**(11): p. 886-903.
68. Xu, X., et al., *Piezo Channels: Awesome Mechanosensitive Structures in Cellular Mechanotransduction and Their Role in Bone.* International Journal of Molecular Sciences, 2021. **22**(12).
69. Nilius, B. and G. Owsianik, *The transient receptor potential family of ion channels.* Genome Biol, 2011. **12**(3): p. 218.
70. Ellefsen, K.L., et al., *Myosin-II mediated traction forces evoke localized Piezo1-dependent Ca(2+) flickers.* Commun Biol, 2019. **2**: p. 298.
71. McNamara, L.E., et al., *Nanotopographical Control of Stem Cell Differentiation.* Journal of Tissue Engineering, 2010. **1**(1).
72. Turner, L.A. and M.J. Dalby, *Nanotopography - potential relevance in the stem cell niche.* Biomaterials Science, 2014. **2**(11): p. 1574-1594.
73. Cao, S. and Q. Yuan, *An update of nanotopographical surfaces in modulating stem cell fate: a narrative review.* BMT, 2022. **3**(1).
74. Chen, Y.F., *Nanofabrication by electron beam lithography and its applications: A review.* Microelectronic Engineering, 2015. **135**: p. 57-72.
75. Vieu, C., et al., *Electron beam lithography:: resolution limits and applications.* Applied Surface Science, 2000. **164**: p. 111-117.

76. Gates, B.D., et al., *New approaches to nanofabrication: Molding, printing, and other techniques.* Chemical Reviews, 2005. **105**(4): p. 1171-1196.
77. Hulshof, F.F.B., et al., *NanoTopoChip: High-throughput nanotopographical cell instruction.* Acta Biomaterialia, 2017. **62**: p. 188-198.
78. van Dommelen, R., P. Fanzio, and L. Sasso, *Surface self-assembly of colloidal crystals for micro- and nano-patterning.* Adv Colloid Interface Sci, 2018. **251**: p. 97-114.
79. Ozin, G.A., et al., *Nanofabrication by self-assembly.* Materials Today, 2009. **12**(5): p. 12-23.
80. Chua, K.N., et al., *Surface-aminated electrospun nanofibers enhance adhesion and expansion of human umbilical cord blood hematopoietic stem/progenitor cells.* Biomaterials, 2006. **27**(36): p. 6043-6051.
81. Tay, C.Y., et al., *Cellular behavior of human mesenchymal stem cells cultured on single-walled carbon nanotube film.* Carbon, 2010. **48**(4): p. 1095-1104.
82. Ogino, Y., et al., *RhoA-Mediated Functions in C3H10T1/2 Osteoprogenitors Are Substrate Topography Dependent.* Journal of Cellular Physiology, 2016. **231**(3): p. 568-575.
83. Betancourt, T. and L. Brannon-Peppas, *Micro- and nanofabrication methods in nanotechnological medical and pharmaceutical devices.* International Journal of Nanomedicine, 2006. **1**(4): p. 483-495.
84. Tahir, U., et al., *Nanofabrication Techniques: Challenges and Future Prospects.* J Nanosci Nanotechnol, 2021. **21**(10): p. 4981-5013.
85. Yang, Y., et al., *Nanofabrication for Nanophotonics.* ACS Nano, 2025. **19**(13): p. 12491-12605.
86. Wintersinger, C.M., et al., *Multi-micron crisscross structures grown from DNA-origami slats.* Nature Nanotechnology, 2023. **18**(3): p. 281-+.
87. Walsh, M.E., et al., *Maskless photolithography.* Nanolithography: The Art of Fabricating Nanoelectronic and Nanophotonic Devices and Systems, 2014(42): p. 179-193.
88. Chen, Y., et al., *Proximity x-ray lithography as a quick replication technique in nanofabrication: Recent progress and perspectives.* Microelectronic Engineering, 1996. **30**(1-4): p. 191-194.
89. Dong, Z.G., et al., *Ultraviolet Interband Plasmonics With Si Nanostructures.* Nano Letters, 2019. **19**(11): p. 8040-8048.
90. Mendonça, G., et al., *The combination of micron and nanotopography by H2SO4/H2O2 treatment and its effects on osteoblast-specific gene expression of hMSCs.* Journal of Biomedical Materials Research Part A, 2010. **94a**(1): p. 169-179.
91. Chan, L.Y., et al., *Temporal application of topography to increase the rate of neural differentiation from human pluripotent stem cells.* Biomaterials, 2013. **34**(2): p. 382-392.
92. Tonazzini, I., et al., *Neuronal contact guidance and YAP signaling on ultra-small nanogratings.* Scientific Reports, 2020. **10**(1).
93. Viela, F., et al., *Biomechanical Cell Regulation by High Aspect Ratio Nanoimprinted Pillars.* Advanced Functional Materials, 2016. **26**(31): p. 5599-5609.
94. Yim, E.K.F., et al., *Nanopattern-induced changes in morphology and motility of smooth muscle cells.* Biomaterials, 2005. **26**(26): p. 5405-5413.

95. Dalby, M.J., et al., *The control of human mesenchymal cell differentiation using nanoscale symmetry and disorder.* Nature Materials, 2007. **6**(12): p. 997-1003.
96. Sjöström, T., et al., *Fabrication of pillar-like titania nanostructures on titanium and their interactions with human skeletal stem cells.* Acta Biomaterialia, 2009. **5**(5): p. 1433-1441.
97. Delint, R.C., et al., *Mechanotransducive surfaces for enhanced cell osteogenesis, a review.* Biomaterials Advances, 2024. **160**.
98. McNamara, L.E., et al., *Skeletal stem cell physiology on functionally distinct titania nanotopographies.* Biomaterials, 2011. **32**(30): p. 7403-7410.
99. Sjöström, T., et al., *2D and 3D Nanopatterning of Titanium for Enhancing Osteoinduction of Stem Cells at Implant Surfaces.* Advanced Healthcare Materials, 2013. **2**(9): p. 1285-1293.
100. Kantawong, F., et al., *Proteomic analysis of human osteoprogenitor response to disordered nanotopography.* J R Soc Interface, 2009. **6**(40): p. 1075-86.
101. Cavalcanti-Adam, E.A., et al., *Cell adhesion and response to synthetic nanopatterned environments by steering receptor clustering and spatial location.* Hfsp Journal, 2008. **2**(5): p. 276-285.
102. Cavalcanti-Adam, E.A., et al., *Cell spreading and focal adhesion dynamics are regulated by spacing of integrin ligands.* Biophysical Journal, 2007. **92**(8): p. 2964-2974.
103. Romani, P., et al., *Crosstalk between mechanotransduction and metabolism.* Nature Reviews Molecular Cell Biology, 2021. **22**(1): p. 22-38.
104. Paczkowska, M., et al., *Integrative pathway enrichment analysis of multivariate omics data.* Nature Communications, 2020. **11**(1).
105. McCourt, J.L., et al., *Multi-omics analysis of sarcospan overexpression in skeletal muscle reveals compensatory remodeling of cytoskeleton-matrix interactions that promote mechanotransduction pathways.* Skeletal Muscle, 2023. **13**(1).
106. Shiu, Y.T., et al., *Rho mediates the shear-enhancement of endothelial cell migration and traction force generation.* Biophysical Journal, 2004. **86**(4): p. 2558-2565.
107. Plotnikov, S.V., et al., *Force Fluctuations within Focal Adhesions Mediate ECM-Rigidity Sensing to Guide Directed Cell Migration.* Cell, 2012. **151**(7): p. 1513-1527.
108. Raman, P.S., et al., *Probing cell traction forces in confined microenvironments.* Lab on a Chip, 2013. **13**(23): p. 4599-4607.
109. Beningo, K.A., et al., *Traction forces of fibroblasts are regulated by the Rho-dependent kinase but not by the myosin light chain kinase.* Archives of Biochemistry and Biophysics, 2006. **456**(2): p. 224-231.
110. Kolind, K., et al., *Control of proliferation and osteogenic differentiation of human dental-pulp-derived stem cells by distinct surface structures.* Acta Biomaterialia, 2014. **10**(2): p. 641-650.
111. Bickle, M., *The beautiful cell: high-content screening in drug discovery.* Analytical and Bioanalytical Chemistry, 2010. **398**(1): p. 219-226.
112. Altschuler, S.J. and L.F. Wu, *Cellular Heterogeneity: Do Differences Make a Difference?* Cell, 2010. **141**(4): p. 559-563.

113. Way, G.P., et al., *Morphology and gene expression profiling provide complementary information for mapping cell state.* Cell Syst, 2022. **13**(11): p. 911-923 e9.
114. Chandrasekaran, S.N., et al., *Image-based profiling for drug discovery: due for a machine-learning upgrade?* Nature Reviews Drug Discovery, 2021. **20**(2): p. 145-159.
115. Tang, Q.S., et al., *Morphological profiling for drug discovery in the era of deep learning.* Briefings in Bioinformatics, 2024. **25**(4).
116. Pratapa, A., M. Doron, and J.C. Caicedo, *Image-based cell phenotyping with deep learning.* Current Opinion in Chemical Biology, 2021. **65**: p. 9-17.
117. Clarke, C.J. and J.N. Haselden, *Metabolic Profiling as a Tool for Understanding Mechanisms of Toxicity.* Toxicologic Pathology, 2008. **36**(1): p. 140-147.
118. Madama, D., et al., *Metabolomic Profiling in Lung Cancer: A Systematic Review.* Metabolites, 2021. **11**(9).
119. Schumacher-Schuh, A., et al., *Advances in Proteomic and Metabolomic Profiling of Neurodegenerative Diseases.* Frontiers in Neurology, 2022. **12**.
120. Shah, S.H., W.E. Kraus, and C.B. Newgard, *Metabolomic Profiling for the Identification of Novel Biomarkers and Mechanisms Related to Common Cardiovascular Diseas Form and Functiones.* Circulation, 2012. **126**(9): p. 1110-1120.
121. Elshoeibi, A.M., et al., *Proteomic Profiling of Small-Cell Lung Cancer: A Systematic Review.* Cancers, 2023. **15**(20).
122. Pauper, M., et al., *Proteomic Profiling Towards a Better Understanding of Genetic Based Muscular Diseases: The Current Picture and a Look to the Future.* Biomolecules, 2025. **15**(1).
123. Simpson, R.J., S.S. Jensen, and J.W.E. Lim, *Proteomic profiling of exosomes: Current perspectives.* Proteomics, 2008. **8**(19): p. 4083-4099.
124. Bergkvist, A., et al., *Gene expression profiling - Clusters of possibilities.* Methods, 2010. **50**(4): p. 323-335.
125. Van de Vinver, M., *Gene expression profiling of breast cancer.* Ejc Supplements, 2008. **6**(9): p. 67-67.
126. Takáts, Z., J.M. Wiseman, and R.G. Cooks, *Ambient mass spectrometry using desorption electrospray ionization (DESI):: instrumentation, mechanisms and applications in forensics, chemistry, and biology.* Journal of Mass Spectrometry, 2005. **40**(10): p. 1261-1275.
127. Yang, M.X., et al., *Nano-DESI Mass Spectrometry Imaging of Proteoforms in Biological Tissues with High Spatial Resolution.* Analytical Chemistry, 2023. **95**(12): p. 5214-5222.
128. Bergman, H.M. and I. Lanekoff, *Profiling and quantifying endogenous molecules in single cells using nano-DESI MS.* Analyst, 2017. **142**(19): p. 3639-3647.
129. Jovic, D., et al., *Single-cell RNA sequencing technologies and applications: A brief overview.* Clinical and Translational Medicine, 2022. **12**(3).
130. van de Sande, B., et al., *Applications of single-cell RNA sequencing in drug discovery and development.* Nature Reviews Drug Discovery, 2023. **22**(6): p. 496-520.
131. Zhang, Y.J., et al., *Single-cell RNA sequencing in cancer research.* Journal of Experimental & Clinical Cancer Research, 2021. **40**(1).

132. Cimini, B.A., et al., *Optimizing the Cell Painting assay for image-based profiling*. Nature Protocols, 2023. **18**(7): p. 1981-+.
133. Bray, M.A., et al., *A dataset of images and morphological profiles of 30 000 small-molecule treatments using the Cell Painting assay*. Gigascience, 2017. **6**(12): p. 1-5.
134. Caicedo, J.C., et al., *Cell Painting predicts impact of lung cancer variants*. Mol Biol Cell, 2022. **33**(6): p. ar49.
135. Rohban, M.H., et al., *Systematic morphological profiling of human gene and allele function via Cell Painting*. Elife, 2017. **6**.
136. Wong, D.R., et al., *Deep representation learning determines drug mechanism of action from cell painting images*. Digital Discovery, 2023. **2**(5): p. 1354-1367.
137. Chandrasekaran, S.N., et al., *JUMP Cell Painting dataset: morphological impact of 136,000 chemical and genetic perturbations*. bioRxiv, 2023: p. 2023.03.23.534023.
138. Seal, S., et al., *Cell Painting: a decade of discovery and innovation in cellular imaging*. Nat Methods, 2025. **22**(2): p. 254-268.
139. Arevalo, J., et al., *Evaluating batch correction methods for image-based cell profiling*. Nature Communications, 2024. **15**(1).
140. Serrano, E., et al., *Reproducible image-based profiling with Pycytominer*. Nature Methods, 2025. **22**(4).
141. Caicedo, J.C., et al., *Data-analysis strategies for image-based cell profiling*. Nature Methods, 2017. **14**(9): p. 849-863.
142. Siegismund, D., et al., *Benchmarking feature selection methods for compressing image information in high-content screening*. Slas Technology, 2022. **27**(1): p. 85-93.
143. Kessy, A., A. Lewin, and K. Strimmer, *Optimal Whitening and Decorrelation*. American Statistician, 2018. **72**(4): p. 309-314.
144. Hao, Y.H., et al., *Dictionary learning for integrative, multimodal and scalable single-cell analysis*. Nature Biotechnology, 2024. **42**(2).
145. Satija, R., et al., *Spatial reconstruction of single-cell gene expression data*. Nature Biotechnology, 2015. **33**(5): p. 495-U206.
146. van der Maaten, L. and G. Hinton, *Visualizing Data using t-SNE*. Journal of Machine Learning Research, 2008. **9**: p. 2579-2605.
147. McInnes, L. and J. Healy, *UMAP: Uniform Manifold Approximation and Projection for Dimension Reduction*. 2018.
148. Becht, E., et al., *Dimensionality reduction for visualizing single-cell data using UMAP*. Nature Biotechnology, 2019. **37**(1): p. 38-+.
149. Healy, J. and L. McInnes, *Uniform manifold approximation and projection*. Nature Reviews Methods Primers, 2024. **4**(1).
150. Hotelling, H., *Analysis of a complex of statistical variables into principal components*. Journal of Educational Psychology, 1933. **24**: p. 498-520.
151. Kobak, D. and P. Berens, *The art of using t-SNE for single-cell transcriptomics*. Nature Communications, 2019. **10**.
152. Al-Rekabi, Z. and A.E. Pelling, *Cross talk between matrix elasticity and mechanical force regulates myoblast traction dynamics*. Physical Biology, 2013. **10**(6).
153. Li, Q.S., et al., *Micropillar displacements by cell traction forces are mechanically correlated with nuclear dynamics*. Biochemical and Biophysical Research Communications, 2015. **461**(2): p. 372-377.

154. Jay, P.Y., et al., *A Mechanical Function of Myosin-Ii in Cell Motility.* Journal of Cell Science, 1995. **108**: p. 387-393.
155. Discher, D.E., et al., *Matrix elasticity directs stem cell lineage specification.* Biophysical Journal, 2007: p. 32a-32a.
156. Yang, M.T., et al., *Assaying stem cell mechanobiology on microfabricated elastomeric substrates with geometrically modulated rigidity.* Nature Protocols, 2011. **6**(2): p. 187-213.
157. Fu, J.P., et al., *Mechanical regulation of cell function with geometrically modulated elastomeric substrates.* Nature Methods, 2010. **7**(9): p. 733-U95.
158. Wang, J.H.C., *Cell Traction Forces (CTFs) and CTF Microscopy Applications in Musculoskeletal Research.* Operative Techniques in Orthopaedics, 2010. **20**(2): p. 106-109.
159. Polacheck, W.J. and C.S. Chen, *Measuring cell-generated forces: a guide to the available tools.* Nature Methods, 2016. **13**(5): p. 415-423.
160. Dembo, M. and Y.L. Wang, *Stresses at the cell-to-substrate interface during locomotion of fibroblasts.* Biophysical Journal, 1999. **76**(4): p. 2307-2316.
161. Tymchenko, N., et al., *A novel cell force sensor for quantification of traction during cell spreading and contact guidance.* Biophysical Journal, 2007. **93**(1): p. 335-345.
162. De Saram, P., et al., *Micropillars in Cell Mechanobiology: Design, Fabrication, Characterization, and Biosensing Applications.* Small Science, 2025. **5**(4).
163. Ribeiro, A.J.S., et al., *For whom the cells pull: Hydrogel and micropost devices for measuring traction forces.* Methods, 2016. **94**: p. 51-64.
164. Xu, Y. and R. Zhao, *Chapter 2 - Force-sensing micropillar arrays for cell mechanics and mechanobiology*, in *Micro and Nano Systems for Biophysical Studies of Cells and Small Organisms*, X. Liu and Y. Sun, Editors. 2021, Academic Press. p. 23-42.
165. Tan, J.L., et al., *Cells lying on a bed of microneedles: An approach to isolate mechanical force.* Proceedings of the National Academy of Sciences of the United States of America, 2003. **100**(4): p. 1484-1489.
166. Trepat, X., et al., *Physical forces during collective cell migration.* Nature Physics, 2009. **5**(6): p. 426-430.
167. van Hoorn, H., et al., *The Nanoscale Architecture of Force-Bearing Focal Adhesions.* Nano Letters, 2014. **14**(8): p. 4257-4262.
168. Vigliotti, A., et al., *Response of cells on a dense array of micro-posts.* Meccanica, 2021. **56**(6): p. 1635-1651.
169. Ganz, A., et al., *Traction forces exerted through N-cadherin contacts.* Biology of the Cell, 2006. **98**(12): p. 721-730.
170. Zhao, Y., et al., *Cellular force measurements using single-spaced polymeric microstructures: isolating cells from base substrate.* Journal of Micromechanics and Microengineering, 2005. **15**(9): p. 1649-1656.
171. Hui, J.A. and S.W. Pang, *Cell migration on microposts with surface coating and confinement.* Bioscience Reports, 2019. **39**.
172. Ghibaudo, M., et al., *Traction forces and rigidity sensing regulate cell functions.* Soft Matter, 2008. **4**(9): p. 1836-1843.
173. Li, Z., et al., *Cellular traction forces: a useful parameter in cancer research.* Nanoscale, 2017. **9**(48): p. 19039-19044.

174. Saez, A., et al., *Traction forces exerted by epithelial cell sheets.* Journal of Physics-Condensed Matter, 2010. **22**(19).
175. Liu, Z.J., et al., *Mechanical tugging force regulates the size of cell-cell junctions.* Proceedings of the National Academy of Sciences of the United States of America, 2010. **107**(22): p. 9944-9949.
176. Ahn, J., et al., *Micro-/Nanohierarchical Structures Physically Engineered on Surfaces: Analysis and Perspective.* Advanced Materials, 2023.
177. Alameda, M.T., et al., *Multilevel Hierarchical Topographies by Combined Photolithography and Nanoimprinting Processes To Create Surfaces with Controlled Wetting.* Acs Applied Nano Materials, 2019. **2**(8): p. 4727-4733.
178. Cimini-Lab. *CellProfiler 4.2.8 Manual*. [cited 2025 01/10].
179. Lamprecht, M.R., D.M. Sabatini, and A.E. Carpenter, *CellProfiler™: Free, Versatile Software for Automated Biological Image Analysis.* BioTechniques, 2007. **42**(1): p. 71-75.
180. Stirling, D.R., et al., *CellProfiler 4: improvements in speed, utility and usability.* Bmc Bioinformatics, 2021. **22**(1).
181. Lakshminarayanan, V. and A. Fleck, *Zernike polynomials: a guide.* Journal of Modern Optics, 2011. **58**(7): p. 545-561.
182. Niu, K. and C. Tian, *Zernike polynomials and their applications.* Journal of Optics, 2022. **24**(12).
183. Aaron, J.S., A.B. Taylor, and T.L. Chew, *Image co-localization - co-occurrence versus correlation.* Journal of Cell Science, 2018. **131**(3).
184. Haralick, R.M., *Statistical and Structural Approaches to Texture.* Proceedings of the Ieee, 1979. **67**(5): p. 786-804.
185. Haralick, R.M., K. Shanmugam, and I. Dinstein, *Textural Features for Image Classification.* Ieee Transactions on Systems Man and Cybernetics, 1973. **Smc3**(6): p. 610-621.
186. Huethorst, E., et al., *Customizable, engineered substrates for rapid screening of cellular cues.* Biofabrication, 2020. **12**(2).
187. Vandereyken, K., et al., *Methods and applications for single-cell and spatial multi-omics.* Nature Reviews Genetics, 2023. **24**(8): p. 494-515.
188. Xu, T.R., et al., *Recent advances and typical applications in mass spectrometry-based technologies for single-cell metabolite analysis.* Trac-Trends in Analytical Chemistry, 2022. **157**.
189. Zhang, L.W. and A. Vertes, *Single-Cell Mass Spectrometry Approaches to Explore Cellular Heterogeneity.* Angewandte Chemie-International Edition, 2018. **57**(17): p. 4466-4477.
190. Cao, J.X., et al., *Spatial Transcriptomics: A Powerful Tool in Disease Understanding and Drug Discovery.* Theranostics, 2024. **14**(7): p. 2946-2968.
191. Williams, C.G., et al., *An introduction to spatial transcriptomics for biomedical research.* Genome Medicine, 2022. **14**(1).
192. Rietdijk, J., et al., *Morphological profiling of environmental chemicals enables efficient and untargeted exploration of combination effects.* Science of the Total Environment, 2022. **832**.
193. Hughes, R.E., et al., *High-content phenotypic and pathway profiling to advance drug discovery in diseases of unmet need.* Cell Chemical Biology, 2021. **28**(3): p. 338-355.
194. Simm, J., et al., *Repurposing High-Throughput Image Assays Enables Biological Activity Prediction for Drug Discovery.* Cell Chemical Biology, 2018. **25**(5): p. 611-+.

195. Tegtmeyer, M., et al., *High-dimensional phenotyping to define the genetic basis of cellular morphology.* Nature Communications, 2024. **15**(1).
196. Yang, S.J., et al., *Applying Deep Neural Network Analysis to High-Content Image-Based Assays.* Slas Discovery, 2019. **24**(8): p. 829-841.
197. Li, F.P., et al., *L-type calcium channel activity in osteoblast cells is regulated by the actin cytoskeleton independent of protein trafficking.* Journal of Bone and Mineral Metabolism, 2011. **29**(5): p. 515-525.
198. Botello-Smith, W.M., et al., *A mechanism for the activation of the mechanosensitive Piezo1 channel by the small molecule Yoda1.* Nature Communications, 2019. **10**.
199. Thien, N.D., et al., *Piezo1 and its inhibitors: Overview and perspectives.* European Journal of Medicinal Chemistry, 2024. **273**.
200. Yoneda, M., et al., *PIEZO1 and TRPV4, which Are Distinct Mechano-Sensors in the Osteoblastic MC3T3-E1 Cells, Modify Cell-Proliferation.* International Journal of Molecular Sciences, 2019. **20**(19).
201. Sun, W.J., et al., *The mechanosensitive Piezo1 channel is required for bone formation.* Elife, 2019. **8**.
202. Sugimoto, A., et al., *Piezo type mechanosensitive ion channel component 1 functions as a regulator of the cell fate determination of mesenchymal stem cells.* Scientific Reports, 2017. **7**.
203. Sun, Z., et al., *Simulated microgravity inhibits L-type calcium channel currents partially by the up-regulation of miR-103 in MC3T3-E1 osteoblasts.* Sci Rep, 2015. **5**: p. 8077.
204. Ziomek, G., C. van Breemen, and M. Esfandiarei, *Drop in endo/sarcoplasmic calcium precedes the unfolded protein response in Brefeldin A-treated vascular smooth muscle cells.* European Journal of Pharmacology, 2015. **764**: p. 328-339.
205. Langenbach, F. and J. Handschel, *Effects of dexamethasone, ascorbic acid and β-glycerophosphate on the osteogenic differentiation of stem cells.* Stem Cell Research & Therapy, 2013. **4**.
206. Hamidouche, Z., et al., *FHL2 mediates dexamethasone-induced mesenchymal cell differentiation into osteoblasts by activating Wnt/β-catenin signaling-dependent Runx2 expression.* Faseb Journal, 2008. **22**(11): p. 3813-3822.
207. Ross, E.A., et al., *Nanotopography reveals metabolites that maintain the immunomodulatory phenotype of mesenchymal stromal cells.* Nature Communications, 2023. **14**(1).
208. Quarles, L.D., et al., *Distinct Proliferative and Differentiated Stages of Murine Mc3t3-E1 Cells in Culture - an Invitro Model of Osteoblast Development.* Journal of Bone and Mineral Research, 1992. **7**(6): p. 683-692.
209. Ozdemir, T., et al., *Substrate curvature sensing through Myosin IIa upregulates early osteogenesis.* Integrative Biology, 2013. **5**(11): p. 1407-1416.
210. Gellynck, K., et al., *Cell Cytoskeletal Changes Effected by Static Compressive Stress Lead to Changes in the Contractile Properties of Tissue Regenerative Collagen Membranes.* European Cells & Materials, 2013. **25**: p. 317-325.
211. Wakatsuki, T., et al., *Effects of cytochalasin D and latrunculin B on mechanical properties of cells.* J Cell Sci, 2001. **114**(Pt 5): p. 1025-36.

212. Liu, Q., et al., *Cytochalasin D Promotes Osteogenic Differentiation of MC3T3-E1 Cells via p38-MAPK Signaling Pathway.* Curr Mol Med, 2019. **20**(1): p. 79-88.
213. Shouib, R. and G. Eitzen, *Cdc42 regulates cytokine expression and trafficking in bronchial epithelial cells.* Frontiers in Immunology, 2022. **13**.
214. Holzinger, A., *Jasplakinolide: An Actin-Specific Reagent that Promotes Actin Polymerization.* Cytoskeleton Methods and Protocols, 2009. **586**: p. 71-87.
215. Morimoto, Y., et al., *The protein phosphatase inhibitors okadaic acid and calyculin A induce apoptosis in human osteoblastic cells.* Experimental Cell Research, 1997. **230**(2): p. 181-186.
216. Chartier, L., et al., *Calyculin-a Increases the Level of Protein-Phosphorylation and Changes the Shape of 3t3 Fibroblasts.* Cell Motility and the Cytoskeleton, 1991. **18**(1): p. 26-40.
217. Gupton, S.L., W.C. Salmon, and C.M. Waterman-Storer, *Converging populations of F-actin promote breakage of associated microtubules to spatially regulate microtubule turnover in migrating cells.* Current Biology, 2002. **12**(22): p. 1891-1899.
218. Fürst, R., *Narciclasine - an Amaryllidaceae Alkaloid with Potent Antitumor and Anti-Inflammatory Properties.* Planta Medica, 2016. **82**(16): p. 1389-1394.
219. Lefranc, F., et al., *Narciclasine, a plant growth modulator, activates Rho and stress fibers in glioblastoma cells.* Molecular Cancer Therapeutics, 2009. **8**(7): p. 1739-1750.
220. Alvarez, C. and E.S. Sztul, *Brefeldin A (BFA) disrupts the organization of the microtubule and the actin cytoskeletons.* European Journal of Cell Biology, 1999. **78**(1): p. 1-14.
221. Lázaro-Diéguez, F., et al., *Actin filaments are involved in the maintenance of Golgi cisternae morphology and intra-Golgi pH.* Cell Motility and the Cytoskeleton, 2006. **63**(12): p. 778-791.
222. Nobes, C.D. and A. Hall, *Rho, Rac, and Cdc42 Gtpases Regulate the Assembly of Multimolecular Focal Complexes Associated with Actin Stress Fibers, Lamellipodia, and Filopodia.* Cell, 1995. **81**(1): p. 53-62.
223. Walsh, A.B., et al., *SCH 51344-induced reversal of RAS-transformation is accompanied by the specific inhibition of the RAS and RAC-dependent cell morphology pathway.* Oncogene, 1997. **15**(21): p. 2553-2560.
224. Zhu, S.Y., et al., *Cell signaling and transcriptional regulation of osteoblast lineage commitment, differentiation, bone formation, and homeostasis.* Cell Discovery, 2024. **10**(1).
225. Raucher, D. and M.P. Sheetz, *Cell spreading and lamellipodial extension rate is regulated by membrane tension.* Journal of Cell Biology, 2000. **148**(1): p. 127-136.
226. Batchelder, E.L., et al., *Membrane tension regulates motility by controlling lamellipodium organization.* Proceedings of the National Academy of Sciences of the United States of America, 2011. **108**(28): p. 11429-11434.
227. Nishiya, Y., et al., *A potent 1,4-dihydropyridine L-type calcium channel blocker, benidipine, promotes osteoblast differentiation.* Calcified Tissue International, 2002. **70**(1): p. 30-39.

228. Jing, L., M.K. Ng, and J.Z. Huang, *An entropy weighting algorithm for subspace clustering of high-dimensional sparse data.* Ieee Transactions on Knowledge and Data Engineering, 2007. **19**(8): p. 1026-1041.
229. Yu, Y.L., et al., *Regulation of osteogenesis by micro/nano hierarchical titanium surfaces through a Rock-Wnt5a feedback loop.* Colloids and Surfaces B-Biointerfaces, 2018. **170**: p. 1-10.
230. Willis, C., J. Nyffeler, and J. Harrill, *Phenotypic Profiling of Reference Chemicals across Biologically Diverse Cell Types Using the Cell Painting Assay.* Slas Discovery, 2020. **25**(7): p. 755-769.
231. Cross-Zamirski, J.O., et al., *Label-free prediction of cell painting from brightfield images.* Scientific Reports, 2022. **12**(1).
232. Tuvshindorj, U., et al., *The Galapagos Chip Platform for High-Throughput Screening of Cell Adhesive Chemical Micropatterns.* Small, 2022. **18**(10).
233. Yu, S., et al., *Integrating inflammatory biomarker analysis and artificial-intelligence-enabled image-based profiling to identify drug targets for intestinal fibrosis.* Cell Chemical Biology, 2023. **30**(9): p. 1169-+.
234. Akbarzadeh, M., et al., *Morphological profiling by means of the Cell Painting assay enables identification of tubulin-targeting compounds.* Cell Chemical Biology, 2022. **29**(6): p. 1053-+.
235. Nyffeler, J., et al., *Application of Cell Painting for chemical hazard evaluation in support of screening-level chemical assessments.* Toxicology and Applied Pharmacology, 2023. **468**.
236. Unadkat, H.V., et al., *An algorithm-based topographical biomaterials library to instruct cell fate.* Proceedings of the National Academy of Sciences of the United States of America, 2011. **108**(40): p. 16565-16570.
237. Kolind, K., et al., *A combinatorial screening of human fibroblast responses on micro-structured surfaces.* Biomaterials, 2010. **31**(35): p. 9182-9191.
238. Lovmand, J., et al., *The use of combinatorial topographical libraries for the screening of enhanced osteogenic expression and mineralization.* Biomaterials, 2009. **30**(11): p. 2015-2022.
239. Moe, A.A.K., et al., *Microarray with Micro- and Nano-topographies Enables Identification of the Optimal Topography for Directing the Differentiation of Primary Murine Neural Progenitor Cells.* Small, 2012. **8**(19): p. 3050-3061.
240. Conner, A.A., et al., *High-throughput analysis of topographical cues for the expansion of murine pluripotent stem cells.* Nanotechnology, 2024. **35**(45).
241. Zeng, Y.K., et al., *Human mesenchymal stem cell basal membrane bending on gratings is dependent on both grating width and curvature.* Scientific Reports, 2018. **8**.
242. Tan, K.K.B., et al., *Enhanced differentiation of neural progenitor cells into neurons of the mesencephalic dopaminergic subtype on topographical patterns.* Biomaterials, 2015. **43**: p. 32-43.
243. Hu, J.Q., et al., *High-Throughput Mechanobiology Screening Platform Using Micro- and Nanotopography.* Nano Letters, 2016. **16**(4): p. 2198-2204.
244. Leuning, D.G., et al., *The cytokine secretion profile of mesenchymal stromal cells is determined by surface structure of the microenvironment.* Scientific Reports, 2018. **8**.

245. Anderson, D.G., S. Levenberg, and R. Langer, *Nanoliter-scale synthesis of arrayed biomaterials and application to human embryonic stem cells.* Nature Biotechnology, 2004. **22**(7): p. 863-866.
246. Mei, Y., et al., *Combinatorial development of biomaterials for clonal growth of human pluripotent stem cells.* Nature Materials, 2010. **9**(9): p. 768-778.
247. Pudjihartono, N., et al., *A Review of Feature Selection Methods for Machine Learning-Based Disease Risk Prediction.* Frontiers in Bioinformatics, 2022. **2**.
248. Lefin, N., et al., *Review and perspective on bioinformatics tools using machine learning and deep learning for predicting antiviral peptides.* Molecular Diversity, 2024. **28**(4): p. 2365-2374.
249. Larrañaga, P., et al., *Machine learning in bioinformatics.* Briefings in Bioinformatics, 2006. **7**(1): p. 86-112.
250. Bannigan, P., et al., *Machine learning models to accelerate the design of polymeric long-acting injectables.* Nature Communications, 2023. **14**(1).
251. Lin, S.C., et al., *Osteoinductive biomaterials: Machine learning for prediction and interpretation.* Acta Biomaterialia, 2024. **187**: p. 422-433.
252. Johnson, R.D.a.W., D. W., *Applied Multivariate Statistical Analysis.* Vol. 6. 2007: Pearson Prentice-Hall.
253. Seber, G.A.F., *Multivariate Observations.* 1984: Wiley Series in Probability and Mathematical Statistics: Probability and Mathematical Statistics. New York: John Wiley & Sons.
254. Wang, H.T., et al., *Finding the needle in a high -dimensional haystack: Canonical correlation analysis for neuroscientists.* Neuroimage, 2020. **216**.
255. Gonzalez, I., et al., *CCA: An R package to extend canonical correlation analysis.* Journal of Statistical Software, 2008. **23**(12): p. 1-14.
256. Zhang, H., et al., *Single cell migration dynamics mediated by geometric confinement.* Colloids and Surfaces B-Biointerfaces, 2016. **145**: p. 72-78.
257. Lee, K., et al., *Contribution of actin filaments and microtubules to cell elongation and alignment depends on the grating depth of microgratings.* Journal of Nanobiotechnology, 2016. **14**.
258. Refaaq, F.M., X. Chen, and S.W. Pang, *Effects of topographical guidance cues on osteoblast cell migration.* Scientific Reports, 2020. **10**(1).
259. Arnold, M., et al., *Activation of integrin function by nanopatterned adhesive interfaces.* Chemphyschem, 2004. **5**(3): p. 383-388.
260. Huang, J.H., et al., *Impact of Order and Disorder in RGD Nanopatterns on Cell Adhesion.* Nano Letters, 2009. **9**(3): p. 1111-1116.
261. Arnold, M., et al., *Cell interactions with hierarchically structured nano-patterned adhesive surfaces.* Soft Matter, 2009. **5**(1): p. 72-77.
262. Schvartzman, M., et al., *Nanolithographic Control of the Spatial Organization of Cellular Adhesion Receptors at the Single-Molecule Level.* Nano Letters, 2011. **11**(3): p. 1306-1312.
263. Huethorst, E., et al., *Enhanced Human-Induced Pluripotent Stem Cell Derived Cardiomyocyte Maturation Using a Dual Microgradient Substrate.* ACS Biomater Sci Eng, 2016. **2**(12): p. 2231-2239.
264. Reynolds, P.M., et al., *A dual gradient assay for the parametric analysis of cell-surface interactions.* Small, 2012. **8**(16): p. 2541-7.

265. Linzer, D.A. and J.B. Lewis, *poLCA: An R Package for Polytomous Variable Latent Class Analysis.* Journal of Statistical Software, 2011. **42**(10): p. 1-29.
266. Curtis, A. and C. Wilkinson, *Topographical control of cells.* Biomaterials, 1997. **18**(24): p. 1573-1583.
267. Curtis, A.S.G. and C.D. Wilkinson, *Reactions of cells to topography.* Journal of Biomaterials Science-Polymer Edition, 1998. **9**(12): p. 1313-1329.
268. Curtis, A. and M. Riehle, *Tissue engineering: the biophysical background.* Physics in Medicine and Biology, 2001. **46**(4): p. R47-R65.
269. Flemming, R.G., et al., *Effects of synthetic micro- and nano-structured surfaces on cell behavior.* Biomaterials, 1999. **20**(6): p. 573-588.
270. Luo, J.J., et al., *The influence of nanotopography on cell behaviour through interactions with the extracellular matrix - A review.* Bioactive Materials, 2022. **15**: p. 145-159.
271. Casanellas, I., J. Samitier, and A. Lagunas, *Recent advances in engineering nanotopographic substrates for cell studies.* Frontiers in Bioengineering and Biotechnology, 2022. **10**.
272. Narayanan, K.B., *Nanotopographical Features of Polymeric Nanocomposite Scaffolds for Tissue Engineering and Regenerative Medicine: A Review.* Biomimetics, 2025. **10**(5).
273. Britland, S., et al., *Synergistic and hierarchical adhesive and topographic guidance of BHK cells.* Experimental Cell Research, 1996. **228**(2): p. 313-325.
274. Teixeira, A.I., et al., *Epithelial contact guidance on well-defined micro- and nanostructured substrates.* Journal of Cell Science, 2003. **116**(10): p. 1881-1892.
275. Yeung, T., et al., *Effects of substrate stiffness on cell morphology, cytoskeletal structure, and adhesion.* Cell Motility and the Cytoskeleton, 2005. **60**(1): p. 24-34.
276. Zhou, D.W., et al., *Effects of substrate stiffness and actomyosin contractility on coupling between force transmission and vinculin-paxillin recruitment at single focal adhesions.* Molecular Biology of the Cell, 2017. **28**(14): p. 1901-1911.
277. Liang, E.I., et al., *Correlation of focal adhesion assembly and disassembly with cell migration on nanotopography.* Integrative Biology, 2017. **9**(2): p. 145-155.
278. Curtis, A.S.G., et al., *Cells react to nanoscale order and symmetry in their surroundings.* Ieee Transactions on Nanobioscience, 2004. **3**(1): p. 61-65.
279. Yim, E.K.F., et al., *Nanotopography-induced changes in focal adhesions, cytoskeletal organization, and mechanical properties of human mesenchymal stem cells.* Biomaterials, 2010. **31**(6): p. 1299-1306.
280. Zhou, Q.H., et al., *Mechanical Properties of Aligned Nanotopologies for Directing Cellular Behavior.* Advanced Materials Interfaces, 2016. **3**(18).
281. Comelles, J., et al., *Soft topographical patterns trigger a stiffness-dependent cellular response to contact guidance.* Materials Today Bio, 2023. **19**.
282. Park, J., et al., *Quantitative Analysis of the Combined Effect of Substrate Rigidity and Topographic Guidance on Cell Morphology.* Ieee Transactions on Nanobioscience, 2012. **11**(1): p. 28-36.

283. Birket, M.J., et al., *Contractile Defect Caused by Mutation in MYBPC3 Revealed under Conditions Optimized for Human PSC-Cardiomyocyte Function.* Cell Reports, 2015. **13**(4): p. 733-745.
284. Pasqualini, F.S., et al., *Traction force microscopy of engineered cardiac tissues.* Plos One, 2018. **13**(3).
285. Lyall, M., et al., *Measuring contractile forces in vascular smooth muscle cells.* Vascular Pharmacology, 2025. **159**.
286. Liew, H.Y., et al., *Cellular Traction Force Holds the Potential as a Drug Testing Readout for In Vitro Cancer Metastasis.* Cellular and Molecular Bioengineering, 2024. **17**(3): p. 203-217.
287. Eschenbruch, J., et al., *From Microspikes to Stress Fibers: Actin Remodeling in Breast Acini Drives Myosin II-Mediated Basement Membrane Invasion.* Cells, 2021. **10**(8).
288. Janmey, P.A., D.A. Fletcher, and C.A. Reinhart-King, *Stiffness Sensing by Cells.* Physiological Reviews, 2020. **100**(2): p. 695-724.
289. Chien, F.C., et al., *Flexible nanopillars to regulate cell adhesion and movement.* Nanotechnology, 2016. **27**(47).
290. Wolfenson, H., et al., *Tropomyosin controls sarcomere-like contractions for rigidity sensing and suppressing growth on soft matrices.* Nature Cell Biology, 2016. **18**(1): p. 33-+.
291. Scharin-Mehlmann, M., et al., *Nano- and Micro-Patterned S-, H-, and X-PDMS for Cell-Based Applications: Comparison of Wettability, Roughness, and Cell-Derived Parameters.* Frontiers in Bioengineering and Biotechnology, 2018. **6**.
292. Qin, D., Y.N. Xia, and G.M. Whitesides, *Soft lithography for micro- and nanoscale patterning.* Nature Protocols, 2010. **5**(3): p. 491-502.
293. Odom, T.W., et al., *Improved pattern transfer in soft lithography using composite stamps.* Langmuir, 2002. **18**(13): p. 5314-5320.
294. Hui, J. and S.W. Pang, *Dynamic Tracking of Osteoblastic Cell Traction Force during Guided Migration.* Cellular and Molecular Bioengineering, 2018. **11**(1): p. 11-23.
295. Gangnaik, A.S., Y.M. Georgiev, and J.D. Holmes, *New Generation Electron Beam Resists: A Review.* Chemistry of Materials, 2017. **29**(5): p. 1898-1917.
296. Grigorescu, A.E. and C.W. Hagen, *Resists for sub-20-nm electron beam lithography with a focus on HSQ: state of the art.* Nanotechnology, 2009. **20**(29).
297. Saifullah, M.S.M., et al., *Patterning at the Resolution Limit of Commercial Electron Beam Lithography.* Nano Letters, 2022.
298. Guarino, V., M.L. Focarete, and D. Pisignano, *Advances in Nanostructured Materials and Nanopatterning Technologies Applications for Healthcare, Environmental and Energy 1st ed.* Journal of Print and Media Technology Research, 2020. **9**(1): p. 48-48.
299. Sharma, E., et al., *Evolution in Lithography Techniques: Microlithography to Nanolithography.* Nanomaterials, 2022. **12**(16).
300. Zailer, I., et al., *Crosslinked PMMA as a high-resolution negative resist for electron beam lithography and applications for physics of low-dimensional structures.* Semiconductor Science and Technology, 1996. **11**(8): p. 1235-1238.

301. Kostic, I., et al., *PMMA resist profile and proximity effect dependence on the electron-beam lithography process parameters.* 21st International Summer School on Vacuum, Electron and Ion Technologies, 2020. **1492**.
302. Murata, K., *Monte Carlo Simulation of Electron Scattering in Resist Film/Substrate Targets.* Scanning Electron Microscopy, 1982. **1982**(1, 27): p. 311-329.
303. Murata, K., D.F. Kyser, and C.H. Ting, *Monte Carlo simulation of fast secondary electron production in electron beam resists.* Journal of Applied Physics, 1981. **52**(7): p. 4396-4405.
304. Campbell, F.A., *Design and optimised production of an integrated nanopillar platform*, in *College of Science and Engineering*. 2020, University of Glasgow. p. 166.
305. Schmid, H. and B. Michel, *Siloxane polymers for high-resolution, high-accuracy soft lithography.* Macromolecules, 2000. **33**(8): p. 3042-3049.
306. Choi, K.M. and J.A. Rogers, *A photocurable poly(dimethylsiloxane) chemistry designed for soft lithographic molding and printing in the nanometer regime.* Journal of the American Chemical Society, 2003. **125**(14): p. 4060-4061.
307. Kim, K.H., et al., *Mechanical characteristics of the hard-polydimethylsiloxane for smart lithography.* Ekc2008: Proceedings of the Eu-Korea Conference on Science and Technology, 2008. **124**: p. 229-+.
308. Scharin, M., et al., *Bioactivation of Plane and Patterned PDMS Thin Films by Wettability Engineering.* Bionanoscience, 2014. **4**(3): p. 251-262.
309. Schoen, I., et al., *Probing Cellular Traction Forces by Micropillar Arrays: Contribution of Substrate Warping to Pillar Deflection.* Nano Letters, 2010. **10**(5): p. 1823-1830.
310. Fruncillo, S., et al., *Lithographic Processes for the Scalable Fabrication of Micro- and Nanostructures for Biochips and Biosensors.* Acs Sensors, 2021. **6**(6): p. 2002-2024.
311. Pimpin, A. and W. Srituravanich, *Review on Micro- and Nanolithography Techniques and their Applications.* Engineering Journal-Thailand, 2012. **16**(1): p. 37-55.
312. Seisyan, R.P., *Nanolithography in microelectronics: A review.* Technical Physics, 2011. **56**(8): p. 1061-1073.
313. del Campo, A. and C. Greiner, *SU-8: a photoresist for high-aspect-ratio and 3D submicron lithography.* Journal of Micromechanics and Microengineering, 2007. **17**(6): p. R81-R95.
314. Lee, J.B., K.H. Choi, and K. Yoo, *Innovative SU-8 Lithography Techniques and Their Applications.* Micromachines, 2015. **6**(1): p. 1-18.
315. Liu, J., et al., *Process research of high aspect ratio microstructure using SU-8 resist.* Microsystem Technologies-Micro-and Nanosystems-Information Storage and Processing Systems, 2004. **10**(4): p. 265-268.
316. Amato, L., et al., *Fabrication of high-aspect ratio SU-8 micropillar arrays.* Microelectronic Engineering, 2012. **98**: p. 483-487.
317. Schindelin, J., et al., *Fiji: an open-source platform for biological-image analysis.* Nature Methods, 2012. **9**(7): p. 676-682.
318. Yasin, S., D.G. Hasko, and H. Ahmed, *Comparison of MIBK/IPA and water/IPA as PMMA developers for electron beam nanolithography.* Microelectronic Engineering, 2002. **61-2**: p. 745-753.
319. Zhang, J., et al., *Reduction of diffraction effect for fabrication of very high aspect ratio microchannels in SU-8 over large area by soft cushion*

technology. Microsystem Technologies-Micro-and Nanosystems-Information Storage and Processing Systems, 2005. **11**(7): p. 519-525.
320. Chaterji, S., et al., *Synergistic Effects of Matrix Nanotopography and Stiffness on Vascular Smooth Muscle Cell Function*. Tissue Engineering Part A, 2014. **20**(15-16): p. 2115-2126.

9. Appendix

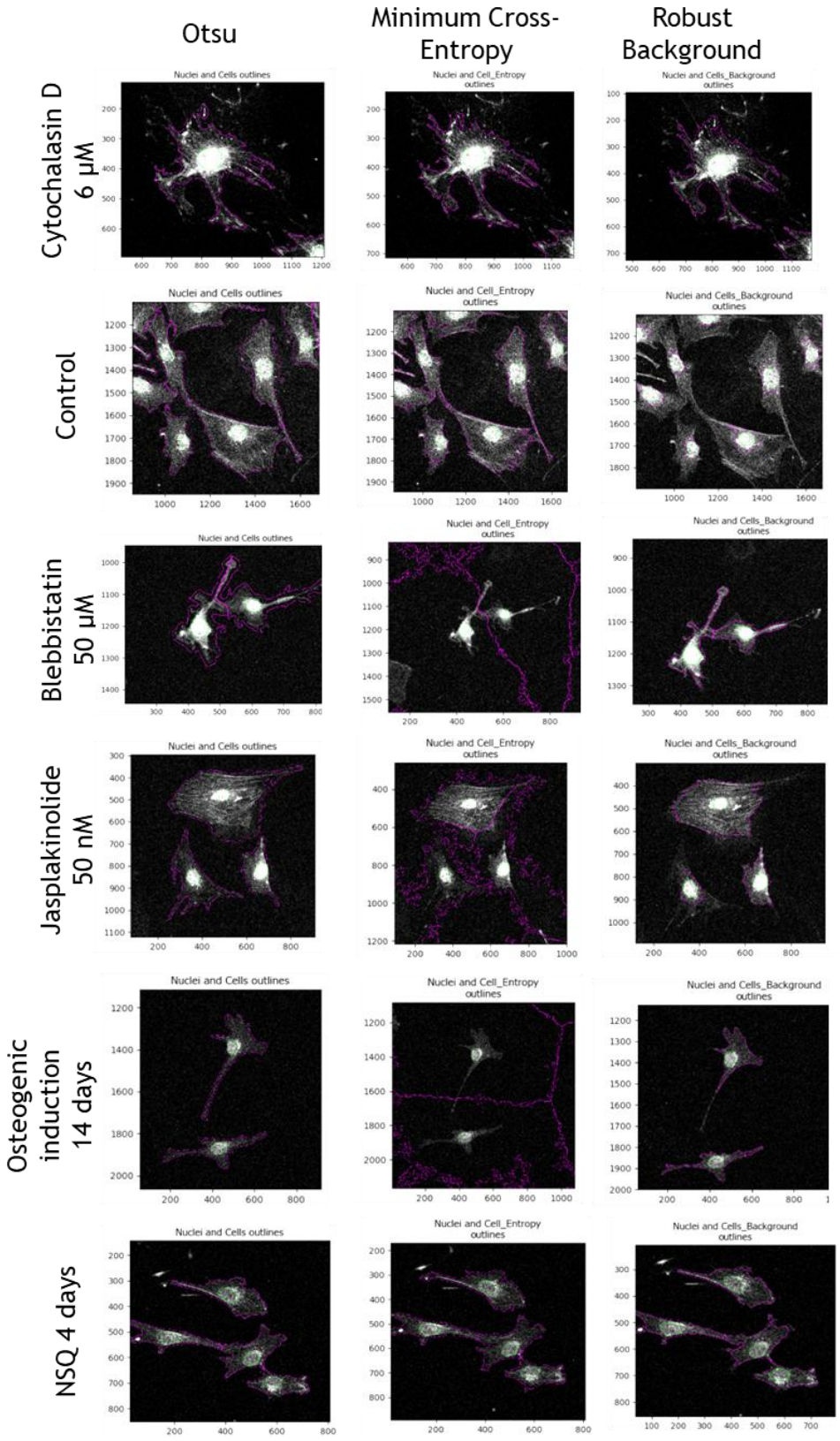

***Figure A3.1**: Example images of the cell segmentation using Otsu, minimum cross-entropy and robust background method. The segmentation is shown on MC3T3 cells with 6 µM cytochalasin D, a control, 50 µM blebbistatin, 50 nM jasplakinolide, 14 days of osteogenic induction, and 4 days on NSQ nanopits.*

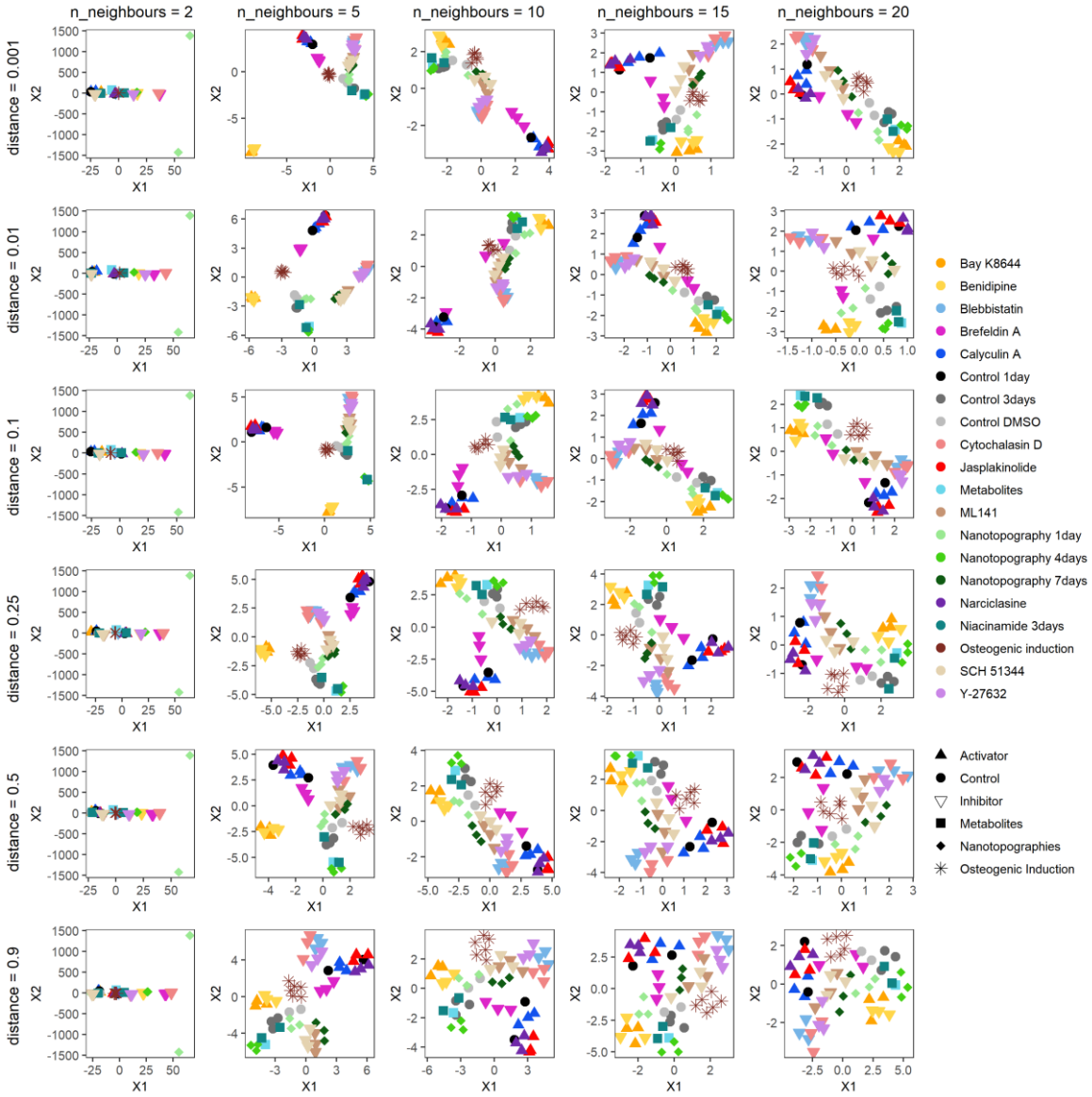

***Figure A4.1**: UMAP projections of median features for each condition with varying distance and varying number of neighbours.*

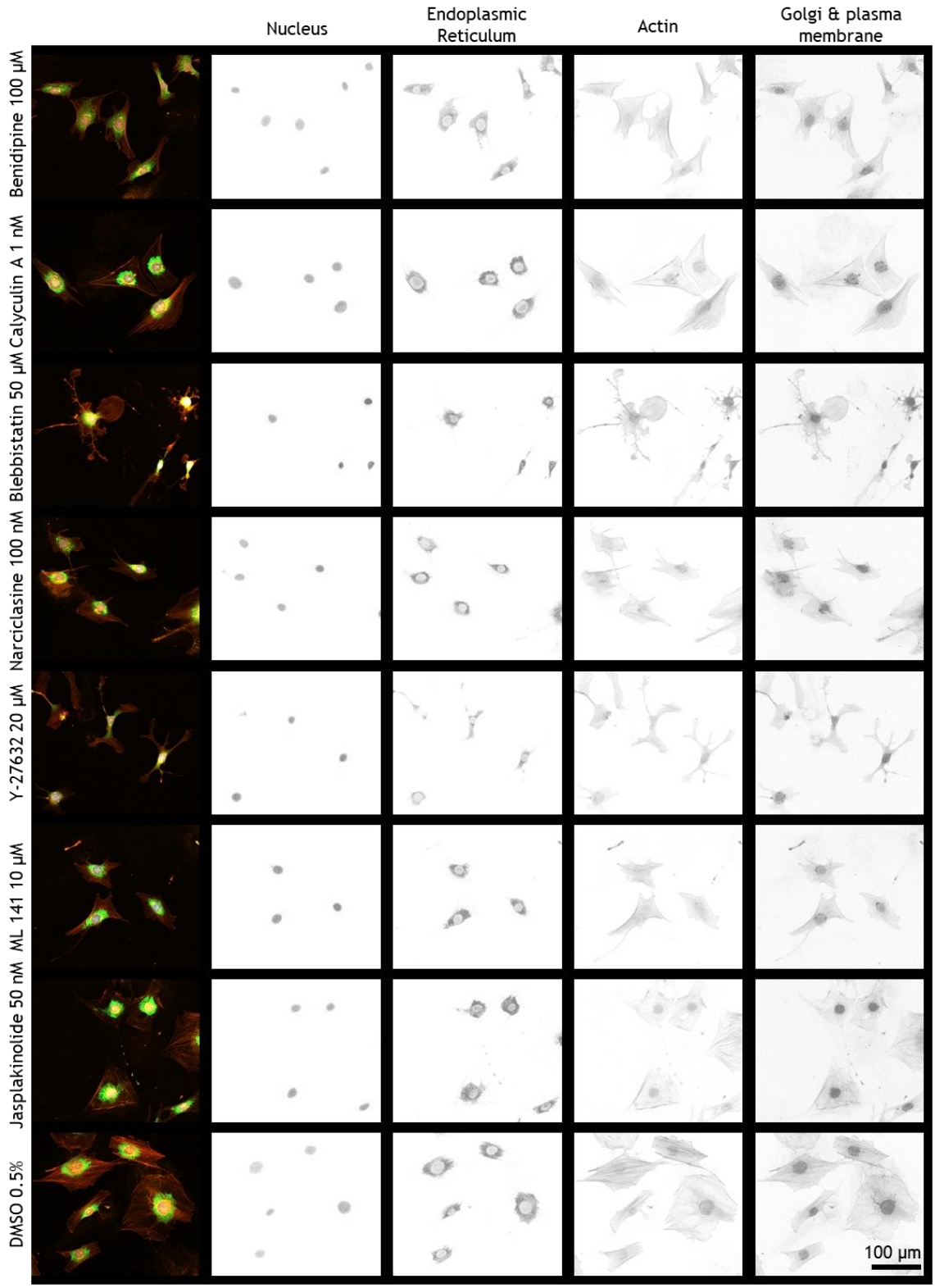

***Figure A4.2**: Cell Painting images of MC3T3 cells stained for the Nucleus with HOECHST 33342 (blue), Endoplasmic reticulum with concanavalin A – Alexa Fluor 488 (green), actin cytoskeleton with phalloidin - Alexa Fluor 568 (red), and the Golgi and plasma membrane with wheat-germ agglutinin (WGA) – Alexa Fluor 555 (orange). The cells are shown with the highest concentration of each activator and inhibitor.*

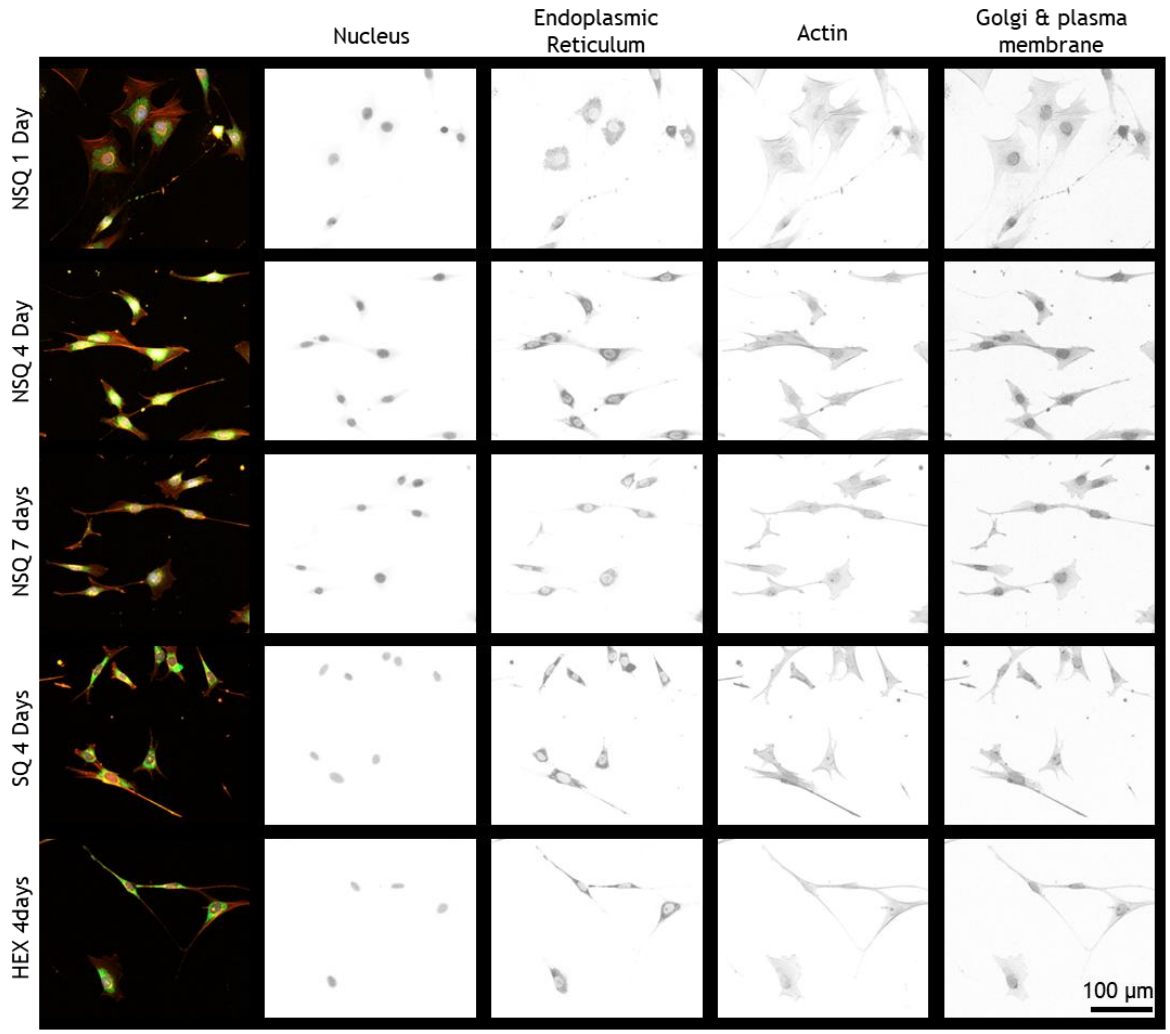

***Figure A4.3**: Cell Painting images of MC3T3 cells stained for the Nucleus with HOECHST 33342 (blue), Endoplasmic reticulum with concanavalin A – Alexa Fluor 488 (green), actin cytoskeleton with phalloidin - Alexa Fluor 568 (red), and the Golgi and plasma membrane with wheat-germ agglutinin (WGA) – Alexa Fluor 555 (orange). Example images of the cells on NSQ after 1, 4 and 7 days, as well as cells on HEX and NSQ after 4 days.*

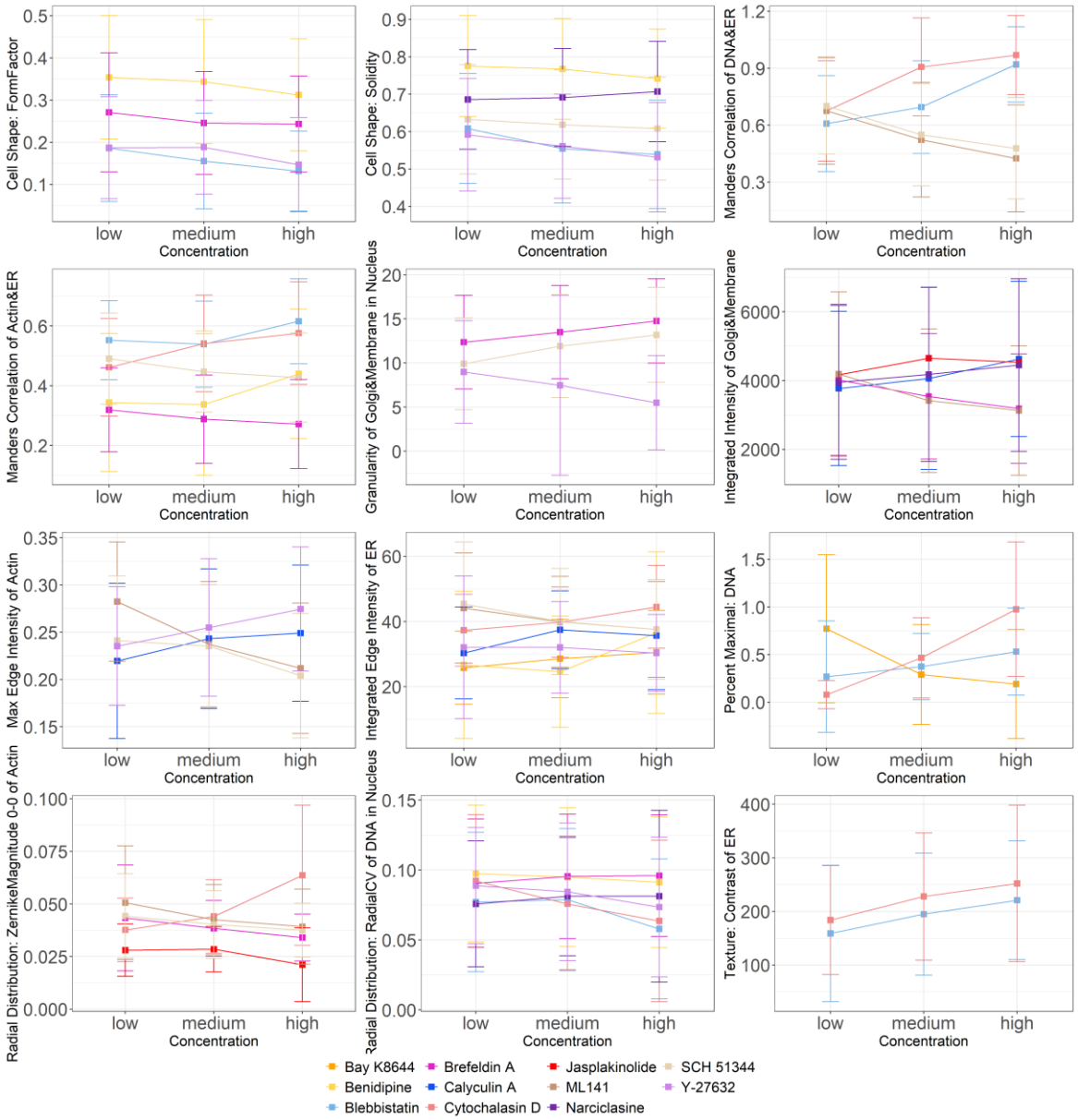

***Figure A4.4**: These are examples that visualize the concentration dependencies of the features measured by CellProfiler. For clarity, the various concentrations of activators and inhibitors are categorized into low, medium, and high concentrations. Those features are selected to give a broad overview of different feature categories and to highlight that concentration dependencies are visible in all activators and inhibitors.*

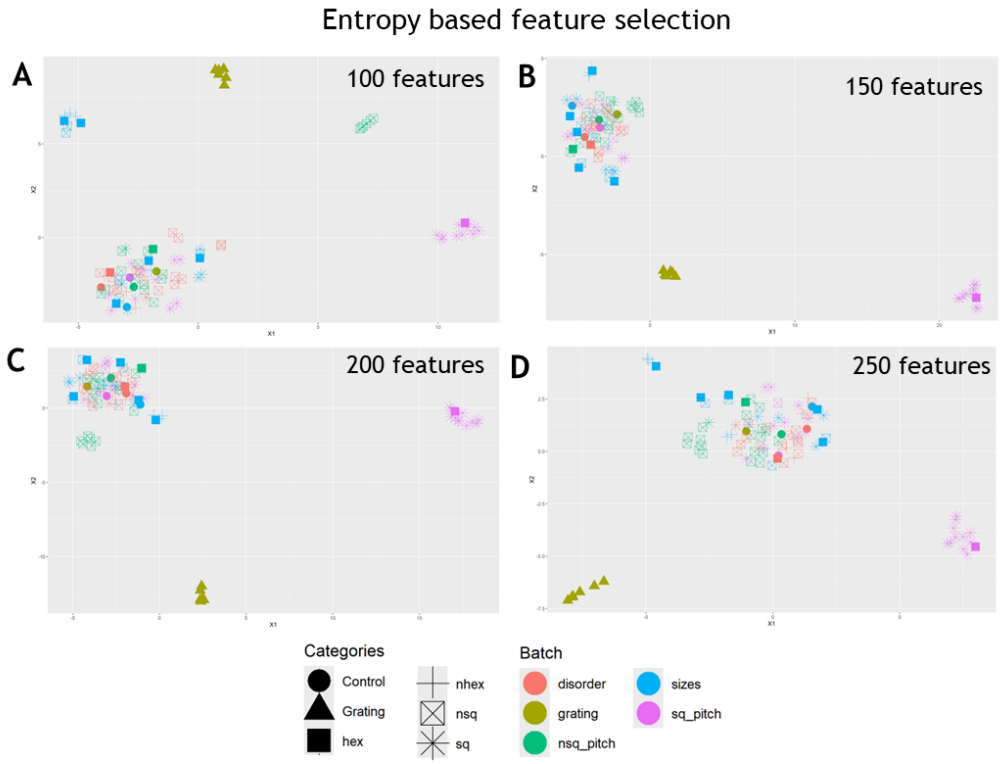

***Figure A5.1**: UMAP plots of nanotopography library datasets with entropy based feature selection. The 100 (A), 150 (B), 200 (C), and 250 (D) features with the highest impact in entropy reduction are picked.*

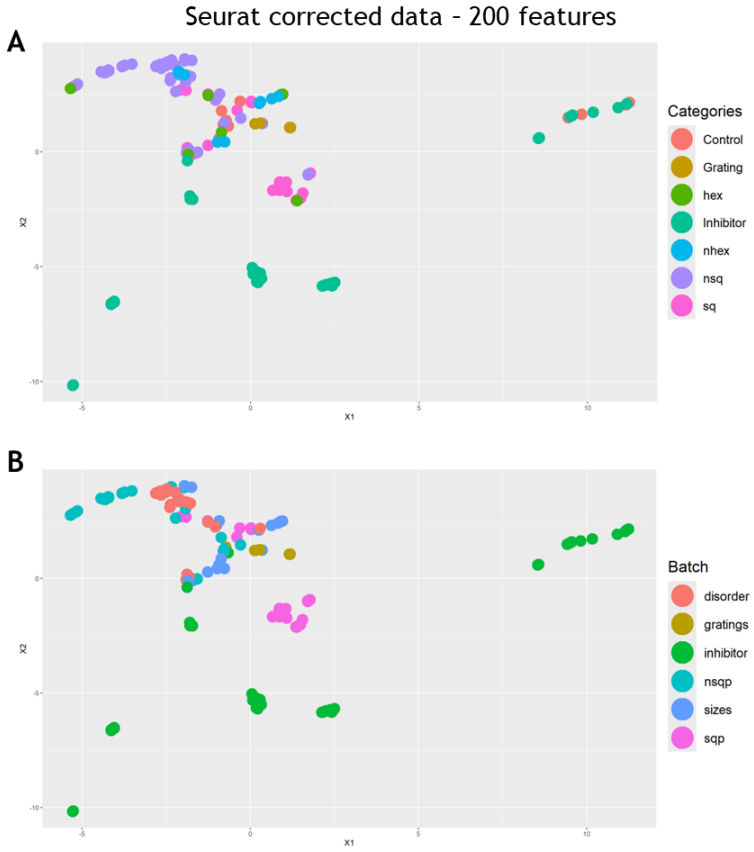

***Figure A5.2**: UMAP plot of Seurat corrected data and 200 selected features by entropy. The datapoints are coloured by their nanotopography category (A) and their batch (B) to show a potential batch effect.*

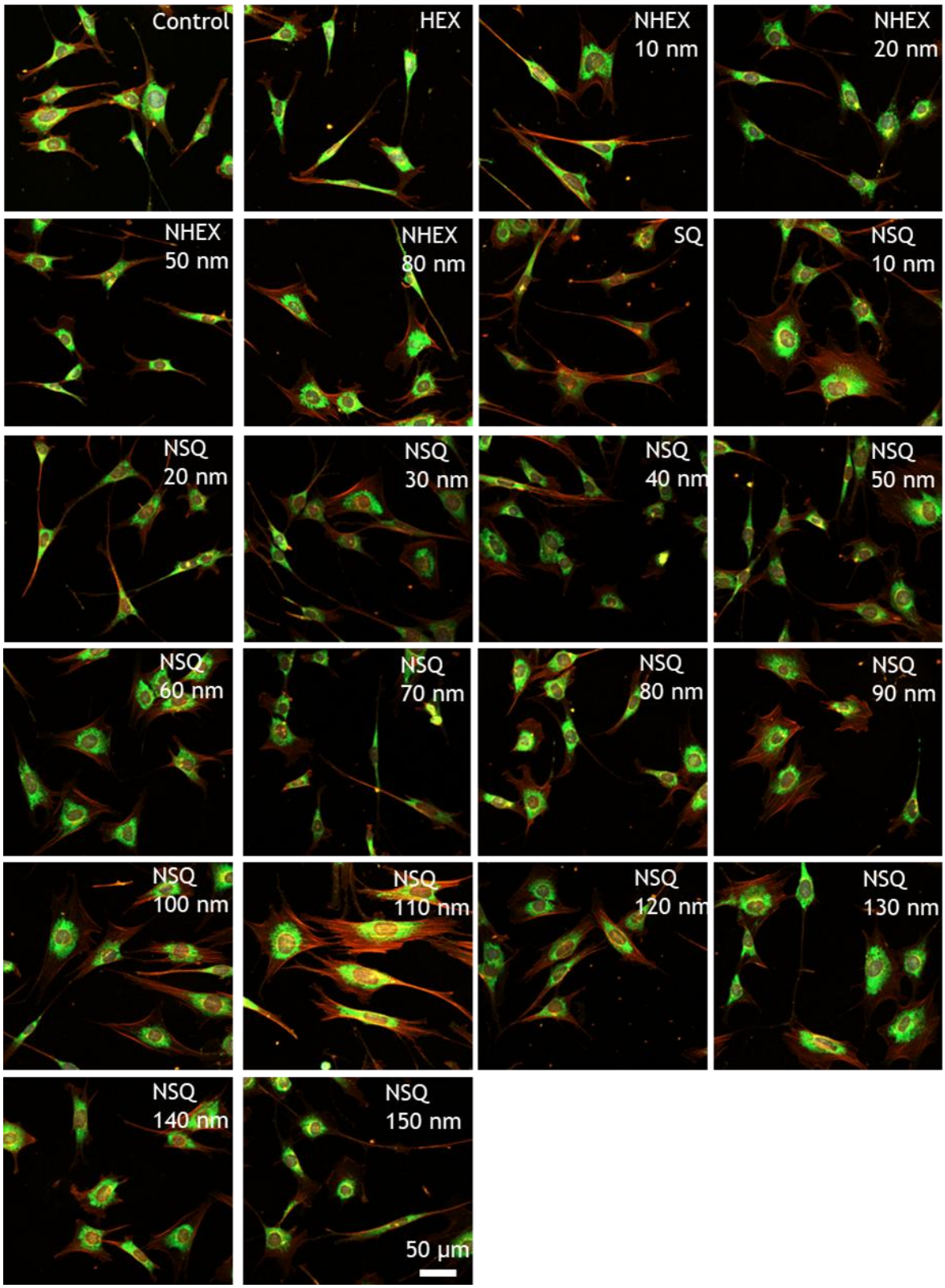

***Figure A5.3**: Cell Painting images of MC3T3 cells for the disorder array. The cells are stained for the Nucleus with HOECHST 33342 (blue), Endoplasmic reticulum with concanavalin A – Alexa Fluor 488 (green), actin cytoskeleton with phalloidin - Alexa Fluor 568 (red), and the Golgi and plasma membrane with wheat-germ agglutinin (WGA) – Alexa Fluor 555 (orange). The fluorescence channels are merged in the images.*

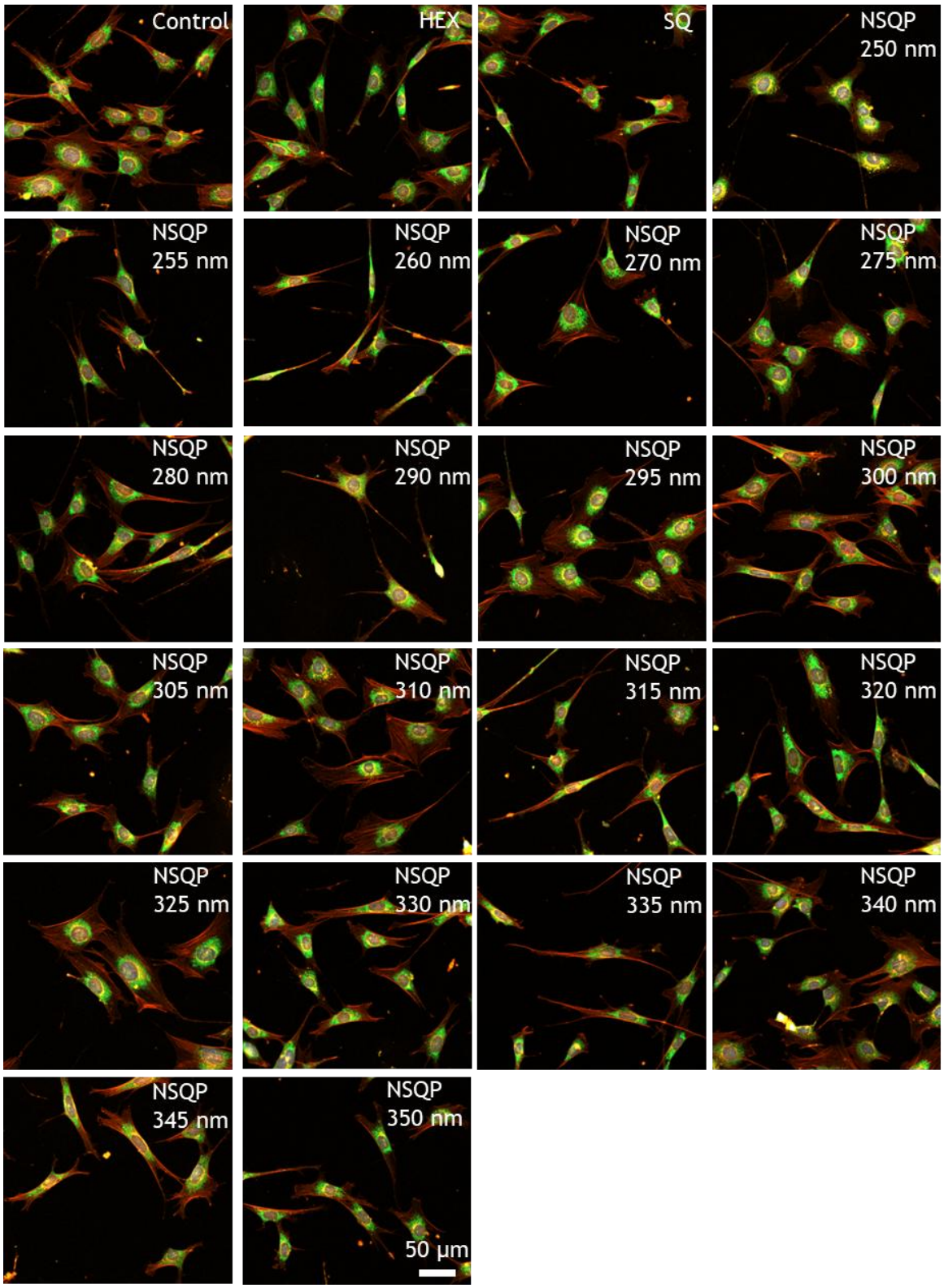

Figure A5.4: *Cell Painting images of MC3T3 cells for the NSQ pitch array. The cells are stained for the Nucleus with HOECHST 33342 (blue), Endoplasmic reticulum with concanavalin A – Alexa Fluor 488 (green), actin cytoskeleton with phalloidin - Alexa Fluor 568 (red), and the Golgi and plasma membrane with wheat-germ agglutinin (WGA) – Alexa Fluor 555 (orange). The fluorescence channels are merged in the images.*

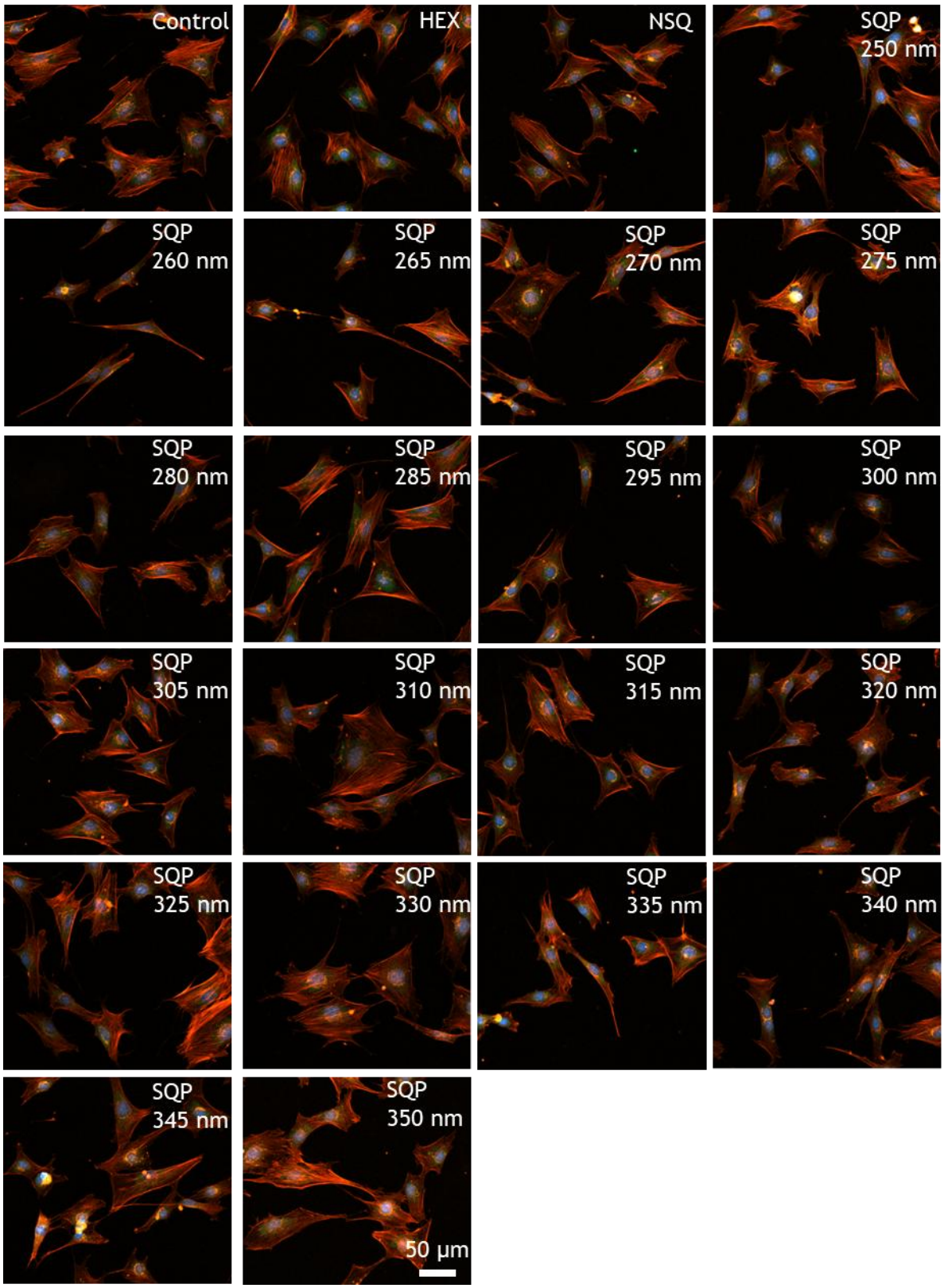

Figure A5.5: *Cell Painting images of MC3T3 cells for the SQ pitch array. The cells are stained for the Nucleus with HOECHST 33342 (blue), Endoplasmic reticulum with concanavalin A – Alexa Fluor 488 (green), actin cytoskeleton with phalloidin - Alexa Fluor 568 (red), and the Golgi and plasma membrane with wheat-germ agglutinin (WGA) – Alexa Fluor 555 (orange). The fluorescence channels are merged in the images.*

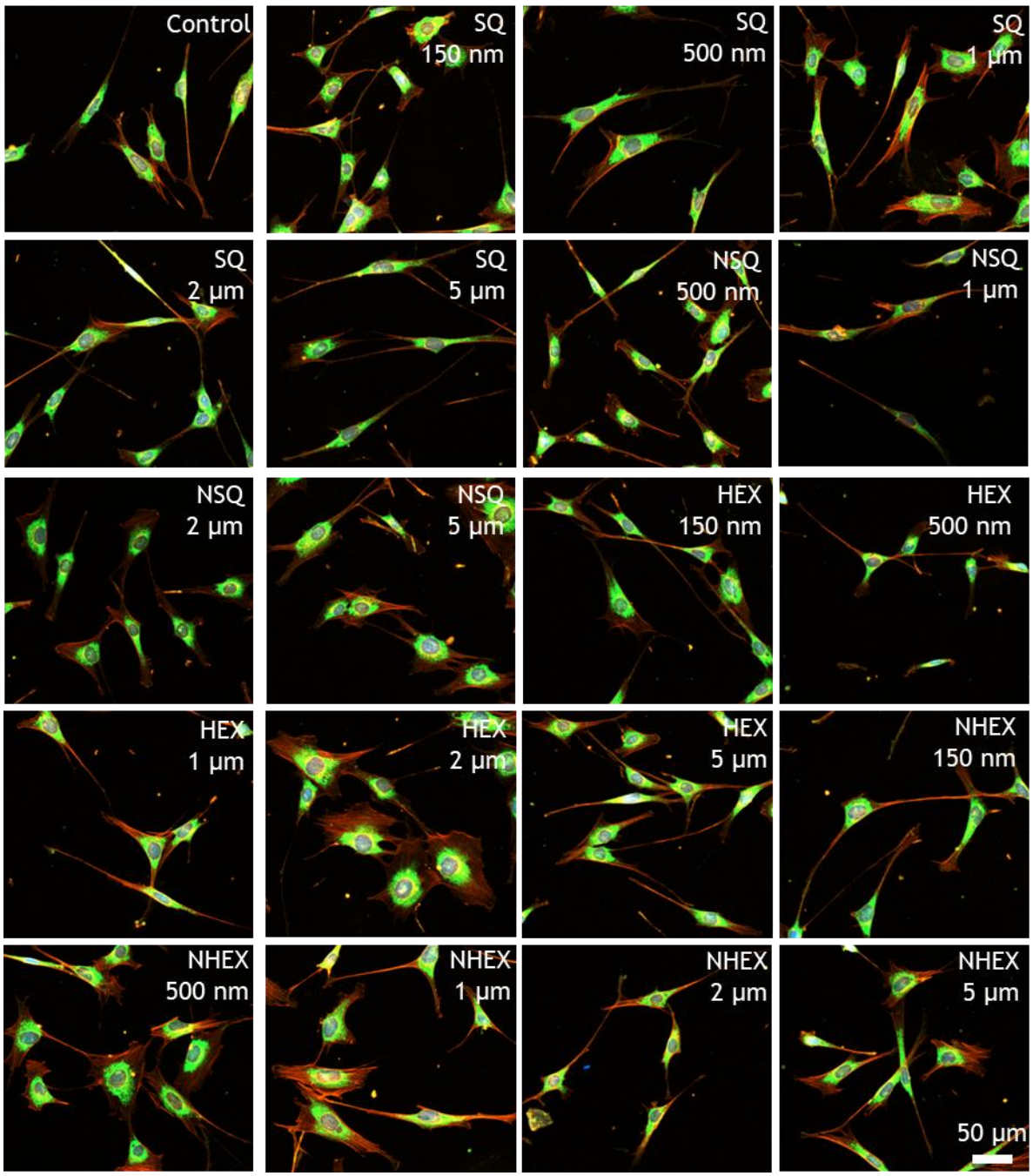

***Figure A5.6**: Cell Painting images of MC3T3 cells for the varying size array. The cells are stained for the Nucleus with HOECHST 33342 (blue), Endoplasmic reticulum with concanavalin A – Alexa Fluor 488 (green), actin cytoskeleton with phalloidin - Alexa Fluor 568 (red), and the Golgi and plasma membrane with wheat-germ agglutinin (WGA) – Alexa Fluor 555 (orange). The fluorescence channels are merged in the images.*

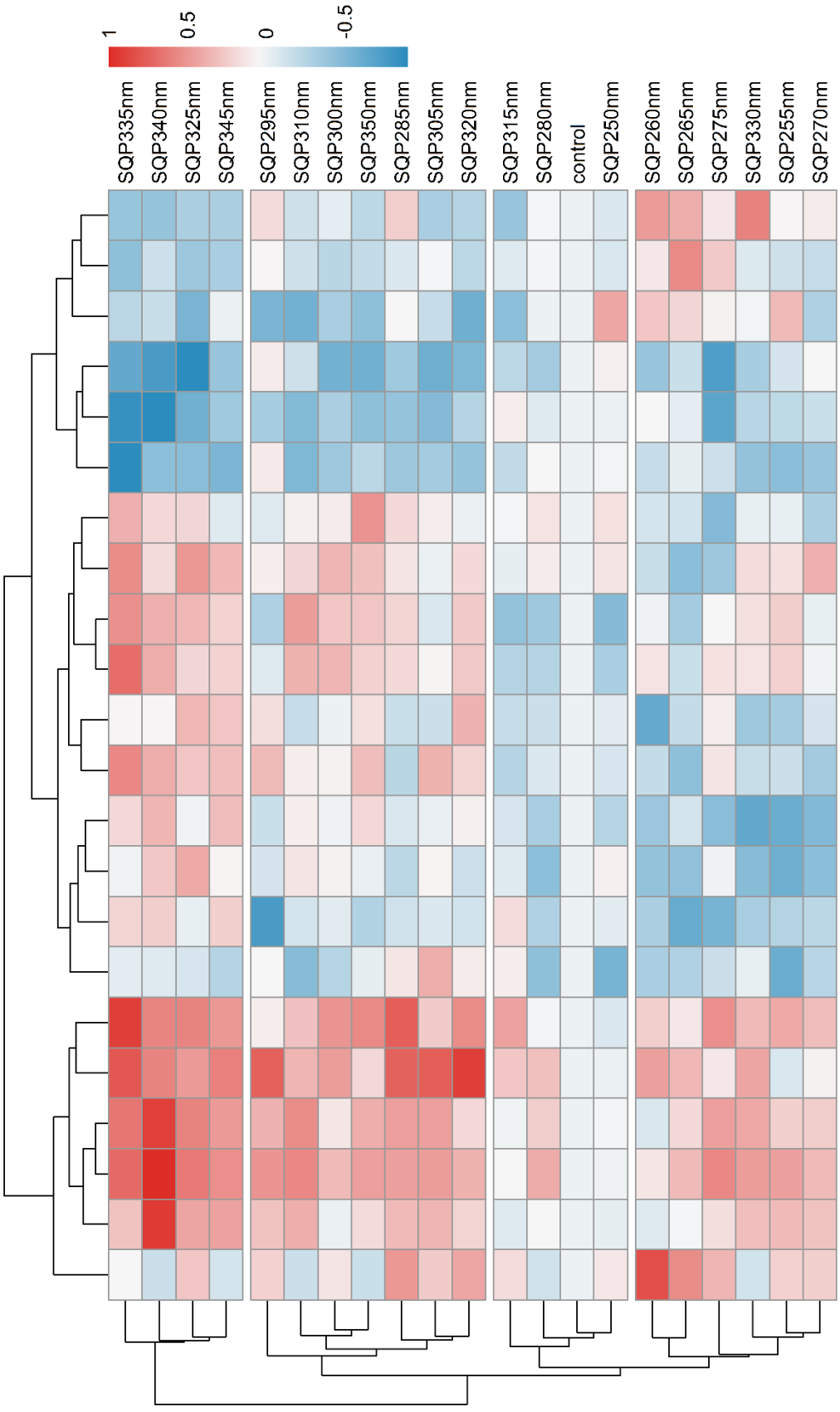

***Figure A5.7**: Heatmap of the morphome depending on the pitch of nanopits in the SQ pitch array. The heatmap is ordered by hierarchical clustering using Euclidean distances. The features are normalized between 0 and 1 and corrected against the control by dividing the control from the other substrates. The number behind the geometry describer corresponds to the centre-to-centre spacing.*

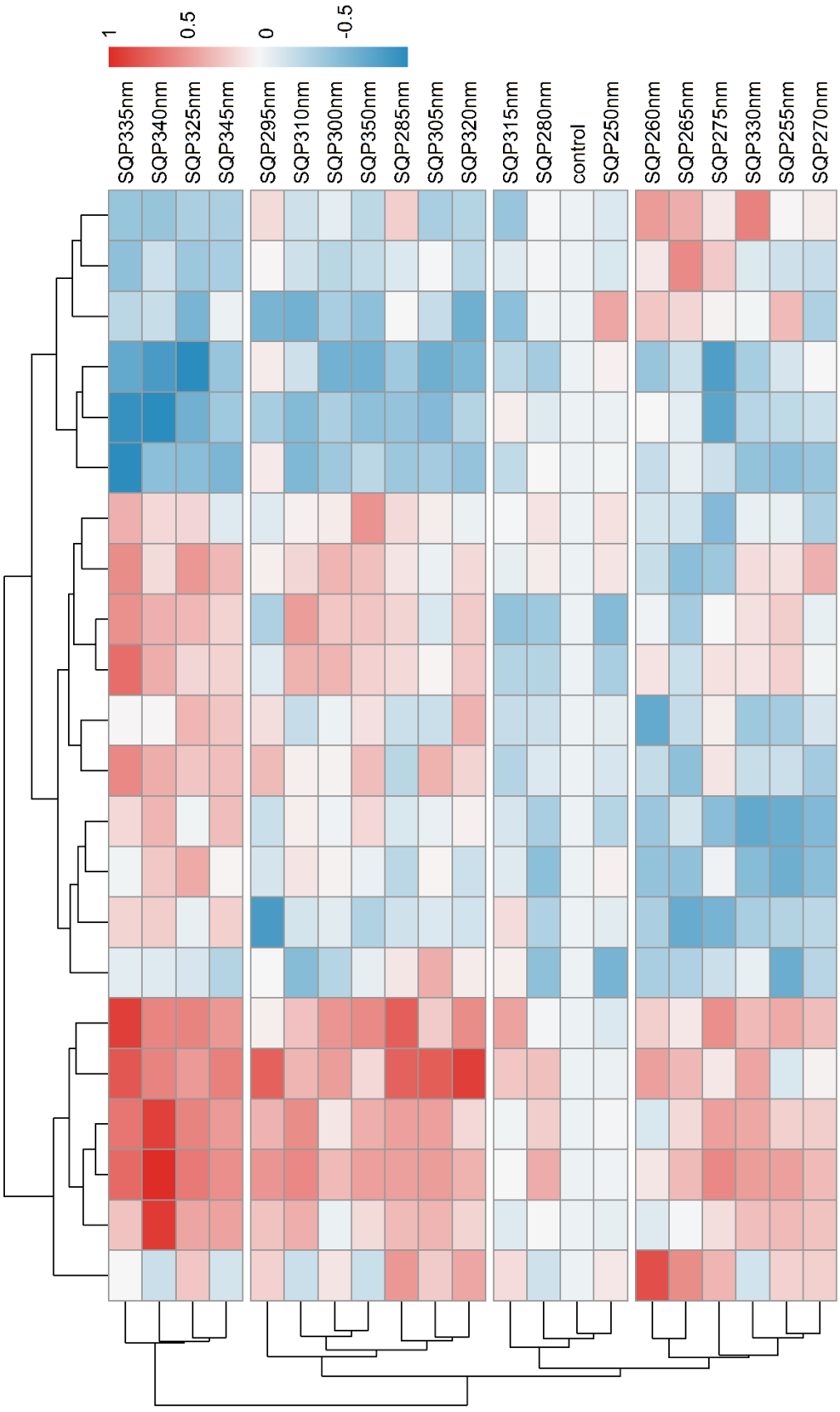

***Figure A5.8**: Heatmap of the morphome depending on the pitch of nanopits in the NSQ pitch array. The heatmap is ordered by hierarchical clustering using Euclidean distances. The features are normalized between 0 and 1 and corrected against the control by dividing the control from the other substrates. The number behind the geometry describer corresponds to the centre-to-centre spacing.*